

Uniwersytet Wrocławski  
Wydział Fizyki i Astronomii

Maciej P. Lewicki

# Charged hadron production in central Ar+Sc collisions at the CERN SPS

Produkcja naładowanych hadronów w centralnych  
zderzeniach Ar+Sc w CERN SPS

Doctoral dissertation prepared  
under advisory of  
**prof. dr hab. Ludwik Turko**  
at the Institute of Theoretical Physics  
University of Wrocław



## Acknowledgements

I would like to express my gratitude to the people who helped on the course of completing this work.

Prof. Ludwik Turko for the scientific guidance and invaluable motivation when it was most needed.

Prof. Marek Gaździcki and prof. Peter Seyboth for the most reliable care of scientific merits of the project.

My colleagues in the NA61/SHINE Collaboration, whose efforts particularly contributed to the successful completion of this work: Michał Naskręt, Piotr Podlaski, Emil Kaptur, Szymon Puławski, Andrey Seryakov, and Evgeny Andronov.

My parents and sister for never-ending support.

Finally, completing this work would not have been possible without limitless patience and countless sacrifices of my family. To my wife Ola and my son Józio: thank you so much!

Project was supported by Narodowe Centrum Nauki (grants: PRELUDIUM 2017/27/N/ST2/00778, HARMONIA 2012/04/M/ST2/00816 and HARMONIA 2015/18/M/ST2/00125).

## Abstract

### Research Objectives

The main goal of this work was to identify and obtain spectra of charged hadrons produced in Ar+Sc interactions at six beam momenta in the range of 13A-150A GeV/c. The project is a vital part of the NA61/SHINE programme, which main research goal is to study the collisions of intermediate systems, searching for the signatures of the *onset of deconfinement* and the *critical point*.

Measured properties of hadron production in Ar+Sc collisions suggest that this particular reaction is on the boundary between "heavy" and "light" systems. Ar+Sc may be the smallest of studied systems, in which colliding nucleons create not a number of isolated N+N events, but a collectively evolving fireball, with a possible formation of quark-gluon plasma at top SPS energies.

### Methodology

Collisions of Ar+Sc were recorded in 2015 by the NA61/SHINE Collaboration. The work presented in this thesis involves the selection of events in terms of quality and physics relevance, identification of the most abundant charged hadrons and calculation of their kinematic spectra. The final results of this thesis deliver key information on the properties of  $\pi^+$ ,  $\pi^-$ ,  $K^+$ ,  $K^-$ ,  $p$ , and  $\bar{p}$  produced in strong and electromagnetic interactions in the most central collisions of Ar+Sc. The spectra in transverse momentum and rapidity were measured for each of the listed particle species and mean multiplicities of charged kaons were calculated.

### Impact on studies of strongly interacting matter

The project presented in this dissertation delivers important information on the influence of the sizes of colliding ions on the properties of hadron production. In particular, the measurement of strangeness production ( $K^+/\pi^+$ ) in Ar+Sc establishes a puzzling system size dependence, that none of the commonly used theoretical models can reproduce, therefore motivating further phenomenological studies. Similarly, measured longitudinal spectra of protons and anti-protons provide interesting input for studies of the equation of state in a baryon-rich medium. Broader knowledge about system size dependence of hadron production properties will surely bring important insight into the basic properties of strongly interacting matter in the vicinity of the onset of deconfinement.

## Streszczenie

### Cele naukowe

Podstawowym celem tej pracy była identyfikacja i pomiar widm naładowanych hadronów wyprodukowanych w centralnych zderzeniach Ar+Sc przy sześciu pędach wiązki w przedziale 13A-150A GeV/c. Badania te są ważną częścią programu Kolaboracji NA61/SHINE, której głównym celem jest poszukiwanie oznak początku spontanicznego uwolnienia kwarków oraz punktu krytycznego chiralnej przemiany fazowej.

Wykonane pomiary własności produkcji hadronów w zderzeniach Ar+Sc sugerują, że reakcja ta jest na swoistej granicy pomiędzy “ciężkimi” a “lekкими” systemami. Tzn., możliwe jest, że zderzenia Ar+Sc to najmniejszy z badanych układów, w którym zderzenia poszczególnych nukleonów tworzą nie oddzielne klastry N+N, a kolektywnie ewoluujący układ, w którym może być tworzona plazma kwarkowo-gluonowa w najwyższych energiach SPS.

### Metodologia

Dane o zderzeniach Ar+Sc zebrane zostały w roku 2015 przez kolaborację NA61/SHINE. Proces analizy tych danych prezentowany tutaj dotyczy kolejno wyboru badanych zderzeń zarówno ze względu na jakość pomiaru, jak i na badaną fizykę, następnie identyfikację najliczniej produkowanych naładowanych hadronów oraz wreszcie wyznaczenie ich widm. Uzyskane rezultaty dostarczają najważniejszych informacji dotyczących  $\pi^+$ ,  $\pi^-$ ,  $K^+$ ,  $K^-$ ,  $p$  oraz  $\bar{p}$  produkowanych w oddziaływaniach silnych i elektromagnetycznych w najbardziej centralnych zderzeniach Ar+Sc. Widma pędu poprzecznego oraz pośpieszności zostały zmierzone dla każdej z wymienionych cząstek oraz obliczone zostały średnie krotności naładowanych kaonów.

### Znaczenie dla badań oddziaływań silnych

Rezultaty referowanych badań pozwalają przede wszystkim na poznanie wpływu rozmiaru zderzanych jonów na własności produkcji hadronów. W szczególności, zaobserwowana zależność produkcji dziwności ( $K^+/\pi^+$ ) od rozmiaru układu nie może być wytłumaczona w ramach stosowanych powszechnie modeli teoretycznych zderzeń ciężkich jonów, dostarczając tym samym motywacji do dalszych badań fenomenologicznych. Podobnie zmierzone widma pośpieszności protonów i antyprotonów pozwalają na dalsze badania równania stanu w materii o wysokiej gęstości barionowej. Szczegółowa wiedza na temat zależności produkcji hadronów od rozmiarów zderzanych układów z pewnością przyczyni się do lepszego zrozumienia podstawowych własności silnie oddziałującej materii w pobliżu początku spontanicznego uwolnienia kwarków.



## Contents

<b>1</b>	<b>Introduction</b>	<b>8</b>
<b>2</b>	<b>Glossary</b>	<b>12</b>
<b>I</b>	<b>Theory</b>	<b>14</b>
<b>3</b>	<b>Quantum Chromodynamics</b>	<b>14</b>
<b>4</b>	<b>Phases of strongly interacting matter</b>	<b>14</b>
<b>5</b>	<b>Heavy-ion collisions</b>	<b>16</b>
<b>6</b>	<b>Wounded Nucleon Model</b>	<b>18</b>
<b>7</b>	<b>Thermal model</b>	<b>19</b>
7.1	System size dependence . . . . .	20
<b>8</b>	<b>Statistical Model of Early Stage</b>	<b>22</b>
8.1	Key assumptions . . . . .	22
8.2	Enhancement of entropy . . . . .	23
8.3	Strangeness at phase transition . . . . .	24
8.4	Collision temperature . . . . .	25
8.5	Predictions for intermediate size systems . . . . .	26
<b>9</b>	<b>Strangeness production at SPS energies</b>	<b>26</b>
<b>10</b>	<b>Summary on phenomenology of deconfinement</b>	<b>28</b>
<b>II</b>	<b>Experiment</b>	<b>30</b>
<b>11</b>	<b>NA61/SHINE facility</b>	<b>30</b>
11.1	SPS beam . . . . .	30
11.2	Trigger and Sc target . . . . .	33
11.3	Time Projection Chambers and Tracking . . . . .	34
11.4	Time Of Flight . . . . .	36
11.5	Projectile Spectator Detector and Centrality . . . . .	37
11.6	Future upgrades . . . . .	38
<b>12</b>	<b>Data</b>	<b>39</b>
12.1	Reconstruction . . . . .	39
12.2	Ionisation energy loss measurement . . . . .	40
12.2.1	Calibration and corrections . . . . .	41
12.2.2	Mean energy loss calculation . . . . .	42
12.3	Simulation . . . . .	43

<b>III</b>	<b>Analysis</b>	<b>45</b>
<b>13</b>	<b>Overview of analysis procedure</b>	<b>45</b>
13.1	Complementary analyses . . . . .	45
<b>14</b>	<b>Data refinement</b>	<b>46</b>
14.1	Event selection . . . . .	46
14.2	Event centrality . . . . .	49
14.3	Track selection . . . . .	50
14.4	Acceptance . . . . .	51
<b>15</b>	<b>Particle identification</b>	<b>51</b>
15.1	Basic model of $dE/dx$ distribution . . . . .	51
15.2	Remarks on model and data . . . . .	52
15.3	Toy simulation of $dE/dx$ distributions . . . . .	53
15.4	Model and parameter estimation . . . . .	54
15.4.1	Alternative models . . . . .	54
15.4.2	Simultaneous fit in multiple bins of $p_T$ . . . . .	55
15.4.3	Fit refinement . . . . .	57
15.5	Identity method . . . . .	59
15.5.1	Identity method with interpolation . . . . .	60
<b>16</b>	<b>Corrections</b>	<b>61</b>
16.1	Simulation and event selection . . . . .	61
16.2	Geometrical correction . . . . .	62
16.3	Feed-down from weak decays . . . . .	63
16.4	Tuning of MC corrections . . . . .	63
16.5	Total corrections . . . . .	64
<b>17</b>	<b>Uncertainties</b>	<b>64</b>
17.1	Statistical uncertainty estimation with bootstrapping . . . . .	65
17.1.1	Systematic uncertainties . . . . .	65
17.1.2	Uncertainties in rapidity spectra and mean multiplicities . . . . .	67
<b>IV</b>	<b>Results and discussion</b>	<b>73</b>
<b>18</b>	<b>Charged pions</b>	<b>73</b>
<b>19</b>	<b>Charged kaons</b>	<b>77</b>
19.1	Transverse Momentum Spectra . . . . .	77
19.2	Inverse slope parameter $T$ . . . . .	78
19.3	Rapidity spectra . . . . .	78
19.4	Kaon mean multiplicity . . . . .	79

<b>20 Protons and antiprotons</b>	<b>85</b>
20.1 Transverse momentum spectra . . . . .	85
20.2 Rapidity spectra . . . . .	85
20.3 Antiproton mean multiplicities . . . . .	87
<b>21 Collision energy and system size dependence</b>	<b>90</b>
21.1 The lack of horn . . . . .	90
21.2 Hypothesis of the onset of fireball . . . . .	92
21.3 Proton rapidity spectra . . . . .	95
21.4 Comparison with theoretical models . . . . .	96
21.4.1 Statistical models . . . . .	96
21.4.2 Dynamical models . . . . .	97
21.4.3 Proton and antiproton spectra . . . . .	98
21.4.4 Summary on model predictions . . . . .	99
<b>22 Summary and Outlook</b>	<b>104</b>
 <b>V Appendix</b>	 <b>111</b>
<b>A Kinematics</b>	<b>111</b>
A.1 Units and definitions . . . . .	111
A.2 Useful quantities . . . . .	111
<b>B Minimization algorithms</b>	<b>112</b>
B.1 Maximum likelihood for binned data . . . . .	113
B.2 Extension for simultaneous fits . . . . .	113
B.3 Additional remarks . . . . .	114
B.4 Software and technical details . . . . .	114
<b>C Numerical data</b>	<b>115</b>
C.1 Kaon $y$ - $p_T$ spectra . . . . .	115
C.2 Proton $y$ - $p_T$ spectra . . . . .	127
C.3 Kaon rapidity spectra . . . . .	127
C.4 Proton rapidity spectra . . . . .	128
<b>D Supplementary plots of fitted <math>p_T</math> distributions</b>	<b>128</b>
D.1 Two-dimensional spectra . . . . .	129
D.2 Charged kaon $p_T$ distributions . . . . .	130
D.3 Proton and antiproton $p_T$ distributions . . . . .	136

# 1 Introduction

The research presented in this thesis concerns properties of the most abundant charged hadrons ( $\pi^+$ ,  $\pi^-$ ,  $K^+$ ,  $K^-$ ,  $p$ ,  $\bar{p}$ ) produced in collisions of  $^{40}\text{Ar}+^{45}\text{Sc}$  at whole range of SPS beam momenta: 13A, 19A, 30A, 40A, 75A, 150A GeV/c. This project is a vital part of the two dimensional scan performed by the NA61/SHINE Collaboration: besides studying collisions at different energies also the sizes of colliding nuclei are varied. By now a rich dataset was gathered, including reactions of ions: Be+Be, Ar+Sc, Xe+La, Pb+Pb and reference data on  $p+p$  interactions. Ar+Sc reactions studied in this work are particularly interesting, as the measurements indicate this system being on the boundary between "heavy" and "light" ions. The results obtained here establish a system-size dependence of hadron production properties that so far can be explained neither within statistical, nor dynamical models.

## Purpose of this work

The study of collisions of protons and heavy ions offers an incredibly rich source of information about the collective behaviour of strongly interacting matter. It enables us to reach beyond elementary interactions and ask more involved questions: what are the phases of strongly interacting matter? How do the transitions between these phases happen? After almost 50 years of measurements of hadron production at a broad range of collision energies and countless theoretical attempts at explaining quarks and gluons interplay we have some answers, but as it is usually the case in physics – even more questions.

Pioneering studies of deconfinement of strongly interacting matter were conducted by the NA49 Collaboration. The results on Pb+Pb collisions were interpreted as evidence of the *onset of deconfinement* – energy at which the matter created at an early stage of the collision appears in the form of quark-gluon plasma. The quest of understanding this phenomenon is now being continued by a new generation of heavy-ion experiments, most notably: STAR at RHIC and NA61/SHINE at CERN.

Phase structure of hadronic matter becomes more and more involved correspondingly to progress in a theoretical understanding of the subject and collecting more and more experimental data. While the largest experimentally available now energies at LHC and RHIC colliders seem to provide data related to the crossover region between the hadron gas and quark-gluon plasma then the SPS fixed-target NA61/SHINE experiment is particularly suited to explore the hypothetical first-order phase transition line with the critical point included.

The phases of QCD matter depend on two primary parameters: temperature  $T$  and baryo-chemical potential  $\mu_B$ . Varying the energy of the collision enables traversing the phase-diagram in a particular direction – increasing collision energies results in smaller  $\mu_B$  and larger  $T$ . In order to study a broader domain of the QCD phase-space, we also vary the sizes of colliding nuclei.

Hence with the NA61/SHINE's unique two-dimensional scan in collision energy and system size we seek the signatures of the onset of deconfinement, aiming to pinpoint the location of the phase-transition line.

Discussing the purpose of the presented studies, it is important to highlight the advantages of studying collisions of small ions over peripheral collisions of Pb+Pb or Au+Au. Firstly, non-central collisions of heavy-ions are characterized by significant asymmetries of the created fireball, resulting in large anisotropies in transverse momentum distribution. Secondly, a system volume in selected most central collisions of small ions is well defined and such a set can be determined experimentally with high precision. Finally, peripheral collisions may be affected by interaction with fragments that did not interact inelastically.

## Experimental results

In this thesis, measurements of transverse momentum and rapidity spectra of the most abundantly produced charged hadrons,  $\pi^+$ ,  $\pi^-$ ,  $K^+$ ,  $K^-$ ,  $p$ , and  $\bar{p}$ , are presented. Two other analyses are performed in parallel:

- “ $h^-$ ” analysis delivers information on negatively charged pions in large acceptance. Most recent results are referred in [1] by Michał Naskręć;
- “ $tof-dE/dx$ ” analysis measuring charged hadron spectra close to mid-rapidity. Most recent results were reported in [2] by Piotr Podlaski.

It is important to note, that simultaneous analyses of the same dataset performed by different persons, though seemingly redundant, gives an important cross-check, ensuring the correctness of analysis procedures. Results of each method overlap in limited regions of the acceptance, allowing for direct comparison. In the preparation of final results some of the preliminary measurements from complementary analyses ( $h^-$  and  $tof-dE/dx$ ) were used.

The main quantities studied here are the kinematic spectra and the absolute yields of particles (when they are possible to determine). The two-dimensional kinematic spectra are analysed in terms of collision dynamics: rapidity spectra  $dn/dy$  provide information on the longitudinal evolution of the fireball, while  $\frac{d^2n}{dy dp_T}$  spectra can be studied for transverse expansion of the system. The hadron yields and the ratios of produced species are analysed in terms of the conditions created in the fireball through comparison with theoretical models and data on other systems.

The results on Ar+Sc collisions compiled with data on  $p+p$ , Be+Be, and Pb+Pb establish a system size dependence of key properties of hadron production, constituting a central subject of this dissertation.

## Thesis structure

The first part of this thesis is devoted to a summary of the theoretical and phenomenological description of strongly interacting matter, focusing on topics

relevant to this work, in particular particle production and strangeness production in the vicinity of the onset of deconfinement. Special attention is paid to the system size dependence of observables.

In the second part, the NA61/SHINE experimental setup is described with the main focus given to detector components closely related to particularities of the  $dE/dx$  hadron identification method.

The third part includes details of data analysis: event selection, refinement of data quality, particle identification, and the estimation of measurement uncertainties and corrections.

The last part of this thesis discusses the final results, which are compiled with data on other systems. The emerging system size dependence is discussed in confrontation with theoretical predictions.

## Author's contribution

In large collaborations, it is usually a collective effort of many scientists that enables the realization of high reaching goals. Therefore it is important to highlight what work was done by the author.

My role in the presented research starts from the data taking campaign in 2015 at CERN's North Area, overseeing the operation of the experiment during multiple "shifts" and participating in experimental service work.

In the first step of data treatment a set of basic quality cuts on collision events and particle tracks was established (sec. 14) in cooperation with other Ar+Sc data analysers: Evgeny Andronov, Michał Naskręt, and Andrey Seryakov. Similarly, the procedure of determination of collision centrality was developed (sec. 14.2).

Later I further extended the list of event and track selection rules to fit the needs of forward rapidity analysis and particle identification through  $dE/dx$  measurements. A complex and tedious process of examining the  $dE/dx$  distributions resulted with the best possible quality data, which is crucial for reliable particle identification and consequently a correct calculation of yields and spectra.

Following the improvements of the quality of the data I similarly worked on improvements of particle identification procedure (sec. 15). In the first step, I designed a physics motivated toy simulation of  $dE/dx$  distribution, later to be used in tests of statistical models fitted to the data. A multitude of models was tested and validated against both the simulated and recorded datasets. Some important improvements were made, in particular concerning the dependence of model parameters on the number of measured ionization points (sec. 15.3). In the following step, I designed and implemented a statistical method of fitting multiple model-histogram pairs with shared parameters, which turned out crucial for fit stability.

In the next stage of analysis I have recalculated the identified hadron  $\frac{d^2n}{dp dp_T}$  spectra into  $\frac{d^2n}{dy dp_T}$  spectra using the identity method, which I extended implementing an interpolation procedure (sec. 15.5).

In parallel, I have analysed the Monte Carlo simulations of the Ar+Sc reactions, which is used to correct raw experimental data for a number of effects, including acceptance geometry or weak decays. I have calculated corrections originating from various sources and applied them to obtain the final  $\frac{d^2n}{dy dp_T}$  spectra, which were also integrated to obtain  $\frac{dn}{dy}$  distributions. I have combined my results with the results of a complementary analysis of  $tof-dE/dx$  in order to obtain larger rapidity coverage and extract mean kaon multiplicities.

The final results are compared with relevant data from other reactions and collision energies, as well as theoretical models. Additionally, a recalculation of system size dependence within the statistical model was done.

## 2 Glossary

### Acronyms

ADC	Analogue to Digital Conversion
BPD	Beam Position Detector
CERN	The European Organization for Nuclear Research, acronym derived from <i>Conseil européen pour la recherche nucléaire</i>
CE, GCE	Canonical Ensemble, Grand Canonical Ensemble
CP	Critical Point
HRG	Hadron Resonance Gas
LHC	Large Hadron Collider
MC	Monte-Carlo (simulation)
MIP	Minimum Ionization Particle
MWPC	Multi-Wire Proportional Chamber
NA61/SHINE	North Area 61 / SPS Heavy Ion and Neutrino Experiment
QCD	Quantum ChromoDynamics
QGP	Quark-Gluon Plasma
PID	Particle IDentification
PSD	Projectile Spectator Detector
RHIC	Relativistic Heavy Ion Collider
RMS	Root Mean Squared
SMES	Statistical Model of the Early Stage
SPS	Super Proton Synchrotron
TOF	Time of Flight
TPC	Time Projection Chamber, also VTPC is Vertex-TPC and MTPC is Main-TPC
WNM	Wounded Nucleon Model



## Specific nomenclature

Acceptance	Momentum space region from where detectable particles originate from.
Centrality	Measure of how close the centres of colliding ions are on the plane perpendicular to beam axis; alternatively: a measure corresponding to the number of nucleons that participated in the collision.
Wounded nucleons	Nucleons that interacted inelastically in the collision of ions.
Collision spectators	Nucleons that did not interact inelastically in the collision and continue to propagate further close to their original trajectory (beam axis).
Mid-rapidity	Values of rapidity $y$ close to $y = 0$ , with varying ranges of proximity.
Reconstruction	Process of reading raw detector data and calculation of physical quantities (such as momentum or charge) through a series of dedicated algorithms.
Residuals	At given $x$ : $(\text{data}(x) - \text{model}(x)) / \text{data uncertainty}(x)$ .
Tracking	Detection of particle trajectories.

---

## Part I

# Theory

### 3 Quantum Chromodynamics

Quantum Chromodynamics (QCD) describes the strong nuclear interactions, one of the four currently distinguished fundamental forces. It is a part of the Standard Model, a theory that unifies three of these forces, including also electromagnetic and weak interactions. QCD is a SU(3) gauge theory, where the degrees of freedom in the Lagrangian are defined in terms of quark fields  $q_{\alpha f}^c$  where  $\alpha = 1, \dots, 4$  is a Dirac spinor index,  $c = 1, 2, 3$  is a colour index and  $f$  iterates flavour: up, down, charm, bottom and top. Interactions are encoded within gluon vector fields  $A_\mu^a$ , where  $a$  labels an octet of gluon colour states. The Lagrangian takes a deceptively simple form:

$$\mathcal{L} = -\frac{1}{4}G_{\mu\nu}^a G_{\mu\nu}^a + \sum_f^{N_f} \bar{q}_f (i\gamma^\mu D_\mu - m_f) q_f, \quad (1)$$

where  $G_{\mu\nu}^a$  is the field strength tensor:

$$G_{\mu\nu}^a = \partial_\mu A_\nu^a - \partial_\nu A_\mu^a + g f^{abc} A_\mu^b A_\nu^c, \quad (2)$$

$f^{abc}$  are the SU(3) structure constants,  $D_\mu$  denotes covariant derivative and  $m_f$  stands for quark masses.

Among many captivating features of QCD, one is particularly interesting in the context of heavy-ion collisions. The dimensionless coupling constant  $g$  decreases logarithmically with increasing energy scale (or decreasing length scale). At energies much lower than QCD scale parameter  $\Lambda_{QCD}$ , quarks and gluons are always confined within colourless hadrons, while at sufficiently large momenta they become nearly free. The colour confinement as well as the asymptotic freedom are perhaps the two most profound properties of the theory. Both of the phenomena, together with intrinsic symmetries of QCD determine the phase structure of strongly interacting matter.

### 4 Phases of strongly interacting matter

The phases of matter at zero baryon density  $\mu_B = 0$  are well established, as they can be studied with non-perturbative *ab initio* simulations on a lattice of points in space and time (lattice-QCD). At low baryon density, the constituents of hadronic matter are mostly mesons, and the dominant interaction is resonance formation. With increasing temperature, different resonance species of increasing mass are formed, leading to a gas of ever-increasing degrees of freedom. The calculations performed with physical quark masses show us that there is a

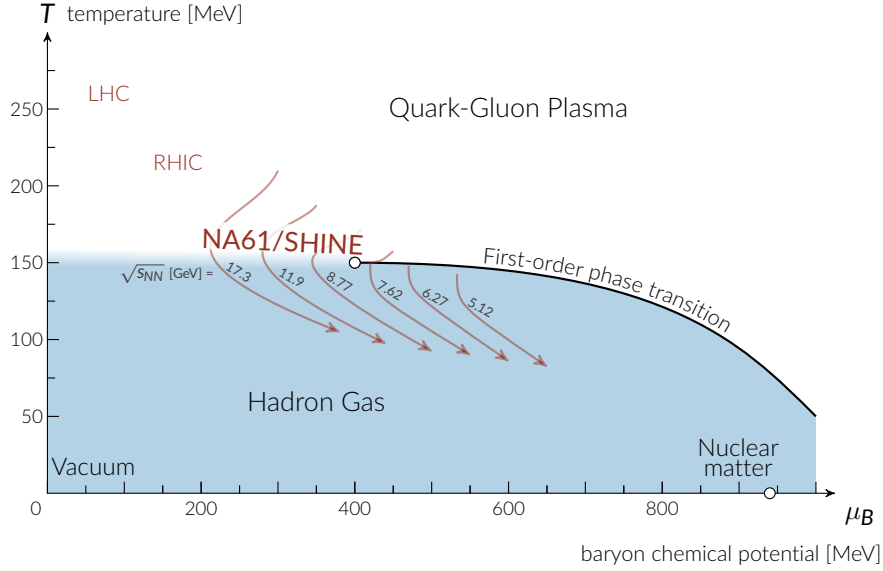


Figure 1: Schematic phase diagram of strongly interacting matter in temperature  $T$  and baryon chemical potential  $\mu_B$ . Red lines show possible trajectories of the evolution of the fireball created in collisions at SPS energy range. See text for a description of phases and critical phenomena pictured in the diagram.

pseudo-critical temperature  $T_C \approx 155$  MeV [3] at which a rapid crossover takes place into a regime dominated by quarks and gluons – quark-gluon plasma (QGP). Such conditions describe well the state of the Universe as young as few microseconds, also well approximated by the midrapidity region in heavy ion collisions at Large Hadron Collider (LHC) and highest energy collisions at Relativistic Heavy Ion Collider (RHIC).

With increasing baryon density the number of quarks dominates over the number of antiquarks. At low temperatures, this translates directly to the growing contribution of baryons and baryonic resonances in the gas of hadrons. The region of the boundary between the meson- and baryon-dominated matter, close to the critical temperature  $T_C$  is accessible by the Super Proton Synchrotron (SPS) (see Fig. 1). Arguments based on a variety of models [4] indicate that the chiral symmetry restoration transition is first order at large  $\mu$ . Crossover phase transition at low  $\mu_B$  together with the first-order transition at high  $\mu_B$  leads to a straight-forward conclusion: the phase diagram features a critical point (CP). The presence and location of the CP is a matter of extensive theoretical studies and a variety of models propose widely scattered estimates [5]. Higher baryon densities are accessible by low energy heavy-ion collisions in experiments such as AGS, HADES, or at planned future facilities at FAIR and NICA.

## 5 Heavy-ion collisions

In this section let us summarize what is known about the sequence of events in collisions of (ultra-)relativistic heavy ions. In the centre of mass reference frame, the collision is initiated by two Lorentz contracted nuclei incoming from opposite directions at velocities close to the speed of light. The contraction of the nuclei is on the level of  $\gamma=2.7\text{---}9.2$  at SPS energies, reaching over 100 at top RHIC energy and another order of magnitude higher at LHC, while the velocities differ from the speed of light only about 0.15%, 0.0001% and 0.0000001% at SPS, RHIC, and LHC top energies respectively.

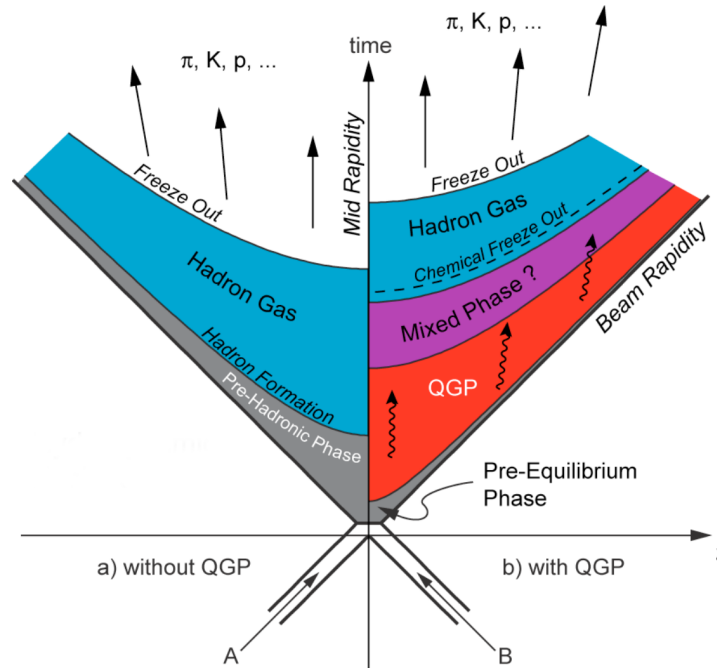


Figure 2: Schematic visualization of the time evolution of the fireball created in collisions with (b) and without QGP formation (a). (Attempts of determination of the original author of this graphic were not successful.)

In the initial stage of the collision two Lorentz contracted discs overlap, creating a high energy density region. At this point, the colour fields and charges interact and some colour charge exchange may occur. In the collision energy regime relevant in this thesis the interactions are soft, meaning that they involve little transverse momentum ( $p_T$ ) transfer. The momentum of incident ions determines the further evolution of the system. At low collision energies, the baryons are stopped entirely and a fireball of high baryon content is created. At sufficiently large energies the colliding ions traverse each other, creating a high energy density, low baryon density system around the mid-

point between the two receding discs. The baryon content is then cumulated at high absolute values of rapidity ( $|y| \lesssim y_{\text{beam}}$ ). If the early stage fireball reaches the critical temperature the hadrons dissolve and create a droplet quark-gluon plasma. The onset of the formation of QGP, as well as its effect on entropy production, are being extensively studied both theoretically and experimentally.

The hot and dense fireball equilibrates, expands, and cools down – this phase of the system evolution is well described by hydrodynamic simulations [6]. The early stage together with hydrodynamic evolution is estimated at the order of  $10^{-22}$  s since the impact, after which hadron rescattering takes place. Once the strong interactions between the constituents of the fireball cease, the system achieves a chemical freeze-out – the particle composition of the fireball no longer changes. The gas of hadrons still interacts elastically through electromagnetic forces, briefly reaching a kinetic freeze-out – the momenta of produced particles no longer change. The final state hadrons decouple from the system to be registered by the detectors. However, measured momentum distribution can be further altered, as some of the produced hadrons may decay through weak channels.

The right half of the diagram in Fig. 2 shows schematically a possible evolution of the fireball described above. However, at low energies or in collisions of small systems we do not expect a QGP to form, as shown in the left part of the diagram. We believe that this scenario describes the dynamics of collisions of protons, therefore  $p+p$  interactions serve as a baseline for comparisons with heavy-ion collisions. Possible signatures of QGP formation are identified through the comparison with properties of  $p+p$  collisions.

The scheme of fireball evolution presented above yields several important consequences, relevant for good understanding of the theoretical description of heavy-ion collisions, as well as for the correct interpretation of experimental data.

Our insight into the early stage of the collision is heavily limited and there are no direct probes accessible experimentally at SPS energy regime. The first key observable is the chemical composition of detected particles. The absolute yields of produced hadrons can be analysed in terms of thermal production (see next section), enabling to extract information about temperature and density of the fireball. However, these parameters only describe the system at the moment of freeze-out, delivering no direct information on the medium prior to this moment. However, some studies show that the entropy and strangeness production in the early stage of the collision influences final yields of hadrons, thus making it possible to distinguish the degrees of freedom before freeze-out [7, 8].

It is important to note, that the statistical description of collisions assumes thermal equilibrium is reached. Tests of this assumption show an excellent agreement with grand canonical formulation for high energies achieved at LHC and a reasonable agreement at RHIC or even SPS energies. At lower collision energies, such as AGS, local conservation laws must be implemented within the canonical formulation of the model. However, the assumption of thermal equilibrium is not a trivial one. It can be argued that the system is

born into equilibrium, as the number of rescatterings necessary to achieve a thermalized system starting from a non-equilibrium state is much higher than physically possible [9, 10].

Even though the dynamics of heavy-ion collisions are explored for almost 40 years ([11, 12]), many crucial aspects are still unclear or controversial. At which energy can we expect QGP to be formed? What is the order of the phase-transition? Does chiral symmetry restoration coincide with the deconfinement? How can we describe a fireball created in small systems? Moreover, the collisions of  $p+p$ , treated so far as reference data, are recently debated in terms of possible QGP formation [13, 14].

## 6 Wounded Nucleon Model

In order to learn the details of the hot and dense medium created in heavy-ion collisions, a simple reference model is needed. As it was already mentioned in the previous section, we consider  $p+p$  interactions as a baseline, well suited to identify non-trivial behaviour of the fireball, such as QGP formation or collective flow. In Glauber models, nuclear collisions can be described as a superposition of independent nucleon-nucleon interactions, based on experimental information on  $N+N$  cross-sections. Particularly useful for a purpose of the reference model is the Wounded Nucleon Model (WNM) [15]. Few properties of WNM are described in this paragraph to establish a nomenclature used in the following parts of this thesis.

In a straight-forward geometrical approach, we consider two nuclei moving towards themselves along the beam axis. In this work (and in fixed-target experiments in general) the nuclei are distinguished as target and projectile. The distance between the trajectories of the centres of the nuclei is called the impact parameter  $b$ , which determines the centrality. The two nucleons on a collision course (cross-sections of the nucleons overlap in the transverse plane) can either interact – elastically, or inelastically – or pass through each other without any interaction at all. The probability of the interaction is set by measured  $N+N$  cross-sections and in this case only inelastic interactions will be considered, as only these contribute to particle production. The total number of nucleons interacting inelastically  $N_W$  (number of “wounded” nucleons) can be determined solely from collision geometry and the interaction cross-sections.

The particle production within such a model is a superposition of independent nucleon-nucleon collisions. As remarked at the beginning of this paragraph, such a model paired with experimental data on  $p+p$  collisions serves as a baseline for studies of heavy-ion collisions. Deviations from the WNM are attributed to the non-trivial collective behaviour of the system.

There exist dynamical microscopic models, which incorporate more complex mechanisms on top of the described superposition procedure. EPOS [16], UrQMD [17] or PHSD [18] are successful in description of many aspects of particle production in collisions of heavy ions. However, these models are charac-

terized by a very large number of parameters. Even though some of these can be tuned based on experimental results of  $p+p$  collisions, the mechanisms allowing to extend the model to nucleus-nucleus collisions are not obvious.

## 7 Thermal model

The Hadron Gas Model is the most successful implementation of the thermal production of particles in heavy-ion collisions. The degrees of freedom of the final state of the collision are described as a gas of hadrons and resonances.

In such a description, the number densities and momentum distributions of particles are determined by the list of available states (hadrons and resonances) and by the number density of particles in each state, which in turn depends on the energy and the temperature.

The basic quantity required to calculate the hadron yields within the thermal model is the partition function  $Z(T, V)$ . In the grand canonical (GC) ensemble, the partition function for species  $i$  is given by:

$$\ln Z_i^{GC} = \frac{V g_i}{2\pi^2} \int_0^\infty \pm p^2 dp \ln[1 \pm \exp(-(E_i - \mu_i)/T)] \quad (3)$$

The resulting particle density  $n_i$  for a species of particles  $i$  is:

$$n_i = N_i/V = -\frac{T}{V} \frac{\partial \ln Z_i^{GC}}{\partial \mu} = \frac{g_i}{2\pi^2} \int_0^\infty \frac{p^2 dp}{\exp[(E_i - \mu_i)/T] \pm 1} \quad (4)$$

where  $g_i$  is the degeneracy factor,  $T$  is the temperature and  $E$  is the total energy and  $\mu_i$  stands for chemical potential. The (+) and (-) signs are for fermions and bosons respectively. Hadron  $i$  is characterised by baryon number  $B_i$ , third component of the isospin  $I_{3i}$  and strangeness  $S_i$ . The chemical potentials related to baryon number ( $\mu_b B_i$ ), isospin ( $\mu_{I_3} I_{3i}$ ), strangeness ( $\mu_S S_i$ ) ensure the conservation (on average) of the respective quantum numbers. Sum of listed potentials totals to  $\mu_i$ . The (net) baryon number  $N_B$  and the total isospin  $I_3$  of the system are input values that need to be specified according to the colliding nuclei studied. These numbers cannot be precisely determined experimentally, so in a sense, they become parameters of the model, albeit their influence of hadron ratios is not significant.

Taking into account the conservation laws the only parameters of the model are the volume  $V$ , temperature  $T$ , and the baryo-chemical potential  $\mu_B$ . These parameters are fitted with rich data on particle yields [20] (see Fig. 3). In practice the ratios of particle yields are used instead of absolute yields, which allows eliminating the dependence on volume  $V$ , leaving only two free parameters in the model. Fig. 4 shows the results of cited calculations for a wide range of collision energies.

It is important to note in the context of this work, that the thermal model is highly successful in reproducing hadron yields at SPS energies. Even the sharp peak in  $K^+/\pi^+$  ratio is reasonably well fitted once the resonance spectrum is

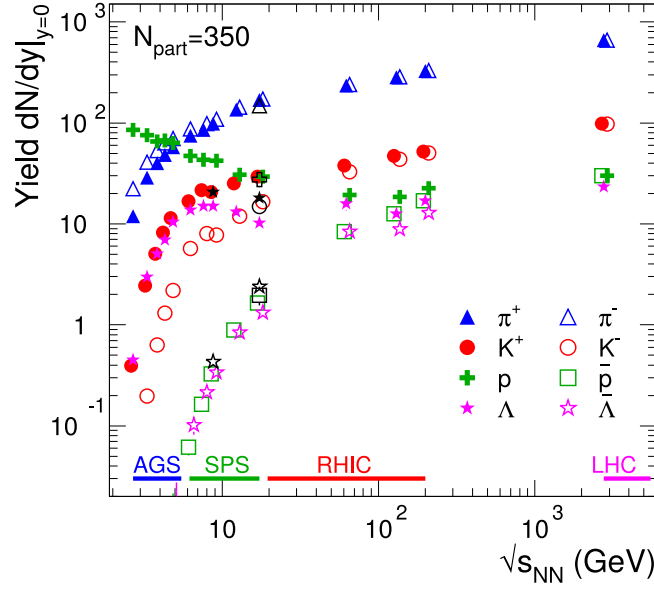


Figure 3: Yields of hadrons produced in heavy ion collisions at energy ranging from less than 3 GeV at AGS up to almost 3 TeV at LHC. Figure adapted from Ref. [19]

extended towards heavier resonances and the  $\sigma$  meson is included in the calculations [21]. The authors of Ref. [21] point out that the improvement of the description of hadron yields at Pb+Pb reactions at 30A GeV/c caused by the inclusion of  $\sigma$  meson is a strong clue of the onset of QCD phase transition.

### 7.1 System size dependence

The grand canonical ensemble is a well-justified choice for systems with a large number of produced hadrons. However, in the case of small systems and low energy collisions, the particle production needs to be calculated with the canonical ensemble (CE). The phase space available for particle production in CE is heavily reduced with respect to GCE, as conservation laws must be implemented locally on an event-by-event basis. Such a feature, also known as “canonical suppression” is particularly important for reliable estimation of strangeness production. It was found that it is the main mechanism explaining the differences of strangeness production between  $p+p$  and Pb+Pb collisions [22].

Let us consider a gas of hadrons with strangeness  $s = +1, 0, -1$  and with total strangeness  $S = 0$ . Thermal density of kaons in the (C) formulation is given as:

$$n_K = \frac{Z_K^1}{V} \frac{S_1}{\sqrt{S_1 S_{-1}}} \frac{I_1(x_1)}{I_0(x_1)} \quad (5)$$



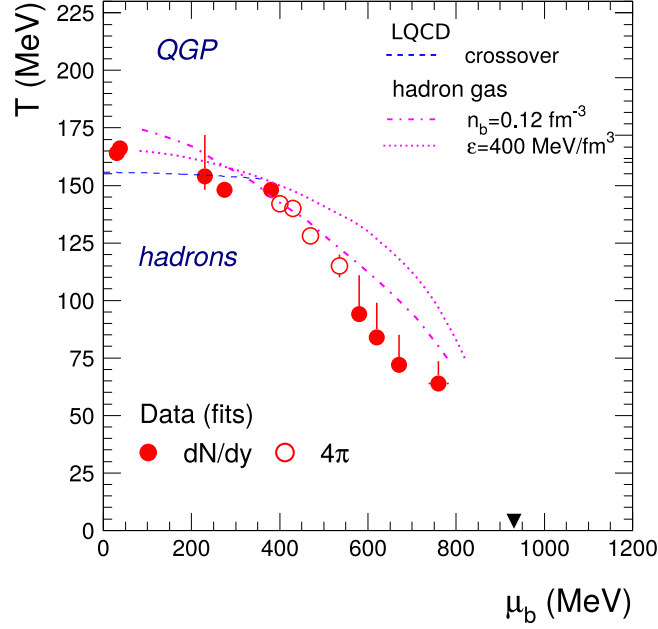


Figure 4: Results of thermal model fits [8] to the data on hadron production in heavy ion collisions. Also pictured: cross-over phase transition (based on IQCD calculations) and hypothetical freeze-out lines of constant energy density and baryon density. Figure adapted from Ref. [8] (IQCD results were updated).

where  $Z_K^1$  is a one-particle partition function of kaon:

$$Z_K^1 = V \frac{g_K}{2\pi^2} m_K^2 T K_2 \left( \frac{m_K}{T} \right). \quad (6)$$

$S_1, S_{-1}$  are the sums over all strangeness 1 and -1 one-particle partition functions:

$$S_1 = Z_K^1 + Z_\Lambda^1 + Z_{K^*}^1 + \dots, \quad (7)$$

$I_1, I_0$  and  $K_2$  are modified Bessel and Hankel functions and  $x_1$  is defined as:

$$x_1 \equiv 2\sqrt{S_1 S_{-1}} \propto V \quad (8)$$

The volume is assumed to be linear in  $N_{\text{part}}$  and given by:

$$V = \frac{V_0}{2} N_{\text{part}} \quad (9)$$

where  $V_0 \approx 7\text{fm}^3$  is taken as the correlation volume which accounts for the locality of the conservation laws. The “canonical suppression factor” measuring the deviation of kaon density from its GC value  $n_K^{\text{GC}}$  can be defined as:

$$F_{CS1} = \frac{I_1(x_1)}{I_0(x_1)} \quad (10)$$

Fig. 5 shows the dependence of  $F_{CS1}$  on the  $N_{\text{part}}$  calculated with an updated list of strange hadrons [23] for three collision energies: lowest and highest SPS with highest energy RHIC for comparison.

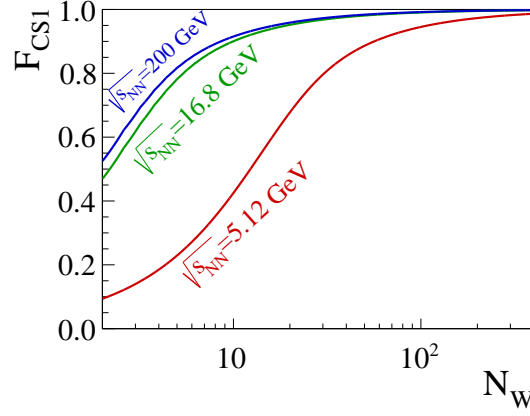


Figure 5: Strangeness suppression factor  $F_{CS1}$  calculated for lowest and highest SPS and top RHIC collision energies.

## 8 Statistical Model of Early Stage

A multitude of implementations of the thermal model were employed in describing hadron production in the vicinity of suspected QGP phase transition. The Statistical Model of Early Stage (SMES) [7, 24] uses a unique approach, featuring a deconfinement as one of its assumptions.

While the HRG model describes well the situation at the freeze-out, we are still blind to anything that happens before. The Statistical Model of the Early Stage (SMES) identifies hadron production signatures that are inherently tied to QGP formation or lack thereof. Some quantities, like strangeness production, are greatly influenced by the degrees of freedom of the medium in the fireball. The model assumes the creation of the early-stage matter according to the principle of maximum entropy. It features a first-order phase transition, thus in consequence the matter appears in three phases – confined, mixed, and deconfined – depending on which phase maximises the entropy.

### 8.1 Key assumptions

The basic assumption of the SMES is that the production of new degrees of freedom during the early stage of A+A collisions is a statistical process. Thus the formation of all microscopic states allowed by conservation laws is equally probable, i.e. a macroscopic state probability  $P$  is:

$$P \sim e^S \quad (11)$$

where  $S$  is the entropy of the macroscopic state. The properties of the state produced at the early stage are entirely defined by the available energy and the volume in which production takes place.

Elementary particles of strong interactions are quarks and gluons. The deconfined state is considered to be composed of  $u$ ,  $d$ , and  $s$  quarks, and the corresponding anti-quarks each with the internal number of degrees of freedom equal to 6 (3 colour states  $\times$  2 spin states). The contribution of  $c$ ,  $b$  and  $t$  quarks is neglected due to their large masses. The internal number of degrees of freedom for gluons is 16 (8 colour states  $\times$  2 spin states). The masses of gluons and non-strange (anti-)quarks are taken to be 0, the strange (anti-)quark mass is taken as 175 MeV.

It is further assumed that the matter created at the early stage expands, hadronizes and freezes-out. During these stages the total entropy and the total number of  $s$  and  $\bar{s}$  quarks created in the early stage are conserved. The only process which changes the entropy content of the produced matter during the expansion is assumed to be the interaction with the baryonic subsystem.

The model defined with listed assumptions predicts numerous signatures of the phase transition in a form of heating curves of strongly interacting matter, shown in Fig. 6.

## 8.2 Enhancement of entropy

The entropy production in heavy ion collisions should depend on the form of matter present at the early stage of the fireball. The deconfined matter is expected to lead to a final state with higher entropy than that created by confined matter. As the majority of all particles produced in high energy interactions are pions, they are also the main carriers of produced entropy. It is then natural to expect an enhanced production of pions when the deconfined state is formed in the collision.

We further consider the pion multiplicity proportional to the initial entropy. The experimental ratio  $\langle\pi\rangle/\langle N_P\rangle$  dependence on the collision energy can be parametrized as:

$$\frac{\langle\pi\rangle}{\langle N_P\rangle} \propto g^{1/4} F, \quad \left( F = \frac{(\sqrt{s_{NN}} - 2m_N)^{3/4}}{(\sqrt{s_{NN}})^{1/4}} \right) \quad (12)$$

where  $g$  is the number of internal degrees of freedom, which is substantially different in the confined phase and in QGP [25], namely:

$$\left( \frac{g_Q}{g_W^{ns}} \right)^{1/4} = \left( \frac{47.5}{16} \right)^{1/4} \approx 1.31 \quad (13)$$

Such a substantial difference in entropy production is indeed visible in the rich experimental data available [25] and is frequently called *the kink*.

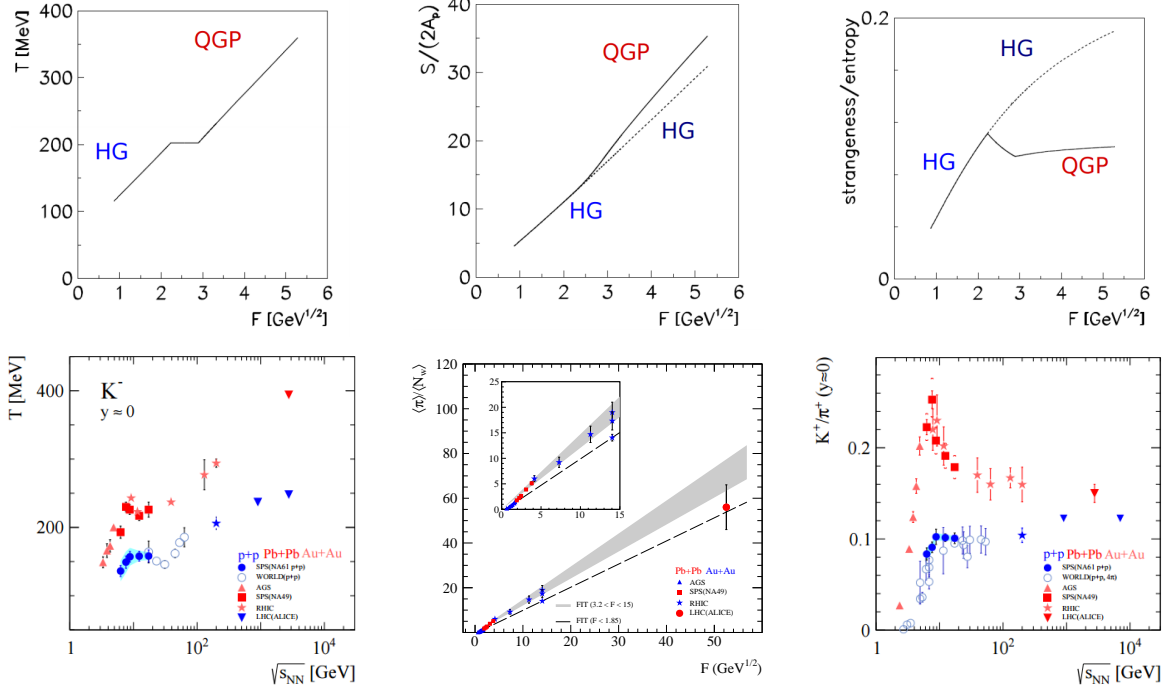


Figure 6: Heating curves of strongly interacting matter predicted by SMES [7]: (left) a plateau in temperature, (middle) an enhancement of entropy production and (right) sharp peak in strangeness to entropy production ratio in dependence on the collision energy ( $F$  is approximately  $\propto s_{NN}^{1/4}$ ). The top row shows model predictions and the bottom row shows corresponding experimental data – see text for details.

### 8.3 Strangeness at phase transition

There is no strange content in the colliding nuclei, so any (anti-)strange contribution recorded in the detectors is produced in the strong interactions, during the collision. Therefore (anti-)strange particles serve as an excellent probe of the phase transition dynamics.

The predictions of SMES of the strangeness dependence on collision energy invoke the Boltzmann approximation:

$$\langle N_i \rangle = \frac{gV}{(2\pi)^3} \int d^3p \frac{1}{e^{E/T} \pm 1} \quad (14)$$

which is approximated for heavy and light particles respectively:

$$(\text{heavy:}) \approx gV \left( \frac{MT}{2\pi} \right)^{3/2} e^{-M/T}, \quad (\text{light:}) \approx gV \frac{2\pi^2}{4 \cdot 45} T^3 \quad (15)$$

In the confined phase  $m_K \gg T$ , total strangeness production is proportional to  $T^{3/2} \exp(-m_h/T)$  and the entropy produced is proportional to  $T^3$ . Therefore, the strangeness to pion production ratio is approximately  $\propto T^{3/2} \exp(-m_K/T)$  and strongly increases with the collision energy. In the deconfined phase, on the other hand, the mass of the strangeness carriers is significantly smaller ( $m_s \approx 175\text{MeV}$ , the strange quark mass). Due to the lower mass ( $m_s < T$ ) the strangeness yield becomes approximately proportional to the entropy (both are proportional to  $\propto T^3$ ) and the strangeness to entropy production ratio becomes constant with energy.

In order to compare the values obtained for confined matter and QGP we investigate the number of strange degrees of freedom present in both cases –  $g_W^s, g_Q^s$  (W – hadronic matter, "W-state"; Q – quark-gluon plasma, "Q-state"). The entropy carried by strange (and antistrange) particles is given by  $S_s = \frac{g_s}{g} S$ . For massless particles of  $j$ -th species we have a relation:  $S_j = 4N_j$ , and  $N_s + N_{\bar{s}} = \frac{S}{4} \frac{g_s}{g}$ . And the strangeness to entropy ratio is equal:

$$\frac{N_s + N_{\bar{s}}}{S} = \frac{1}{4} \frac{g_s}{g} \quad (16)$$

Substitution of  $g_W^s, g_Q^s$  into the equation above results with following ratios:

$$\text{Q-state: } g_Q^s/g_Q \approx 0.22, \quad \text{W-state: } g_W^s/g_W \approx 0.5 \quad (17)$$

This gives us a naive estimate (for massless degrees of freedom) of the ratio of strangeness to entropy production in W- and Q-state.

Therefore a phase transition from W- to Q-state should lead to a decrease of the strangeness to entropy ratio by a factor of about 2. This simple picture is modified significantly due to the non-zero mass of strange degrees of freedom and is in general strongly dependent on collision energy. However, these simple calculation gives us a good intuition of strangeness production at the border of phases. We expect a "jump" in the energy dependence from the larger value for the confined matter to the lower value for the deconfined matter. Thus, within the SMES, the non-monotonic energy dependence of the strangeness to entropy production ratio followed by a plateau at the deconfined value is expected as a direct consequence of the onset of deconfinement.

Experimental results on the strangeness to entropy ratio is perhaps the most famous confirmation of SMES prediction. A very pronounced peak (*the horn*) in the energy dependence is visible for Pb+Pb and Au+Au collisions measurements, while a smooth evolution is observed in the case of  $p+p$  (see: Fig. 6).

## 8.4 Collision temperature

The energy density at the early stage increases with increasing collision energy. Outside the transition region, this leads to an increase in the initial temperature and pressure. On the other hand, one can expect an anomaly in the energy dependence in the phase transition region.

An increase in temperature results in an increase of the transverse expansion of the produced matter and consequently a flattening of the transverse mass spectra of final state hadrons. SMES predicts that at the border of phases the temperature and pressure should stay approximately constant.

The experimental data on transverse spectra are usually parametrized by an exponential dependence:

$$\frac{dN}{m_T dm_T} \cong C \exp\left(-\frac{m_T}{T}\right) \quad (18)$$

Such a parametrization is imperfect though. The Boltzmann  $m_T$  spectrum is modified by a hydrodynamical transverse collective flow. It results in an unstable fit strongly dependent on fit range. However, it is different in the case of kaons, which are only weakly affected by hadron re-scattering and resonance decays during the post-hydrodynamic hadron cascade. Moreover, the effects of collective flow are negligible in kaons spectra.

Due to highly complex dynamics of transverse expansion the parameter  $T$  in Eq. 18 cannot be directly interpreted as a fireball temperature. Considering however that the temperature of the medium has the greatest influence on the transverse spectra and assuming that this dependence survives through the next stages of fireball evolution it is interesting to examine experimental measurements of kaon spectra, which are widely available. As seen in Fig. 6 there is indeed a plateau in the parameter  $T$  in dependence on collision energy, usually referred to as *the step*.

### 8.5 Predictions for intermediate size systems

In SMES the properties of the created state are entirely defined by the volume in which production takes place, the available energy, and a partition function. In the case of collisions of large nuclei, the thermodynamical approximation can be used and the dependence on the volume and the energy reduces to the dependence on the energy density. A smooth evolution of heating curves with varying system size is expected within such an approach. But does the thermodynamical approximation holds for smaller systems? What is the influence of the system volume on the creation and evolution of QGP?

## 9 Strangeness production at SPS energies

In previous sections, we have discussed details of hadron production in the energy domain of the SPS accelerator. Let us further investigate the properties of the production of strangeness and strange hadrons from a more practical, experimental perspective.

As was already discussed, strangeness production is of particular interest in the context of this thesis. Firstly, we note that there is no strange content in the initial state of colliding nuclei and secondly the production of strangeness is sensitive to the state of matter created in the fireball (as demonstrated in the

previous section). Following the reasoning presented in the description of thermal models, strangeness is frequently referred to as a probe of deconfinement.

Strange and antistrange quarks  $s$  and  $\bar{s}$  produced in the collision are distributed among hadrons, which are then registered by the detectors. Diagram in Fig. 7 shows schematically the approximate quantities of the most abundant strange and antistrange hadrons produced at high baryon densities. A first observation is that the production of  $\Lambda$  and  $\bar{\Lambda}$  will be highly affected by the baryon density. Consequently the yields of  $K^-$  and  $\bar{K}^0$  will be similarly affected considering most frequent reactions, that require the least energy to produce strange particles, for example:

- $p + p \rightarrow p + \Lambda + K^+ + \pi^0$   
 $\approx [\text{GeV}] 0.94 + 0.94 \rightarrow 0.94 + 1.12 + 0.49 + 0.14$
- $p + p \rightarrow p + p + K^+ + K^-$   
 $\approx [\text{GeV}] 0.94 + 0.94 \rightarrow 0.94 + 0.94 + 0.49 + 0.49$

Note, that the first reaction is almost 200MeV “cheaper”. Thus most of the  $\bar{s}$  quarks will go into  $K^+$  and  $K^0$ , while the  $s$  quarks will be more equally distributed among  $K^-$ ,  $\bar{K}^0$  and  $\Lambda$ .

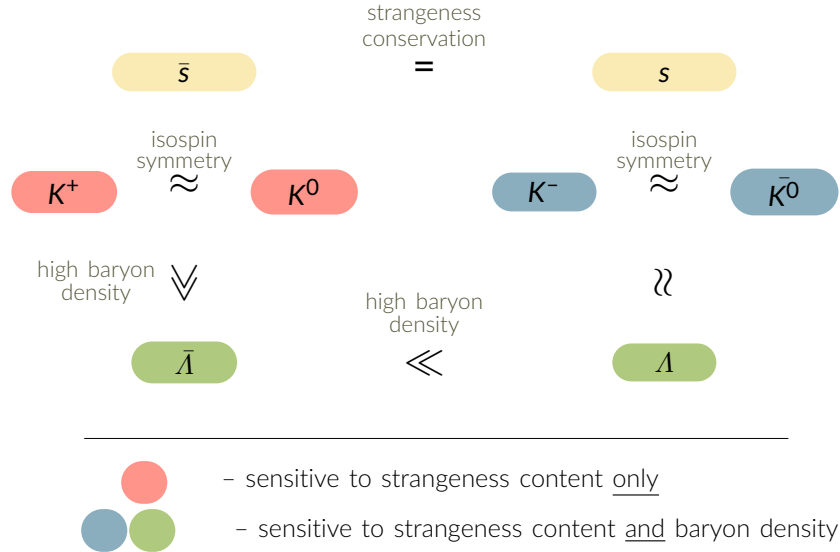


Figure 7: Schematic representation of symmetries and approximations one can make in the baryon rich energy regime of SPS concerning production of strange and antistrange hadrons. Figure based on [25].

This consideration justifies a few approximations used in the interpretation of experimental data. In particular we frequently refer to the strangeness to

entropy ratio, which is experimentally approximated with:

$$E_S = \frac{\langle \Lambda \rangle + \langle K + \bar{K} \rangle}{\langle \pi \rangle} \approx \frac{2 \cdot \langle N_{s\bar{s}} \rangle}{\langle \pi \rangle} \quad (19)$$

where  $\langle N_{s\bar{s}} \rangle$  is the mean number of  $s\bar{s}$  pairs being produced:

$$2 \cdot \langle N_{s\bar{s}} \rangle = \langle \Lambda + \bar{\Lambda} \rangle + \langle K + \bar{K} \rangle + \langle \phi \rangle + \dots \quad (20)$$

which is here well approximated by:

$$2 \cdot \langle N_{s\bar{s}} \rangle \approx \langle \Lambda \rangle + \langle K^+ + K^- + K^0 + \bar{K}^0 \rangle \quad (21)$$

Also an assumption is made that the production of entropy is proportional to the number of produced pions  $\langle \pi \rangle$ .

Considering the wide availability of experimental data on most abundant charged hadrons ( $\pi^+, \pi^-, K^+, K^-$ ) we frequently study the strangeness production in terms of  $K^+/\pi^+$  ratio:

$$\langle N_{s\bar{s}} \rangle \approx \langle K^+ \rangle + \langle K^0 \rangle \approx 2 \cdot \langle K^+ \rangle, \quad \langle \pi \rangle \approx \frac{3}{2} (\langle \pi^+ \rangle + \langle \pi^- \rangle) \quad (22)$$

$$\frac{\langle N_{s\bar{s}} \rangle}{\langle \pi \rangle} \approx \frac{2 \langle K^+ \rangle}{3 \langle \pi^+ \rangle}, \quad E_S \approx \frac{4 \langle K^+ \rangle}{3 \langle \pi^+ \rangle} \quad (23)$$

## 10 Summary on phenomenology of deconfinement

Particle production in heavy ion collisions is a complex, dynamical process influenced by multiple stages of fireball evolution. However, some of its aspects can be effectively described with remarkably simple models. In HRG model particle yields can be closely reproduced in terms of statistical production from a thermal source. SMES delivers qualitative predictions of observable signatures of the deconfined matter being produced in the collisions. More involved, comprehensive models, such as PHSD, are also to some extent successful in reproducing particle spectra and their anisotropies. Interestingly all of the listed models share an important common feature, as each of them hints a creation of deconfined phase in the collisions of heavy ions already at SPS energies.

In the HRG model, it was found that the  $K^+/\pi^+$  ratio is most accurately described when the  $\sigma$  meson and heavy resonances are included in the calculations [21], showing it is deeply rooted in the features of hadronic mass spectrum and linked to QCD phase transition.

Predictions of SMES are directly tied to the presence of phase transition and they have found a very solid confirmation in the experimental data, mostly renowned in  $K^+/\pi^+$  ratio.

Also the authors of PHSD remark in a recent update [18], that the sharp peak in  $K^+/\pi^+$  ratio is best reproduced when chiral phase transition and deconfinement are included in the modelling.



An important remark at this point is that the term *phase transition* is frequently used interchangeably in the context of both deconfinement and chiral symmetry restoration, while the distinction of these two phenomena needs to be highlighted. It is still unclear what is the connection between the two or whether they coincide. Models considered in this section (SMES, PHSD) implement both, chiral phase transition and deconfinement.

Another aspect is the order of the phase transition. While it is a central part of the theoretical description it is difficult to determine in an experiment. Rapid cross-over and first-order phase transition might be indistinguishable in the analysis of experimental data, especially considering global observables, such as mean multiplicities or spectra. This topic is therefore not discussed in detail in this thesis.

Summarizing, leading theoretical models provide strong hints towards the onset of creation of deconfined matter in the collisions of heavy ions at SPS energies. As the main attention is frequently directed to explaining the sharp peak of the  $K^+/\pi^+$  ratio in dependence of collision energy, similarly it shall be a central point of consideration in the discussion of experimental results in section 21.

---

## Part II

# Experiment

### 11 NA61/SHINE facility

The measurements presented in this thesis are a part of the experimental program of the NA61/SHINE Collaboration. The experiment's facility is a fixed-target setup located in the North Area of the European Centre for Nuclear Research (CERN) in Geneva. It uses the H2 beam-line of the CERN Super Proton Synchrotron (SPS), utilizing its wide energy range: from  $\sqrt{s_{NN}} = 5.12\text{GeV}$  ( $p_{lab} = 13\text{GeV}/c$  per nucleon) up to  $\sqrt{s_{NN}} = 17.3\text{GeV}$  ( $p_{lab} = 158\text{GeV}/c$  per nucleon).

The NA61/SHINE is a multi-purpose spectrometer measuring particle production in hadron-hadron, hadron-nucleus, and nucleus-nucleus collisions. It has been designed to measure a large fraction of particles produced into the forward hemisphere of the collision down to zero transverse momentum  $p_T=0.0\text{ GeV}/c$ , allowing for the calculation of mean multiplicities of hadrons produced in the whole phase-space ( $4\pi$ ).

The main components of the detector are large Time Projection Chambers (TPCs) which combine a momentum measurement with particle identification capabilities through a measurement of the ionisation energy loss. Additional detectors provide monitoring of the incoming beam, the information on forward energy, and the time-of-flight of produced particles.

In this chapter the main experimental instrumentation will be described in brief, focusing on features most relevant in view of this analysis. The detailed information about the NA61/SHINE facility can be found in the ref. [26], and also [27].

#### 11.1 SPS beam

The SPS accelerator, measuring nearly 7km in circumference is the second-largest synchrotron at CERN. Since its commissioning in 1976, it served as the main particle collider for tens of experiments in North, West, and Underground Areas (NA, WA and UA). The SPS enabled advancement of our understanding of the inner structure of protons, nature's preference for matter over antimatter, or extreme conditions in the early Universe. Most notably, the SPS-accelerated proton-antiproton collisions have brought the discovery of W and Z bosons by the UA1 and UA2 experiments.

The SPS has been adapted to various purposes throughout its operation: from  $p+\bar{p}$  collider, through  $e^-e^+$  injector for Large Electron-Positron Collider (LEP) to heavy ion accelerator for NA and Large Hadron Collider (LHC) experiments. Currently, it provides hadron and ion beams for LHC, NA62, COMPASS, and NA61/SHINE. It is capable of delivering a large range of beam momenta: 13–450 GeV/c for protons and 13–158 GeV/c per nucleon in case of

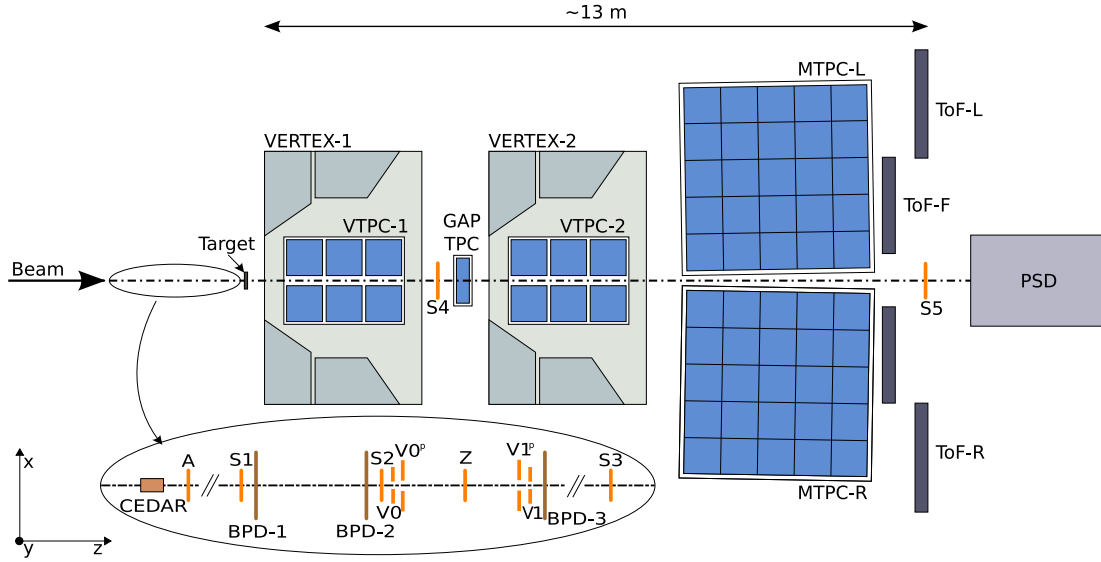


Figure 8: Schematic layout of the NA61/SHINE experimental setup. Image taken from Ref. [26].

ions. The upper limit is due to the magnetic field strength in the bending magnets and charge-to-mass ratio  $Z/A$ , while the lower bound is determined by the beam stability. It is capable of handling an impressively wide range of accelerated particles. Within NA61/SHINE's strong interaction programme the SPS delivered beams of protons and ions:  $^7\text{Be}$ ,  $^{40}\text{Ar}$ ,  $^{131}\text{Xe}$  and  $^{208}\text{Pb}$ . As protons and ions follow different paths in the pre-injector chain to the PS a brief description of both is necessary.

The proton beam originates from hydrogen gas – it is extracted with a duo-plasmatron ion source and injected into the Radio Frequency Quadrupole (RFQ2). Protons reach 750 keV and are extracted into LINAC2, a three-tank Alvarez drift tube linear accelerator. LINAC2 accelerates the proton beam to 50 MeV, which is then distributed into the four rings of the PS Booster (PSB). Each ring accumulates over  $10^{13}$  protons. Once the beam reaches 1.4 GeV/ $c$  it is extracted to be sent to CERN's oldest accelerator – Proton Synchrotron, where it reaches up to 14 GeV/ $c$ . The author finds it fascinating, that the machinery constructed in 1959, still functions as a vital part of a laboratory on the very frontier of science.

The ion acceleration chain is very different and it required a dedicated infrastructure first designed in the 1990's and later upgraded in the naughties to fit the demands of high-luminosity LHC ion beams. The first step in the preparation of the beam is the ionization of atoms with the electron cyclotron resonance (ECR) source, where repetitive microwave pulses create the oxygen plasma, which in turn ionizes the sample. The ionized gas is then electrostat-

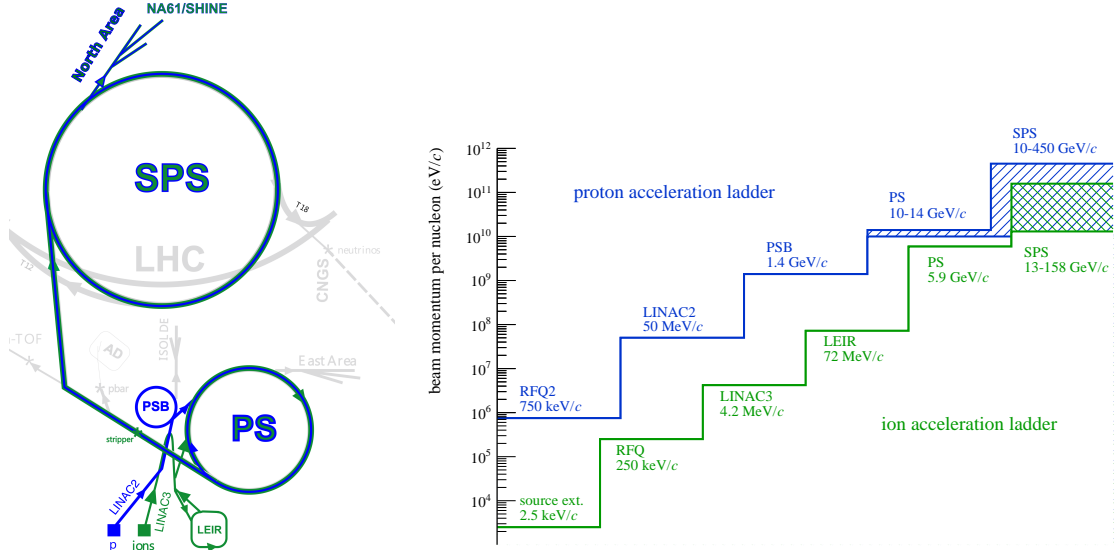


Figure 9: *Left*: An illustration of CERN accelerator chain highlighting components relevant for NA61/SHINE. *Right*: A quantitative visualisation of consecutive steps of beam acceleration for protons (blue) and ions (green).

ically extracted into the spectrometer, which injects atoms of selected ionization level into the LINAC3. The RFQ, followed by a Radio-Frequency cavity increases the beam energy to 4.2 MeV and once again a spectrometer selects given charge state of ions and delivers the beam into the Low Energy Ion Ring (LEIR). In this step of acceleration, the beam is bunched and reaches energy of 72 MeV. The beam is then directed into the PS, where the energy is further increased to 5.9 GeV. At the exit of the PS, the ions traverse a 1 mm thick aluminium foil, where they are stripped from remaining electrons, reaching their final charge state.

Both proton and ion beams reach the desired energy in the SPS, from where they are extracted through H2 beamline to the Experimental Hall North 1 (EHN1). The H2 optics allows for a precise selection of momentum and collimation of the beam. A set of scintillation and Cherenkov counters as well as the beam position detectors located upstream of the target provide precise timing reference, along with charge and position measurement of the incoming beam particles. Fig. 10 shows the configuration of beam detectors during the Ar+Sc run in 2015.

## 11.2 Trigger and Sc target

A set of scintillators (S, V), Cherenkov counters and beam position detectors (BPD) situated on the beamline provide precise information on timing reference, charge and position of incoming beam particles, which are necessary to assess the quality of the beam and to set up the event trigger. Table 1 shows the dimensions of the beam counters and table 2 lists the definitions of triggers used during Ar+Sc data taking.

Detector	Size [cm]
S1	6×6×0.02 (rotated 45° in $xy$ )
S2	4×4×0.02
V1	10×10×1, with hole $\phi=1$
S5	$\phi=2\times 0.1$

Table 1: Beam counters dimensions.

Trigger	definition	description
T1	$S1 \times S2 \times \bar{V}1$	beam
T2	$S1 \times S2 \times \bar{V}1 \times \bar{S}5 \times PSD$	central collision
T3	$S1 \times S2$	beam halo
T4	$S1 \times S2 \times \bar{V}1 \times \bar{S}5$	minimum bias

Table 2: Trigger logic definitions. PSD refers here to 16 small modules in the middle of Projectile Spectator Detector.

Signals from S1 and S2 scintillators are used in coincidence in the trigger logic, while V1 and S5 in a so-called "veto mode" (anti-coincidence). V1 serves the purpose of removing the beam halo, while the signal in S5, more precisely lack thereof, determines whether the beam particle interacted with the target. The Projectile Spectator Detector (PSD, described in more detail in sec. 11.5) also contributes to the trigger logic in veto mode. If the summed signal from 16 small middle modules does not exceed a certain threshold value, the event is marked as T2. The threshold value is determined beforehand, in such a way, that the T2 trigger collects  $\approx 20\text{-}35\%$  of most central events (in relation to minimum bias, T4).

The  $^{40}\text{Ar}$  beam extracted from the SPS accelerator was directed at  $^{45}\text{Sc}$  target – stack of six plates  $2\times 2\text{ cm}^2$  wide and 1 mm thick, located  $\approx 80\text{ cm}$  upstream of VTPC-1. Mass concentrations impurities measured for the sample are on the level of 0.3% [28], resulting in a negligibly small increase in pion multiplicity ( $<0.2\%$ ) due to a presence of heavier elements.

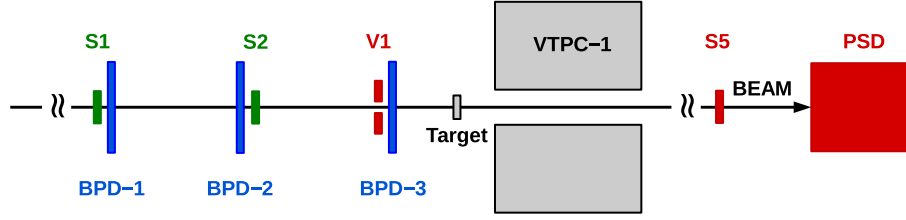


Figure 10: Configuration of beam detectors during 2015 Ar+Sc run. Counters pictured in green contribute to trigger logic in coincidence mode and the components marked in red in anti-coincidence.

### 11.3 Time Projection Chambers and Tracking

The main tracking devices of the NA61/SHINE experiment are five large volume Time Projection Chambers (TPC), totalling to about  $40\text{m}^3$  of active volume. Two of them (Vertex TPCs: VTPC-1 and VTPC-2) provide tracking in the magnetic field and are thus crucial for momentum calculation and reconstruction of vertices. They are located in the gap between coils of two superconducting dipole magnets: VERTEX-1 and VERTEX-2, which provide a maximum field of 1.5 T and 1.1 T respectively (9 Tm bending power in total). The field is polarised downwards (toward negative values of  $y$ ), bending positive particles to the  $+x$  direction (left) and negatives to  $-x$  (right). The magnetic field is homogeneous in the central parts of both vertex TPCs, but non-vertical components may appear at the edges of the VTPCs. A detailed map of the magnetic field is used in the track reconstruction procedure to account for described inhomogeneities.

Two other chambers (Main TPCs: MTPC-L and MTPC-R) are positioned downstream of the magnets symmetrically to the beamline. They provide most of the sensitivity for the ionisation energy loss measurement. In addition, a smaller TPC (GAP-TPC) is placed between the two VTPCs, centered on the beamline to measure particles with the smallest production angles. A large number of particles produced in collisions of heavy ions (Ar+Sc, Xe+La, Pb+Pb) render the signals from different tracks indistinguishable at small angles. Therefore the GTPC was removed from the tracking region for these runs.

Key properties of NA61/SHINE's TPCs design were introduced to handle a large number of tracks in central Pb+Pb collisions. The highest resolution for two-track separation was achieved by selecting a drift-gas mixture and a design of the read-out planes which minimise the width of measured charge clusters. In addition, a minimum amount of material surrounds the active volume, to minimise the production of secondary particles in the detector material.

Charged particle traversing the gas medium of TPCs leaves a trail of ionization clusters on its trajectory. The composition of the gas mixture affects greatly the properties of the ionization. The mixture chosen by NA61/SHINE consists only of argon and carbon dioxide (90%/10% in VTPCs and 95%/5% in MTPCs). Argon as the main component is characterised by a large number

of electrons produced in the primary ionisation and carbon dioxide addition serves as a quenching gas, limiting an uncontrolled growth of the cascade.

The electrons created in primary ionization drift in the uniform electric field, which is provided by the field cage surrounding the active volume made of strips of aluminised mylar foil. The velocity of the drift  $v_D$  is strongly dependent on temperature and pressure, both of which are precisely measured and used in the calculation of  $v_D$  for the reconstruction procedure.

The charge clouds drifting towards the read-out plane consist of a relatively low number of electrons (several to several hundreds per cm). Therefore it is necessary to amplify their signal with the Multi-Wire Proportional Chamber (MWPC). It consists of the cathode wires, the pad-plane, and the sense-wires. The amplification section is additionally separated from the drift volume with a so-called gating grid, which isolates the MWPC from drifting charges in between the triggered events. Sense wires voltage generate a high gradient electric field, in which drifting electrons accelerate and collide with gas atoms causing the secondary ionisation. The process repeats creating an avalanche of electrons, which develops until all the electrons are collected on the anode wire. The disappearance of the electrons and movement of the positive gas ions repelled from the anode wire induce an electromagnetic pulse on the pad plane. The distance between the sense-wires and the pads was kept small (down to 2 mm) to ensure a narrow distribution of charge on the pads. The operation of the TPCs described above is schematically pictured in Fig. 11.

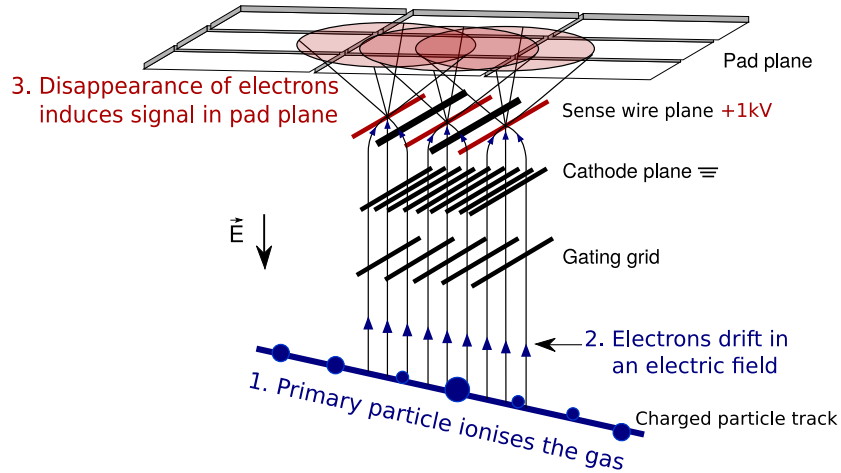


Figure 11: Schematic visualization of the operation of TPCs in NA61/SHINE. Primary particle ionizes the gas, creating an electron cloud which drifts in the electric field towards the MWPC, where the signal is amplified and registered on the read-out pad plane. Figure adapted from [27].

The read-out pad array consists of slightly over 182000 pads organized into rows and further into sectors, each being connected to the data acquisition

system with a separate set of wiring. The pad position determines the  $x$  and  $z$  coordinates of the cluster position, while  $y$ -position is derived from the drift time  $\Delta t$  and measured drift velocity  $v_D$ . The width of the pads (between 3.5 and 5.45 mm) is optimized such that each charge cluster induces a signal in more than one pad. The signal registered in a single event is sampled into 256 8-bit ADC values in 50  $\mu\text{s}$  time interval. The analysis of residual distributions, with respect to track fit, shows that the overall precision of  $(x, y, z)$  position measurement is on the level of about 200  $\mu\text{m}$  [27]. Finally, the number of pad-rows determines the maximum number of measured points (234) on a single track traversing the detector.

The signal registered by the pads allows not only to determine the spatial position of the cluster, but also the ionization energy. A pulse generated on the pads is proportional to the charge deposit from primary ionization. The energy loss per unit length ( $dE/dx$ ) can be extracted, which depends on the velocity of the particle rather than its momentum. When combined with the independent measurement of the momentum it allows for particle identification. The relation between the average ionisation energy loss  $\langle dE/dx \rangle$  and the velocity  $\beta = v/c$  of relativistic particles ( $0.1 \lesssim \beta\gamma \lesssim 1000$ ) is well described by the “Bethe equation”:

$$\left\langle -\frac{dE}{dx} \right\rangle = \frac{A}{\beta^2} \left[ \ln B\beta^2\gamma^2 - 2\beta^2 - \delta(\beta\gamma) \right] \quad (24)$$

where  $A$  and  $B$  are given in terms of the ionisation energy of the medium and some fundamental constants (for details see: [29]). The first two terms are the original Bethe-Bloch formula and the third term limits the energy loss to finite values in the logarithmic-rise region. In practice, parameters  $A$  and  $B$  are determined from the data. Fig. 12 shows the  $\langle dE/dx \rangle$  dependence on velocity in a very broad range. The region relevant for this analysis is highlighted with a thick red line. The measurement of the mean energy loss is discussed in more detail in section 12.2. and the methods of particle identification are extensively described in section 15.4.

#### 11.4 Time Of Flight

The experimental setup includes time-of-flight (TOF) detectors to extend the particle identification capabilities at low momenta. In particular, TOF-L and TOF-R used in ion runs (Be+Be, Ar+Sc, Xe+La, and Pb+Pb) are designed to provide measurements of charged kaon spectra at mid-rapidity.

The detector measures the arrival time of particles at the wall relative to a start-counter (S1) with a precision of about 60 ps. Combined measurement of track length  $l$ , momentum  $p$  and its time of flight  $tof$  allows to extract particle’s mass:

$$m^2 = \left( \frac{p}{c} \right)^2 \left( \frac{c^2 tof^2}{l^2} - 1 \right) \quad (25)$$

Each of the two TOF arrays consists of two-dimensional arrays of scintillator detectors, totalling 1792 pixels and covering the total area of 4.4  $\text{m}^2$ . Be-



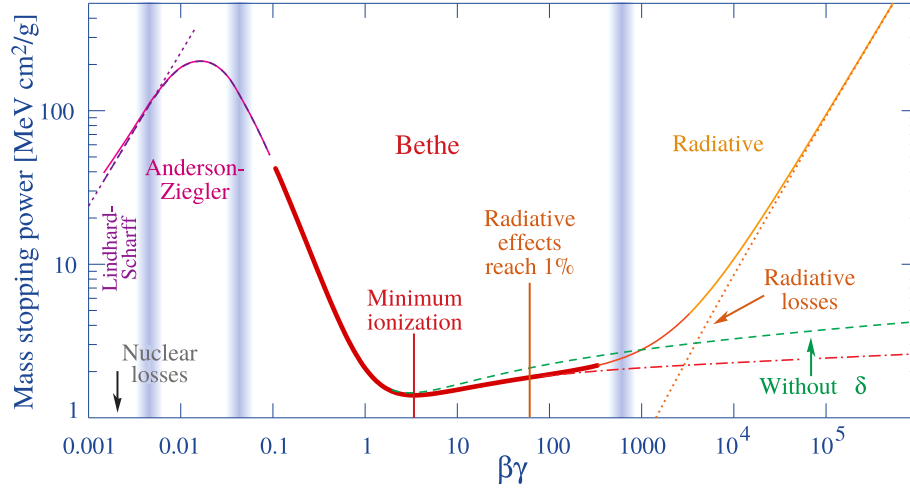


Figure 12: The mean energy loss  $\langle dE/dx \rangle$  dependence on  $\beta\gamma$ . The region relevant for this analysis is highlighted with thick red line. Figure adapted from [29].

sides measuring the arrival time of the particles, each pixel measures also the total deposited charge to distinguish double hits. In the reconstruction chain, registered hits are assigned with the last point tracked in the main TPCs.

TOF detectors were not used in this analysis. The data on the time of flight combined with  $dE/dx$  is however used in the complementary analysis of charged hadrons at low momenta, which results are discussed later in detail.

### 11.5 Projectile Spectator Detector and Centrality

The Projectile Spectator Detector (PSD) is a zero-degree hadronic calorimeter, measuring the projectile spectator energy in the forward hemisphere of the collision. The forward energy  $E_F$  is used to select central collisions at both the trigger level and in offline physics analysis.

The PSD calorimeter consists of 44 modules which cover a transverse area of almost 2.5 m<sup>2</sup>. The central part of the PSD consists of 16 small modules with transverse dimensions of 10x10 cm<sup>2</sup> and the outer part of the PSD consists of 28 large 20x20 cm<sup>2</sup> modules. Each module consists of 60 pairs of alternating lead plates and scintillator tiles with 16 mm and 4 mm thickness, respectively. Lead plates, with their high interaction cross-section, serve as a stopping material and scintillators register the signal from created particle showers.

The geometry and granulation of the PSD result with a fantastic resolution (up to one nucleon), which allows for a very good estimation of the number of interacting nucleons. In fact, it allows redefining the whole procedure of centrality selection in nucleus-nucleus collisions, which is described in detail in section 14.2.

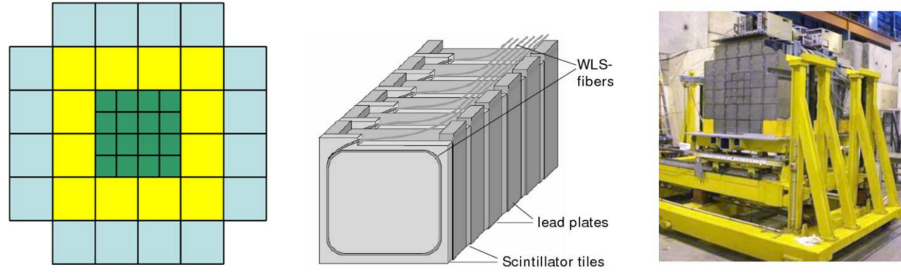


Figure 13: The PSD: schematic front view (left), schematic view of single module (center) and a picture of the detector in the experimental hall (right).

### 11.6 Future upgrades

The second stage of the NA61 experiment, starting after the Long Shutdown 2 (LS2) would include measurements of charmed hadron production in Pb+Pb collisions. The main objective is to obtain the first data on the mean number of  $\bar{c}c$  pairs produced in the full phase space in heavy ion collisions. For this purpose a significant upgrade of experimental equipment is ongoing. In particular, a Small Acceptance Vertex Detector was recently added to the setup with a possibility to install the target within the device. Other upgrades involve extending the tracking system with three forward time projection chambers: FTPC-1, -2, and -3, which greatly improve tracking capabilities in the most forward rapidity region. Additionally, the read-out electronics are being exchanged, with new setup allowing for much faster rates of data acquisition.

## 12 Data

The NA61/SHINE recorded data on Ar+Sc collisions in between February and April 2015 at six beam momenta::

$p_{\text{beam}}$ (per nucleon)	13	19	30	40	75	150	[GeV/c]
$\sqrt{s_{NN}}$	5.12	6.12	7.62	8.77	11.9	16.8	[GeV]

Datasets at each collision energy consists of about 3.5 to 10 million events (see tab. 3). A subset of data with a preliminary selection of  $\approx 20\text{-}35\%$  most central events, a T2 trigger (see sec. 11.2), was used as a starting point of this analysis. Further details concerning the selection of events are explored in sec. 14.1.

$p_{\text{beam}}$ (per nucleon) [GeV/c]	total recorded events	T2 trigger events (bad events discarded)	0-10% most central after cuts
13	$3.9 \cdot 10^6$	$2.95 \cdot 10^6$	$5.22 \cdot 10^5$
19	$4.2 \cdot 10^6$	$2.97 \cdot 10^6$	$5.35 \cdot 10^5$
30	$5.2 \cdot 10^6$	$4.09 \cdot 10^6$	$9.14 \cdot 10^5$
40	$1.0 \cdot 10^7$	$6.36 \cdot 10^6$	$1.28 \cdot 10^6$
75	$4.8 \cdot 10^6$	$3.08 \cdot 10^6$	$1.14 \cdot 10^6$
150	$3.7 \cdot 10^6$	$1.54 \cdot 10^6$	$5.56 \cdot 10^5$

Table 3: Numbers of events recorded by the NA61/SHINE for each beam momentum with corresponding numbers of events used in the analysis.

The raw signal recorded by the detector undergoes a complex process of calibration followed by the reconstruction of physical quantities, such as charge, momentum, or energy loss. In order to learn a precise estimation of detector inefficiencies, a set of Monte-Carlo simulated events is generated, which is then used to emulate a full detector response. Simulation of the detector combined with original, undistorted data enables the calculation of relevant efficiency corrections. In the next sections, the reconstruction procedure is sketched briefly and a more detailed description of collision events and particle track selection is presented.

### 12.1 Reconstruction

The process of reconstruction of physical observables from the raw TPC signal can be broken down into the following steps:

- **Finding points.** The data recorded by single pads in TPCs are analysed for signal peaks in adjacent pads and in consecutive time slices. The clusters found in this way are recorded as ionization points if certain quality

requirements are met, such as number of clustered pads, number of consecutive time-slices, or ADC values. An  $(x, y, z)$  position of the cluster is calculated as a weighted mean of pads positions and time slices with respect to the ADC signal measured.

- **Local tracking.** An algorithm searches for groups of clusters proximate both spatially and temporarily. Such groups are then fitted with a parametrised trajectory in each of TPCs, forming a so-called local track.
- **Global tracking.** Local tracks in each TPC are merged into a global track if possible. A precise fit of particle momentum with a detailed map of the magnetic field is done. Also a “truncated mean” energy loss is calculated for each track as an average  $dE/dx$  of 50% clusters with the lowest values of  $dE/dx$ .
- **Finding primary vertex.** All global tracks are extrapolated back to the proximity of the target in order to locate the primary vertex  $z$ -position. The  $x$  and  $y$  coordinates are identified with an extrapolated beam trajectory measured by BPDs. The distance in the  $x - y$  plane between the primary vertex and an extrapolated track is called an *impact parameter*  $\vec{b}$ . Note that it is a technical quantity, useful in assessing the quality of the fit, not to be confused with the impact parameter defining collision centrality in Glauber models.
- **Finding secondary vertices.** For each pair of tracks, an algorithm attempts to find a secondary vertex. These vertices originate mostly from weak decays of  $\Lambda$  and  $K_S^0$ .

At the output of reconstruction procedure, each particle trajectory is assigned with the following quantities: the sign of electric charge, momentum vector at interaction vertex, mean energy loss  $\langle dE/dx \rangle$ , number of measured points and impact parameter  $\vec{b}$ .

## 12.2 Ionisation energy loss measurement

The ionisation energy loss of the particle traversing the detector gas ( $dE/dx$ ) depends on the velocity of the particle. Combined with an independent measurement of the momentum from track curvature in the magnetic field provides an indirect measurement of mass, thus enabling identification of the particle species. An introduction concerning the measurement of the mean energy loss is already provided in sec. 11.3.

In this paragraph, the calculation of the mean  $dE/dx$  value will be briefly discussed as well as the calibration and corrections of ionization measurement (a more detailed description can be found in [30]). Also the Ar+Sc reactions dataset will be reviewed in detail, focusing on the key properties of  $dE/dx$  distributions in analysed momentum range.

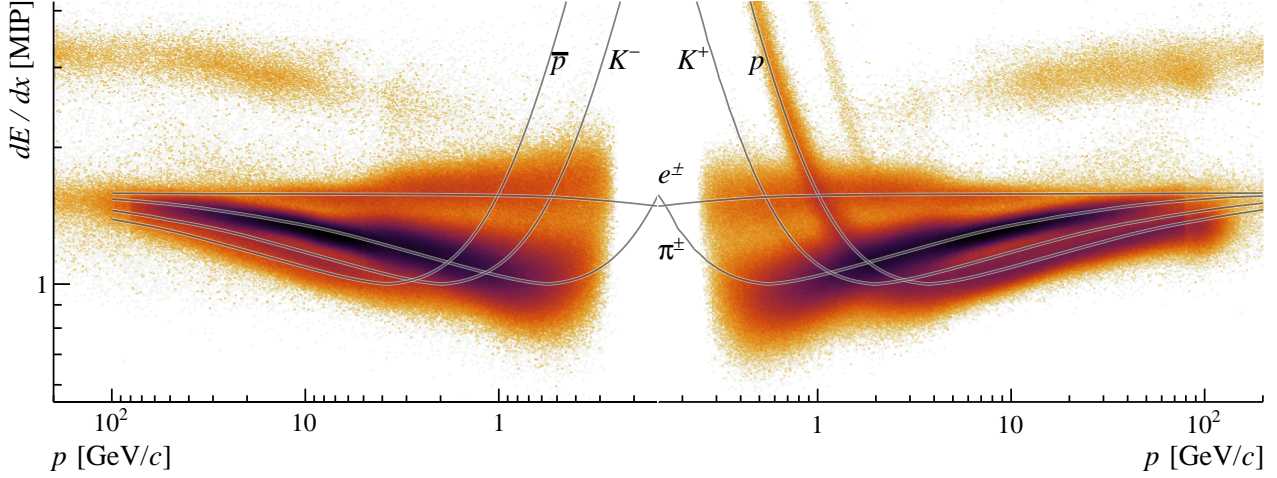


Figure 14: Distribution of mean energy loss versus independently measured momenta at  $p_{\text{beam}}=150A$  GeV/c. Measurement of both quantities simultaneously provides particle identification capabilities. The curves are tabulated Bethe-Bloch functions for all identified particle species:  $\pi^+$ ,  $\pi^-$ ,  $K^+$ ,  $K^-$ ,  $p$  and  $\bar{p}$ .

The starting point of the calculation of  $dE/dx$  is the signal registered by the pads in TPCs readout. An integrated signal from the cluster of fired pads is proportional to the energy deposited by a charged particle in a single ionization point, which in turn is also proportional to the amount of the energy that the particle has lost,  $-dE$ . The energy loss  $-dE$  is a random variable governed by a highly-skewed Landau (or Landau-Vavilov) distribution, called *straggling function*. Such distribution is characterized by a long tail towards highly energetic ionizations and thus has an undefined mean and variance. Therefore a so-called *truncated mean* is constructed to obtain a well-defined average – the mean is calculated for only 50% of the lowest ionization energy measurements. Such a procedure additionally reduces the width of  $dE/dx$  distribution by effectively cutting off long “Landau tail”, which directly translates to an improvement of PID resolution.

### 12.2.1 Calibration and corrections

A series of corrections is additionally imposed on charge deposit data. Firstly, a measurement of ionization signal, proportional to  $dE$  needs to be calibrated with respect to electronic gains of each pad, chip, and sector. The pad-by-pad calibration is done by injecting the TPCs with radioactive Kr gas – the unstable Kr isotopes decay with known energy spectrum. By comparison of peak positions in spectra for different channels, relative gain factors are calculated.

Chip and sector gains are calibrated in a separate iterative procedure for each reaction. The correction of the amplification factors aims to correct for possible construction differences and other effects, such as different settings of high voltage supply in each sector. Another factor contributing to the measured charge is a time-dependent gas ionization gain, caused by a change of density with constantly changing pressure. The cluster charge is divided by a fixed quadratic form in the measured atmospheric pressure. The most difficult effect to correct for is the cut-off of cluster charge distribution due to the 5 ADC threshold used in TPCs readout for the suppression. Such a threshold removes tails of clusters, which amplitude is difficult to estimate, as their shape depends on the drift length and pad-track angle. In order to properly correct the cluster charge, a simulation of cluster shapes is performed for a given gas mixture. On top of this correction, the signal needs to be corrected for  $y$ -dependence. An electron cloud associated with the cluster widens during the drift because of diffusion and might be additionally distorted by other electromagnetic effects.

### 12.2.2 Mean energy loss calculation

The first step of the calculation is dividing the registered charges by the estimated track length  $dx$  associated with a given cluster to obtain a measure proportional to  $dE/dx$ . As the truncation procedure removes 50% of the highest energy points along a given track, a special weighting scheme is needed to account for the oscillatory behaviour of the mean depending on whether even or odd number of entries is taken.

The truncation procedure results with measured mean systematically lower than the mean defined by Bethe-Bloch functions. Moreover, the truncated mean, as well as the width of its distribution, depend on the number of clusters  $n_{pts}$  taken into account. Analysis of simulated dataset (see sec. 15.3) show that also the asymmetry of the  $dE/dx$  distributions is a function of  $n_{pts}$ . Fig. 15 shows sample distributions of clusters in different kinematic bins. Note how particles of different momenta traverse different regions of the detector and the track length ( $\equiv n_{pts}$ ) changes. All these features affect the final signal fitted in the PID procedure.

The end product of the calculation is a truncated mean of particle energy loss expressed in units of MIP (minimum ionization particle) and as such is used in the PID procedure (see sec. 15.4).

It is important to acknowledge, that described procedures of calibration and calculation of the  $dE/dx$  signal are burdened with some known problems. Firstly, there is a 0.5% to 2.5% discrepancy between the actual  $dE/dx$  peak positions with respect to the Bethe-Bloch function employed in the calibration. Secondly, the peak positions display non-trivial dependence on transverse momentum. The possible reason for this problem is a faulty  $y$ -dependence calibration, which results additionally with a significant drift of  $dE/dx$  values with varying azimuthal angle  $\phi$ . Unfortunately, the sources of listed problems have not been found and analysed data on Ar+Sc collisions suffers all described inaccuracies. These biases in  $dE/dx$  distributions affect the analysis method-

ology, in particular an additional cut on azimuthal angle  $|\phi| < 30^\circ$  had to be introduced (sec. 14.3) and the fitting procedure has been tuned to correct for these effects (sec. 15.4).

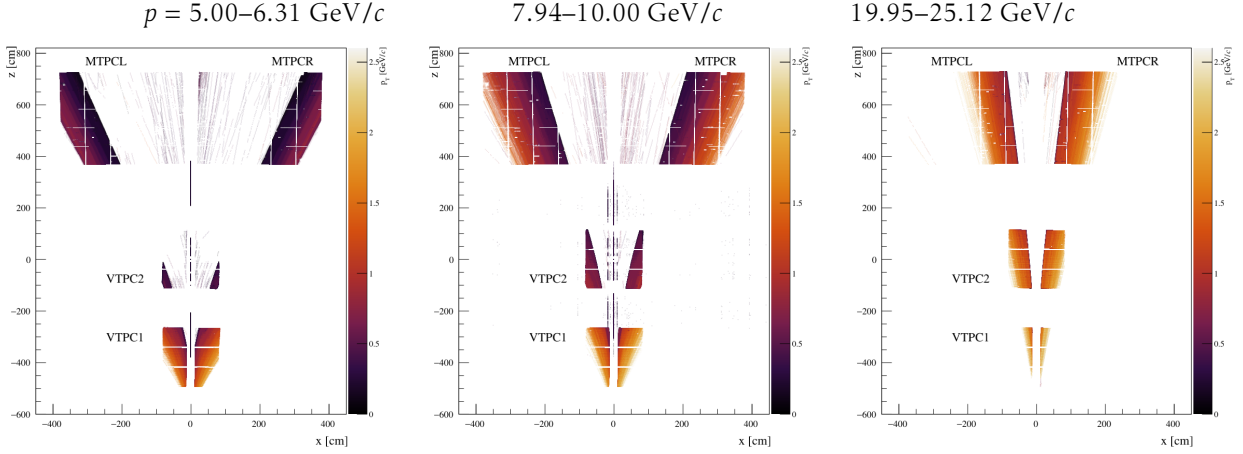


Figure 15: Sample distributions of clusters registered by the TPCs for following momentum bins:  $p = 5.00\text{--}6.31$ ,  $7.94\text{--}10.00$  and  $19.95\text{--}25.12$  GeV/c. Colour scale denotes transverse momentum  $p_T$ . Note how the proportional contribution of clusters measured by VTPC1, VTPC2 and MTPCs changes with  $p$  and  $p_T$ .

### 12.3 Simulation

As mentioned in the preamble of this section a Monte-Carlo simulation is a crucial tool for the correction of raw results. In particular, it is possible to estimate the effects of geometrical acceptance, detector response, reconstruction efficiency, and contamination of vertex tracks with ones produced in secondary interaction. Particle production in inelastic Ar+Sc collisions was simulated using EPOS 1.99 model [16] and the transport of particles was emulated with GEANT 3.21 [31]. Several MC models were tested for particle production and EPOS was found to be the most suitable for spectra analyses in the NA61/SHINE Collaboration [32]. One of the most important features of EPOS, especially relevant for the analysis of intermediate size systems is the fragmentation of colliding nuclei. Both EPOS and GEANT are widely tested by the community, successful in reproducing most of the relevant physics in SPS energy range and their limitations are well understood.

Particle tracks and interaction points extracted from the model are fed into a sequence of algorithms simulating the response of the detector for the purpose of running the very same reconstruction chain as used for experimental data. This way we are provided with two sets of simulated events:

1. **Generated events** (later referred to as *MCgen*). Pure simulated events, containing precise information on generated particles produced in inelastic interactions: trajectory, momentum, hadron species, and their origin – whether created in primary vertex, hadronic reinteraction, or through decays.
2. **Reconstructed events** (later referred to as *MCrec*). Generated events, that were injected into the simulation of detector response and reconstruction. Data on these events include all the output information of the standard reconstruction chain.

Reconstructed tracks can be matched to the corresponding generated tracks with an algorithm finding the highest number of generated MC points geometrically common with reconstructed MC clusters. A comparison of generated and reconstructed datasets provides a precise quantitative estimation of distortions and inefficiencies of reconstruction of experimental data. A detailed description of MC-driven corrections applied in this work is given in sec. 16.



---

## Part III

# Analysis

### 13 Overview of analysis procedure

In this part of the thesis, the analysis procedure is described starting from clean up and selection of relevant data, through methods of particle identification, ending with the calculation of corrections and uncertainties. Before focusing on the details of each step, a brief overview of the whole procedure is in place.

The initial form of data considered in this chapter is the reconstructed events of Ar+Sc interactions. Each event contains information on beam measurements, interaction vertices, particle tracks, and supplementary details concerning detectors. Firstly, the data is reviewed in terms of time stability, (mal-)functioning of subdetectors, and the quality of the measured raw signal. Faulty runs are identified and removed. For the purpose of further improvement of data quality, a set of cuts is imposed on events and tracks, details of which are presented in the following section.

The good quality data is further filtered in terms of physics of interest. Requiring the interaction point position being within the target and selecting event centrality ensures a precise determination of physical conditions of analysed system.

The central point of this study is the particle identification through simultaneous measurement of momentum  $p$  and mean energy loss  $dE/dx$ . A majority of the author's time and effort was invested in perfecting the procedure, as its reliability translates directly into the quality of final results. A detailed description of  $dE/dx$  data and employed statistical methods is given in sections 15.3 through 15.5.

#### 13.1 Complementary analyses

Validity of  $dE/dx$  particle identification method is limited to tracks which momentum is at least 5 GeV/c. As can be seen in Fig. 14 below this value the characteristic mean energy loss for protons and kaons and their peaks become indistinguishable. Below  $p=5$  GeV/c a supplementary measurement is needed to ensure PID capabilities (see Fig. 16). Measurement of the particle's time of flight in this region allows for precise determination of particle species when combined with  $dE/dx$  data.

Simultaneous analysis with  $dE/dx$  and  $tof$ - $dE/dx$  methods provides coverage of almost full forward rapidity hemisphere in the measurement of charged kaons, protons, and anti-protons. Charged pions on the other hand pose more difficulties, as the acceptance is severely reduced near mid-rapidity at small transverse momenta. In this region a contribution of feed-down from decays is significant, therefore any extrapolation is problematic and results with large error. Thus the third method of analysis is employed – “h-minus” analysis. It is

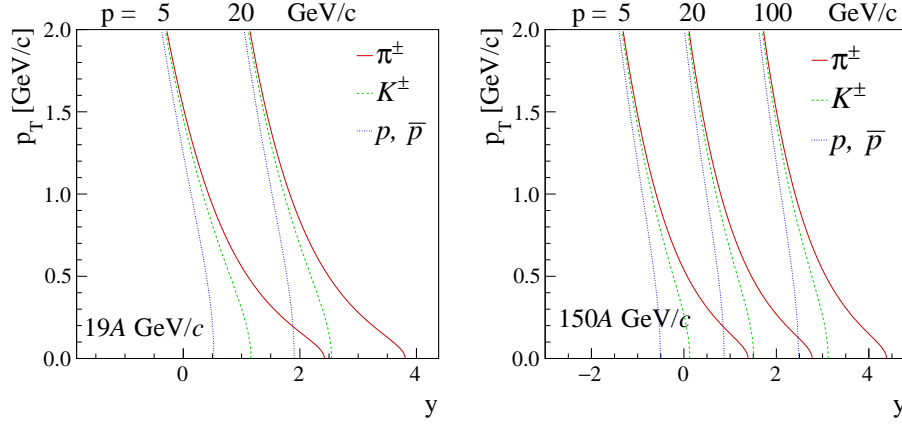


Figure 16: The  $p = 5$  GeV/c threshold required for  $dE/dx$  PID results with reduction of acceptance in mid-rapidity region. Note that the rapidity range changes for different particle types and beam momenta.

based on the fact that in the SPS collision energy regime the vast majority of all produced negatively charged hadrons are in fact pions. The remaining contribution of kaons, anti-protons, and others ( $\lesssim 10\%$ ) is removed with model-based correction.

It should be noted that combined results of all three analyses methods not only allow for calculation of spectra in the whole forward hemisphere but also enable direct comparison of obtained results. As these analyses are performed entirely independently, the probability of any errors in the analysis procedures is greatly reduced. Any discrepancies discovered already on the level of  $y$ - $p_T$  spectra are investigated and corrected.

## 14 Data refinement

The very first step of the analysis is a selection of studied data with two basic criteria: data quality and physics relevance. The first criterium is realized through a series of cuts on event and track parameters, ensuring that the analysed data consists only of properly reconstructed events, in this way minimizing potential errors of the experimental method. The second criterium, the relevance in terms of studied physics, implies that only well defined central inelastic events of Ar+Sc collisions are selected.

### 14.1 Event selection

The initial set of standard cuts rejects bad events based on monitoring the beam and detector before the collision takes place (later referred to as “up-stream” cuts). As such, these cuts do not introduce any biases in studied data:

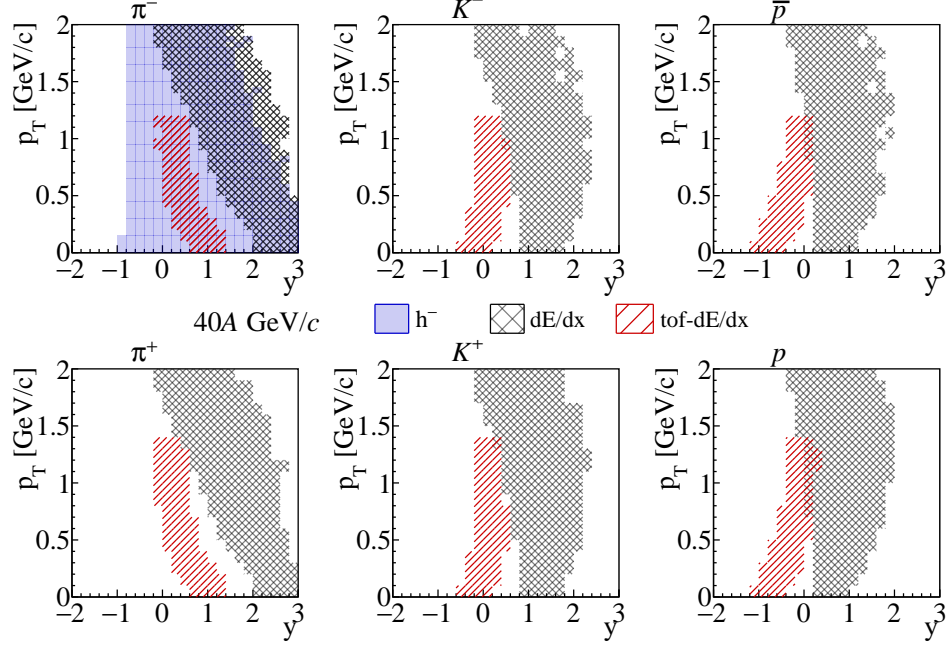


Figure 17: Acceptance of three complementary analysis methods:  $h^-$ ,  $dE/dx$  and  $tof-dE/dx$  pictured for  $p_{\text{beam}} = 40A \text{ GeV}/c$ . At lower beam momenta the gap between  $dE/dx$  and  $tof-dE/dx$  acceptances increases, while at higher collision energies they overlap allowing for direct comparison. The combination of results of these analyses allows for calculation of  $4\pi$  mean multiplicities of presented results.

- **Off-time particles.** The aim of this cut is to reduce the probability that more than one beam particle interacts within one trigger event. The time structure of the signal in beam counters is examined and any particle that appears within  $4 \mu\text{s}$  window with respect to the trigger particle is rejected. Moreover, events in which off-time particle interacted within  $25 \mu\text{s}$  window around the trigger are discarded as well.
- **Beam quality.** The events were only accepted when the trajectory of the beam particle was precisely measured. Specifically, measurements in both planes of BPD-1, -2, and -3 were required and additional cut on BPDs charge signal was imposed due to unusual profile of the beam.
- **Detector malfunction.** Various problems with detectors were encountered during the data taking. In particular, the PSD calorimeter, still being a fresh addition to the NA61/SHINE setup at the time of data-taking, suffered several failures of either single or multiple modules. Some mi-

nor issues with BDPs were found as well. Events registered with faulty subdetectors had to be discarded.

- **Time stability** of recorded data was verified by reviewing the raw signals (e. g. clusters distributions) during data-taking and by examining following quantities in offline analysis of reconstructed data: mean multiplicity of recorded tracks, mean PSD energy (in central 28 modules) and mean transverse momentum. If some puzzling, non-trivial time dependence was discovered, its reasons were traced back in the logs. If the problems could not have been removed or if they were not identified the subsets of unstable runs were dismissed from further analyses.

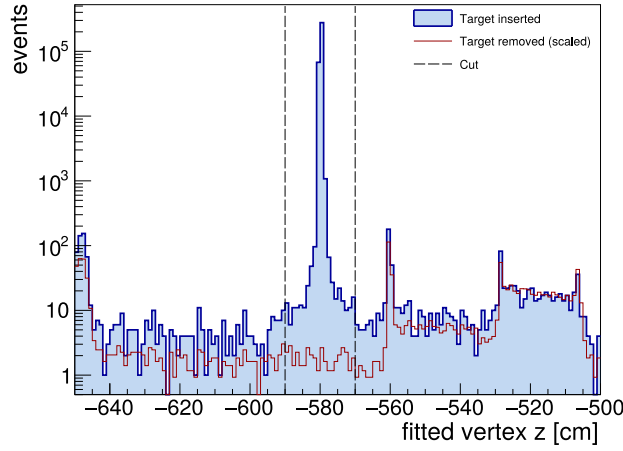


Figure 18: Fitted  $z$ -coordinate of the main vertex with target in the beam line (bold blue) and target removed (red, scaled by an arbitrary constant) for a sub-sample of events.

Two more selection criteria were imposed on the data. As they concern the selection of valid main vertices they should be considered as potentially biasing:

- **Presence of the main vertex** was required, along with the best quality of the fit of the vertex point from extrapolated tracks.
- **Position of the main vertex.** The event was accepted only if the fitted  $z$ -position of the main vertex was within 10 cm from the middle of the target. Fig. 18 shows the distribution of the fitted main vertex  $z$ -positions in two cases: 1) the target was inserted in the target holder, 2) the target was removed. Note that the number of interactions outside of the target is very low, similarly, the contribution of off-target interactions that would not be removed with this cut is negligibly small.

## 14.2 Event centrality

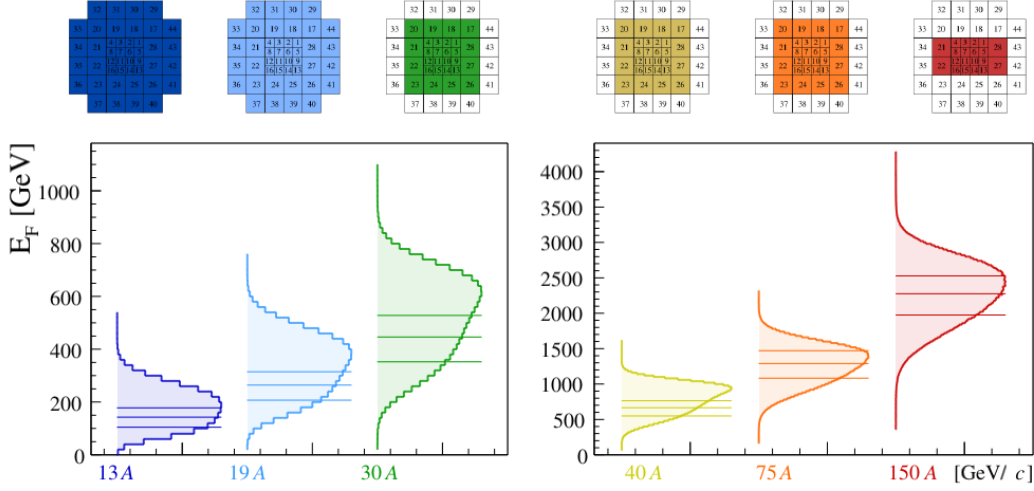


Figure 19: Event centrality selection using the forward energy ( $E_F$ ) measured by the PSD calorimeter. Distributions of  $E_F$  are shown for all beam momenta, with lines denoting values of  $E_F$  energies determining 5%, 10% and 15% of most central events. Shaded areas on the front face diagram of the PSD indicate modules selected for calculation of  $E_F$ . Choice of modules is based on correlation studies between  $E_F$  and track multiplicity measured by the TPCs.

The preliminary selection of the most central events is done by limiting the analysis to T2 trigger only. It is an approximate selection, effectively marking  $\approx 20\%$ - $35\%$  most central collisions (see details in sec. 11.2). A more precise selection of events is necessary, as concerning the physics of interest a well defined narrow range of system volume is desired.

A proper selection of most central events presents a unique experimental challenge, especially so in the case of collisions of small ions. While proton-proton interactions can be classified as elastic or inelastic and central collisions of very large ions of lead can be in some sense distinguished based on the multiplicity of produced particles, neither method is well suited for "intermediate" systems like Be+Be or Ar+Sc. Moreover, the latter method may lead to a bias, as particle multiplicity depends on the physics of interest. A procedure used in this study relies on the measurement of forward energy  $E_F$  of collision spectators in PSD. In each module, a correlation of forward energy and track multiplicity is studied. Modules, which show the strongest correlation are selected for calculation of the sum  $E_F$  of projectile spectators. The most central collisions deposit the smallest energy  $E_F$ . Fig. 19 shows  $E_F$  distribution for each of analysed beam momenta, including also a diagram of sets of modules used in the calculation. The described procedure allows for a precise and reproducible selection of central events. Measurement of forward energy

of projectile spectators is a trait reserved for fixed-target experiments.

It should be noted that the off-line selection of centrality classes explained here uses a different set of modules than was used in the case of T2 trigger preliminary selection of most central collisions (16 middle modules). For that particular reason selection of more peripheral centrality classes might suffer some bias. Fig. 19 shows the distributions of  $E_F$  with lines indicating energy thresholds for 5%, 10% and 15% most central events. Note that the 15% threshold is above the peak of the  $E_F$  distribution, which suggests that this bin of centrality might be a subject to a trigger bias.

Due to a heavily limited number of tracks in the acceptance of  $tof-dE/dx$  analysis it was decided to use 10% of the most central events in main analyses of Ar+Sc data. However, the number of valid tracks in  $dE/dx$  analysis is much larger, thus allowing to obtain results additionally for finer binning of centrality: 0-5%, 5-10%, and 10-15%. Summarizing, the key results concerning combined  $dE/dx$  and  $tof-dE/dx$  analysis of spectra and mean multiplicities are performed at 0-10% centrality, while the rapidity spectra of kaons and protons calculated with  $dE/dx$  also include 0-5%, 5-10%, and 10-15% centrality bins.

### 14.3 Track selection

The main motivation behind the selection of relevant track cuts is to maximize track finding efficiency and the  $dE/dx$  resolution. In many cases, the choice of selection criteria results with a severe reduction of the acceptance, as the quality of the data is of primary concern. Following track cuts were used in this study:

- **Track rigidity**  
Only tracks with positive x-component of rigidity ( $q \cdot p_x > 0$ ) are selected. The readout pads in TPCs are tilted with respect to the beamline to minimise the average angle between the positive rigidity tracks and a given pad in the horizontal plane  $x - z$ . This optimisation reduces the width of the measured clusters, as well as the impact of the ionisation fluctuations along the particle trajectory. This cut is crucial for the quality of  $dE/dx$  information.
- **Impact parameter**  
The distance in the  $x - y$  plane between the primary vertex and an extrapolated track  $\vec{b} = (b_x, b_y)$  is required to fulfil geometrical conditions:  $b_x < 4$  cm,  $b_y < 2$  cm. This cut increases the probability that the track was produced in primary interaction.
- **Total number of measured clusters**  
Minimum of 30 clusters in total is required to ensure high resolution of  $dE/dx$  measurements (see details in sec. 12.2).
- **Number of clusters measured in VTPCs**  
15 points in VTPCs is determined as the minimal number of clusters that ensures a reliable fit of track momentum.

- **Azimuthal angle**

Only tracks with azimuthal angle  $|\phi| < 30^\circ$  were accepted, thus most of the tracks that leave the detector at the top and bottom planes are rejected. It was found that due to persistent problems with  $dE/dx$  calibration the absolute value of mean energy loss was shifted in top and bottom regions of TPCs, with respect to their middle region. Rejection of tracks with high azimuthal angles results with significant improvement of  $dE/dx$  resolution, especially at low momenta ( $p = 5\text{--}12\text{ GeV}/c$ ).

Note that the list of cuts presented above does not refer directly to track quality quantities, such as track fit residuals, or ratio of the number of recorded cluster to the number of expected ones, etc. Such cuts would result in uncontrolled tracking acceptance and reconstruction efficiency dependent on a number of unknown parameters (e. g. track multiplicity). Instead, each of the listed cuts could be in fact translated into a selection of well-defined momentum space region, thus ensuring: 1) almost perfect reconstruction efficiency within the acceptance, 2) similarly well-defined corrections can be constructed. The topic of corrections imposed on the data is continued in sec. 16.

#### 14.4 Acceptance

The acceptance region of this analysis is determined by the track cuts described in the previous section, but also by the properties of the  $dE/dx$  particle identification method. Firstly, a sharp cut at total momentum magnitude  $p = 5\text{ GeV}/c$  defines the “left” edge of the acceptance. The boundaries at other directions are determined by an additional criterium imposed on the number of entries in the histograms at each  $p$ - $p_T$  bin used in the identification procedure. Namely, it is required that at given  $p$  and  $p_T$  the number of entries in bins of both positively and negatively charged particles must be greater than 100. Figures 16 and 17 show more details concerning the final shape of the acceptance. It should be noted that the same acceptance is later imposed on simulated data in order to construct the corrections (more in sec. 16).

### 15 Particle identification

#### 15.1 Basic model of $dE/dx$ distribution

The contributions of  $e^+$ ,  $e^-$ ,  $\pi^+$ ,  $\pi^-$ ,  $K^+$ ,  $K^-$ ,  $p$ ,  $\bar{p}$  and  $d$  are obtained by fitting the  $dE/dx$  distributions in bins of laboratory momentum  $p$  and transverse momentum  $p_T$ . The data were divided into 13 logarithmic bins in  $p$  in the range  $5\text{--}100\text{ GeV}/c$  and into linear bins in  $p_T$ . Thin binning in  $p_T$  was used up to  $p_T = 0.6\text{ GeV}/c$  (bin width  $0.05\text{ GeV}/c$ ) and wider bins were used above this value ( $0.1\text{ GeV}/c$ ).

Fits to the  $dE/dx$  distributions in these intervals consider five particle types:  $i = \pi^\pm, K^\pm, p/\bar{p}, e^\pm, d$ . The signal shape for a given particle type is parametrized

as the sum of asymmetric Gaussians with widths  $\sigma_{i,l}$  depending on the particle type  $i$  and the number of points  $l$  measured in the TPCs. Simplifying the notation in the fit formulas,  $n_{pts}$  is shortened to  $l$ , the  $dE/dx$  is denoted with  $x$  and the peak position of the  $dE/dx$  distribution for particle type  $i$  is expressed as  $x_i$ :

$$f(x) = \sum_{i=p,K,\pi,e,d} N_i \frac{1}{\sum_l n_l} \sum_l \frac{n_l}{\sqrt{2\pi} \sigma_{i,l}} \exp \left[ -\frac{1}{2} \left( \frac{x - x_i}{(1 \pm \delta) \sigma_{i,l}} \right)^2 \right] \quad (26)$$

where  $n_l$  is the number of tracks with number of points  $l$  in the sample and  $N_i$  is the amplitude of the contribution of particles of type  $i$ . Summation over  $l$  is a weighted average of Gaussians with different widths, which depend on  $l$  in following way:

$$\sigma_{i,l} = \frac{\sigma_0}{\sqrt{l}} \left( \frac{x_i}{x_\pi} \right)^\alpha \quad (27)$$

where  $\sigma_0$ , similarly to  $\delta$  in the previous equation, is assumed to be common for all particle types and  $\alpha$  is a universal constant.

Consequently, each track characterized by a given charge  $q$ , momentum  $p$ , transverse momentum  $p_T$ , and energy loss  $dE/dx$  can be assigned a probability of being of given species from the list of particle species included in the model. Multiplicities of particles at a given bin are calculated with the identity method, described in detail in sec. 15.5. However, before we advance towards the calculation of spectra, let us first consider details of employed statistical methods.

## 15.2 Remarks on model and data

The described fit model was introduced originally in the analysis of NA49's Pb+Pb data by Marco van Leeuwen [33, 34]. It is important to remark that the study presented in this thesis is strongly rooted in the methods of  $dE/dx$  particle identification devised in cited NA49's analysis. However, with significant detector upgrades in NA61/SHINE many properties of the dataset have changed, e. g. the helium pipe added on the beamline resulted in significantly reduced production of  $\delta$ -electrons. Moreover, the track multiplicities in Ar+Sc collisions are much lower than ones in Pb+Pb interactions. Both of these features allowed to include  $dE/dx$  measurements in VTPCs in the global  $dE/dx$  calculation, additionally making it possible to loosen some of track cuts criteria. On one hand, it increases the number of points measured along the tracks, thus increasing the resolution. On the other hand, VTPC data is less accurate due to higher track density and magnetic field presence and its contribution to global  $dE/dx$  calculation might introduce some uncontrolled effects. Indeed, a restrictive cut on azimuthal angle  $\phi$  had to be introduced to ensure the best resolution for PID, while still extending the acceptance towards lower momenta (and higher  $p_T$ ) thanks to VTPC measurements.



Finally, the number of Ar+Sc collision events analysed here is far greater than in the case of NA49's Pb+Pb data. An obvious advantage is a reduction of statistical uncertainties, however, it should be noted that with increasing statistics any imperfections of the model become more pronounced. At the same time we do not expect the model, however sophisticated would it be, to describe the data perfectly. In the limit of an infinitely large number of analysed events, the fit residuals would explode to infinity as well, as the uncertainty of data approaches zero. With this in mind, we advance to the following sections, which describe attempts to improve the model, understand its biases, and devise a fitting procedure that ensures stable and correct parameter estimation. In the next section, a simple toy model of  $dE/dx$  distributions based on simulated cluster charges is discussed. The origins and properties of model parameters are investigated and described. Sec. 15.4 presents alternative models that have been tested and a method of simultaneous fitting of multiple bins with shared parameters. Further, the estimation of fit parameters is discussed in terms of possible biases.

### 15.3 Toy simulation of $dE/dx$ distributions

In order to understand the main mechanisms that shape the distributions of  $dE/dx$  measurement a simple simulation was implemented. The cluster charges (scaled with  $dx$ , hence  $dE/dx$ ) along the tracks with fixed number of measured points ( $n_{pts}$ ) were generated (see Fig. 20, left). For each track a calculation of truncated mean  $\langle dE/dx \rangle_{tr}$  was performed by averaging 50% of the lowest values of simulated  $dE/dx$  (Fig. 20, right). The distributions of  $\langle dE/dx \rangle_{tr}$  were fitted with the model defined with Eq. 26.

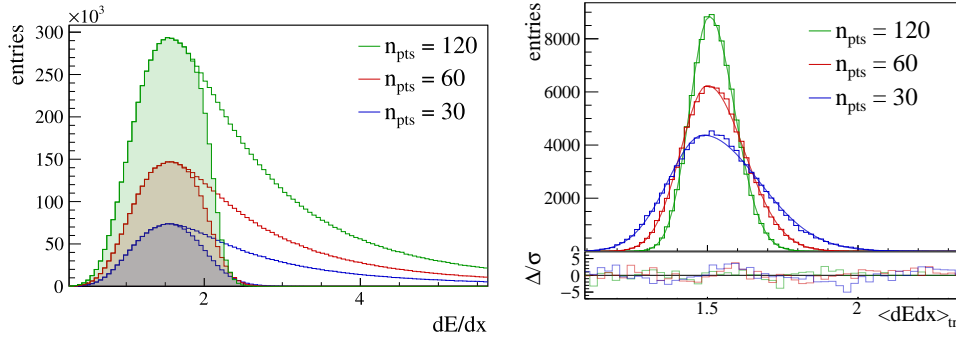


Figure 20: Left: cluster charges generated with Landau-Vavilov distribution for 100k tracks at  $n_{pts} = 30, 60$  and 120 (shaded histograms show values after 50% truncation). The long tail of the distribution is removed, allowing for stable calculation of the mean. Right: the distribution of truncated mean  $dE/dx$  calculated with the simulated set of cluster charges, fitted with the asymmetric Gaussian. See how the fit residuals (bottom panel) decrease with increasing number of points.

The main property investigated with this simulation is the influence of track length on fitted parameters: mean, width  $\sigma$  and asymmetry  $\delta$  (see Fig. 21). The dependence of the width on the track length was well known and implemented in the basic model (Eq. 26). The drift of the mean is accounted for in the  $dE/dx$  calculation procedure, however the  $n_{pts}$  dependence of the asymmetry was never tested. The model was updated to include this feature by following substitution:  $\delta = \delta_0/n_{pts}$ , with  $\delta_0$  being the new fit parameter. Consequently, another modification of the model was made – instead of fitting the peak position it was found that fitting the mean gives more stable results. Finally the model takes a following form ( $n_{pts} \equiv l$ ):

$$\left\langle \frac{dE}{dx} \right\rangle_i = N_i \frac{1}{\sum_l n_l} \sum_l \frac{n_l}{\sqrt{2\pi}\sigma_{i,l}} \exp \left[ -\frac{1}{2} \left( \frac{x - (x_i - \frac{2}{\sqrt{2\pi}}\delta\sigma)}{(1 \pm \delta)\sigma_{i,l}} \right)^2 \right] \quad (28)$$

with  $\sigma_{i,l}$  definition left unchanged (Eq. 27) and  $\delta$  substituted with  $\delta = \delta_0/l$ .

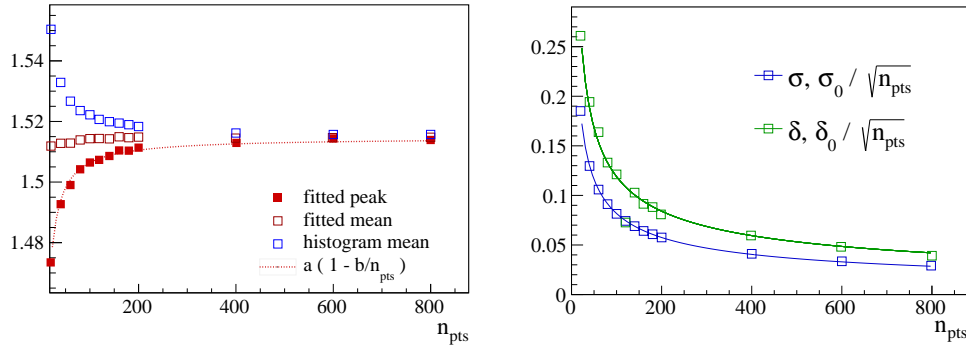


Figure 21: Left: dependence of the mean, peak position and histogram mean on the track length ( $n_{pts}$ ). Right: influence of  $n_{pts}$  on width  $\sigma$  and asymmetry  $\delta$  of the distribution. The track length dependence of plotted parameters can be parametrized with good accuracy.

## 15.4 Model and parameter estimation

### 15.4.1 Alternative models

Two extensions of the model were tested in an attempt to account for changing values of mean  $dE/dx$  within given momentum bin [35], as the position of the peaks ( $x_i$ ) can differ up to 3.5% between the edges of the momentum bin.

In the first approach a flat distribution of momentum within a bin was assumed and so the Gaussian peak could be integrated in range  $x_i \in (\mu_1, \mu_2)$ :

$$\int_{\mu_1}^{\mu_2} \frac{1}{\sqrt{2\pi}\sigma} \exp \left( -\frac{(x-\mu)^2}{2\sigma^2} \right) d\mu = \frac{1}{4} \left( \operatorname{erf} \left( \frac{\mu_2 - x}{\sqrt{2}\sigma} \right) - \operatorname{erf} \left( \frac{\mu_1 - x}{\sqrt{2}\sigma} \right) \right) \quad (29)$$

With normalization taken into account and assuming no asymmetry ( $\delta = 0$ ) we obtain:

$$\left\langle \frac{dE}{dx} \right\rangle = \sum_{i=d,p,K,\pi,e} N_i \frac{1}{\sum_l n_l} \sum_l \frac{n_l}{\sqrt{2\pi}\sigma_{i,l}} \frac{1}{2(\mu_1 - \mu_2)} \left( \operatorname{erf} \left( \frac{\mu_2 - x}{\sqrt{2\sigma_{i,l}^2}} \right) - \operatorname{erf} \left( \frac{\mu_1 - x}{\sqrt{2\sigma_{i,l}^2}} \right) \right) \quad (30)$$

In the second proposed extension the momentum distribution was not assumed flat. Instead it was integrated based on the measured momentum distribution in a similar fashion as the weighting is done in case of the number of clusters  $n_{\text{pts}}$ :

$$\left\langle \frac{dE}{dx} \right\rangle_{\text{tot}} = \sum_{i=d,p,K,\pi,e} N_i \frac{1}{\sum_l n_l} \sum_l \frac{n_l}{\sqrt{2\pi}\sigma_{i,l}} \frac{1}{\sum_j n_j} \sum_j n_j \exp \left[ -\frac{1}{2} \left( \frac{x - x_{i,j}}{(1 \pm \delta) \sigma_{i,l}} \right)^2 \right] \quad (31)$$

where index  $j$  enumerates the bins in momentum distribution and  $n_j$  refers to the number of entries in the bin. Means are then modified with:

$$x_{i,j} = x_i + \Delta_{i,j}, \quad \Delta_{i,j} = BB(i, p_{\text{center}}) - BB(i, p_j)$$

where  $BB(i, p)$  stands for the value of Bethe-Bloch function for  $i$ -th particle species at given momentum  $p$ .

It was found that neither of the proposed extensions provided a significant improvement of the quality of the fit [36]. Moreover, it became clear that the details of  $dE/dx$  calculation and its calibration have far greater influence on the stability of the fit. In particular, the introduction of the cut on the azimuthal angle  $\phi$  resulted in the reduction of tails in the proton peak, which earlier were erroneously identified as deuterons. Nevertheless, the topic will likely be revisited once again, as a new procedure of  $dE/dx$  calibration is currently in development. Better quality of the  $dE/dx$  signal might enable using more sophisticated models.

#### 15.4.2 Simultaneous fit in multiple bins of $p_T$

There is total number of 13 parameters in the model defined in Eq. 28: 5 amplitudes  $N_i$ , 5 peak positions  $x_i$ , width  $\sigma_0$ , width scaling  $\alpha$  and asymmetry  $\delta_0$ . It is practically impossible to fit this many parameters at once. However, some of these parameters might be common for multiple bins, being independent on  $p_T$ , charge, or being a universal constants. For the purpose of precise determination of global parameters a procedure of simultaneous fitting of multiple pairs of model and histograms was implemented (see more in appendix B). In the first stage of fitting the model was simultaneously fitted to up to 20 bins in  $p_T$  at each momentum in three subsets of bins: 1) positive charge, 2) negative charge, 3) both charges. Only three parameters were assumed to be  $p_T$  independent: width scaling  $\alpha$  and relative peak positions of kaons and protons w. r. t. pions ( $x_p/x_\pi$ ,  $x_K/x_\pi$ ). Additionally, in this stage the asymmetry is set at

$\delta = 0$  and relative peak position of deuterons w. r. t. proton peak was fixed at value derived from Bethe-Bloch parametrization, as the  $dE/dx$  resolution does not allow for a more precise estimation. At all stages of fitting the number of antideuterons is set to zero.

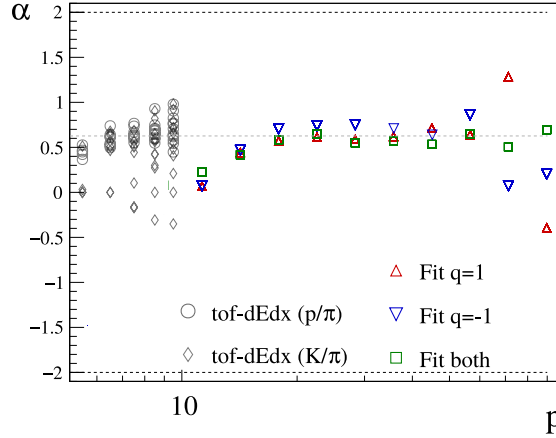


Figure 22: Width scaling parameter  $\alpha$  was fitted simultaneously in up to 20  $p_T$  bins at given  $p$ , using positively charged tracks (red triangles), negatively charged tracks (blue triangles) and both charges at once (green squares). Also plotted are the direct calculations of this parameter with fit performed with  $tof-dE/dx$  method (black circles and diamonds) and horizontal line stands for the value used in Pb+Pb analysis at NA49 [34].

Figure 22 shows fitted values of  $\alpha$  parameter at each momentum bin. Obtained estimations agree with the value determined in earlier NA49's analysis (0.625), as well as with direct calculations of this parameter with free fits on  $tof-dE/dx$  data:

$$\alpha = \frac{\log \frac{\sigma_p}{\sigma_\pi}}{\log \frac{x_p}{x_\pi}}, \quad \alpha = \frac{\log \frac{\sigma_K}{\sigma_\pi}}{\log \frac{x_K}{x_\pi}}$$

where  $\sigma_p$ ,  $\sigma_K$  and  $\sigma_\pi$  are the fitted widths of peaks of labelled particles. Moreover it was verified that fitted spectra are only weakly affected by the  $\alpha$  parameter. With these considerations in mind the  $\alpha$  was fixed at 0.625 globally. On the other hand, the fits of peak positions of kaons and protons are significantly affecting fitted yields of particles (more in sec. 17.1.1). Therefore it was crucial to obtain a reliable estimation of these parameters. Figure 23 shows results of simultaneous fits of  $x_p/x_\pi$  and  $x_K/x_\pi$  at multiple  $p_T$  bins of both charges at given  $p$ . While the fits of  $x_p/x_\pi$  are stable, giving similar values at each beam momentum, the estimation of  $x_K/x_\pi$  breaks down at lower energies. As the baryon density increases, the amplitude of proton peak increases as well, relatively to the contribution from other particle species. Consequently, the kaon peak can no longer be reliably distinguished in between the large peaks of protons and

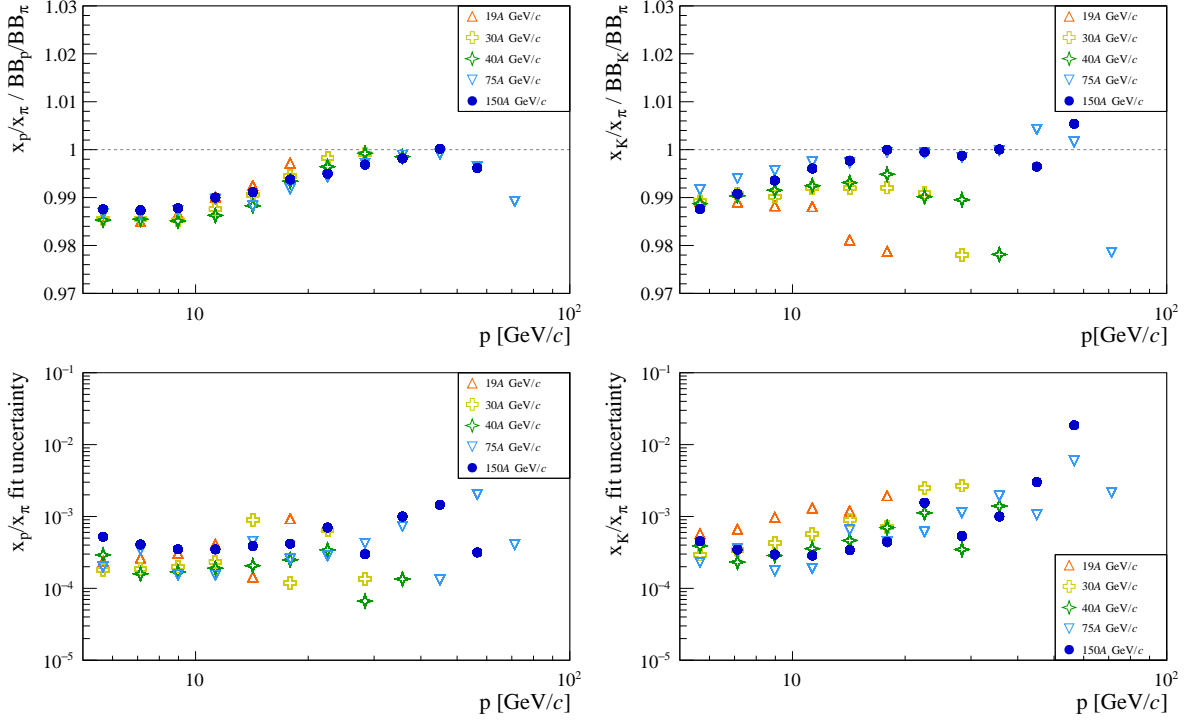


Figure 23: Results of simultaneous fits of relative peak positions at multiple  $p_T$  bins at given  $p$ . Relative proton peak position  $x_p/x_\pi$  was fitted at very similar values at each beam momentum. Relative kaon position  $x_K/x_\pi$  fit breaks down at lower energies. As the baryon density increases the proton peak “absorbs” kaon peak. Values obtained for 150A GeV/c are used as prefits in the second stage of fitting at all beam momenta and above  $p = 40$  GeV/c the values are fixed from Bethe-Bloch function. The relative fit uncertainty is typically on the level of  $3\text{--}6 \times 10^{-4}$ .

pions. Since the properties of data on  $dE/dx$  distributions are very similar for all recorded collision energies, the obtained  $x_p/x_\pi$  and  $x_K/x_\pi$  estimations for 150A GeV/c are used as prefits in the second stage of fitting at all beam momenta. Furthermore, above  $p = 40$  GeV/c the relative peak positions are fixed at values derived from Bethe-Bloch functions. The relative fit uncertainty is typically on the level of  $3\text{--}6 \times 10^{-4}$ .

#### 15.4.3 Fit refinement

At second stage of fitting the parameters are estimated simultaneously in both bins of charge at given  $p$  and  $p_T$ . With the relative peak positions  $x_p/x_\pi$  and  $x_K/x_\pi$  fixed, the  $\delta$  is released and a refinement of initial parameters is possible. In

this stage some parameters are shared among both charges –  $\sigma_0$  and  $\delta_0$ , while others are determined separately for each charge: amplitudes  $N_i$  and pion peak position  $x_\pi$ . There is total of 2 shared and 6 unique parameters.

Repeating the fits additionally allows for better stability and a more accurate evaluation of errors. It is particularly important for bins with a low number of entries, as the calculation of global likelihood function is dominated with contribution from abundantly populated bins in the first stage, thus even though a global minimum is reached, the best fit at each bin is not assured.

The results obtained in this stage are presented in figures 24–28 and Fig. 29 shows a sample fit at two charge bins at given  $p$  and  $p_T$ . A brief summary of parameter properties is given below, while more specific details can be found in the captions of listed figures.

Firstly, it should be noted that imperfections of  $dE/dx$  calibration procedure, while vividly visible in the results (particularly in Fig. 24), were successfully accounted for. The fits are stable, insusceptible to variations of starting parameters and parameter limits. Fitted widths of the distributions (Fig. 25,

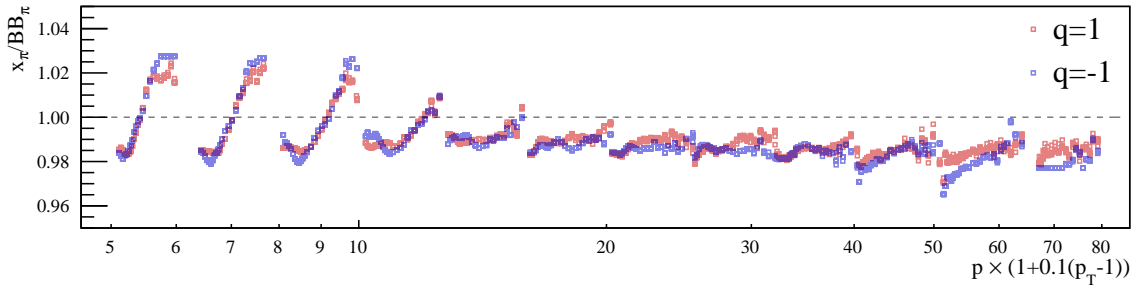


Figure 24: Fitted mean  $x_\pi$  plotted in relation to Bethe-Bloch value used in calibration. The discrepancies reach over 2%. The distributions drift significantly with transverse momentum as well. The points are plotted on horizontal axis in such a way, that they are scattered with  $p_T$  around the centre of the momentum bin. In other words each "chunk" of points corresponds to given momentum bin, while points within chunks show  $p_T$  dependence. Similar way of plotting is used in following figures.

26) feature a smooth dependence on both  $p$  and  $p_T$ , which reflects well known properties of data, detector and  $dE/dx$  reconstruction. The asymmetry  $\delta_0$  is much less precisely defined parameter, dependent predominantly on two factors: truncation procedure and shift of measured  $dE/dx$  with  $y$ -coordinate in the detector. As the fitted values of  $\delta_0$  only vaguely correspond to the properties derived from the toy simulation presented in sec. 15.3 a natural conclusion would be that the latter of listed effects dominates. Finally, the analysis of fit residuals is reassuring in terms of collective measure of  $\chi^2/ndf$  – typically close to 1, exceeding 2 only in rare cases at lowest momentum bin. A strong correlation between the number of entries and fit's  $\chi^2/ndf$  is seen. As already discussed in sec. 15.2, an ideal agreement between the model and the

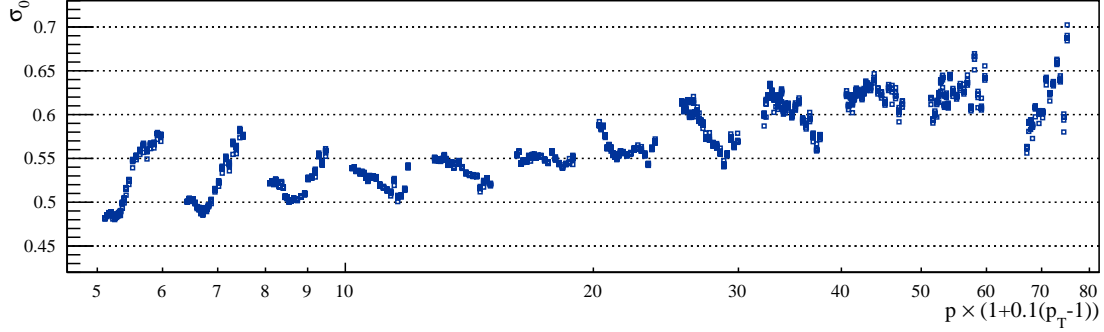


Figure 25: Widths  $\sigma_0$  fitted simultaneously in negative and positive charge bins at all analysed  $p$ - $p_T$  bins. The evolution of fitted values is smooth and an increase of width coincides with shortening of tracks populating respective kinematic bins.

data is not expected – it would be impossible to account for all phenomena affecting the data. Therefore once a threshold is reached when the uncertainty of the data falls below the uncertainty of the model (resulting from its imperfections) it is expected to observe statistically more significant discrepancies between the two. With the advent of new generation experiments collecting enormous amounts of data it might become a frequently reoccurring issue.

### 15.5 Identity method

The model fitted to  $dE/dx$  distribution is now used to calculate the spectra of identified hadrons. Note that the particle identification presented here is not unique on a track-by-track basis. In fact, any experimental measurement of particle mass (PID) is of finite resolution and with continuous distributions of observed masses, it is usually the case that particles are not uniquely identified. In such cases an identity method [37] can be used to extract observable quantities of identified particles without any information loss.

Each track characterized by given charge  $q$ , momentum  $p$ , transverse momentum  $p_T$  and energy loss  $dE/dx$  can be assigned a probability of being of given species from the list of particle species  $i$  included in the model,  $i = \pi^\pm, K^\pm, p, \bar{p}, e^\pm, d$ :

$$P_i(p, p_T, dE/dx) = \frac{f_i(p, p_T, dE/dx)}{\sum_i f_i(p, p_T, dE/dx)} \quad (32)$$

Then, multiplicities of particles at given bin can be calculated with:

$$n_{i \in \{\pi^\pm, K^\pm, p, \bar{p}, e^\pm, d\}} = \sum_{j=1}^m P_i \quad (33)$$

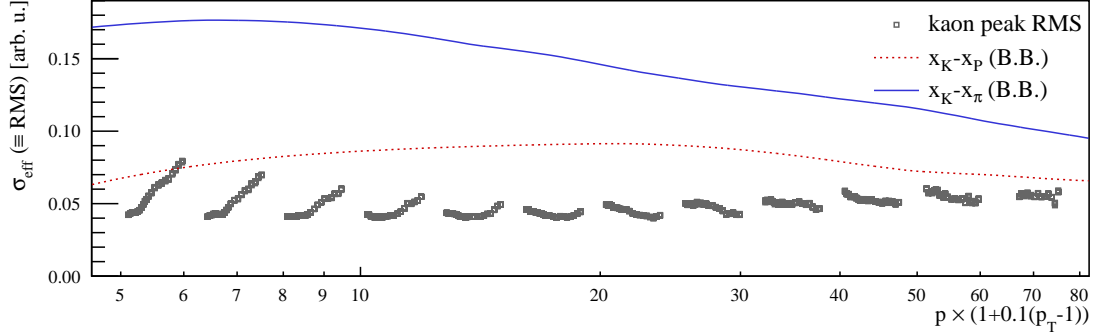
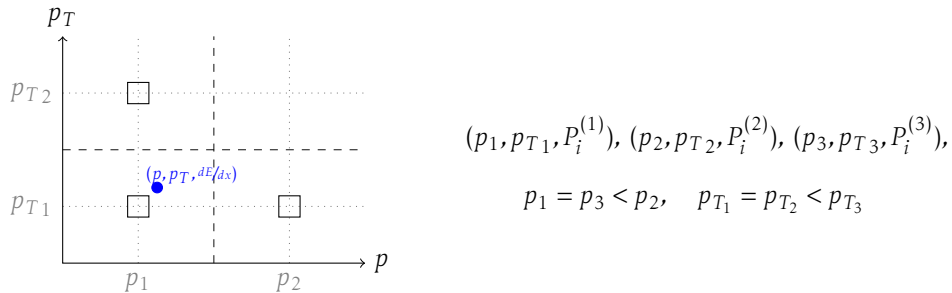


Figure 26: Assessment of achieved resolution. The plot shows an effective width (RMS) of the  $K^+$  peak fitted to  $dE/dx$  distributions at all analysed kinematic bins at 150A GeV/c. Note that the typical value of the peak width is half the distance between the peaks of protons and kaons. The functions  $x_K - x_p$  and  $x_K - x_\pi$  are plotted as functions of  $p$ .

where the summation runs over the number of particles  $m$  in the bin. Hence from the model fits to  $dE/dx$  data in bins of  $p$ - $p_T$  (and charge), histograms of  $y$ - $p_T$  for each particle species can be populated in a following way: for a track characterized with  $(p, p_T, dE/dx)$  rapidity  $y$  can be calculated and the track is added to  $y$ - $p_T$  histogram of particle  $i$  with weight  $P_i$ .

### 15.5.1 Identity method with interpolation

An extension of this method was proposed to reduce an influence of finite size binning of particle identification. The probabilities  $P_i$  can in fact be interpolated between the centres of kinematic bins, this way eliminating the “jumps” of  $P_i$  values when crossing the border between two bins of PID. Each track at given  $(p, p_T)$  can be assigned with three closest bins of identified particles:



A linear interpolation is then done in  $p$ :

$$P_i^{(12)} = P_i^{(1)} + (p - p_1) \frac{P_i^{(2)} - P_i^{(1)}}{p_2 - p_1} \quad (34)$$



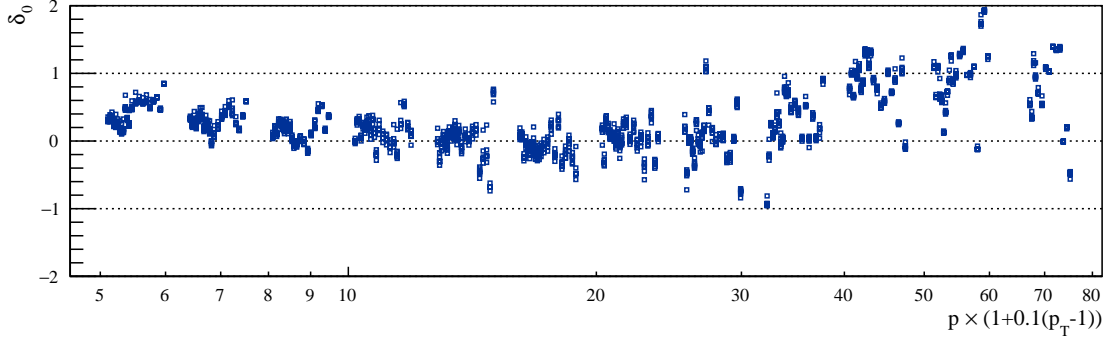


Figure 27: Fitted values of  $\delta_0$  parameter, which affect the asymmetry of the spectra. Note that the  $\delta_0$  appears in the model (Eq. 28) as  $\delta = \delta_0/n_{pts}$ . Thus the largest asymmetries are effectively witnessed, where the majority of tracks is short, in particular at lowest momenta and high  $p_T$  and at highest fitted momenta.

and  $p_T$ :

$$P_i^{(123)} = P_i^{(3)} + (p_T - p_{T1}) \frac{P_i^{(12)} - P_i^{(3)}}{p_{T3} - p_{T1}} \quad (35)$$

$P_i^{(123)}$  are the final interpolated probabilities (weights) assigned while populating the  $y$ - $p_T$  histograms.

## 16 Corrections

### 16.1 Simulation and event selection

Corrections of the raw data were based on simulation of Ar+Sc interactions described in sec. 12.3. Two sets of data are used to calculate the corrections:

- Generated, *MCgen* – pure physics simulation of collision,
- Reconstructed, *MCrec* – simulated events were fed into detector emulation and full data reconstruction chain.

Firstly, both subsets are filtered for event centrality that matches the one used in the analysis of real data. The simulation allows for extracting the number of forward spectators, which is the closest measure (in the absence of reliable PSD simulator) corresponding to centrality selection performed with cuts on forward energy. Specifically, 10% of events with the lowest number of forward spectators were chosen to calculate the corrections.

A set of event cuts is used to select reconstructed events (*MCrec*) mirroring the criteria used in the selection of real events. As no quality cuts are necessary in case of simulated data a following downstream (biasing) cuts were used:

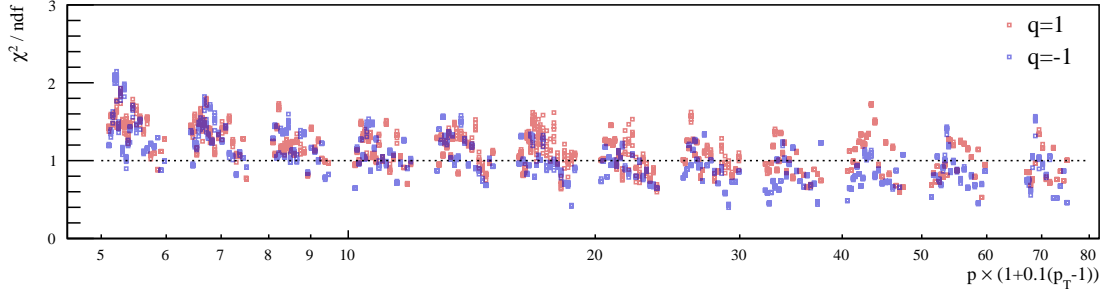


Figure 28: The fit test  $\chi^2$  per number of degrees of freedom. Most of the values fall close to 1, while almost never exceeding 2. Some of the values falling significantly lower than 1 is an artefact of multiple zero-bins in the fitted histogram.

- **Main vertex** is present and fitted with the highest quality.
- **Position of the main vertex** is within 10 cm from the middle of the target.

Similarly, the exact same set of track cuts is used in *MCrec* events as it was used for the experimental data. Additionally, an acceptance map is used to remove tracks, which are not included in the momentum space in which the  $dE/dx$  PID was performed.

## 16.2 Geometrical correction

At each momentum space bin, a ratio of the number of tracks generated in *MCgen* events to the number of tracks reconstructed in *MCrec* events provides information on the track losses due to imposed cuts. Such a ratio is treated as a geometrical correction of the real data. The main sources of this correction are:

- Choosing only the tracks with a positive  $x$ -component of rigidity ( $p_x \cdot q > 0$ ) results with approximately half of tracks being rejected in all momentum space.
- Selecting only the tracks which leave the main vertex at an azimuthal angle  $|\phi| < 30^\circ$  further reduces the number of accepted tracks by 2/3 globally.
- Other cuts on tracks affect mostly the shape of the acceptance.
- Reconstruction efficiency and reinteractions are also taken into account, although their contribution is very small.

Geometrical corrections are calculated in bins on rapidity  $y$  and transverse momentum  $p_T$  reflecting the binning used in the analysis of real data. The typical value of such correction is  $\gtrsim 6.0$ , which agrees with the consideration presented above.

### 16.3 Feed-down from weak decays

Another source of contamination of experimental results are the secondary particles originating from weak decays, that are reconstructed as primary ones. Fig. 31 shows the relative cumulative contribution of weak decays feed-down to measured particle spectra. While it is negligibly small in case of kaons ( $K^+$  and  $K^-$ ) it becomes significant in case of pions ( $\pi^+$  and  $\pi^-$ ) and even larger for protons and anti-protons. It is clear that precise estimation of feed-down contribution is crucial for correct calculation of spectra and mean multiplicities.

### 16.4 Tuning of MC corrections

While the geometrical corrections are practically insensitive to the model used in the simulation it is not the case for decay feed-down corrections. On the contrary, the simulated yields of decaying particles are directly affecting the corrections. Specifically, the model used in the simulation (EPOS) does not reproduce the properties of strangeness enhancement, thus the yields of strange mesons and strange baryons are typically largely underestimated. A procedure of tuning the contribution of weak decays was developed to improve the precision of calculated corrections. It is based on data derived quantities, namely mean multiplicities of particles estimated in real data are compared with ones extracted from MC simulation. Thus using the preliminary results on kaon multiplicities in Ar+Sc reactions [2] it is possible to construct a tuning factor for yields of  $K_S^0$ :

$$K_{S(EPOS\ tuned)}^0 = K_{S(EPOS)}^0 \times \frac{\langle K^+ \rangle_{data} + \langle K^- \rangle_{data}}{\langle K^+ \rangle_{(EPOS)} + \langle K^- \rangle_{(EPOS)}} \quad (36)$$

Conversely, devising a proper tuning for strange (anti-)baryons is not so straightforward, as there are no data on their production in Ar+Sc collisions. Since the best possible estimation of decay feed-down corrections is crucial for calculation of (anti-)proton spectra an attempt was made to construct such tuning factors based on some approximations. At SPS collision energies the multiplicities of  $\Lambda$  are well approximated by a following relation:

$$\langle \Lambda \rangle = \alpha \cdot (\langle K^+ \rangle - \langle K^- \rangle) \quad (37)$$

where  $\alpha$  is usually very close to 1. A relevant estimation of  $\alpha$  can be extracted from NA49's Pb+Pb data [38] and used to get an approximate estimate on  $\Lambda$  yield in Ar+Sc at each collision energy. Scaling yields of  $\Lambda$  and  $\Sigma^\pm$  can be done through:

$$\Lambda_{EPOS\ corrected} = \Lambda_{EPOS} \times \frac{\alpha \cdot (\langle K^+ \rangle - \langle K^- \rangle)}{\langle \Lambda \rangle_{EPOS}} \quad (38)$$

Summarizing obtained tuning factors we get:

$p_{\text{beam}}$	13	19	30	40	75	150
$K$ tuning factor	1.339	1.339	1.297	1.371	1.332	1.307
$\alpha$	0.89	0.89	1.00	1.08	1.12	0.95
$\Lambda$ tuning factor	1.582	1.582	1.562	1.634	1.522	1.507

species	tuning	assigned uncertainty
$K_S^0$	$K$ enh.	5%
$\Lambda$	$\Lambda$ enh.	10%
$\Sigma^+$	$\Lambda$ enh.	10%
$\Sigma^-$	$\Lambda$ enh.	10%

Furthermore, the yields of other strange and multi-strange baryons were tuned with the same factors as  $\Lambda$  and  $\Sigma^\pm$  and the assigned uncertainty was increased to 20% and 50% respectively. In Fig. 34 the total uncertainty introduced by contribution of secondary particles is denoted with a grey line.

## 16.5 Total corrections

The total corrections of raw spectra are defined in a following way:

$$n_i^{\text{corrected}} = (n_i^{\text{raw data}} - n_i^{\text{MCrec decay}}) \times \frac{n_i^{\text{MCgen}}}{n_i^{\text{MCrec primary}}} \quad (39)$$

where,  $n_i$  are the number of entries per event in bins of  $y$ - $p_T$  histograms at bin  $i$ , more specifically:

$n_i^{\text{corrected}}$	stands for corrected yield.
$n_i^{\text{raw data}}$	stands for raw data yield.
$n_i^{\text{MCrec decay}}$	is a contribution of feed-down from weak decays in <i>MCrec</i> . The
$n_i^{\text{MCrec primary}}$	is a contribution of primary particles in <i>MCrec</i> .
$n_i^{\text{MCgen}}$	is a pure MC simulated yield.

correction of spectra due to weak decays contamination ( $n_i^{\text{MCrec decay}}$ ) is weakly correlated with the primary hadron yields, therefore this contribution is accounted for in an additive way. The geometrical correction is applied as the quotient in the second term of the equation of the numbers of reconstructed primary tracks and all simulated tracks in a given momentum space bin.

Note that no correction for off-target interactions is made, as its relative contribution was estimated on the level of  $10^{-4}$  (as demonstrated in Fig. 18) and thus neglected.

## 17 Uncertainties

The final step of the analysis is the estimation of statistical and systematic uncertainties of calculated spectra. As the analysis of identified particles is

a complex, multi-level process the proper calculation of errors is equally involved. Statistical uncertainties were calculated with a very robust method of bootstrapping, while the estimation of systematic uncertainties was based on a variation of cut parameters, fitting parameters, and errors of feed-down correction. Both procedures of uncertainty calculation of double differential spectra  $dn/dy dp_T$  are described in detail throughout the following sections.

### 17.1 Statistical uncertainty estimation with bootstrapping

Due to the usage of identity method (sec. 15.5) in calculation of  $y$ - $p_T$  spectra, it is not clear how to propagate the statistical errors from raw  $p$ - $p_T$  data. Whenever a direct propagation of uncertainties is not possible, a method of bootstrapping can be employed. The general idea is to repeat the whole analysis procedure many times using sets constructed from original data by resampling. Such simulated samples are later referred to as bootstrap samples (BS). The resampling of original data is done by random sampling with replacement. A schematic representation of the bootstrap samples can be illustrated with a following example:

original events	BS1	BS2	BS3	BS4	...
1	1	2	1	1	
2	1	2	1	3	
3	1	3	3	3	
4	3	3	4	4	
5	5	4	5	4	
6	6	6	5	5	

Effectively, each event appears  $m$  times in each BS, where  $m$  follows multinomial distribution:

$$P(m) = \binom{M}{m} p^m (1-p)^{(M-m)} \quad (40)$$

in which  $p=1/M$  and  $M$  is the number of events. 100 bootstrap samples were created through random sampling with replacement done on the level of events (not tracks). Each bootstrap sample is then injected into the procedure of particle identification and calculation of  $y$ - $p_T$  spectra. The errors are then estimated as standard deviations of yields at all bootstrap samples. It was verified [39] that the number of bootstrap samples was large enough to confirm that the distribution of yields is normal, allowing to assign the standard deviation as the statistical error. Fig. 32 shows relative statistical uncertainties obtained from bootstrapping for  $y$ - $p_T$  spectra of identified hadrons.

The contribution to statistical uncertainties from the MC correction factors was calculated from the binomial distribution.

#### 17.1.1 Systematic uncertainties

Following sources of systematic uncertainties were considered in this study:

- Biases of **fitting procedure**.  
In the  $dE/dx$  PID the parameters of relative peak positions of kaons and protons have a significant influence on particle yields, while being also the most difficult ones to determine. The strategy used in this study involved fixing these parameters at pre-fitted values and assuming their independence on changing  $p_T$ . As can be seen in Fig. 33, releasing these parameters in bin-by-bin fits results with slightly different values. The spread of  $x_K/x_\pi$  and  $x_p/x_\pi$  in well fitted bins was estimated at 0.1%. Therefore in order to determine a potential bias introduced by fixing relative peak positions, they are varied by  $\pm 0.1\%$ . A contribution to the uncertainty from other fit parameters was neglected, due to much lower sensitivity of the fits on those parameters.
- Errors due to selection of particular **event cuts** criteria were estimated through an independent variation of these criteria:
  1. Removal of events contaminated by **off-time particles** – the time window in which no second beam particle is allowed was varied by  $\pm 2\mu s$  w. r. t. nominal value of  $4\mu s$ . The maximal difference of the results was assigned as the systematic uncertainty of the selection.
  2. **Fitted main vertex position** – the range of allowed main vertex z-coordinate was varied  $\pm 5$  cm at both ends.
- The contribution to systematic uncertainty from **track selection** criteria were similarly estimated by varying these criteria:
  1. The effect of cut on **total number of clusters** was studied by changing the required number by +5 and -5 points.
  2. Similarly, the **number of clusters in VTPCs** was varied with  $\pm 5$  points. Note that both of the cuts on  $n_{pts}$  affect the acceptance of the PID as well, which was also taken into account.
  3. The influence of the selection of **azimuthal angle** was investigated by comparing the results obtained for  $|\phi| < 30^\circ$  (original value),  $|\phi| < 20^\circ$  and  $|\phi| < 40^\circ$ .
- Uncertainties of **weak decays feed-down** contribution were accounted for as described in sec. 16.4.

Fig. 34 shows the contribution of each of listed sources in the systematic uncertainties of final spectra of identified particles at 150A GeV/c. The total uncertainty of each hadron species is below or slightly above 10%, slightly increasing at lower collision energies.

It should be noted that systematic uncertainties due to centrality selection are not considered in this work. Preliminary analysis of the influence of module selection in the calculation of  $E_F$  threshold in determining the centrality classes showed differences of  $dn/dy dp_T$  yields on the level of 1%. However, a more sophisticated and more accurate procedure of calculation of centrality

selection biases is in development and will be released as a separate study for both Be+Be and Ar+Sc interactions.

### 17.1.2 Uncertainties in rapidity spectra and mean multiplicities

The uncertainties of double differential spectra  $dn/dy dp_T$  are directly propagated into the calculation of rapidity distribution and its errors. However, additional sources of uncertainty appear due to employed extrapolation procedures. Firstly, it should be remarked, that the  $p_T$  spectra are fitted to histograms, which were assigned a quadratic sum of statistical and systematic errors:  $\sigma_{\text{total}} = \sqrt{\sigma_{\text{stat}}^2 + \sigma_{\text{sys}}^2}$ . Then in the calculation of statistical errors of  $dn/dy$  only the histogram statistical uncertainties are propagated, while the error of integrated extrapolated function is added to systematic uncertainties.

Consequently, a similar procedure is done in case of extrapolation of  $dn/dy$  spectra in order to calculate mean multiplicities – the error of fitted extrapolated function integral is added to the systematic uncertainty. Unsurprisingly, the error increases significantly towards lower beam momenta, due to a shrinking range of measurements. Fig. 44 shows the share of the extrapolated region in the calculation of mean multiplicities, together with the relative systematic error.

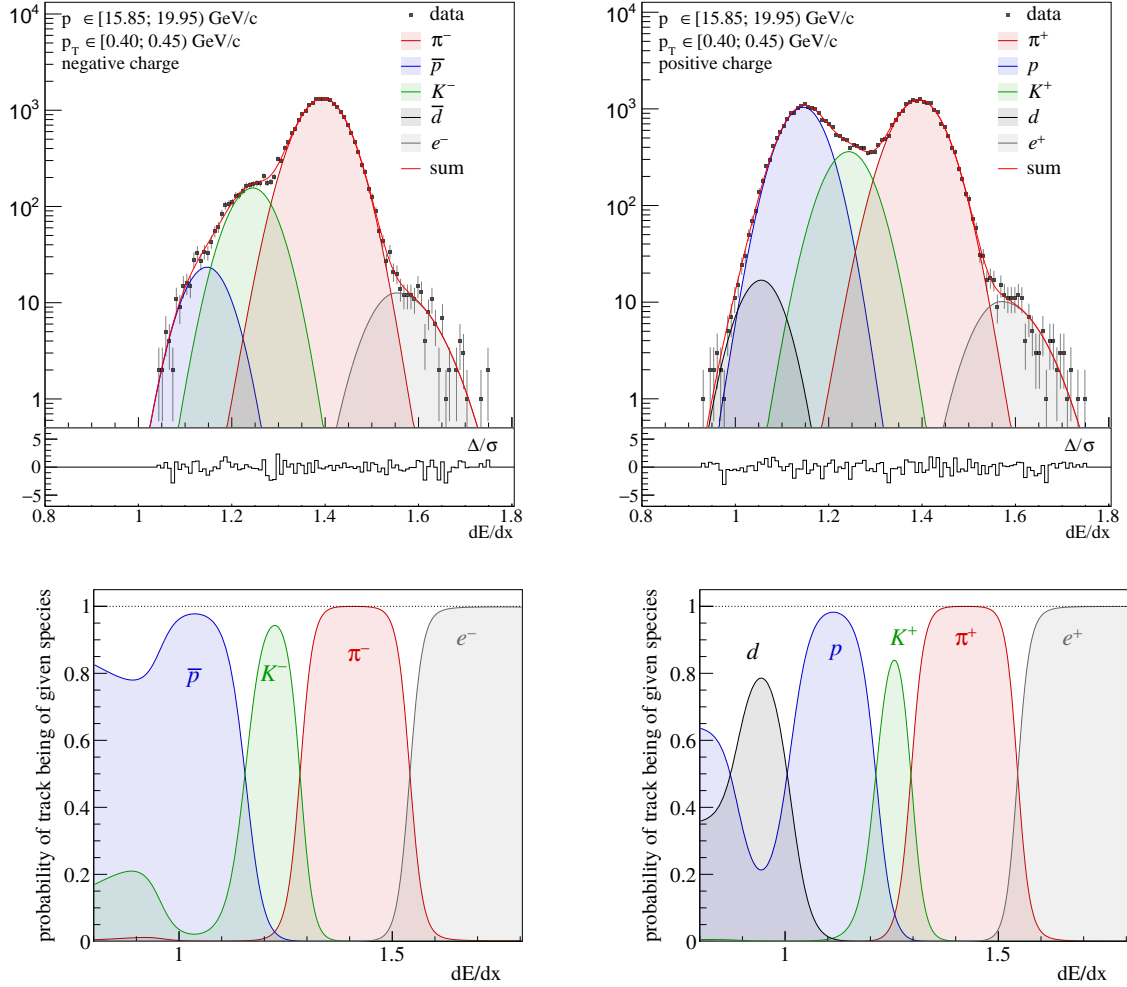


Figure 29: Top: Example of  $dE/dx$  distributions fitted with model in Eq. 28. Note the low values of fit residuals ( $\Delta/\sigma$ ) and their flat distribution. Bottom: Probabilities of identifying a track with given  $dE/dx$  as certain species, derived from the fits in the top panel.



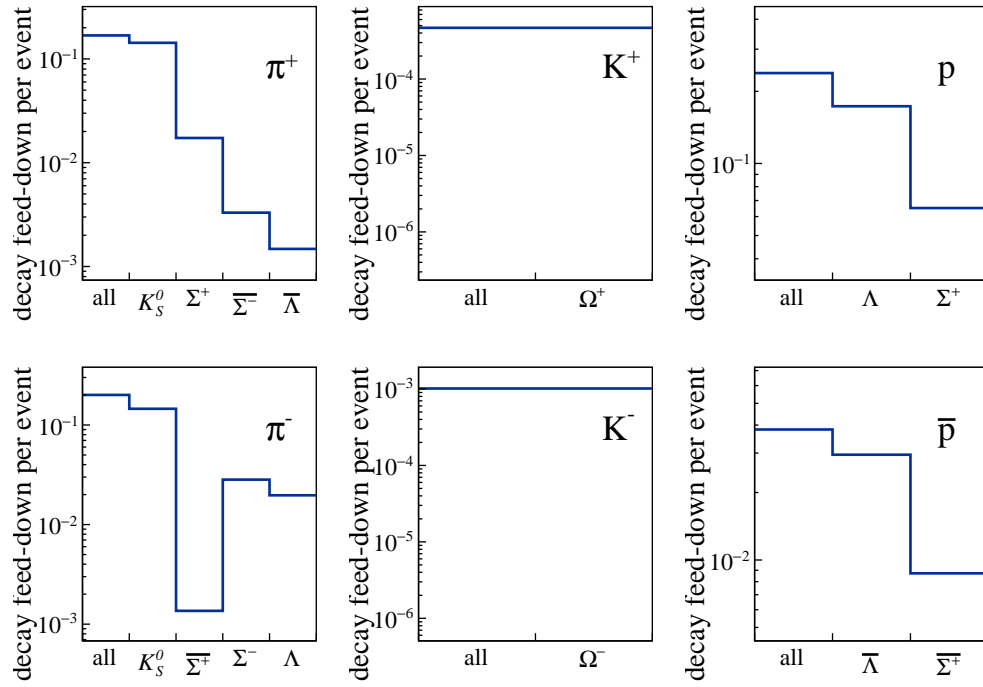


Figure 30: Per event contribution of reconstructed secondary tracks originating from weak decays and erroneously identified as products of primary interaction (based on EPOS).

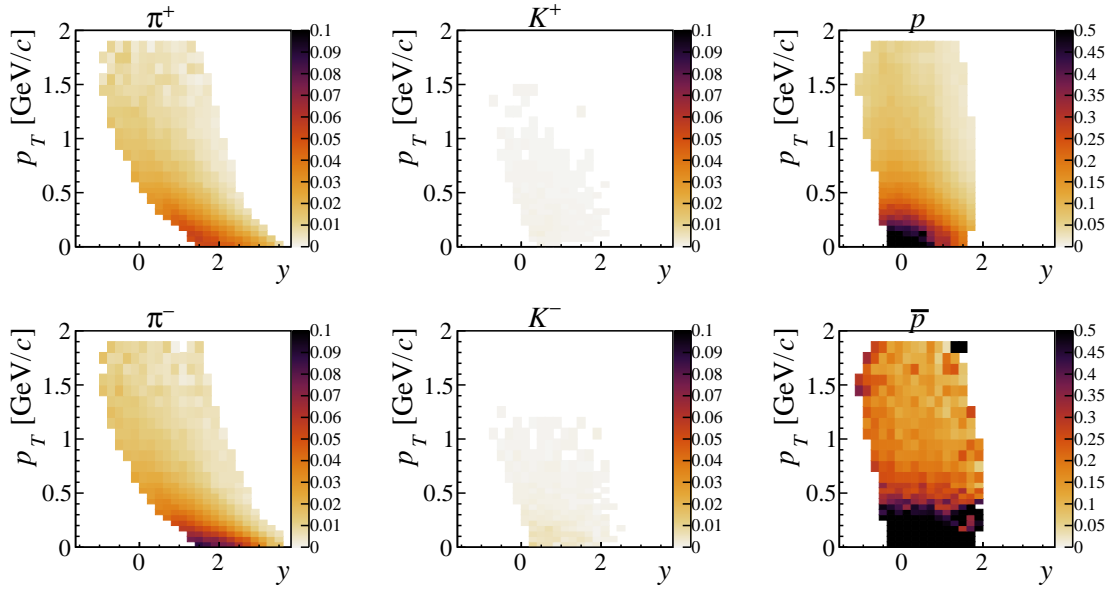


Figure 31: Relative contribution of weak decays products in spectra of identified hadrons. The corrections are based on EPOS Model [16] with data-derived tuning (see text for details). The feed-down for  $\pi^-$  and  $\pi^+$  is typically on the level of 1%-3%, reaching up to 10% in case of low- $p_T$   $\pi^-$ . Secondary kaons can only originate from sparsely produced  $\Omega^+$  and  $\Omega^-$  decays, thus the correction is well below 1%. Spectra of protons and anti-protons are heavily influenced by the decays of  $\Lambda$  and  $\Sigma^+$  ( $\bar{\Lambda}$  and  $\bar{\Sigma}^+$  for anti-protons) – in these cases feed-down correction can reach over 50% at low  $p_T$ . Similar numbers hold true for all collision energies.

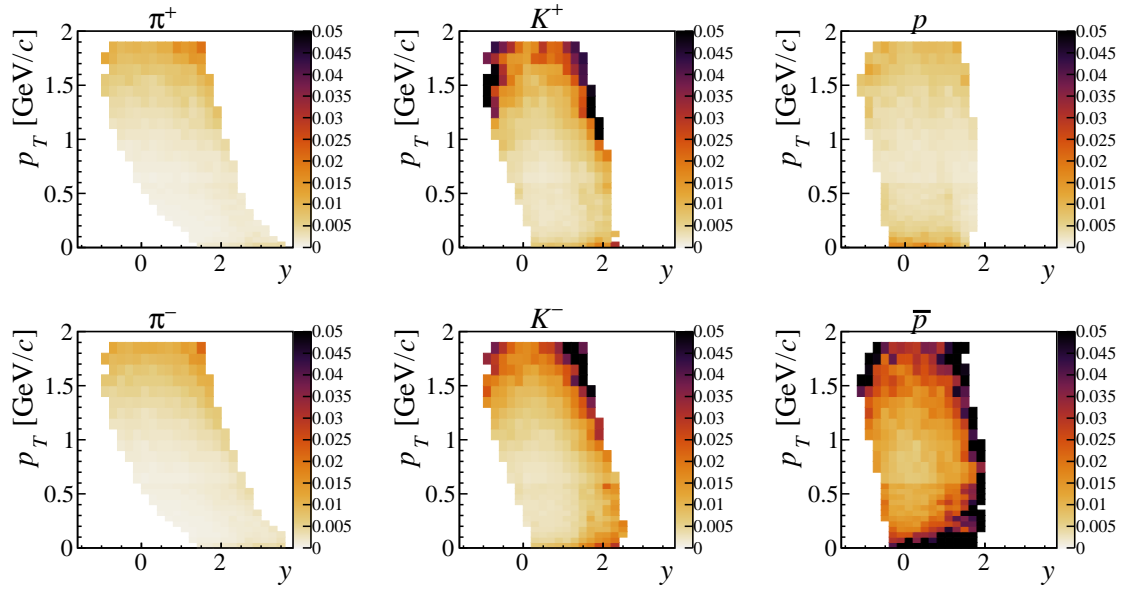


Figure 32: Relative statistical uncertainty calculated with the bootstrap method plotted for each identified particle species (at  $p_{\text{beam}}=150A$  GeV/c). The uncertainties exceed the typical level of  $\approx 1\%$  only at acceptance edges of  $K^+$ ,  $K^-$  spectra and in some regions of  $\bar{p}$  measurements. The values of statistical uncertainty are similar at all beam momenta.

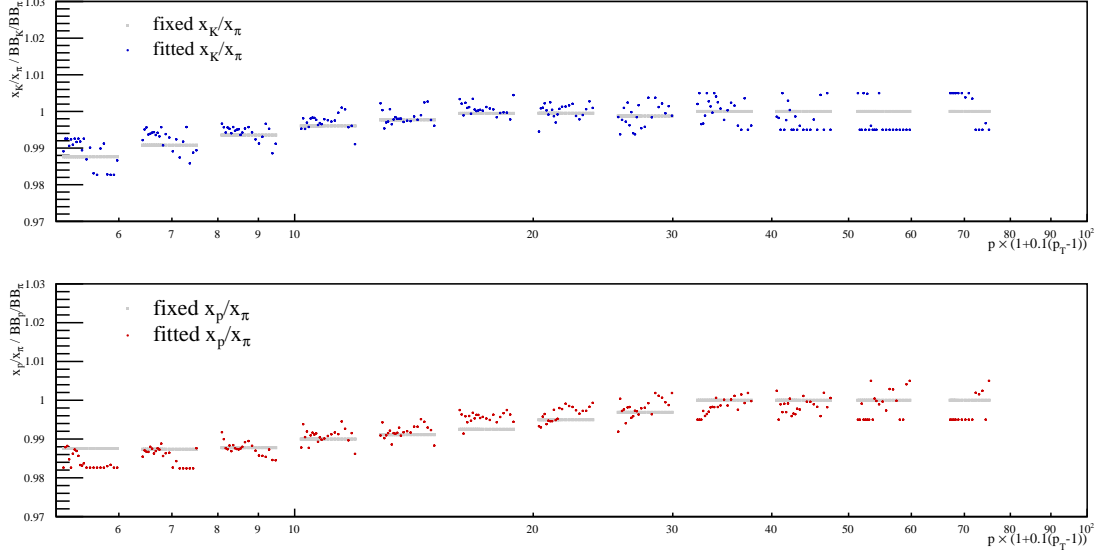


Figure 33: Relative differences of fitted  $K^+$  ( $K^-$ ) and  $p$  ( $\bar{p}$ ) peak positions. Coloured points show results obtained for simultaneous fit of  $dE/dx$  distributions of both charges in each of  $(p, p_T)$  bins, while grey lines show results of simultaneous fit of up to 18 charge and  $p_T$  bins within given momentum bin.

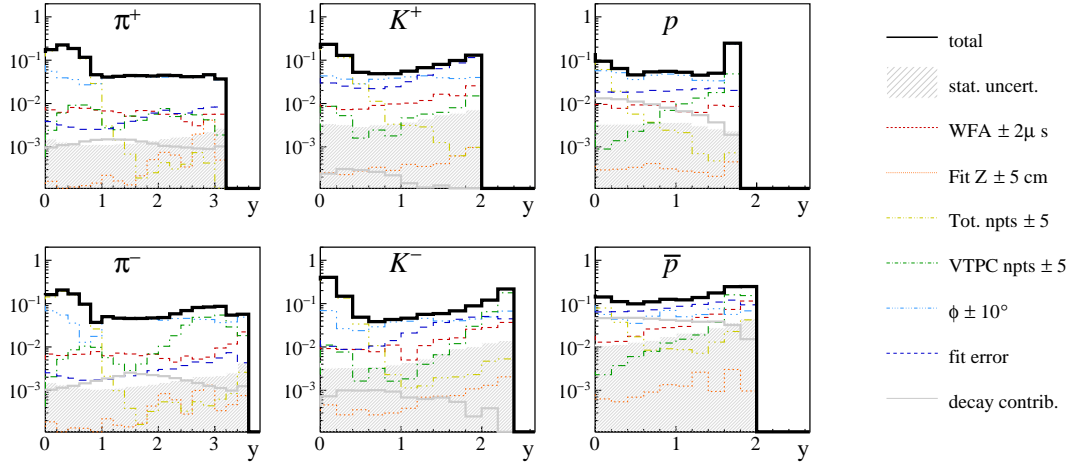


Figure 34: Systematic uncertainty for each identified particle species in dependence on rapidity  $y$  at  $p_{\text{beam}} = 150A$  GeV/c. Different contributions to the total uncertainty are plotted, along with statistical error (shaded area).

---

## Part IV

# Results and discussion

This part is devoted to presentation and discussion of charged hadron production properties measured in central  $^{40}\text{Ar}+^{45}\text{Sc}$  collisions at incident projectile momenta 13A-150A GeV/c.

The primary focus of analysis presented in this thesis is the kinematic spectra of six identified charged hadrons: charged pions ( $\pi^+$  and  $\pi^-$ ), charged kaons ( $K^+$  and  $K^-$ ), protons and antiprotons.

Section 18 describes the results concerning charged pions  $\pi^+, \pi^-$ . They serve as a cross-check for measurements in  $h$ -minus analysis, showing a good agreement between the two methods. Also  $\pi^+/\pi^-$  ratio is discussed in view of approximation of  $\langle\pi^+\rangle$  multiplicity.

In Section 19 the production of charged kaons ( $K^+, K^-$ ) is discussed. Double differential spectra are extrapolated in transverse momentum and rapidity, which allows for the calculation of mean multiplicities of  $K^+$  and  $K^-$  mesons.

Similarly, Section 20 describes measurements of protons ( $p$ ) and antiprotons ( $\bar{p}$ ), including methods of extrapolation of double dimensional spectra in  $y$  and  $p_T$  and calculation of antiproton mean multiplicities.

It should be noted, that in this chapter only a summary of the most important results is included, while Appendix C contains numerical values of measured quantities and Appendix D includes supplementary plots.

Finally, Section 21 reviews presented measurements in terms of collision energy and system size dependence, including additionally a comparison with relevant models.

Section 22 concludes the dissertation with a summary of presented results and gives an outline of future perspectives in the studies of the onset of deconfinement.

## 18 Charged pions

The sample measurements of charged pion  $y$ - $p_T$  spectra at 30A and 150A GeV/c are presented in Fig. 35. The limit imposed on minimum momentum in PID procedure ( $p > 5$  GeV/c) results with a heavily skewed shape of the acceptance, thus large portion of measurements at mid-rapidity and low  $p_T$  is missing.

Combining  $dE/dx$  and  $tof$ - $dE/dx$  (not yet completed) analyses allows to cover more phase space, although still not enough to obtain full forward hemisphere yields. Moreover, any extrapolation of spectra towards low  $p_T$  cannot be done easily, as the contribution of decays is significant for both  $\pi^+$  and  $\pi^-$ . Full forward rapidity measurements of negatively charged pions can be obtained with the  $h$ -minus method (described in Sec. 13.1). Preliminary results on  $\langle\pi^-\rangle$  mean multiplicities are already available [1] and a cross-check of obtained measurements can be done. Figure 36 displays a comparison of results

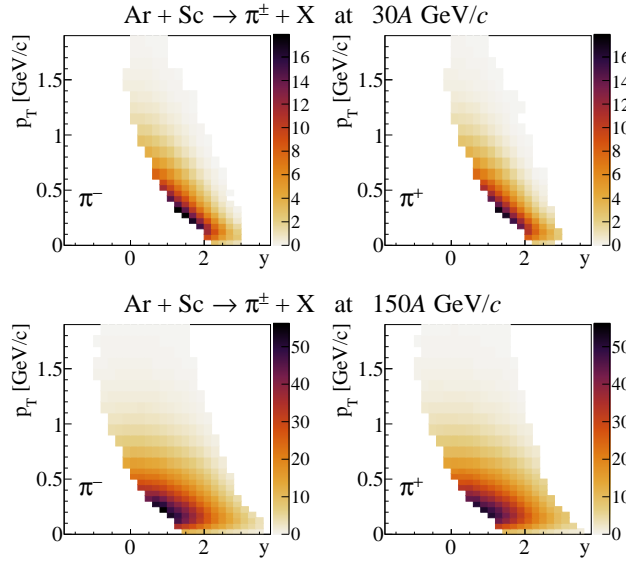


Figure 35:  $d^2n/dy dp_T$  spectra of charged pions produced in central Ar+Sc collisions measured at 30A GeV/c (top) and 150A GeV/c (bottom).

of the two methods at 150A GeV/c on the level of double differential spectra in  $y$  and  $p_T$ , showing a good agreement – typical discrepancies are on the level of 1–3%.

The  $\langle\pi^-\rangle$  mean multiplicities obtained with  $h$ -minus method will be used in studying collision energy and system size dependence through  $\langle K^-\rangle/\langle\pi^-\rangle$  ratios in Sec. 21. However, as  $\langle K^+\rangle/\langle\pi^+\rangle$  ratios are even more interesting in terms of studied physics, an estimation of positively charged pions mean multiplicity is desired. In order to obtain a good approximation of  $\langle\pi^+\rangle$  yield we study  $\pi^+/\pi^-$  ratio in:

1. Simulated events with EPOS [16].  
Figure 37 shows a  $\pi^+/\pi^-$  ratio calculated on the level of double differential spectra in  $y$  and  $p_T$  for  $dE/dx$  analysis results and for EPOS MC simulation. Although the model does not reproduce all the features observed in experimental data (such as electromagnetic interactions or flow) the general trends are well approximated.
2. Integrated pion measurements obtained with  $dE/dx$  method within limited acceptance.

Values close to 1 are expected based on an approximate isospin symmetry of collided system. Following table lists  $\pi^+/\pi^-$  ratios obtained for all analysed collision momenta:

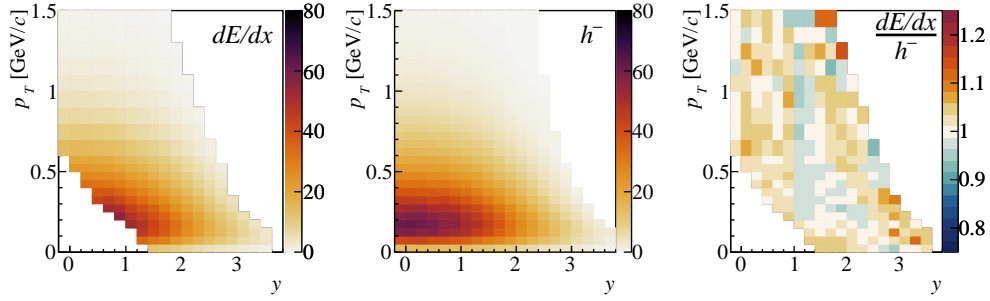


Figure 36: Left and middle panel show  $d^2n/dydp_T$  [(GeV/c) $^{-1}$ ] distributions of  $\pi^-$  measured at 150A GeV/c with  $dE/dx$  and  $h^-$  methods respectively. Right panel shows ratio of results obtained with these two methods, showing good agreement – visible discrepancies rarely exceed 2.5%.

$p_{\text{beam}}$ [GeV/c]	13A	19A	30A	40A	75A	150A
$\pi^+/\pi^-$ EPOS	0.954	0.961	0.969	0.972	0.978	0.983
$\pi^+/\pi^-$ in $dE/dx$ acc.	0.884	0.949	0.933	0.929	0.952	0.975

The calculated ratios are indeed close to 1. In EPOS, at all energies the  $\pi^+$  and  $\pi^-$  yields are within 5%. Comparing pion multiplicities obtained with  $dE/dx$  analysis it is important to remark that the acceptance shrinks considerably at lower collision energies, thus leading to unavoidable biases. In conclusion it was decided, that a following approximation will be used for pion yields measured in Ar+Sc collisions:

$$\langle \pi^+ \rangle \approx \langle \pi^- \rangle$$

Since the  $\pi^+/\pi^-$  ratio cannot be determined precisely at the moment with experimental data, the 5% additional uncertainty on  $\langle \pi^+ \rangle$  mean multiplicity will be imposed.

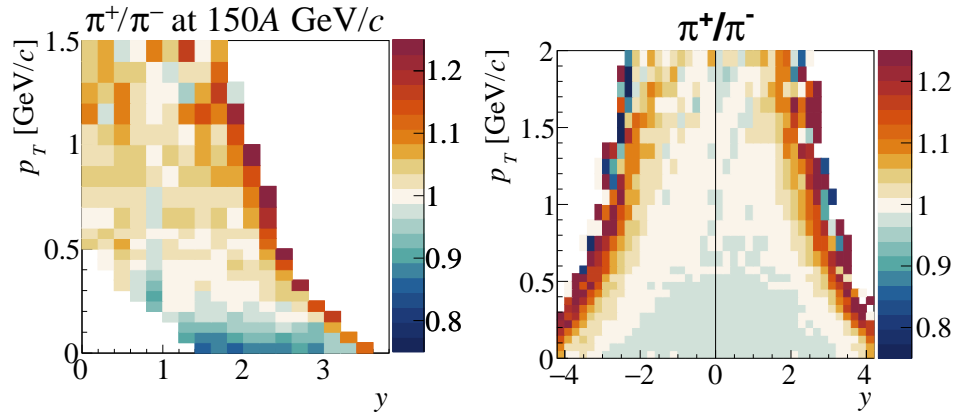


Figure 37: Both plots show ratios of  $\pi^+$  and  $\pi^-$   $d^2n/dy dp_T$  yields at 150A GeV/c – on the left are results of this analysis and on the right yields from EPOS MC simulation are displayed. Note that the dip in  $\pi^+/\pi^-$  ratio at small  $p_T$  is an effect of electromagnetic interactions and it is not reproduced by used model.



## 19 Charged kaons

Measurements of charged kaon production properties are perhaps the most interesting results presented in this thesis. Kaon mesons are the lightest carriers of strange quarks, thus providing valuable information concerning strangeness production. In this section the  $y$ - $p_T$  spectra of  $K^+$  and  $K^-$  produced in central Ar+Sc collisions at 13A-150A GeV/c are presented, then methods of their extrapolation are discussed and finally charged kaon mean multiplicities are calculated.

### 19.1 Transverse Momentum Spectra

Let us first focus on double differential yields per event  $d^2n/(dy dp_T)$ . Figure 38 displays an example of transverse momentum distributions of  $K^-$  in slices of rapidity  $y$  at  $p_{\text{beam}}=150A$  GeV/c. In order to obtain  $dn/dy$  yields, the data is

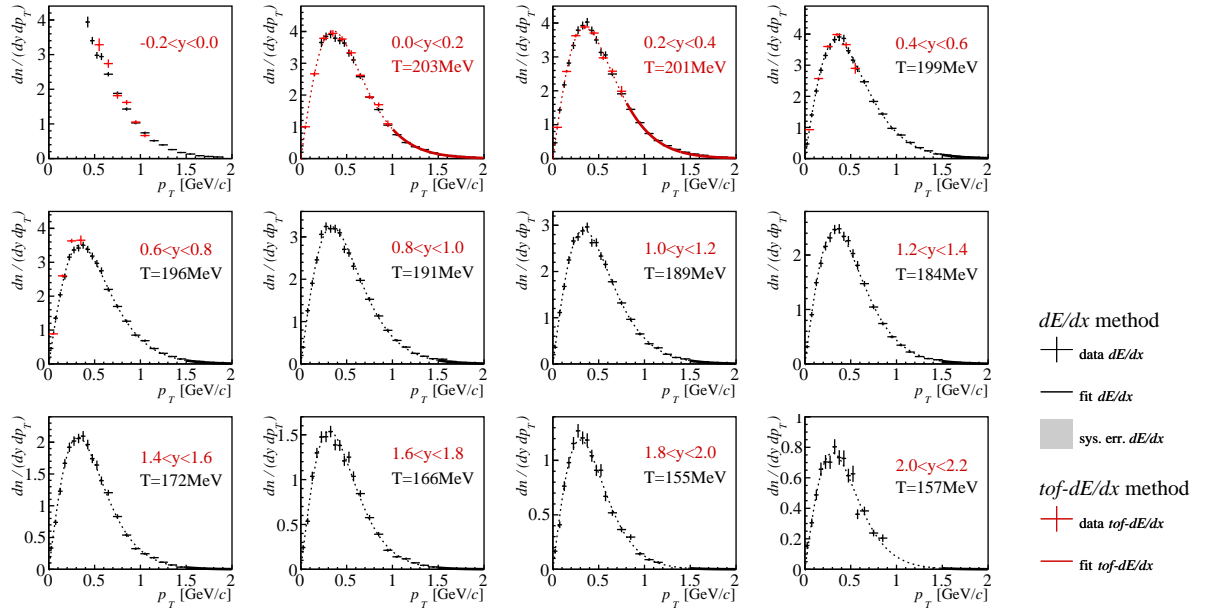


Figure 38: A sample set of  $d^2n/(dp_T dy) [(\text{GeV}/c)^{-1}]$  distributions of  $K^-$  at 150A GeV/c. Red points stand for preliminary results of  $\text{tof-}dE/dx$  analysis contributing to the measurements in mid-rapidity region and black points are the results of  $dE/dx$  method (this work). Statistical uncertainties are plotted with vertical lines at points and systematic uncertainty of  $dE/dx$  results is marked with grey bands. At high collision momenta (150A, 75A GeV/c) large portion of acceptance of both methods overlap, allowing a precise cross-check of analyses results. Note a good agreement of measurements of the spectra with  $\text{tof-}dE/dx$  and  $dE/dx$  methods.

extrapolated in  $p_T$  to account for unmeasured regions at high values of  $p_T$  and in rare cases at low  $p_T$  as well. Exponential dependence in  $p_T$  is assumed – incidentally, kaon spectra are well approximated by simple exponential fits. Firstly, the effects of collective flow bend spectra up (or down) in case of lighter (or more massive) particles, while kaon  $p_T$  distribution remains approximately exponential. Secondly, the contribution of secondary kaons is insignificant, thus the spectra are almost unaffected by decays. With this consideration in mind, a following function is used to fit kaon  $p_T$ -spectra:

$$\frac{1}{p_T} \frac{d^2 n}{dp_T dy} = \frac{dn/dy}{T \cdot (m_K + T)} \cdot e^{-(m_T - m_K)/T} \quad (41)$$

The function is fitted in the acceptance region and its integral beyond the acceptance is added to the measured data. Only the experimental results up to  $p_T \leq 1.5$  GeV/c are considered, since the (unaccounted for) contribution of split tracks is too high at higher  $p_T$  values. The contribution of the extrapolation towards high  $p_T$  is typically of the order of 1%, while in the rare cases of extrapolation at  $p_T$  close to zero it can amount to over 10%.

## 19.2 Inverse slope parameter $T$

The fit of transverse momentum spectra with Eq. 41 determines the inverse slope parameter  $T$ . As the slope of the spectra can be determined with a simple exponent at all reactions, it is possible to compare obtained values with other reactions (namely  $p+p$ , Be+Be, and Pb+Pb). The physical interpretation of the  $T$  parameter is not straightforward, although within hydrodynamical models it reflects the temperature at freeze-out modified by effects of transverse flow [25].

The results obtained for the three analysed collision energies are shown in Fig. 39. An extrapolation of Ar+Sc  $dE/dx$  results at forward rapidity data to  $y \approx 0$  agrees with measurements obtained with *tof*- $dE/dx$  analysis and approaches values fitted in Pb+Pb collisions. Additionally, at 75A and 150A GeV/c it can be observed that fitted values of  $T$  are approximately constant up to  $y \approx 0.8$ , which agrees with observations made in the analysis of Pb+Pb [34]. Small systems ( $p+p$ , Be+Be) show significantly lower values of  $T$ .

## 19.3 Rapidity spectra

Rapidity distributions are obtained through integration of the double differential spectra in  $p_T$  at each bin of rapidity and by addition of extrapolated yields in unmeasured regions. Fig. 40 shows final rapidity distributions for each of analysed collision energies. The spectra are fitted with a sum of two Gaussians placed symmetrically w. r. t.  $y=0$ :

$$f_{fit}(y) = \frac{A}{\sigma\sqrt{2\pi}} \exp\left(-\frac{(y-y_0)^2}{2\sigma^2}\right) + \frac{A}{\sigma\sqrt{2\pi}} \exp\left(-\frac{(y+y_0)^2}{2\sigma^2}\right) \quad (42)$$

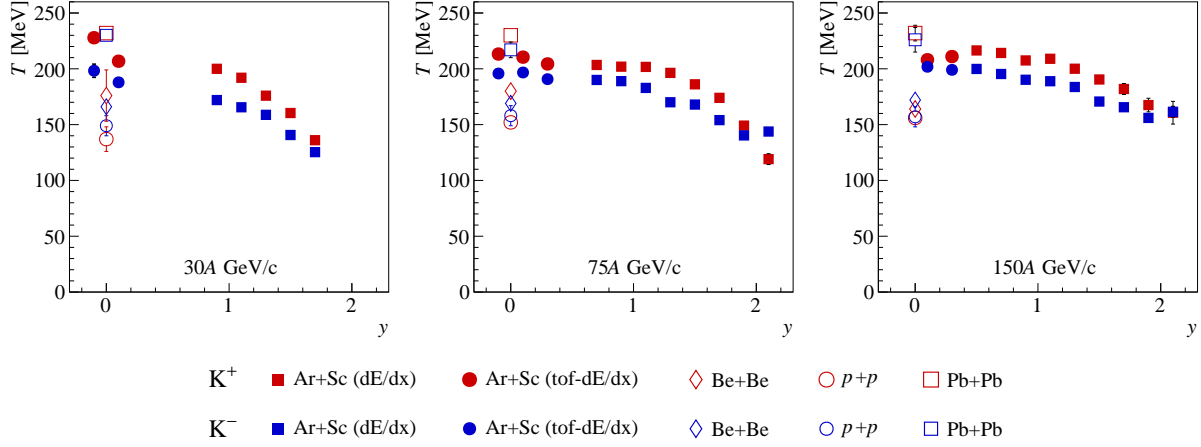


Figure 39: Inverse slope parameter  $T$  fitted to charged kaon  $p_T$  distributions at 30A, 75A and 150A GeV/c. Main highlight of these results is the fact that measured slope in Ar+Sc reactions is close to the one obtained in Pb+Pb.

where  $\sigma, y_0$  and  $A$  are free fit parameters. An exception are the spectra at 13A GeV/c, where in the absence of measurements at mid-rapidity  $\sigma$  was fixed at value extrapolated from higher collision energies (see Fig. 41). Note that symmetry of amplitudes in forward and backward hemispheres is assumed, which might not be true in case of collisions of asymmetric systems (due to different masses of beam and target particles).

As already mentioned, Fig. 41 shows properties of parameters fitted to rapidity distributions of  $K^+$  and  $K^-$  at six beam momenta. Firstly, let us note a smooth evolution of the fitted parameters. Secondly, an expected constant increase of spectra width is observed (here measured as an RMS of the distribution). Figures 42 and 43 show additionally rapidity distributions of  $K^+$  and  $K^-$  in three bins of centrality: 0-5%, 5-10% and 10-15%. The yields at more central collisions are higher than at more peripheral ones.

#### 19.4 Kaon mean multiplicity

In order to obtain the full phase space ( $4\pi$ ) mean kaon multiplicity, the measured  $\frac{dn}{dy}$  spectra are supplemented with extrapolated yields by integrating the fitted function defined in Eq. 42. Figure 40 illustrates both the measured data and the fitted model. The mean multiplicities of  $K^+$  and  $K^-$  calculated at each beam momentum are given by:

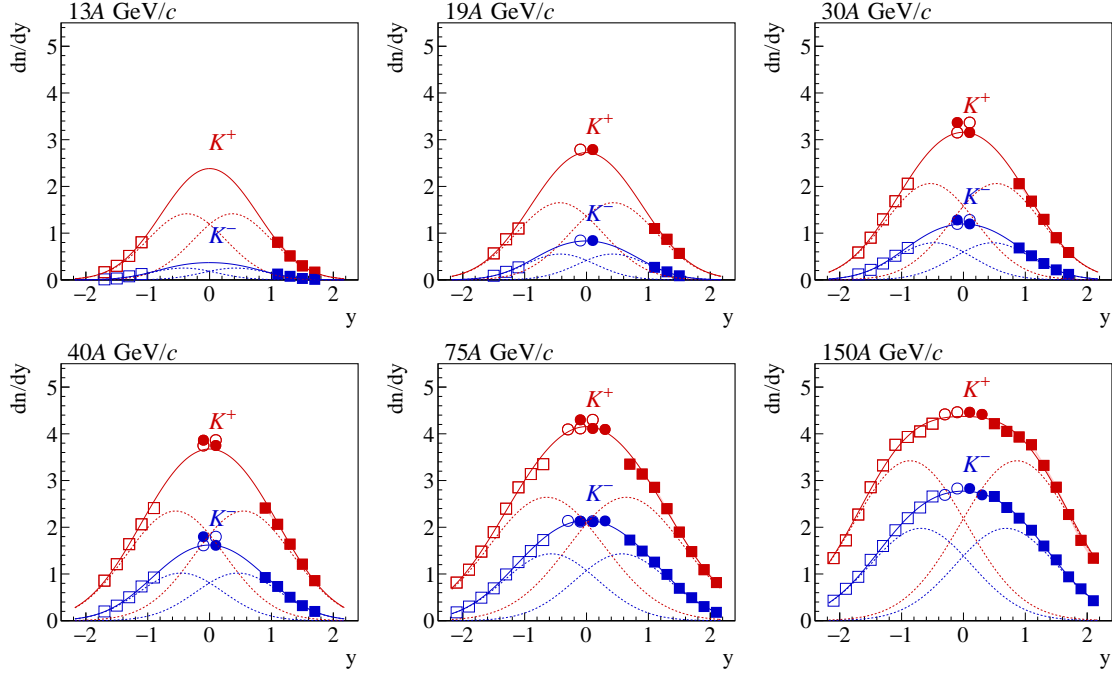


Figure 40: Rapidity distributions of  $K^+$  and  $K^-$  measured at 13A–150A GeV/c. The acceptances of both  $dE/dx$  and  $tof-dE/dx$  methods change with collision energy, covering maximum of whole forward hemisphere at 150A GeV/c. Double-Gaussian fitted to the spectra describes the data well, allowing to extrapolate  $dn/dy$  yields in unmeasured regions with satisfactory precision. The open points represent measured data reflected w. r. t.  $y = 0$ .

$p_{\text{beam}}^A$ [A GeV/c]	$\langle K^+ \rangle$	$\langle K^- \rangle$
13	$4.470 \pm 0.192 \pm 1.234$	$0.671 \pm 0.009 \pm 0.187$
19	$5.814 \pm 0.250 \pm 0.750$	$1.555 \pm 0.044 \pm 0.361$
30	$7.544 \pm 0.324 \pm 0.311$	$2.499 \pm 0.023 \pm 0.150$
40	$9.248 \pm 0.398 \pm 0.282$	$3.450 \pm 0.023 \pm 0.151$
75	$12.28 \pm 0.528 \pm 0.265$	$5.418 \pm 0.015 \pm 0.074$
150	$15.68 \pm 0.674 \pm 0.570$	$8.105 \pm 0.025 \pm 0.129$

Additionally using the preliminary results from "h-minus" analysis method (as described in Sec. 18)  $K/\pi$  multiplicity ratios can be calculated:

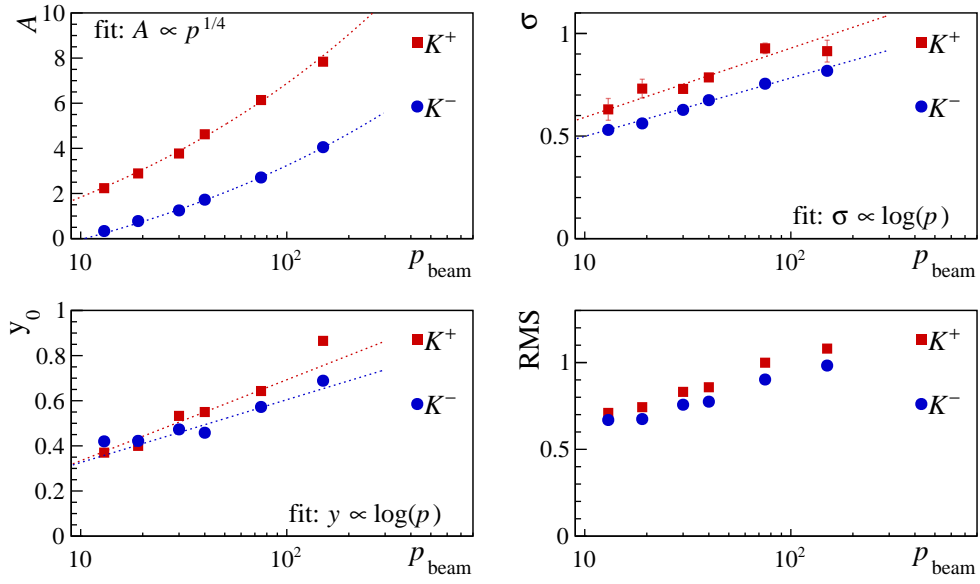


Figure 41: Fit parameters obtained in fitting kaon rapidity spectra with the function defined in Eq. 42 and total width of the distributions (RMS). Due to the lack of measurements at mid-rapidity at 13A GeV/c, width  $\sigma$  is fixed at an extrapolated value from fits at higher beam momenta.

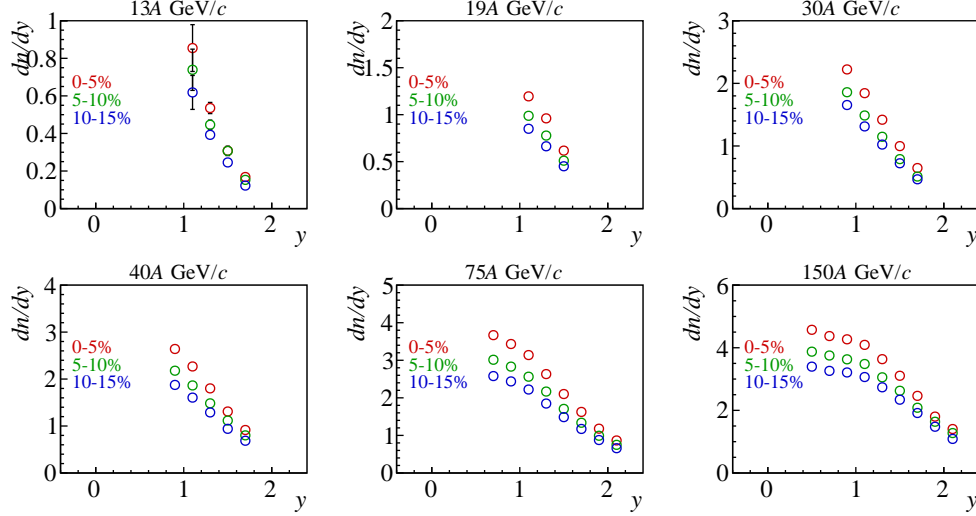


Figure 42: Rapidity spectra of  $K^+$  produced in Ar+Sc interactions at 13A-150A GeV/c measured at three bins of centrality: 0-5%, 5-10% and 10-15%. The  $dn/dy$  yields are higher at more central collisions.

$p_{\text{beam}}$ [A GeV/c]	$\langle K^+ \rangle / \langle \pi^+ \rangle$	$\langle K^- \rangle / \langle \pi^- \rangle$
13	$0.135 \pm 0.006 \pm 0.038$	$0.0188 \pm 0.0003 \pm 0.0053$
19	$0.131 \pm 0.006 \pm 0.018$	$0.0325 \pm 0.0009 \pm 0.0077$
30	$0.135 \pm 0.006 \pm 0.009$	$0.0414 \pm 0.0004 \pm 0.0032$
40	$0.145 \pm 0.006 \pm 0.009$	$0.0503 \pm 0.0003 \pm 0.0033$
75	$0.154 \pm 0.007 \pm 0.009$	$0.0631 \pm 0.0002 \pm 0.0033$
150	$0.155 \pm 0.007 \pm 0.010$	$0.0744 \pm 0.0002 \pm 0.0039$

Let us repeat a remark concerning systematic uncertainties originating from the extrapolation procedure. As the region of measurement shrinks, the calculation of multiplicity relies more on the fitted model and its uncertainty. Figure 44 displays the share of extrapolated region in calculation of mean multiplicities, together with the relative systematic uncertainty, which grows from the values below 5% at 40A-150A GeV/c, through over 10% at 19A GeV/c up to  $\approx 30\%$  at 13A GeV/c (where there are no mid-rapidity measurements).

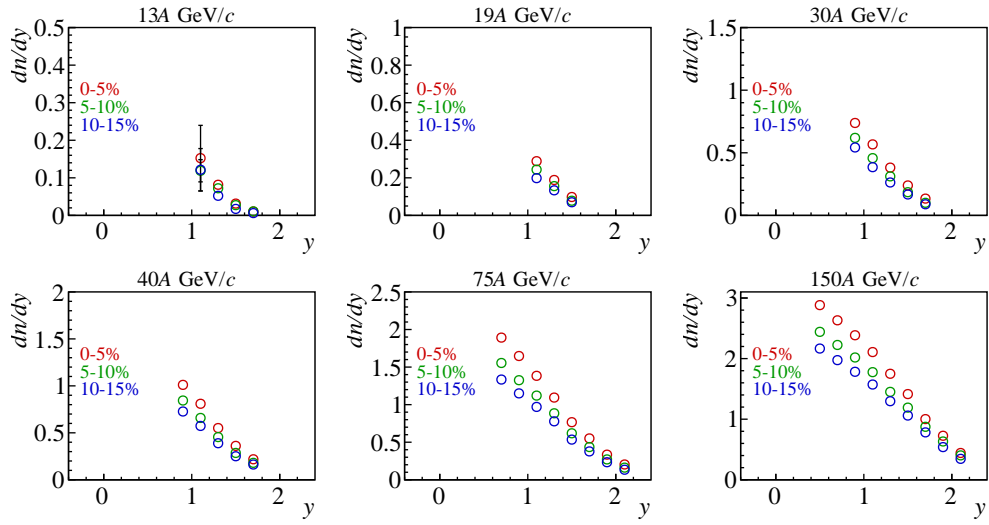


Figure 43: Rapidity spectra of  $K^-$  produced in Ar+Sc interactions at 13A-150A GeV/c measured at three bins of centrality: 0-5%, 5-10% and 10-15%. The  $dn/dy$  yields are higher at more central collisions.

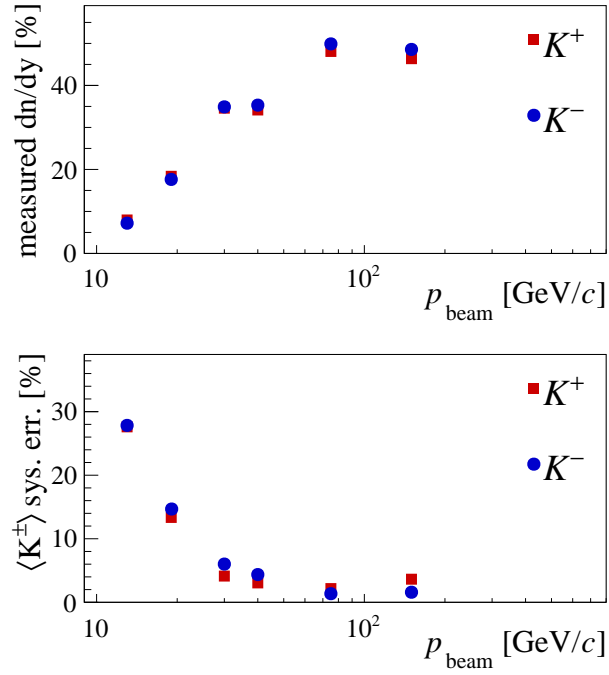


Figure 44: Top: Relative share of measured  $dn/dy$  to the total calculated multiplicity. Bottom: Relative systematic uncertainty of calculated mean kaon multiplicities ( $\langle K^+ \rangle$ ,  $\langle K^- \rangle$ ). Note how with decreasing range of measured  $dn/dy$  yields the systematic error increases. In particular, in the absence of mid-rapidity measurements at  $p_{\text{beam}}=13A$  GeV/c, the error of extrapolation becomes large.



## 20 Protons and antiprotons

### 20.1 Transverse momentum spectra

While a simple exponential fit might be well suitable for description of kaon transverse spectra, it is no longer true in case of proton  $p_T$  distributions. In order to extrapolate missing regions of acceptance a more sophisticated model has to be used, that explicitly accounts for effects of transverse flow. In this analysis a blast-wave model was used to fit the measured proton and antiproton spectra and to extrapolate the  $dn/dydp_T$  yields in unmeasured regions. Specifically, a version of the model that implements Gibbs-Boltzmann statistic was used [40], in which the transverse spectra are parametrized in a following fashion:

$$\frac{dn}{p_T dp_T} \propto \int_0^R r dr m_T I_0\left(\frac{p_T \sinh \rho}{T}\right) K_1\left(\frac{m_T \cosh \rho}{T}\right) \quad (43)$$

where  $\rho$  is a boost angle:

$$\rho = \text{atanh}(\beta_T(r)). \quad (44)$$

The model assumes, that hadrons decouple from a system in local thermal equilibrium with temperature  $T$ , which expands both longitudinally and in the transverse direction. The transverse velocity profile is parametrized according to a power law:

$$\beta_T(r) = \beta_s (r/R)^\alpha, \quad (45)$$

where  $\beta_s$  is the maximum surface flow velocity and the  $\alpha$  exponent describes the flow profile at radius  $r$  ( $r < R$ ,  $R$  is the maximum radius of the source). Additionally, a mean transverse velocity can be calculated as:

$$\langle \beta_T \rangle = \beta_s / (1 + \alpha/2) \quad (46)$$

Figure 45 shows an example of  $p_T$  distributions and blast-wave model fits and Fig. 46 shows parameters of fitted function. It can be seen, that even though the fit was performed for just a single particle species it gives stable and reasonable estimations of  $T$  and  $\langle \beta_T \rangle$ . However, in order to infer any physics conclusions from the fit parameters a simultaneous fit to multiple particle species must be made, with a detailed inspection of fit residuals. In this work, the main purpose of using blast-wave model is to obtain an accurate extrapolation. Similarly to fits of kaon  $p_T$  spectra, the contribution of the extrapolation towards high  $p_T$  is very low ( $\lesssim 1\%$ ), while in case of extrapolation at small  $p_T$  it can exceed 10%.

### 20.2 Rapidity spectra

Rapidity distributions are obtained through integration of the double differential spectra in  $p_T$  at each bin of  $y$  and by an addition of extrapolated yields in unmeasured regions. Figure 47 shows final proton and antiproton rapidity

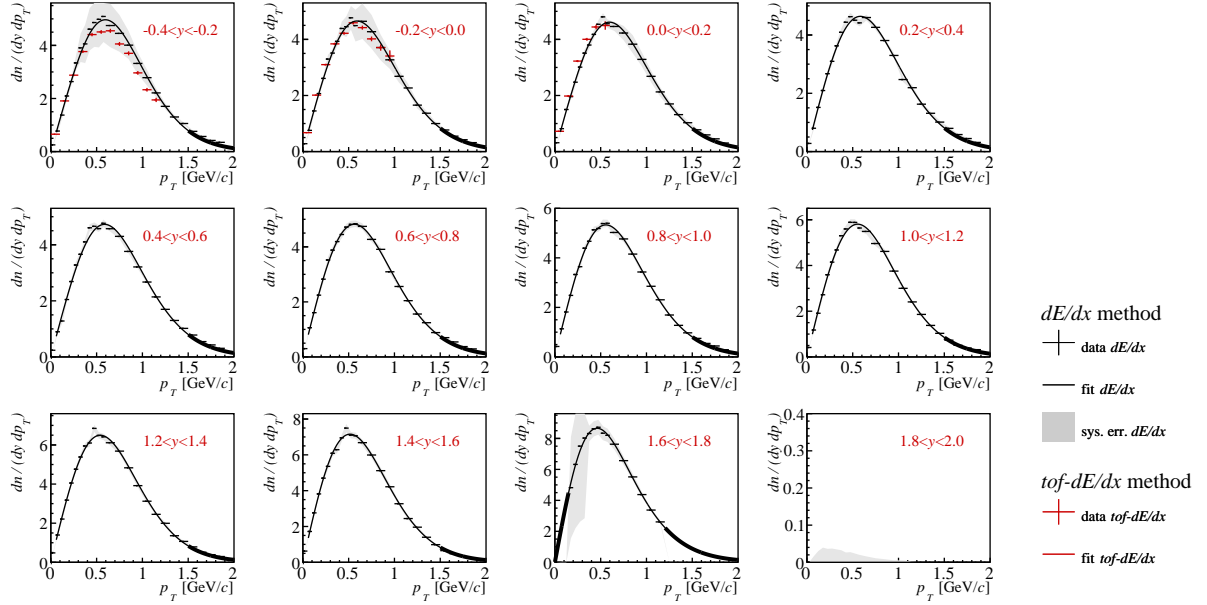


Figure 45: A sample set of  $d^2n/(dp_T dy)$  distributions of protons produced in Ar+Sc interactions at 150A GeV/c. Red points stand for preliminary results of  $tof-dE/dx$  analysis contributing to the measurements in mid-rapidity region and black points are the results of  $dE/dx$  method (this work). Statistical uncertainties are plotted with vertical lines at points and systematic uncertainty of  $dE/dx$  results is marked with grey bands. At high collision momenta (150A, 75A GeV/c) large portion of acceptance of both methods overlap, allowing a precise cross-check of analyses results. Note a very good agreement in measurements of the spectra with  $tof-dE/dx$  and  $dE/dx$  methods.

distributions for each of analysed collision energies. In models of heavy-ion collisions, rapidity spectra of protons are very sensitive to changes in the equation of state [41]. In the EPOS model, the shape of the spectra is approximately reproduced, although the overall accuracy in absolute yields is low. Due to large discrepancies of the experimental data and the model, an extrapolation in rapidity was not performed and as a consequence mean multiplicities were not calculated either. Contrarily to well-understood model extrapolations in  $y$ -spectra of kaons, a similar procedure cannot be employed here. The shape of proton rapidity distributions changes significantly with beam momentum and the unmeasured regions constitute a significant portion of total multiplicity. In order to correctly estimate mean multiplicities of protons, a better theoretical understanding of the spectra shape is necessary. However, calculation of mean multiplicities of antiprotons was possible and details are presented in the following section.

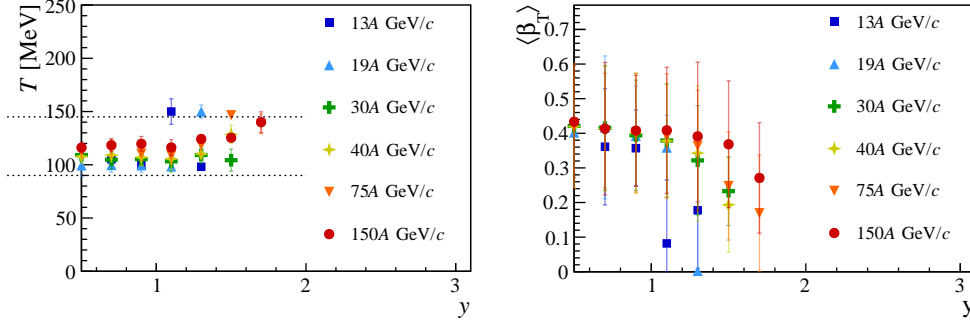


Figure 46: Parameter  $T$  fitted to transverse momentum distribution of protons produced in Ar+Sc interactions (*left*), together with mean transverse velocity calculated based on the fits (*right*).

Additionally to main results obtained for 10% of most central events an analysis at three different bins of centrality was performed: 0-5%, 5-10% and 10-15%. Figures 48 and 49 show rapidity distributions of protons and antiprotons at listed centrality intervals. In agreement with our expectations, more central events are characterized with higher  $dn/dy$  yields. Moreover in some cases (e. g. at  $p_{\text{beam}}=30A$  GeV/c) a subtle change of spectra shape is visible.

### 20.3 Antiproton mean multiplicities

Mean antiproton multiplicities ( $4\pi$ ) were calculated in a similar way as in case of charged kaons. Measured  $\frac{dn}{dy}$  spectra were supplemented in missing acceptance with integral of the symmetric double Gaussian (Eq. 42) fitted to the data. Figure 47 illustrates both the measured data and the fitted model. The  $\bar{p}$  mean multiplicities calculated at each beam momentum are given by:

$p_{\text{beam}}$ [GeV/c]	30A	40A	75A	150A
$\langle \bar{p} \rangle$	0.119	0.213	0.518	1.08
stat. unc.	0.038	0.038	0.054	0.089
sys. unc.	0.038	0.060	0.123	0.208

Similarly as discussed in Sec. 19.4, employed extrapolation procedure results with a systematic uncertainty, that increases with shrinking acceptance towards lower energies. The fraction of measured multiplicity contribution to the total multiplicity varies from over 50% at top SPS collision energy to only  $\approx 10\%$  at 13A GeV/c. This effect, combined with large uncertainties of antiproton  $dn/dy$  data prevented calculation of mean multiplicities at 13A and 19A GeV/c – total uncertainties were on the level of 100% of measured yields.

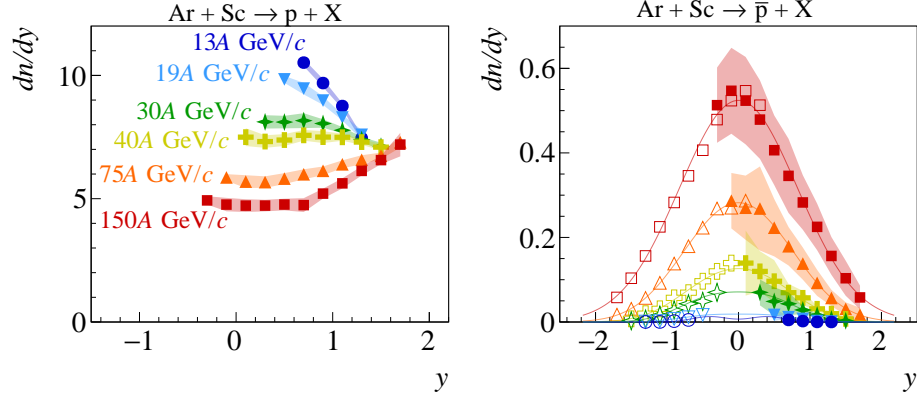


Figure 47: Rapidity spectra of protons and antiprotons produced in Ar+Sc interactions at six beam momenta from 13A to 150A GeV/c.

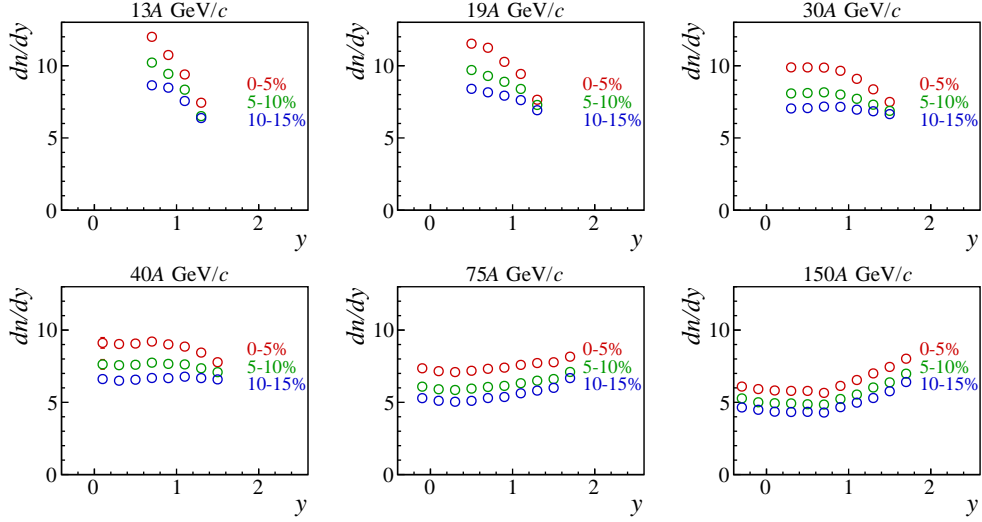


Figure 48: Rapidity spectra of protons produced in Ar+Sc interactions at six beam momenta 13A–150A GeV/c in three bins of centrality: 0-5%, 5-10% and 10-15%.

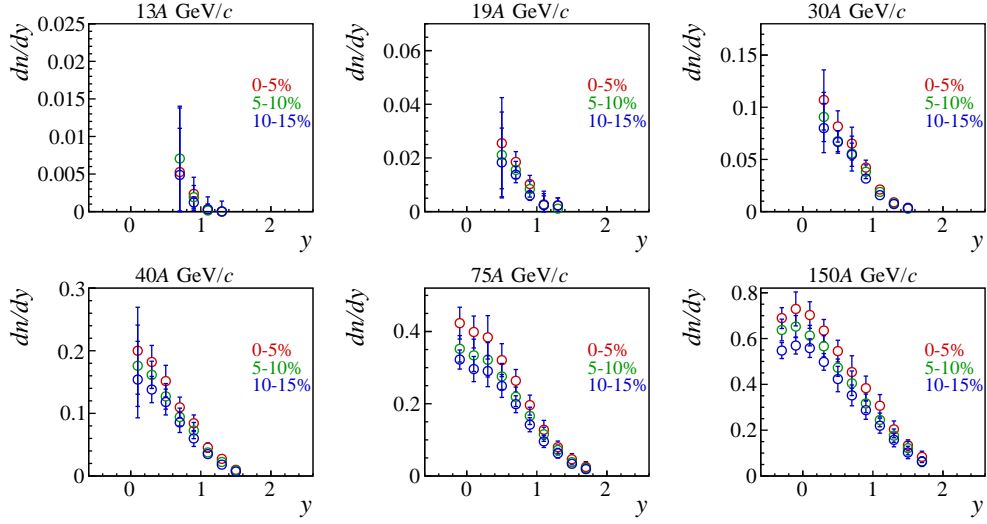


Figure 49: Rapidity spectra of antiprotons produced in Ar+Sc interactions at six beam momenta 13A–150A GeV/c in three bins of centrality: 0-5%, 5-10% and 10-15%.

## 21 Collision energy and system size dependence

### 21.1 The lack of horn

So what new do we learn from the data on Ar+Sc reactions? Let us first focus on the most prominent hypothesized signature of the onset of deconfinement – the "horn". Characteristic, non-monotonic behaviour of the  $K^+$  over  $\pi^+$  ratio in central heavy ion collisions (see: Pb+Pb and Au+Au in Fig. 50) agrees with predictions of SMES [7], in which quarks and gluons are the relevant degrees of freedom in the early stage of the collision. In the case of intermediate size systems however, no such vivid structure is present. Nevertheless, two interesting features demand attention. Firstly, a clear distinction between two datasets is visible –  $p+p$  and Be+Be results cluster around similar values, while Pb+Pb, Au+Au and Ar+Sc show much higher  $K^+/\pi^+$  ratios. Secondly, although Ar+Sc is clearly separated from small systems its energy dependence does not resemble the peak seen in heavy-ion reactions. No theoretical description can reproduce this behaviour – neither statistical [22, 7, 42] nor dynamical models [43] (see Sec. 21.4, figures 58 and 61).

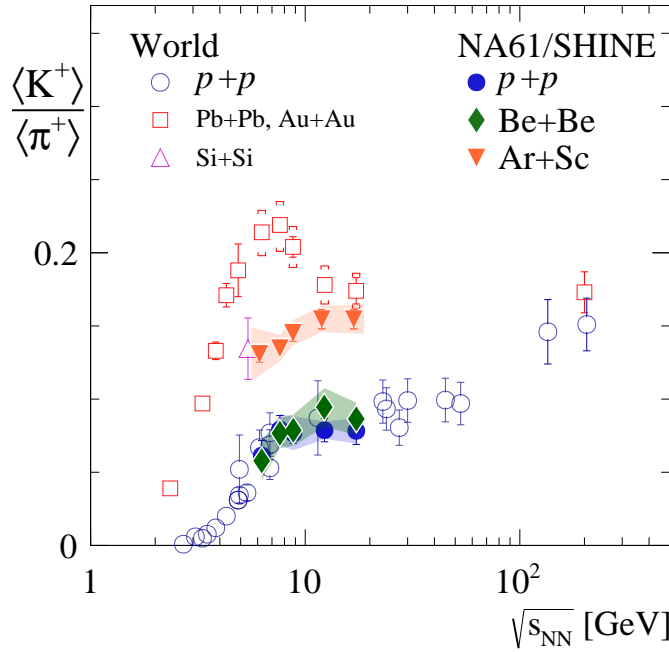


Figure 50: Rapid changes of  $K^+/\pi^+$  ratio visible in heavy ion collisions of Pb+Pb and Au+Au are not observed in collisions of Ar+Sc. In fact, at low SPS energies yields obtained for Ar+Sc collisions are in the middle between  $p+p$  and Pb+Pb values. At higher collision energies Ar+Sc data points closer resemble heavy ion results.

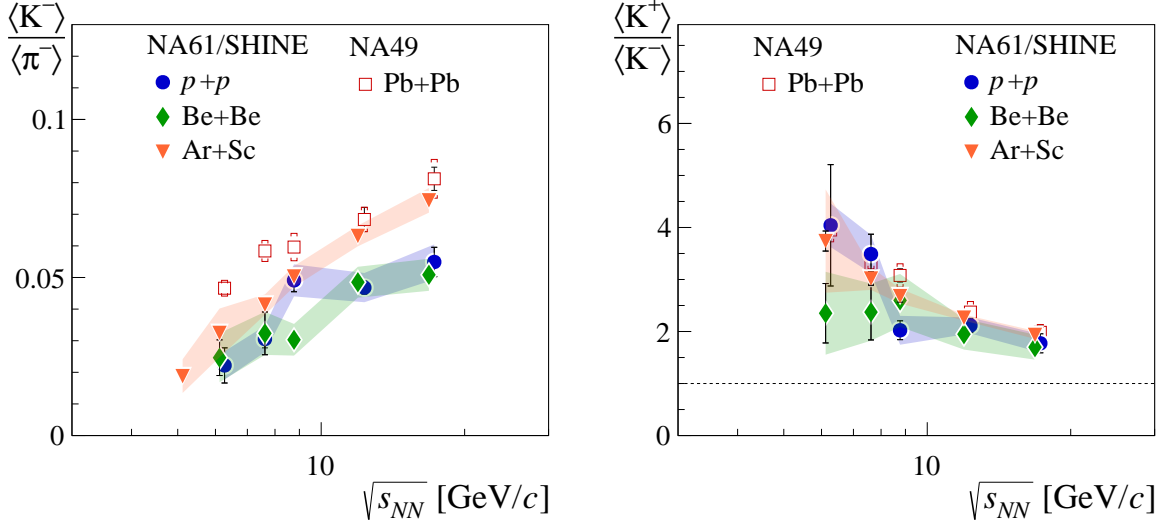


Figure 51: *Left:*  $K^-/\pi^-$  ratio. Characteristic energy dependence of  $K^+/\pi^+$  ratio observed in heavy ion collisions of Pb+Pb and Au+Au is not a feature of  $K^-/\pi^-$  data. The ratio increases smoothly with collision energy for all studied reactions. Nevertheless, a similar conclusions can be drawn as for  $K^+/\pi^+$  ratio, namely: at low SPS energies yields obtained for Ar+Sc collisions are in between  $p+p$  and Pb+Pb values. At higher collision energies Ar+Sc measurements closer resemble heavy ion results. *Right:*  $K^+/K^-$  ratio decreases with increasing collision energy.

While the energy dependence of  $K^+/\pi^+$  ratio is certainly the most interesting, it is educative to also examine  $K^-/\pi^-$  behaviour (Fig. 51). The energetically cheapest production of  $K^+$  and  $\Lambda$  pairs does not find an analogous mechanism with negatively charged kaons, due to high baryon densities at SPS collision energies (for details see Sec. 9). Consequently,  $K^+$  yields are dominantly sensitive to strangeness content, while  $K^-$  production is additionally heavily affected by baryon density. Nevertheless, a similar feature as observed for  $K^+/\pi^+$  ratio can be identified in  $K^-/\pi^-$  data. Namely, the yields obtained for Ar+Sc interactions closely resemble Pb+Pb data at high collision energies (75A, 150A GeV/c) and at low energies (<40A GeV/c) they are more similar to small systems. All plotted reactions show an approximately constant increase of  $K^-/\pi^-$  with collision energy. The analysis of  $\Lambda$  production is currently ongoing, so in a near future it will be possible to study more educative  $K^- + \Lambda$  yields, as a better approximation of  $s$  quark production.

The ratio of  $K^+/K^-$  (Fig. 51) decreases smoothly in Ar+Sc and Pb+Pb collisions, while  $p+p$  and Be+Be data behaves more chaotically, possibly due to large measurement uncertainties.

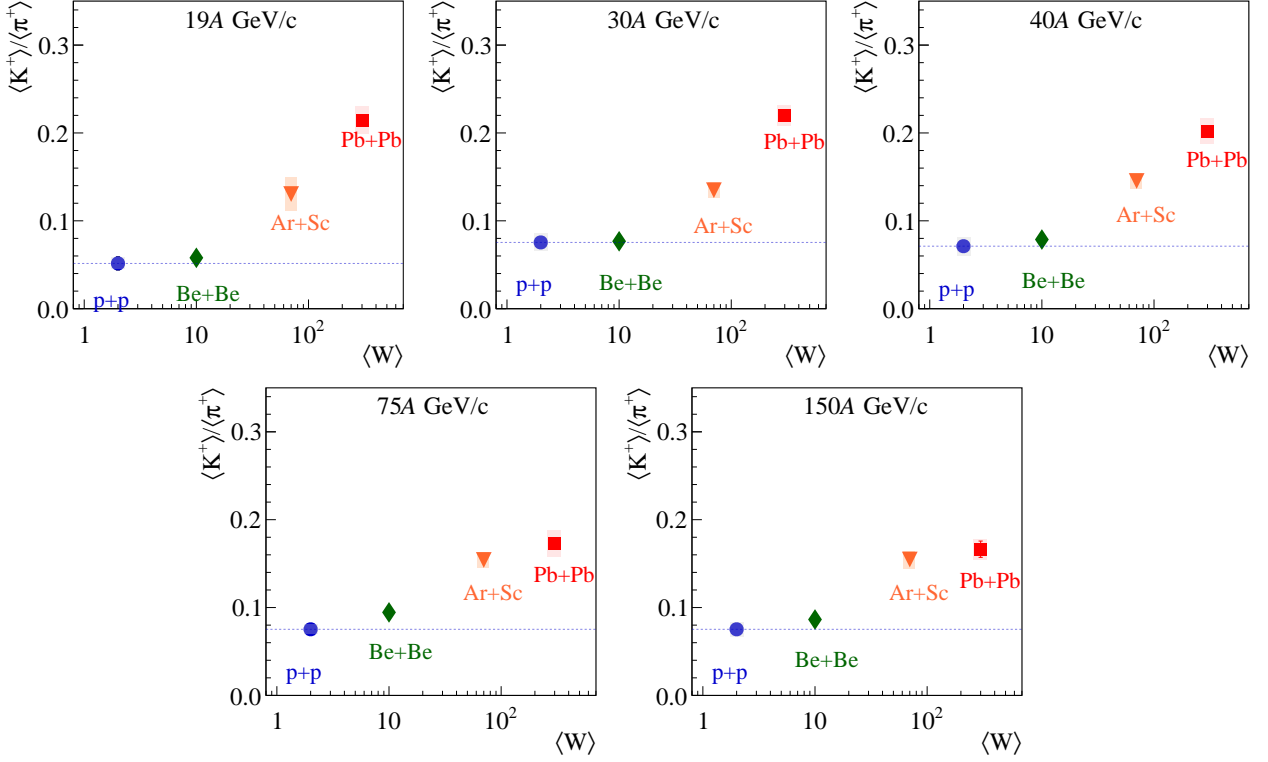


Figure 52: System size dependence of  $K^+/\pi^+$  mean multiplicity ratios measured at 19A-150A GeV/c, showing values for  $p+p$ , Be+Be, Ar+Sc (this study) and Pb+Pb. Here the system size is represented by the mean number of wounded nucleons ( $\langle W \rangle$ ).

## 21.2 Hypothesis of the onset of fireball

The observed rapid change of hadron production properties that starts when moving from Be+Be to Ar+Sc collisions hints some non-trivial threshold mechanism. It was hypothesized [44], that such system size dependence may be attributed to the beginning of the creation of large clusters of strongly interacting matter. The similarities of  $p+p$  and Be+Be systems suggests that interactions of these systems could form small non-equilibrium clusters via binary collisions of nucleons, exactly like in the Wounded Nucleon Model [15]. On the other hand properties of Pb+Pb collisions are well described by statistical and hydrodynamical models, which assume the creation of collectively evolving fireball. Results on Ar+Sc collisions are clearly closer to the Pb+Pb ones than to  $p+p$  and Be+Be measurements. Such a threshold behaviour seen in experimental data earned a particular nickname: *the onset of fireball*. It should be remarked, that this kind of system size dependence is seen not only in mean multiplicity



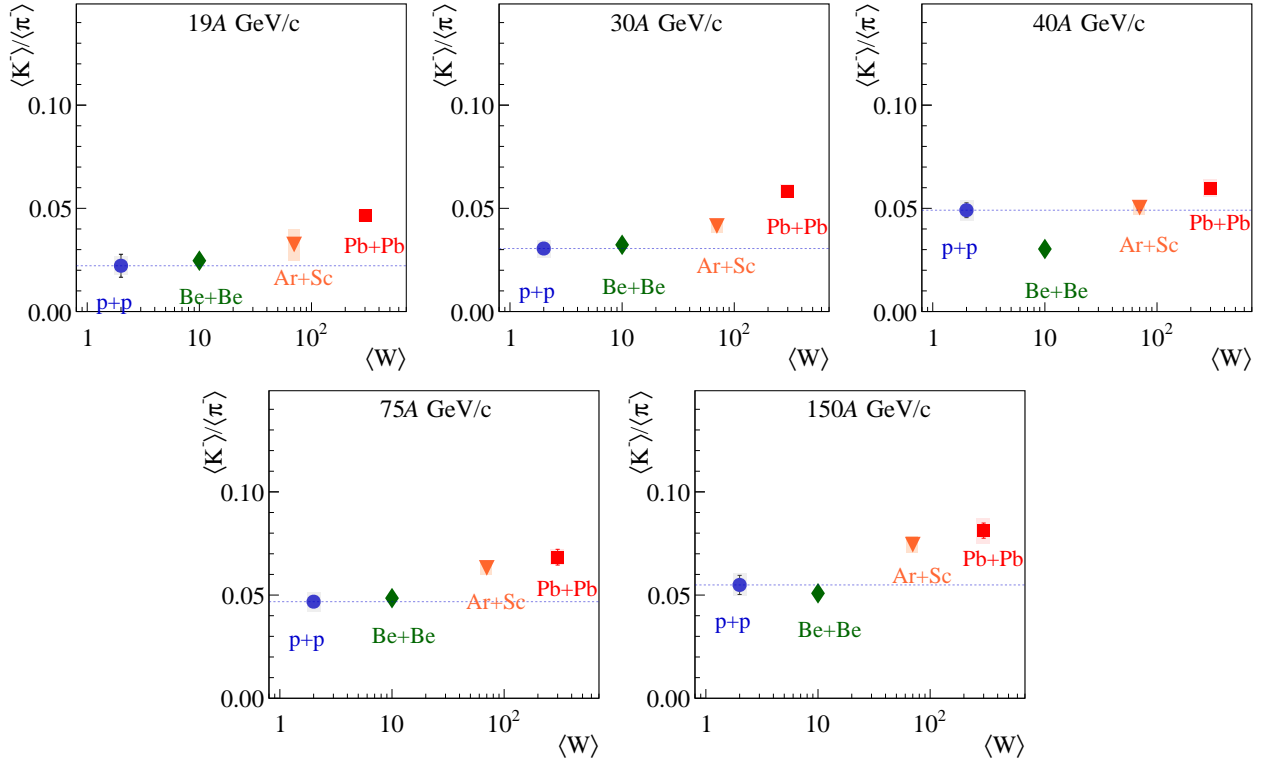


Figure 53: System size dependence of  $K^-/\pi^-$  mean multiplicity ratios measured at 19A-150A GeV/c, showing values for  $p+p$ , Be+Be, Ar+Sc (this study) and Pb+Pb. Here the system size is represented by the mean number of wounded nucleons ( $\langle W \rangle$ ).

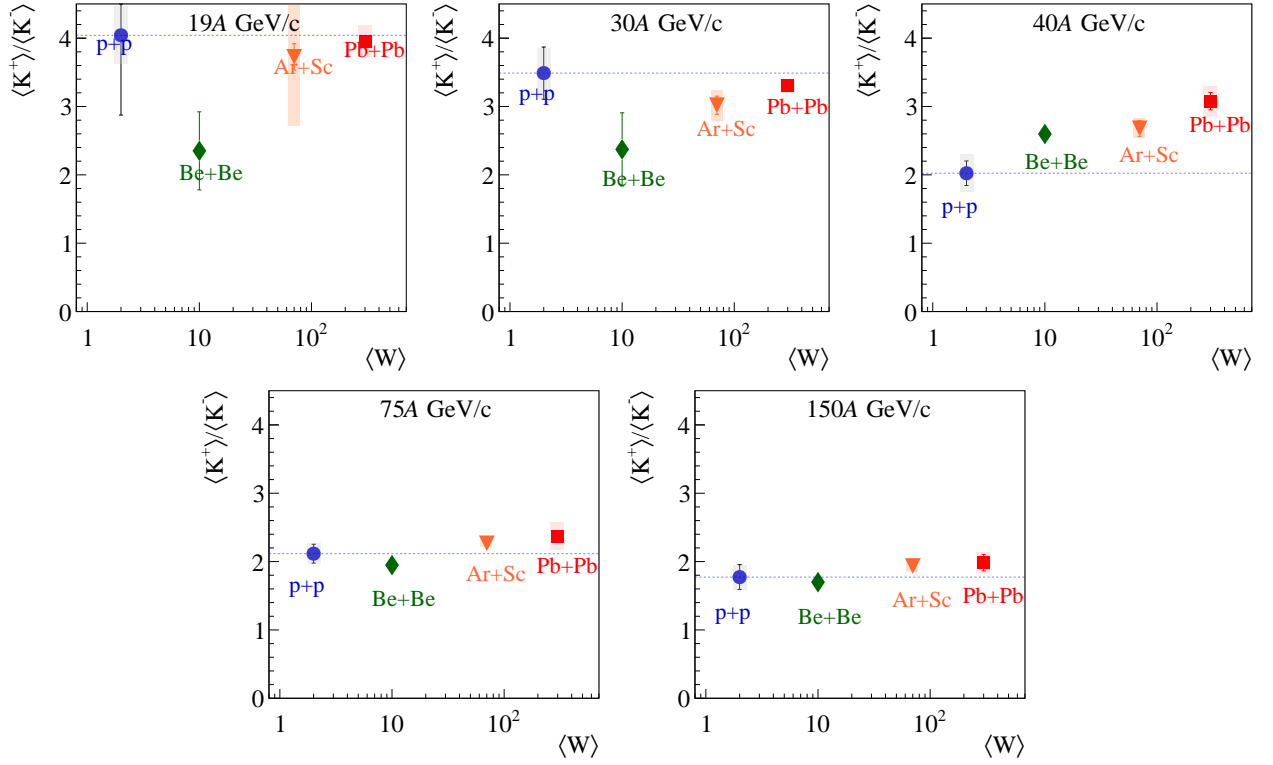


Figure 54: System size dependence of  $K^+/K^-$  mean multiplicity ratios measured at 19A-150A GeV/c, showing values for p+p, Be+Be, Ar+Sc (this study) and Pb+Pb. Here the system size is represented by the mean number of wounded nucleons ( $\langle W \rangle$ ).

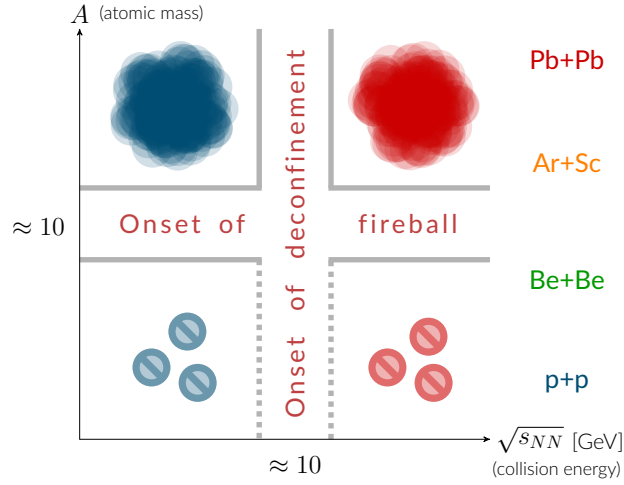


Figure 55: The diagram shows hypothesized four domains that can be assigned to collisions in the SPS energy range. On top of the onset of deconfinement, there is an onset of fireball – beginning of creation of large clusters of strongly interacting matter with increasing system size. It is still unclear how to describe collisions of small nuclei with increasing collision energy.

ratios presented here ( $\langle K^+ \rangle / \langle \pi^+ \rangle$ ,  $\langle K^- \rangle / \langle \pi^- \rangle$ ) but also in other measured quantities, e. g. mid-rapidity measurements:  $K^+ / \pi^+$ , inverse slope parameter  $T$  [2] and more [44]. The "two onsets": onset of deconfinement and onset of fireball effectively divide the two-dimensional scan of collision energy and system size into four distinctive domains, as shown schematically in Fig. 55. The onset of transition to deconfined matter is well established in the fireball region at high masses of the colliding nuclei, while its presence in the small cluster regime is still an open question, currently under investigation [13, 14]

### 21.3 Proton rapidity spectra

Measurements of proton rapidity spectra in central Ar+Sc collisions certainly fit the narration of previous paragraphs. Figures 56 and 57 display comparison of rapidity spectra obtained for  $p+p$ , Be+Be and Pb+Pb interactions at matching collision momenta. At 75A and 150A GeV/c all reactions show approximately similar shape of the longitudinal distribution. At 40A GeV/c an inflection of rapidity spectra is observed in Ar+Sc interactions, which is not the case for small systems. At all analysed collision energies the distribution shape of Ar+Sc data is similar to results on Pb+Pb (see also Fig. 63). The discussion of proton rapidity spectra in view of phenomenological models is continued in Sec. 21.4.3.

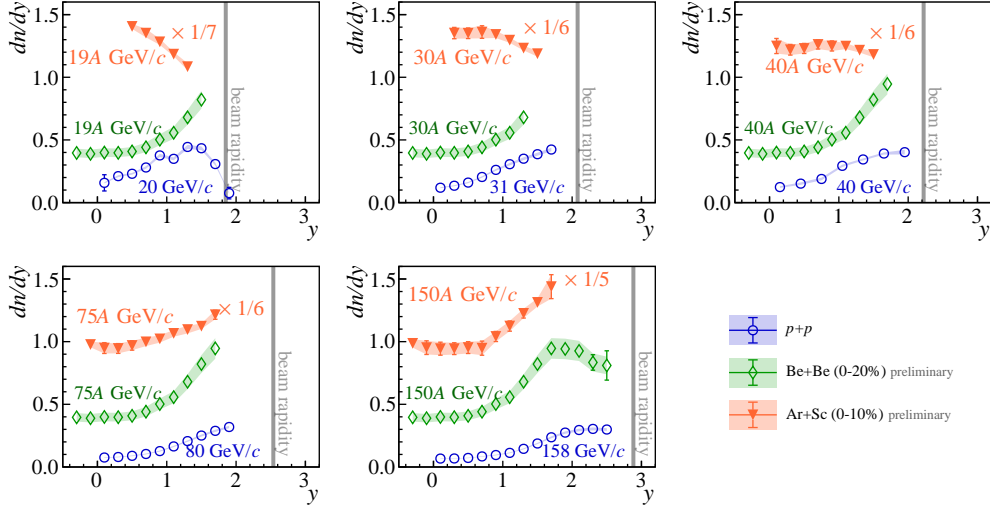


Figure 56: Proton rapidity spectra measured in central Ar+Sc interactions in comparison with other systems:  $p+p$ , Be+Be (central) at five corresponding collision energies.

## 21.4 Comparison with theoretical models

Some features of the results obtained in this thesis can be compared with relevant theoretical models of heavy-ion collisions in terms of particle production in dependence on collision energy and system size. The energy dependence is well established with data on  $p+p$  and Pb+Pb interactions and modern phenomenological models are usually successful in at least approximate description of experimental data. The influence of the system size on particle production properties is not well understood and as it can be seen in this section, the model predictions are largely inaccurate.

In the following paragraphs a comparison of relevant properties of charged hadron production in experimental data and theoretical models is presented. Firstly, the system size dependence in the thermal model is confronted with measurements of  $\langle K^+ \rangle / \langle \pi^+ \rangle$  ratio. Then, particle production properties in dynamical models (EPOS and PHSD) are compared with quantities measured in Ar+Sc collisions. Finally, the proton rapidity spectra are reviewed in terms of the equation of state.

### 21.4.1 Statistical models

The comparison of obtained results with statistical model in terms of system size dependence is presented in Fig. 58. The model calculations are thoroughly explained in Sec. 7.1 and the data chosen for this comparison are the  $\langle K^+ \rangle / \langle \pi^+ \rangle$  ratios already discussed in detail in Sec. 21.2. It should be recalled that the sys-

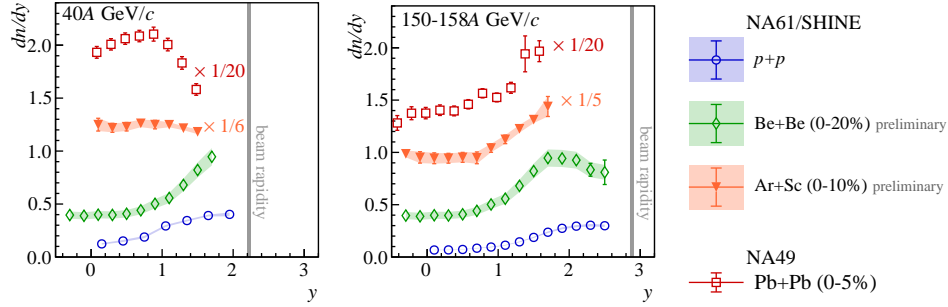


Figure 57: Proton rapidity spectra measured in Ar+Sc interactions in comparison with other systems:  $p+p$ , Be+Be and Pb+Pb at 40A and 150A-158A GeV/c.

tem size dependence in thermal models depends solely on the mechanism of a so called canonical suppression. With decreasing size of created fireball conservation laws must be implemented locally, resulting with a reduced phase-space for production of hadrons. The model was successful in describing the differences between  $p+p$  and Pb+Pb results, however as can be seen in Fig. 58 it does not fit the experimental data on intermediate size systems.

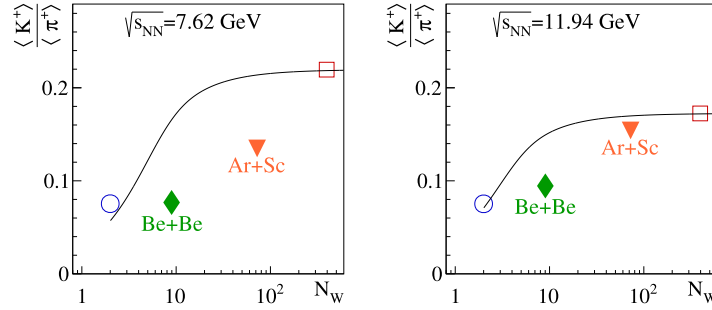


Figure 58: System size dependence of strangeness production in statistical models is based on a mechanism of canonical suppression and does not reproduce measured  $K^+/\pi^+$  ratios. Plotted data points come from NA49 and NA61/SHINE, while the line stands for predictions from Ref. [22] recalculated as demonstrated in Sec. 7.1.

#### 21.4.2 Dynamical models

Let us firstly focus on the results of EPOS simulation in terms of description of kaon and proton spectra. Figures 59 and 60 show comparisons of experimental results on  $K^+$  and  $K^-$  rapidity distributions with model calculations. The most prominent observation is a large difference in  $dn/dy$  yields, which

translates directly to mean multiplicities. The differences in  $K^+$  and  $K^-$  amplitudes are in the range from 35% to 45% depending on collision energy. The discrepancy in kaon yields is mostly due to a lack of strangeness enhancement in the EPOS Ar+Sc simulation. Also the widths of the distributions are significantly underestimated in the model (Fig. 60). Consequently Fig. 62 and 64 display comparison of  $p$  and  $\bar{p}$  rapidity distributions. As already pointed out in previous sections, the proton spectra are qualitatively well described by EPOS, however at most collision energies the  $dn/dy$  yields are underestimated by the model. On the other hand, in the case of antiproton rapidity spectra, the yields are slightly overestimated, but overall the agreement between the simulation and data is rather well.

The second of considered dynamical models, PHSD, delivers predictions concerning system size dependence of  $K^+/\pi^+$  ratio. As can be seen in Fig. 61, the model is successful in the qualitative description of "the horn" (the peak near  $\sqrt{s_{NN}}=8$  GeV) in Au+Au and Pb+Pb, once it implements the chiral symmetry restoration on top of the onset of deconfinement. However, its predictions concerning  $K^+/\pi^+$  yields at other systems are in disagreement with Be+Be and Ar+Sc measurements by the NA61/SHINE. The hierarchy of system sizes below  $\sqrt{s_{NN}}=8$  GeV matches the dependence observed in data, although above this energy, the hierarchy is reverted in the model and no longer agrees with the experiment. The energy dependence of  $K^+/\pi^+$  ratios in  $^{40}\text{Ca}+^{40}\text{Ca}$  collisions (a very similar system to  $^{40}\text{Ar}+^{45}\text{Sc}$ ) does not correspond to the energy dependence observed in measurements of Ar+Sc interactions.

### 21.4.3 Proton and antiproton spectra

Authors of Ref. [41] argue that properties of proton distributions are sensitive to the equation of state, in particular in a scenario of first-order phase transition a characteristic "peak-dip-peak-dip" behaviour is expected in dependence on collision energy. With the data presented here, we see hints, that the second part of mentioned energy dependence can be identified, namely "peak-dip". However, supplementary measurements from  $tof-dE/dx$  are needed at low collision energies to extend the acceptance towards lower rapidity and to confirm this observation. It should be noted, that the inflection point (transition from "the peak" to "the dip") appears at higher beam momentum than for Pb+Pb, however, even though shifted, qualitatively the collision energy dependence is similar in Ar+Sc and Pb+Pb. On the other hand at all measured collision energies, proton  $y$ -spectra for  $p+p$  and Be+Be collisions feature the same shape, which we would call "a dip" in adapted nomenclature. All of the described features of Ar+Sc proton spectra can be reviewed in detail in Fig. 62. Additionally, plots from Ref. [41] are included in Fig. 63 to compare the spectra recorded in Ar+Sc interactions to ones in Pb+Pb and theoretical predictions.

Moreover, the rapidity spectra of protons and antiprotons in Fig. 62 and 64 are overlaid with results from EPOS MC simulation [16]. As already remarked in Sec. 20.2 the EPOS model describes the approximate shape of the proton distribution, although the absolute values of are not well reproduced. Simi-

larly, the EPOS generated spectra of antiprotons are qualitatively similar to measured ones, however, the absolute yields of antiprotons are overestimated in the model.

#### 21.4.4 Summary on model predictions

Neither statistical nor dynamical models can reproduce the kaon production and  $K^+/\pi^+$  ratio measured in Ar+Sc collisions at SPS energies. Moreover, the predictions concerning system size dependence are significantly different than it is observed in the experimental results. It is apparent, that the influence of the system size on particle production, and strangeness production in particular, is not well understood and requires more theoretical and phenomenological studies.

Proton and antiproton spectra are on the other hand in reasonably good agreement with the EPOS model.

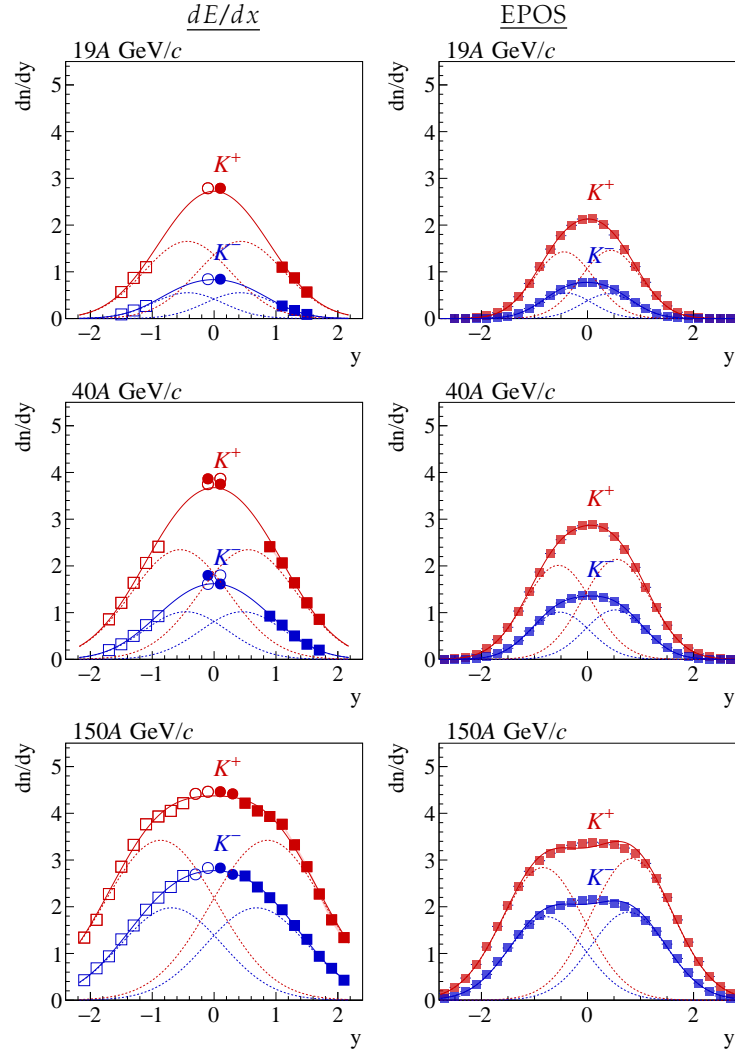


Figure 59: Comparison of  $K^+$  and  $K^-$  rapidity spectra in Ar+Sc interactions measured in this analysis (left) with EPOS simulation (right). Note the differences in amplitudes and widths of compared distributions. Availability of full acceptance data in the simulations allows to calculate the asymmetry of the spectra, which is the largest at top SPS energy and amounts to  $\approx 5\%$ .



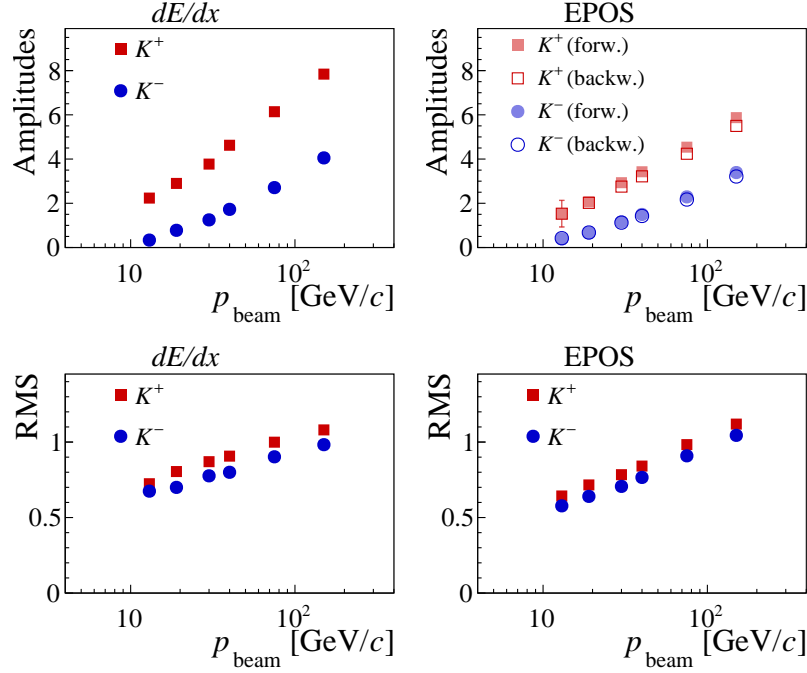


Figure 60: Details of the fits to rapidity distributions presented in Fig. 59. The differences in fitted amplitudes are in range of 35-45% and similar differences are observed in width of the distributions, here represented by the RMS.

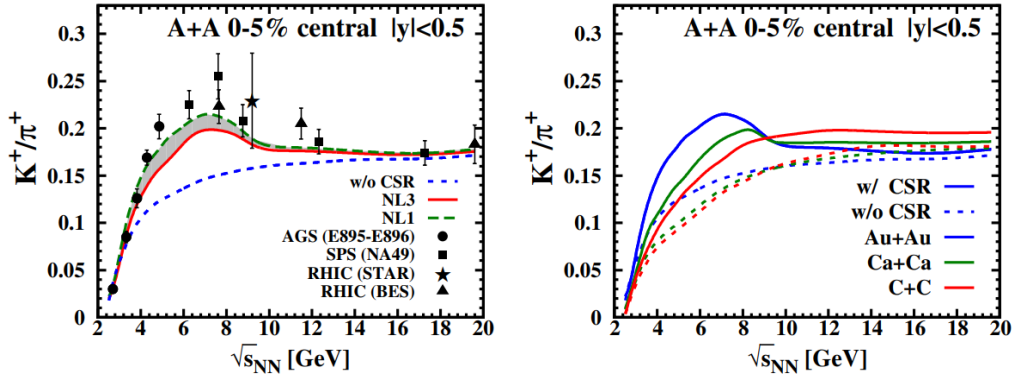


Figure 61:  $K^+/\pi^+$  ratios in PHSD model [43] do not reproduce the system size dependence of experimental data. At collision energies below  $\sqrt{s_{NN}} \approx 9$  GeV/c (corresponding to  $p_{beam} \approx 40A$  GeV/c) the hierarchy of systems w. r. t. their size is similar as seen in data, but above that collision energy there is no more any agreement. Also the dependence on  $\sqrt{s_{NN}}$  is different than seen in experimental results.

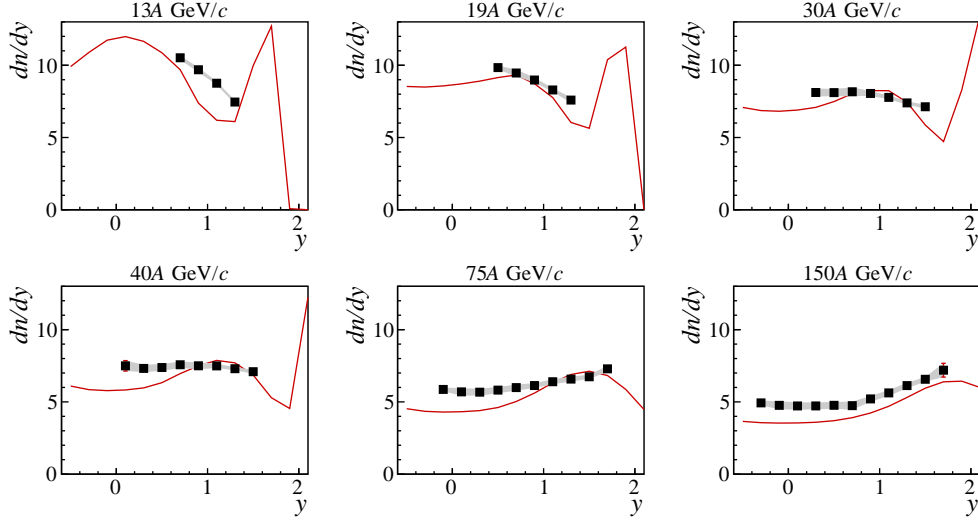


Figure 62: Rapidity spectra of protons produced in Ar+Sc interactions at six beam momenta from 13A to 150A GeV/c. Experimental measurements are plotted with black points, with shaded bands standing for systematic uncertainty. The red line illustrates EPOS model predictions [16].

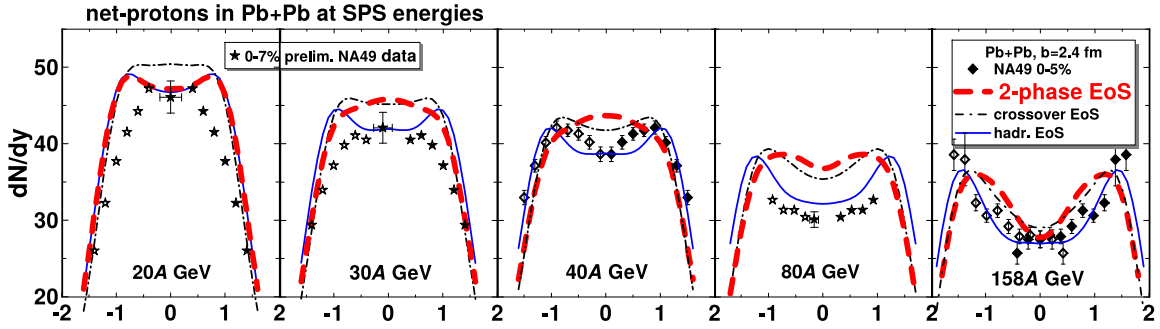


Figure 63: Rapidity spectra of net-protons for SPS energies from central collisions of Pb+Pb (SPS). Image taken from Ref. [41].

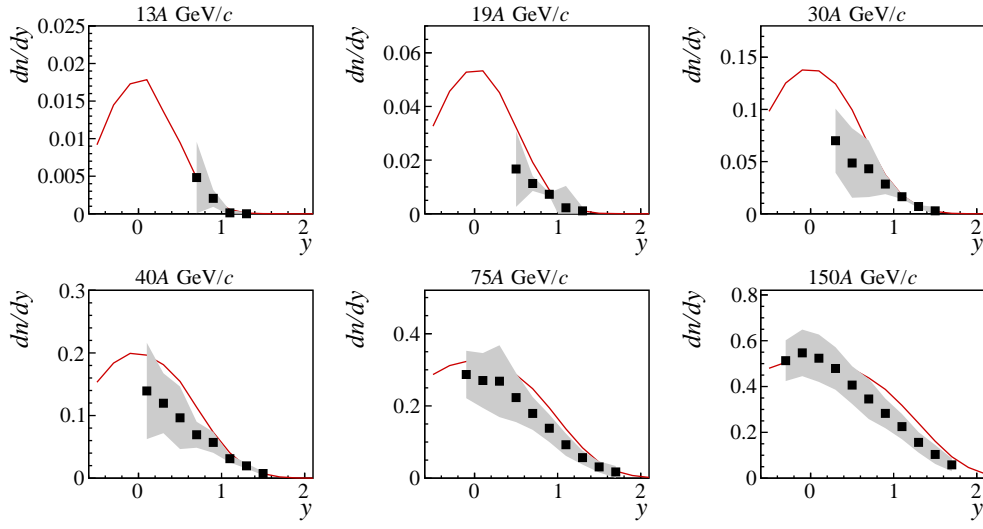


Figure 64: Rapidity spectra of antiprotons produced in Ar+Sc interactions at six beam momenta from 13A to 150A GeV/c. Experimental measurements are plotted with black points, with shaded bands standing for systematic uncertainty. The red line illustrates EPOS model predictions [16].

## 22 Summary and Outlook

This thesis presents experimental results on inclusive spectra of the most abundant charged hadrons,  $\pi^+$ ,  $\pi^-$ ,  $K^+$ ,  $K^-$ ,  $p$  and  $\bar{p}$ , produced in central  $^{40}\text{Ar}+^{45}\text{Sc}$  collisions at six beam momenta: 13A, 19A, 30A, 40A, 75A, 150A GeV/c. The measurements were performed with the NA61/SHINE Collaboration using a large acceptance hadron spectrometer operating at CERN SPS. In a unique experimental program, involving two-dimensional scan of beam energy and systems size, for the first time collisions of As+Sc were studied in the SPS energy range.

Significant progress was made with the analysis procedures based on particle identification through measurement of characteristic mean energy loss. The statistical methods were improved to better describe the data, increasing their stability, and ensuring a high quality of charged hadron identification at forward rapidity and equally reliable calculation of kinematic distributions. Similarly, the estimation of statistical and systematic uncertainties was performed with great care for details.

Two-dimensional particle spectra in rapidity  $y$  and transverse momentum  $p_T$  were obtained for charged hadrons with total momentum  $p > 5$  GeV/c. Kinematic distributions of charged pions were studied in terms of  $\pi^+/\pi^-$  ratios and a good agreement with "h-minus" analysis results on  $\pi^-$  yields was found. Transverse momentum spectra of charged kaons, protons, and antiprotons were extrapolated in order to account for missing acceptance. Characteristics of charged kaon transverse momentum distributions were studied, in particular, the dependence of transverse slope parameter  $T$  on rapidity and collision energy was presented. By integration of  $dn/dy p_T$  distribution in  $p_T$ , the rapidity spectra have been calculated and characteristics of the  $dn/dy$  distributions were examined as well, specifically the width of charged kaon rapidity spectra was extracted and its collision energy dependence was presented. Moreover, the rapidity distribution of charged kaons, protons, and antiprotons were also calculated in different bins of centrality: 0-5%, 5-10%, and 10-15%. All analysed particle species at all studied collision energies show increased  $dn/dy$  yields in more central collisions.

The measurements of charged kaon rapidity spectra were extended with preliminary results of the supplementary analysis based on the combination of the time-of-flight and energy-loss measurements at mid-rapidity ( $tof-dE/dx$ ). The mean multiplicities of charged kaons were calculated and their properties were studied in terms of dependence on collision energy and system size. In particular the ratios of  $\langle K^+ \rangle / \langle \pi^+ \rangle$ ,  $\langle K^- \rangle / \langle \pi^- \rangle$  and  $\langle K^+ \rangle / \langle K^- \rangle$  were examined.

- The energy dependence of  $\langle K^+ \rangle / \langle \pi^+ \rangle$  ratio is unlike the non-monotonic behaviour observed in Pb+Pb (and Au+Au) interactions, the ratio monotonically increases with increasing collision energy. It is also important to highlight that the  $\langle K^+ \rangle / \langle \pi^+ \rangle$  values measured in Ar+Sc collisions are significantly different than at small systems,  $p+p$  and Be+Be. At low collision momenta ( $\leq 40A$  GeV/c) the ratio in Ar+Sc reaction is in the middle

between  $p+p$  and Pb+Pb measurements and at high beam momenta (75A, 150A GeV/c) it closely resembles values of heavy ion collisions (Pb+Pb).

- Similarly, the  $\langle K^- \rangle / \langle \pi^- \rangle$  yields obtained for Ar+Sc interactions closely resemble Pb+Pb data at high collision energies (75A, 150A GeV/c) and at low energies (<40A GeV/c) they are more similar to small systems. All compared reactions,  $p+p$ , Be+Be and Ar+Sc, show an approximately constant increase of  $\langle K^- \rangle / \langle \pi^- \rangle$  with collision energy.
- The ratio of  $\langle K^+ \rangle / \langle K^- \rangle$  measured in Ar+Sc interactions decreases smoothly. Similar energy dependence is observed in Pb+Pb collisions, while  $p+p$  and Be+Be data display a non-monotonic behaviour.

A rapid change of hadron production properties, in  $\langle K^+ \rangle / \langle \pi^+ \rangle$  and  $\langle K^- \rangle / \langle \pi^- \rangle$  ratios in particular, that starts when moving from Be+Be to Ar+Sc collisions was observed. It is hypothesized, that such a distinct threshold behaviour, called here *the onset of fireball*, may be attributed to the beginning of the creation of large clusters of strongly interacting matter. The similarities of  $p+p$  and Be+Be reactions suggest that interactions of these systems could form small non-equilibrium clusters via binary collisions of nucleons, while the properties of Pb+Pb interactions are better described in terms of collectively evolving fireball. Results on Ar+Sc collisions are clearly more similar to Pb+Pb, than to  $p+p$  and Be+Be reactions.

The measurements of proton rapidity spectra show similar trends as discussed in view of charged kaon multiplicities. In particular the shape of the  $dn/dy$  spectra closer resemble Pb+Pb measurements, than small systems of  $p+p$  and Be+Be.

Summarizing, the key experimental results of this dissertation collated with earlier measurements of  $p+p$ , Be+Be (from NA61/SHINE) and Pb+Pb (from NA49) collisions establish a system size dependence, which none of considered theoretical models can reproduce. In particular, the  $\langle K^+ \rangle / \langle \pi^+ \rangle$  ratio is poorly described with either statistical or dynamical models. Clearly, a better understanding of the influence of system size on hadron production properties is needed and results obtained in this thesis may motivate future development of theoretical and phenomenological models.

## Outlook

The study of Ar+Sc collisions continues and multiple analyses of hadron production are currently ongoing. In particular, in a near future, new results on charged hadrons in complementary acceptance regions are expected, as well as measurements of other particle species ( $\phi$ ,  $\Lambda$ , etc.). Combined results of these analyses will allow for a precise estimation of the production of multiple particle species, allowing for a better understanding of the details of hadron production in Ar+Sc. Specifically, measurements that will be available in a near future will enable calculation of  $\mu_B$  and  $T$  parameters of the thermal model. In addition, measurements of multi-strange baryons will complete the picture

of strangeness production in intermediate systems. Additionally, the planned measurements of transverse spectra anisotropies will provide necessary information to interpret the Ar+Sc results in terms of hydrodynamical evolution.

Ongoing analyses of other reactions, Xe+La and Pb+Pb, recorded by the NA61/SHINE will allow for an overall comparison of the results obtained from all the studied systems, thus establishing the final picture of the system size dependence of collision properties at SPS energies.

The currently ongoing experimental upgrade of the NA61/SHINE facility will allow to study charm production, which is a natural extension of the previous investigations of the deconfinement transition. The future programme of the experiment is focused on studying the impact of the onset of deconfinement on the open charm production.

The studies of the properties of strongly interacting matter are continued world-wide in experiments at CERN, GSI and BNL. It should be highlighted, that construction of new facilities is quickly progressing. In particular, the experiments studying heavy ion collisions at high baryon densities are expected to soon deliver new data: NICA (JINR), RHIC-fixed target (BNL) and SIS100 (GSI). Without a doubt, the collective effort of such a wide array of experiments will extend our understanding of the properties of the strongly interacting matter, the onset of deconfinement, the equation of state, the critical point and many more.

## References

- [1] M. Naskręć et al., “News on mean pion multiplicity from NA61/SHINE,” *EPJ Web Conf.*, vol. 171, p. 16006, 2018.
- [2] P. Podlaski, “Strangeness production at the CERN SPS energies.” <https://indico.cern.ch/event/755366/contributions/3357938/>.
- [3] A. Bazavov et al., “Chiral crossover in QCD at zero and non-zero chemical potentials,” *Phys. Lett. B*, vol. 795, pp. 15–21, 2019.
- [4] K. Rajagopal and F. Wilczek, *The Condensed matter physics of QCD (and citations within)*, pp. 2061–2151. 11 2000.
- [5] M. Stephanov, “QCD phase diagram: An Overview,” *PoS*, vol. LAT2006, p. 024, 2006.
- [6] P. Huovinen and P. Ruuskanen, “Hydrodynamic Models for Heavy Ion Collisions,” *Ann. Rev. Nucl. Part. Sci.*, vol. 56, pp. 163–206, 2006.
- [7] M. Gazdzicki and M. I. Gorenstein, “On the early stage of nucleus-nucleus collisions,” *Acta Phys. Polon.*, vol. B30, p. 2705, 1999.
- [8] A. Andronic, P. Braun-Munzinger, and J. Stachel, “The Horn, the hadron mass spectrum and the QCD phase diagram: The Statistical model of hadron production in central nucleus-nucleus collisions,” *Nucl. Phys. A*, vol. 834, pp. 237C–240C, 2010.
- [9] F. Becattini, W. Busza, P. Foka, M. Gazdzicki, B. Hippolyte, C. Pajares, O. Philipsen, and R. Snellings, “Debate on the current understanding of high-energy heavy-ion collisions,” *AIP Conf. Proc.*, vol. 1343, pp. 25–29, 2011.
- [10] U. W. Heinz and G. Kestin, “Jozso’s Legacy: Chemical and Kinetic Freeze-out in Heavy-Ion Collisions,” *Eur. Phys. J. ST*, vol. 155, pp. 75–87, 2008.
- [11] H. Satz, ed., *STATISTICAL MECHANICS OF QUARKS AND HADRONS. PROCEEDINGS, INTERNATIONAL SYMPOSIUM, BIELEFELD, F.R. GERMANY, AUGUST 24-31, 1980*, 1 1981.
- [12] R. Bock and R. Stock, eds., *Proceedings: Workshop on Future Relativistic Heavy Ion Experiments, Darmstadt, Germany, Oct 7-10, 1980*, 1981.
- [13] V. Khachatryan et al., “Evidence for collectivity in pp collisions at the LHC,” *Phys. Lett. B*, vol. 765, pp. 193–220, 2017.
- [14] A. Aduszkiewicz et al., “Proton-Proton Interactions and Onset of Deconfinement,” 12 2019.
- [15] A. Bialas, M. Bleszynski, and W. Czyz, “Multiplicity Distributions in Nucleus-Nucleus Collisions at High-Energies,” *Nucl. Phys. B*, vol. 111, pp. 461–476, 1976.

- [16] T. Pierog and K. Werner, “EPOS Model and Ultra High Energy Cosmic Rays,” *Nucl. Phys. B Proc. Suppl.*, vol. 196, pp. 102–105, 2009.
- [17] H. Petersen, J. Steinheimer, G. Burau, M. Bleicher, and H. Stocker, “A Fully Integrated Transport Approach to Heavy Ion Reactions with an Intermediate Hydrodynamic Stage,” *Phys. Rev. C*, vol. 78, p. 044901, 2008.
- [18] W. Cassing, A. Palmese, P. Moreau, and E. L. Bratkovskaya, “Chiral symmetry restoration versus deconfinement in heavy-ion collisions at high baryon density,” *Phys. Rev.*, vol. C93, p. 014902, 2016.
- [19] A. Andronic, “An overview of the experimental study of quark-gluon matter in high-energy nucleus-nucleus collisions,” *Int. J. Mod. Phys. A*, vol. 29, p. 1430047, 2014.
- [20] A. Andronic, P. Braun-Munzinger, and J. Stachel, “Hadron production in central nucleus-nucleus collisions at chemical freeze-out,” *Nucl. Phys. A*, vol. 772, pp. 167–199, 2006.
- [21] A. Andronic, P. Braun-Munzinger, and J. Stachel, “Thermal hadron production in relativistic nuclear collisions: The Hadron mass spectrum, the horn, and the QCD phase transition,” *Phys. Lett. B*, vol. 673, pp. 142–145, 2009. [Erratum: *Phys.Lett.B* 678, 516 (2009)].
- [22] A. Tounsi and K. Redlich, “Canonical constraints on particle production,” *Journal of Physics G: Nuclear and Particle Physics*, vol. 28, pp. 2095–2102, jun 2002.
- [23] P. M. Lo, M. Marczenko, K. Redlich, and C. Sasaki, “Matching the Hagedorn mass spectrum with Lattice QCD results,” *Phys. Rev. C*, vol. 92, no. 5, p. 055206, 2015.
- [24] R. Poberezhnyuk, M. Gazdzicki, and M. Gorenstein, “Statistical Model of the Early Stage of nucleus-nucleus collisions with exact strangeness conservation,” *Acta Phys. Polon. B*, vol. 46, no. 10, p. 1991, 2015.
- [25] M. Gazdzicki, M. Gorenstein, and P. Seyboth, “Onset of deconfinement in nucleus-nucleus collisions: Review for pedestrians and experts,” *Acta Phys. Polon.*, vol. B42, pp. 307–351, 2011.
- [26] N. Abgrall *et al.*, “NA61/SHINE facility at the CERN SPS: beams and detector system,” *JINST*, vol. 9, p. P06005, 2014.
- [27] S. Afanasiev *et al.*, “The NA49 large acceptance hadron detector,” *Nucl. Instrum. Meth. A*, vol. 430, pp. 210–244, 1999.
- [28] D. Banas, A. Kubala-Kukus, M. Rybczynski, I. Stabrawa, and G. Stefanek, “Influence of target material impurities on physical results in relativistic heavy-ion collisions,” *Eur. Phys. J. Plus*, vol. 134, no. 1, p. 44, 2019.



- [29] M. Tanabashi *et al.*, “Review of Particle Physics,” *Phys. Rev. D*, vol. 98, no. 3, p. 030001, 2018 (2019 update).
- [30] A. J. Marcinek,  *$\phi$  meson production in proton-proton collisions in the NA61/SHINE experiment at CERN SPS*. PhD thesis, Jagiellonian U., 7 2016.
- [31] R. Brun, F. Bruyant, M. Maire, A. C. McPherson, and P. Zancarini, *GEANT 3: user’s guide Geant 3.10, Geant 3.11; rev. version*. Geneva: CERN, 1987.
- [32] A. Aduszkiewicz, *Energy dependence of negatively charged pion production in proton-proton interactions at the CERN SPS*. PhD thesis, Warsaw U., 2016.
- [33] C. Alt *et al.*, “Pion and kaon production in central Pb + Pb collisions at 20-A and 30-A-GeV: Evidence for the onset of deconfinement,” *Phys. Rev.*, vol. C77, p. 024903, 2008.
- [34] M. van Leeuwen, *Kaon and Open Charm Production in Central Lead-Lead Collisions at the CERN SPS*. PhD thesis, Utrecht U., 2003.
- [35] M. Lewicki, “Study of fitting models in  $dE/dx$  analysis of Ar+Sc data.” <https://indico.cern.ch/event/755366/contributions/3357938/>.
- [36] M. Lewicki, “Multi-bin fit in  $dE/dx$  analysis of Ar+Sc data.” <https://indico.cern.ch/event/881007/contributions/3711306/>.
- [37] M. Gazdzicki, K. Grebieszko, M. Mackowiak, and S. Mrowczynski, “Identity method to study chemical fluctuations in relativistic heavy-ion collisions,” *Phys. Rev. C*, vol. 83, p. 054907, 2011.
- [38] N. Collaboration, “Compilation of NA49 Numerical Results and references therein.” <https://edms.cern.ch/document/1075059/4>.
- [39] M. Lewicki, “Uncertainties in  $dE/dx$  analysis of Ar+Sc data.” <https://indico.cern.ch/event/930158/contributions/3909945/>.
- [40] E. Schnedermann, J. Sollfrank, and U. W. Heinz, “Thermal phenomenology of hadrons from 200-A/GeV S+S collisions,” *Phys. Rev. C*, vol. 48, pp. 2462–2475, 1993.
- [41] Y. Ivanov and D. Blaschke, “Baryon stopping in heavy-ion collisions at  $E_{lab} = 2A$ -200A GeV,” *Eur. Phys. J. A*, vol. 52, no. 8, p. 237, 2016.
- [42] A. Motornenko, V. Begun, V. Vovchenko, M. Gorenstein, and H. Stoecker, “Hadron yields and fluctuations at energies available at the CERN Super Proton Synchrotron: System-size dependence from Pb + Pb to  $p+p$  collisions,” *Phys. Rev. C*, vol. 99, no. 3, p. 034909, 2019.
- [43] E. Bratkovskaya, W. Cassing, A. Palmese, and P. Moreau, “Chiral Symmetry Restoration in Heavy-ion Collisions at High Baryon Density,” *Acta Phys. Polon. Supp.*, vol. 10, p. 507, 2017.

- [44] M. Gazdzicki and A. Rybicki, “Overview of Results from NA61/SHINE: Uncovering Critical Structures,” *Acta Phys. Polon. B*, vol. 50, pp. 1057–1070, 2019.
- [45] G. Cowan, *Statistical data analysis*. 1998.

---

## Part V

# Appendix

## A Kinematics

### A.1 Units and definitions

A natural choice of units in high energy physics is defined with:

$$\hbar = c = 1 \quad (47)$$

where  $\hbar = 1.055 \times 10^{-34} \text{ J}\cdot\text{s}$  and  $c = 2.998 \times 10^8 \text{ m}\cdot\text{s}^{-1}$ .

Then the relativistic formula for energy becomes:

$$E^2 = m^2 + p^2 \quad (48)$$

where  $m$  is the mass and  $p$  is the magnitude of the momentum vector  $\vec{p} = (p_x, p_y, p_z)$ . Also in whole thesis a following convention of coordinates is adopted:  $z$  is the direction of the beam,  $z$ - $x$  axes define the horizontal and  $y$ - $z$  vertical plane (whenever these are applicable). With these conventions in mind, following quantities are defined:

- Rapidity:

$$y = \frac{1}{2} \ln \left( \frac{E + p_z}{E - p_z} \right) \quad (49)$$

- Transverse momentum, transverse mass:

$$p_T = \sqrt{p_x^2 + p_y^2}, \quad m_T = \sqrt{m^2 + p_T^2} \quad (50)$$

### A.2 Useful quantities

In the centre of mass reference frame two colliding particles are characterized with their masses and momenta, which also define their energy:

$$m_1, \vec{p}_1, E_1 \quad m_2, -\vec{p}_1, E_2$$

Then the total energy in the centre of mass system is expressed with:

$$\sqrt{s} = E_{cm} = E_1 + E_2$$

However in fixed target experiment it is sometimes more convenient to operate in the laboratory frame, then we have:

$$m_1, \vec{p}_1, E_1 \quad m_2, \vec{p}_2 = \vec{0}, E_2 = m_2$$

and the total centre of mass energy equals:

$$\sqrt{s} = E_{cm} = \sqrt{m_1^2 + m_2^2 + 2E_{proj}m_2}$$

It is also worth to mention how the Lorentz factor  $\gamma$  relates to  $E_{cm}$ :

$$\gamma = \frac{E_C M}{2A m_p} = \frac{\sqrt{s_{NN}}}{2m_p}$$

where  $\sqrt{s_{NN}}$  is a frequently used quantity of nucleon-nucleon centre of mass energy:

$$\sqrt{s} = A \cdot \sqrt{s_{NN}}$$

Usually it most relevant to discuss collision energy and beam momenta per nucleon, however it is worth remembering that the total produced entropy relates to the total collision energy. For example, Ar beam at  $p_{beam}=150A$  GeV/c has the total energy of 6 TeV.

Summary of collision kinematics relevant for SPS heavy-ion programme

$p_{beam}$	$\sqrt{s_{NN}}$ [GeV]	$y_{beam}$	$\beta_{CM}$	$\gamma_{CM}$
13A GeV/c	5.12	1.66	0.983	2.73
19A GeV/c	6.12	1.85	0.988	3.26
20A GeV/c	6.27	1.88	0.989	3.34
30A GeV/c	7.62	2.08	0.992	4.06
40A GeV/c	8.77	2.22	0.994	4.67
75A GeV/c	11.9	2.54	0.997	6.36
80A GeV/c	12.3	2.57	0.997	6.57
150A GeV/c	16.8	2.88	0.998	8.97
158A GeV/c	17.3	2.91	0.999	9.20

At higher collision energies we have similarly:

	$\sqrt{s_{NN}}$ [GeV]:	$y_{beam}$ :	$\beta_{CM}$ :	$\gamma_{CM}$
top RHIC	200	5.36	0.999989	107
lowest LHC	900	6.87	0.9999995	479
LHC ions	2760	7.99	0.99999994	1470
LHC ions	5020	8.59	0.99999998	2675

## B Minimization algorithms

This section contains a brief summary on the details of minimization algorithms used in this work, in particular procedures of  $dE/dx$  distributions fitting are described with use of maximum likelihood estimator for binned data. The implementation of employed algorithms is based on [45].

### B.1 Maximum likelihood for binned data

Let us consider a probability density function (*pdf*)  $f$ , that governs the distribution of random variable  $x$ , dependent on a vector of parameters  $\vec{\theta}$ :

$$f(x; \vec{\theta}), \quad \vec{\theta} = (\theta_1, \dots, \theta_m) \quad (51)$$

In this thesis  $x$  corresponds to  $dE/dx$  variable,  $f$  is the model in eq. 28 and  $\vec{\theta}$  are model parameters described in the same section. Similarly, let us define the vector of experimental measurements (data histogram):

$$\vec{n} = (n_1, \dots, n_N), \quad \sum_{i=0}^N n_i = n_{tot} \quad (52)$$

Consequently a vector of expectation values for the p. d. f. can be defined:

$$\vec{v} = (v_1, \dots, v_N), \quad v_i(\vec{\theta}) = n_{tot} \int_{x_i^{min}}^{x_i^{max}} f(x; \vec{\theta}) dx \quad (53)$$

The histogram  $\vec{n}$  is regarded as a  $N$ -dimensional random vector, thus the joint p. d. f. is given by a multinomial distribution:

$$f_{joint}(\vec{n}; \vec{v}) = \frac{n_{tot}!}{n_1! \dots n_N!} \left( \frac{v_1}{n_{tot}} \right)^{n_1} \dots \left( \frac{v_N}{n_{tot}} \right)^{n_N} \quad (54)$$

The probability of being in bin  $i$  is expressed as  $v_i/n_{tot}$ . Taking the logarithm of the joint p. d. f. gives the log-likelihood function (additive terms dropped):

$$\log L(\vec{\theta}) = \sum_{i=1}^N n_i \log v_i(\vec{\theta}) \quad (55)$$

A slightly modified version of this equation is obtained when number of entries in each bin is treated as independent Poisson random variable, so  $n_{tot}$  is variable as well:

$$\log L(v_{tot}, \vec{\theta}) = -v_{tot} + \sum_{i=1}^N n_i \log v_i(v_{tot}, \vec{\theta}) \quad (56)$$

### B.2 Extension for simultaneous fits

In order to estimate the set of parameters  $\vec{\theta}$  simultaneously for a number of model-data pairs small modification in the estimator are necessary. For  $M$  number of model-data pairs (bins fitted simultaneously):

$$\log L(v_{tot}, \vec{\theta}) \rightarrow \sum_{j=1}^M \log L(v_{j\ tot}, \vec{\theta}_j) \quad (57)$$

where  $j$  iterates over the pairs. Any component of the  $\vec{\theta}_j$  vector can be shared among multiple bins, thus allowing for simultaneous optimization.

### **B.3 Additional remarks**

The contribution to the log-likelihood function differs largely depending on the number of entries in the histogram. Thus contribution from bins with low number of entries might be to some extent neglected due to numerical reasons. This disadvantage is solved through a refinement of parameters with the second stage of fitting described in sec. 15.4.3.

### **B.4 Software and technical details**

From a technical side the fitting procedure was implemented with usage of *Minuit2* package embedded in the *TShine* framework – a software developed originally by Silvestro Di Luise designed especially for the purposes of multi-dimensional fitting of  $dE/dx$  and  $tof$  distributions. The author have contributed to the development of *TShine* with addition of new models and by implementing dedicated minimizers and calculators for multi-bin fitting with shared parameters.

Relevant references:

- ROOT: <https://root.cern.ch/>
- Minuit2: <https://root.cern.ch/doc/master/Minuit2Page.html>
- TShine: <https://gitlab.cern.ch/malewick/shinertools>



K(-);-0.40;0.60;0.70;0.80;0.0000;0.0000;0.0000;0.0000;  
K(-);-0.40;0.60;0.80;0.80;0.90;0.0000;0.0000;0.0000;  
K(-);-0.40;0.60;0.90;1.00;0.0000;0.0000;0.0000;0.0000;  
K(-);-0.40;0.60;1.00;1.00;0.0552;0.0077;0.0023;  
K(-);-0.40;0.60;1.10;1.20;0.0421;0.0077;0.0060;  
K(-);-0.40;0.60;1.20;1.30;0.0338;0.0066;0.0052;  
K(-);-0.40;0.60;1.30;1.40;0.0188;0.0005;0.0000;  
K(-);-0.40;0.60;1.40;1.50;0.0068;0.0003;0.0014;  
K(-);-0.40;0.60;1.50;1.60;0.0049;0.0003;0.0006;  
K(-);-0.40;0.60;1.60;1.70;0.0000;0.0000;0.0000;  
K(-);-0.40;0.60;1.70;1.80;0.0000;0.0000;0.0000;  
K(-);-0.40;0.60;1.80;1.90;0.0000;0.0000;0.0000;  
K(-);-0.40;0.60;1.90;2.00;0.0000;0.0000;0.0000;  
K(-);-0.60;0.80;0.00;0.05;0.0000;0.0000;0.0000;  
K(-);-0.60;0.80;0.05;0.10;0.0000;0.0000;0.0000;  
K(-);-0.60;0.80;0.10;0.15;0.0000;0.0000;0.0000;  
K(-);-0.60;0.80;0.15;0.20;0.0000;0.0000;0.0000;  
K(-);-0.60;0.80;0.20;0.25;0.0000;0.0000;0.0000;  
K(-);-0.60;0.80;0.25;0.30;0.0000;0.0000;0.0000;  
K(-);-0.60;0.80;0.30;0.35;0.0000;0.0000;0.0000;  
K(-);-0.60;0.80;0.35;0.40;0.0000;0.0000;0.0000;  
K(-);-0.60;0.80;0.40;0.45;0.0000;0.0000;0.0000;  
K(-);-0.60;0.80;0.45;0.50;0.0000;0.0000;0.0000;  
K(-);-0.60;0.80;0.50;0.55;0.0000;0.0000;0.0000;  
K(-);-0.60;0.80;0.55;0.60;0.0000;0.0000;0.0000;  
K(-);-0.60;0.80;0.60;0.70;0.0000;0.0000;0.0000;  
K(-);-0.60;0.80;0.70;0.80;0.0000;0.0000;0.0000;  
K(-);-0.60;0.80;0.80;0.90;0.0986;0.0008;0.0193;  
K(-);-0.60;0.80;0.90;1.00;0.0777;0.0088;0.0181;  
K(-);-0.60;0.80;1.00;1.10;0.0422;0.0077;0.0047;  
K(-);-0.60;0.80;1.10;1.20;0.0000;0.0000;0.0000;  
K(-);-0.60;0.80;1.20;1.30;0.0182;0.0005;0.0028;  
K(-);-0.60;0.80;1.30;1.40;0.0000;0.0000;0.0000;  
K(-);-0.60;0.80;1.40;1.50;0.0087;0.0003;0.0009;  
K(-);-0.60;0.80;1.50;1.60;0.0002;0.0002;0.0004;  
K(-);-0.60;0.80;1.60;1.70;0.0000;0.0000;0.0000;  
K(-);-0.60;0.80;1.70;1.80;0.0000;0.0000;0.0000;  
K(-);-0.60;0.80;1.80;1.90;0.0000;0.0000;0.0000;  
K(-);-0.60;0.80;1.90;2.00;0.0000;0.0000;0.0000;  
K(-);-0.80;1.00;0.00;0.05;0.0000;0.0000;0.0000;  
K(-);-0.80;1.00;0.05;0.10;0.0000;0.0000;0.0000;  
K(-);-0.80;1.00;0.10;0.15;0.0000;0.0000;0.0000;  
K(-);-0.80;1.00;0.15;0.20;0.0000;0.0000;0.0000;  
K(-);-0.80;1.00;0.20;0.25;0.0000;0.0000;0.0000;  
K(-);-0.80;1.00;0.25;0.30;0.0000;0.0000;0.0000;  
K(-);-0.80;1.00;0.30;0.35;0.0000;0.0000;0.0000;  
K(-);-0.80;1.00;0.35;0.40;0.0000;0.0000;0.0000;  
K(-);-0.80;1.00;0.40;0.45;0.0000;0.0000;0.0000;  
K(-);-0.80;1.00;0.45;0.50;0.0000;0.0000;0.0000;  
K(-);-0.80;1.00;0.50;0.55;0.0000;0.0000;0.0000;  
K(-);-0.80;1.00;0.55;0.60;0.0000;0.0000;0.0000;  
K(-);-0.80;1.00;0.60;0.70;1.47;0.0311;0.0128;  
K(-);-0.80;1.00;0.70;0.80;0.9555;0.0111;0.0189;  
K(-);-0.80;1.00;0.80;0.90;0.613;0.0009;0.0097;  
K(-);-0.80;1.00;0.90;1.00;0.0615;0.0077;0.0042;  
K(-);-0.80;1.00;1.00;1.10;0.0000;0.0000;0.0000;  
K(-);-0.80;1.00;1.10;1.20;0.0092;0.0005;0.0004;  
K(-);-0.80;1.00;1.20;1.30;0.0000;0.0000;0.0000;  
K(-);-0.80;1.00;1.30;1.40;0.0000;0.0000;0.0000;  
K(-);-0.80;1.00;1.40;1.50;0.0014;0.0002;0.0005;  
K(-);-0.80;1.00;1.50;1.60;0.0000;0.0000;0.0000;  
K(-);-0.80;1.00;1.60;1.70;0.0000;0.0000;0.0000;  
K(-);-0.80;1.00;1.70;1.80;0.0000;0.0000;0.0000;  
K(-);-0.80;1.00;1.80;1.90;0.0000;0.0000;0.0000;  
K(-);-0.80;1.00;1.90;2.00;0.0000;0.0000;0.0000;  
K(-);1.00;1.20;0.00;0.05;0.0000;0.0000;0.0000;  
K(-);1.00;1.20;0.05;0.10;0.0000;0.0000;0.0000;  
K(-);1.00;1.20;0.10;0.15;0.0000;0.0000;0.0000;  
K(-);1.00;1.20;0.15;0.20;0.0000;0.0000;0.0000;  
K(-);1.00;1.20;0.20;0.25;0.0000;0.0000;0.0000;  
K(-);1.00;1.20;0.25;0.30;0.0000;0.0000;0.0000;  
K(-);1.00;1.20;0.30;0.35;0.0000;0.0000;0.0000;  
K(-);1.00;1.20;0.35;0.40;0.0000;0.0000;0.0000;  
K(-);1.00;1.20;0.40;0.45;0.0000;0.0000;0.0000;  
K(-);1.00;1.20;0.45;0.50;0.1973;0.0018;0.0225;  
K(-);1.00;1.20;0.50;0.55;0.1395;0.0019;0.0168;  
K(-);1.00;1.20;0.55;0.60;0.115;0.0016;0.0117;  
K(-);1.00;1.20;0.60;0.70;0.918;0.0011;0.0063;  
K(-);1.00;1.20;0.70;0.80;0.0513;0.0077;0.0077;  
K(-);1.00;1.20;0.80;0.90;0.0403;0.0006;0.0098;  
K(-);1.00;1.20;0.90;1.00;0.0243;0.0006;0.0090;  
K(-);1.00;1.20;1.00;1.10;0.0000;0.0000;0.0000;  
K(-);1.00;1.20;1.10;1.20;0.0048;0.0003;0.0007;  
K(-);1.00;1.20;1.20;1.30;0.0050;0.0003;0.0020;  
K(-);1.00;1.20;1.30;1.40;0.0000;0.0000;0.0000;  
K(-);1.00;1.20;1.40;1.50;0.0000;0.0000;0.0000;  
K(-);1.00;1.20;1.50;1.60;0.0000;0.0000;0.0000;  
K(-);1.00;1.20;1

K(-);1.20;1.40;0.00;0.05;0.00;0.00;0.00;0.00;0.00;0.00;  
K(-);1.20;1.40;0.05;0.10;0.00;0.00;0.00;0.00;0.00;  
K(-);1.20;1.40;0.10;0.15;0.00;0.00;0.00;0.00;0.00;  
K(-);1.20;1.40;0.15;0.20;0.00;0.00;0.00;0.00;0.00;  
K(-);1.20;1.40;0.20;0.25;0.00;0.00;0.00;0.00;0.00;  
K(-);1.20;1.40;0.25;0.30;0.162;0.018;0.0070;  
K(-);1.20;1.40;0.30;0.35;0.174;0.017;0.0073;  
K(-);1.20;1.40;0.35;0.40;0.182;0.016;0.0053;  
K(-);1.20;1.40;0.40;0.45;0.192;0.016;0.0049;  
K(-);1.20;1.40;0.45;0.50;0.0933;0.015;0.004;  
K(-);1.20;1.40;0.50;0.55;0.0755;0.014;0.0088;  
K(-);1.20;1.40;0.55;0.60;0.0675;0.012;0.0076;  
K(-);1.20;1.40;0.60;0.70;0.0000;0.0000;0.0000;  
K(-);1.20;1.40;0.70;0.80;0.0334;0.005;0.0050;  
K(-);1.20;1.40;0.80;0.90;0.0100;0.005;0.0025;  
K(-);1.20;1.40;0.90;1.00;0.0000;0.0000;0.0000;  
K(-);1.20;1.40;1.00;1.10;0.0019;0.002;0.0000;  
K(-);1.20;1.40;1.10;1.20;0.0000;0.0000;0.0000;  
K(-);1.20;1.40;1.20;1.30;0.0000;0.0000;0.0000;  
K(-);1.20;1.40;1.30;1.40;0.0000;0.0000;0.0000;  
K(-);1.20;1.40;1.40;1.50;0.0000;0.0000;0.0000;  
K(-);1.20;1.40;1.50;1.60;0.0000;0.0000;0.0000;  
K(-);1.20;1.40;1.60;1.70;0.0000;0.0000;0.0000;  
K(-);1.20;1.40;1.70;1.80;0.0000;0.0000;0.0000;  
K(-);1.20;1.40;1.80;1.90;0.0000;0.0000;0.0000;  
K(-);1.20;1.40;1.90;2.00;0.0000;0.0000;0.0000;  
K(-);1.40;1.60;0.00;0.05;0.0000;0.0000;0.0000;  
K(-);1.40;1.60;0.05;0.10;0.0463;0.008;0.0083;  
K(-);1.40;1.60;0.10;0.15;0.0481;0.011;0.0025;  
K(-);1.40;1.60;0.15;0.20;0.0727;0.012;0.0026;  
K(-);1.40;1.60;0.20;0.25;0.0877;0.011;0.0024;  
K(-);1.40;1.60;0.25;0.30;0.0858;0.013;0.0042;  
K(-);1.40;1.60;0.30;0.35;0.0683;0.013;0.0022;  
K(-);1.40;1.60;0.35;0.40;0.0000;0.0000;0.0000;  
K(-);1.40;1.60;0.40;0.45;0.0479;0.012;0.0021;  
K(-);1.40;1.60;0.45;0.50;0.0000;0.0000;0.0000;  
K(-);1.40;1.60;0.50;0.55;0.0284;0.010;0.0013;  
K(-);1.40;1.60;0.55;0.60;0.0469;0.010;0.0008;  
K(-);1.40;1.60;0.60;0.70;0.0182;0.005;0.0011;  
K(-);1.40;1.60;0.70;0.80;0.0099;0.003;0.0007;  
K(-);1.40;1.60;0.80;0.90;0.0041;0.003;0.0003;  
K(-);1.40;1.60;0.90;1.00;0.0000;0.0000;0.0000;  
K(-);1.40;1.60;1.00;1.10;0.0000;0.0000;0.0000;  
K(-);1.40;1.60;1.10;1.20;0.0000;0.0000;0.0000;  
K(-);1.40;1.60;1.20;1.30;0.0000;0.0000;0.0000;  
K(-);1.40;1.60;1.30;1.40;0.0000;0.0000;0.0000;  
K(-);1.40;1.60;1.40;1.50;0.0000;0.0000;0.0000;  
K(-);1.40;1.60;1.50;1.60;0.0000;0.0000;0.0000;  
K(-);1.40;1.60;1.60;1.70;0.0000;0.0000;0.0000;  
K(-);1.40;1.60;1.70;1.80;0.0000;0.0000;0.0000;  
K(-);1.40;1.60;1.80;1.90;0.0000;0.0000;0.0000;  
K(-);1.40;1.60;1.90;2.00;0.0000;0.0000;0.0000;  
K(-);1.60;1.80;0.00;0.05;0.0000;0.0000;0.0000;  
K(-);1.60;1.80;0.05;0.10;0.0102;0.006;0.0024;  
K(-);1.60;1.80;0.10;0.15;0.0000;0.0000;0.0000;  
K(-);1.60;1.80;0.15;0.20;0.0514;0.010;0.0054;  
K(-);1.60;1.80;0.20;0.25;0.0576;0.010;0.0079;  
K(-);1.60;1.80;0.25;0.30;0.0186;0.007;0.0010;  
K(-);1.60;1.80;0.30;0.35;0.0153;0.007;0.0014;  
K(-);1.60;1.80;0.35;0.40;0.0212;0.009;0.0018;  
K(-);1.60;1.80;0.40;0.45;0.0224;0.008;0.0021;  
K(-);1.60;1.80;0.45;0.50;0.0000;0.0000;0.0000;  
K(-);1.60;1.80;0.50;0.55;0.0051;0.006;0.0005;  
K(-);1.60;1.80;0.55;0.60;0.0000;0.0000;0.0000;  
K(-);1.60;1.80;0.60;0.70;0.0048;0.003;0.0015;  
K(-);1.60;1.80;0.70;0.80;0.0003;0.002;0.0001;  
K(-);1.60;1.80;0.80;0.90;0.0000;0.0000;0.0000;  
K(-);1.60;1.80;0.90;1.00;0.0000;0.0000;0.0000;  
K(-);1.60;1.80;1.00;1.10;0.0000;0.0000;0.0000;  
K(-);1.60;1.80;1.10;1.20;0.0000;0.0000;0.0000;  
K(-);1.60;1.80;1.20;1.30;0.0000;0.0000;0.0000;  
K(-);1.60;1.80;1.30;1.40;0.0000;0.0000;0.0000;  
K(-);1.60;1.80;1.40;1.50;0.0000;0.0000;0.0000;  
K(-);1.60;1.80;1.50;1.60;0.0000;0.0000;0.0000;  
K(-);1.60;1.80;1.60;1.70;0.0000;0.0000;0.0000;  
K(-);1.60;1.80;1.70;1.80;0.0000;0.0000;0.0000;  
K(-);1.60;1.80;1.80;1.90;0.0000;0.0000;0.0000;  
K(-);1.60;1.80;1.90;2.00;0.0000;0.0000;0.0000;  
K(-);1.80;2.00;0.00;0.05;0.0000;0.0000;0.0000;  
K(-);1.80;2.00;0.05;0.10;0.0000;0.0000;0.0000;  
K(-);1.80;2.00;0.10;0.15;0.0000;0.0000;0.0000;  
K(-);1.80;2.00;0.15;0.20;0.0265;0.007;0.0041;  
K(-);1.80;2.00;0.20;0.25;0.0162;0.006;0.0035;  
K(-);1.80;2.00;0.25;0.30;0.0000;0.0000;0.0000;  
K(-);1.80;2.00;0.30;0.35;0.0108;0.007;0.0015;  
K(-);1.80;2.00;0.35;0.40;0.0000;0.0000;0.0000;  
K(-);1.80;2.00;0.40;0.45;0.0021;0.004;0.0002;  
K(-);1.80;2.00;0.45;0.50;0.0000;0.0000;0.0000;  
K(-);1.80;2.00;0.50;0.55;0.0000;0.0000;0.0000;  
K(-);1.80;2.00;0.55

```

K*[-1.80;0.00;0.70;0.80;0.0000;0.0000;0.0000;0.0000;
K*[-1.80;2.00;0.80;0.80;0.90;0.0000;0.0000;0.0000;0.0000;
K*[-1.80;2.00;0.00;0.90;1.00;0.0000;0.0000;0.0000;0.0000;
K*[-1.80;2.00;1.00;1.10;1.00;0.0000;0.0000;0.0000;0.0000;
K*[-1.80;2.00;1.00;1.10;2.00;0.0000;0.0000;0.0000;0.0000;
K*[-1.80;2.00;1.00;1.20;1.30;0.0000;0.0000;0.0000;0.0000;
K*[-1.80;2.00;1.30;1.40;0.0000;0.0000;0.0000;0.0000;0.0000;
K*[-1.80;2.00;1.40;1.50;0.0000;0.0000;0.0000;0.0000;0.0000;
K*[-1.80;2.00;1.50;1.60;0.0000;0.0000;0.0000;0.0000;0.0000;
K*[-1.80;2.00;1.60;1.70;0.0000;0.0000;0.0000;0.0000;0.0000;
K*[-1.80;2.00;1.70;1.80;0.0000;0.0000;0.0000;0.0000;0.0000;
K*[-1.80;2.00;1.80;1.90;0.0000;0.0000;0.0000;0.0000;0.0000;
K*[-1.80;2.00;1.90;2.00;0.0000;0.0000;0.0000;0.0000;0.0000;

```





```
K{-};0.20;0.40;1.30;1.40;0.0709;0.0007;0.0081;
K{-};0.20;0.40;1.40;1.50;0.0264;0.0006;0.0017;
K{-};0.20;0.40;1.50;1.60;0.0114;0.0004;0.0021;
K{-};0.20;0.40;1.60;1.70;0.0117;0.0003;0.0042;
K{-};0.20;0.40;1.70;1.80;0.0000;0.0000;0.0000;
K{-};0.20;0.40;1.80;1.90;0.0000;0.0000;0.0000;
K{-};0.20;0.40;1.90;2.00;0.0000;0.0000;0.0000;
K{-};0.40;0.60;0.00;0.05;0.0000;0.0000;0.0000;
K{-};0.40;0.60;0.10;0.15;0.0000;0.0000;0.0000;
K{-};0.40;0.60;0.05;0.10;0.0000;0.0000;0.0000;
K{-};0.40;0.60;0.20;0.25;0.0000;0.0000;0.0000;
K{-};0.40;0.60;0.15;0.20;0.0000;0.0000;0.0000;
K{-};0.40;0.60;0.30;0.35;0.0000;0.0000;0.0000;
K{-};0.40;0.60;0.25;0.30;0.0000;0.0000;0.0000;
K{-};0.40;0.60;0.40;0.45;0.0000;0.0000;0.0000;
K{-};0.40;0.60;0.35;0.40;0.0000;0.0000;0.0000;
K{-};0.40;0.60;0.50;0.55;0.0000;0.0000;0.0000;
K{-};0.40;0.60;0.45;0.50;0.0000;0.0000;0.0000;
K{-};0.40;0.60;0.60;0.65;0.0000;0.0000;0.0000;
K{-};0.40;0.60;0.55;0.60;0.0000;0.0000;0.0000;
K{-};0.40;0.60;0.70;0.75;0.0000;0.0000;0.0000;
K{-};0.40;0.60;0.65;0.70;0.0000;0.0000;0.0000;
K{-};0.40;0.60;0.80;0.85;0.0000;0.0000;0.0000;
K{-};0.40;0.60;0.75;0.80;0.0000;0.0000;0.0000;
K{-};0.40;0.60;0.90;0.95;0.0000;0.0000;0.0000;
K{-};0.40;0.60;0.85;0.90;0.0000;0.0000;0.0000;
K{-};0.40;0.60;1.00;1.01;0.1918;0.0014;0.0122;
K{-};0.40;0.60;1.00;1.01;0.1206;0.0012;0.0131;
K{-};0.40;0.60;1.10;1.20;0.0603;0.0009;0.0039;
K{-};0.40;0.60;1.20;1.30;0.0521;0.0006;0.0056;
K{-};0.40;0.60;1.30;1.40;0.0329;0.0005;0.0048;
K{-};0.40;0.60;1.40;1.50;0.0116;0.0004;0.0111;
K{-};0.40;0.60;1.50;1.60;0.0196;0.0003;0.0024;
K{-};0.40;0.60;1.60;1.70;0.0109;0.0003;0.0017;
K{-};0.40;0.60;1.70;1.80;0.0000;0.0000;0.0000;
K{-};0.40;0.60;1.80;1.90;0.0000;0.0000;0.0000;
K{-};0.40;0.60;1.90;2.00;0.0000;0.0000;0.0000;
K{-};0.60;0.80;0.00;0.05;0.0000;0.0000;0.0000;
K{-};0.60;0.80;0.05;0.10;0.0000;0.0000;0.0000;
K{-};0.60;0.80;0.10;0.15;0.0000;0.0000;0.0000;
K{-};0.60;0.80;0.15;0.20;0.0000;0.0000;0.0000;
K{-};0.60;0.80;0.20;0.25;0.0000;0.0000;0.0000;
K{-};0.60;0.80;0.25;0.30;0.0000;0.0000;0.0000;
K{-};0.60;0.80;0.30;0.35;0.0000;0.0000;0.0000;
K{-};0.60;0.80;0.35;0.40;0.0000;0.0000;0.0000;
K{-};0.60;0.80;0.40;0.45;0.0000;0.0000;0.0000;
K{-};0.60;0.80;0.45;0.50;0.0000;0.0000;0.0000;
K{-};0.60;0.80;0.50;0.55;0.0000;0.0000;0.0000;
K{-};0.60;0.80;0.55;0.60;0.0000;0.0000;0.0023;
K{-};0.60;0.80;0.60;0.65;0.0000;0.0000;0.0000;
K{-};0.60;0.80;0.65;0.70;0.0000;0.0000;0.0243;
K{-};0.60;0.80;0.70;0.75;0.3283;0.0022;0.0144;
K{-};0.60;0.80;0.75;0.80;0.2344;0.0017;0.0144;
K{-};0.60;0.80;0.80;0.85;0.00;0.1824;0.0012;0.0142;
K{-};0.60;0.80;0.85;0.90;0.00;0.0981;0.0010;0.0099;
K{-};0.60;0.80;1.00;1.01;0.2005;0.0004;0.0009;0.0034;
K{-};0.60;0.80;1.20;1.30;0.0401;0.0006;0.0042;
K{-};0.60;0.80;1.30;1.40;0.0323;0.0005;0.0011;
K{-};0.60;0.80;1.40;1.50;0.0146;0.0004;0.0015;
K{-};0.60;0.80;1.50;1.60;0.0079;0.0003;0.0012;
K{-};0.60;0.80;1.60;1.70;0.0066;0.0002;0.0026;
K{-};0.60;0.80;1.70;1.80;0.0000;0.0000;0.0000;
K{-};0.60;0.80;1.80;1.90;0.0000;0.0000;0.0000;
K{-};0.60;0.80;1.90;2.00;0.0000;0.0000;0.0000;
K{-};0.80;1.00;0.00;0.05;0.0000;0.0000;0.0000;
K{-};0.80;1.00;0.05;0.10;0.0000;0.0000;0.0000;
K{-};0.80;1.00;0.10;0.15;0.0000;0.0000;0.0000;
K{-};0.80;1.00;0.15;0.20;0.0000;0.0000;0.0000;
K{-};0.80;1.00;0.20;0.25;0.0000;0.0000;0.0000;
K{-};0.80;1.00;0.25;0.30;0.0000;0.0000;0.0000;
K{-};0.80;1.00;0.30;0.35;0.0000;0.0000;0.0000;
K{-};0.80;1.00;0.35;0.40;0.0000;0.0000;0.0000;
K{-};0.80;1.00;0.40;0.45;0.0000;0.0000;0.0000;
K{-};0.80;1.00;0.45;0.50;0.6223;0.0032;0.0627;
K{-};0.80;1.00;0.50;0.55;0.5023;0.0032;0.0416;
K{-};0.80;1.00;0.55;0.60;0.4000;0.0027;0.0346;
K{-};0.80;1.00;0.60;0.70;0.3144;0.0017;0.0261;
K{-};0.80;1.00;0.70;0.80;0.2491;0.0014;0.0266;
K{-};0.80;1.00;0.80;0.90;0.1375;0.0012;0.0128;
K{-};0.80;1.00;0.90;1.00;0.0785;0.0010;0.0090;
K{-};0.80;1.00;1.00;1.10;0.0624;0.0008;0.0039;
K{-};0.80;1.00;1.10;1.20;0.0263;0.0006;0.0033;
K{-};0.80;1.00;1.20;1.30;0.0258;0.0005;0.0021;
K{-};0.80;1.00;1.30;1.40;0.0173;0.0004;0.0025;
K{-};0.80;1.00;1.40;1.50;0.0000;0.0000;0.0000;
K{-};0.80;1.00;1.50;1.60;0.0000;0.0000;0.0000;
K{-};0.80;1.00;1.60;1.70;0.0007;0.0001;0.0002;
K{-};0.80;1.00;1.70;1.80;0.0000;0.0000;0.0000;
K{-};0.80;1.00;1.80;1.90;0.0000;0.0000;0.0000;
K{-};0.80;1.00;1.90;2.00;0.0000;0.0000;0.0000;
K{-};1.00;1.20;0.00;0.05;0.0000;0.0000;0.0000;
K{-};1.00;1.20;0.05;0.10;0.0000;0.0000;0.0000;
K{-};1.00;1.20;0.10;0.15;0.0000;0.0000;0.0000;
K{-};1.00;1.20;0.15;0.20;0.0000;0.0000;0.0000;
K{-};1.00;1.20;0.20;0.25;0.0000;0.0000;0.0000;
K{-};1.00;1.20;0.25;0.30;0.4644;0.0027;0.0278;
K{-};1.00;1.20;0.30;0.35;0.5038;0.0030;0.0239;
K{-};1.00;1.20;0.35;0.40;0.4195;0.0033;0.0225;
K{-};1.00;1.20;0.40;0.45;0.4051;0.0028;0.0393;
K{-};1.00;1.20;0.45;0.50;0.3733;0.0029;0.0202;
K{-};1.00;1.20;0.50;0.55;0.3387;0.0025;0.0369;
K{-};1.00;1.20;0.55;0.60;0.2433;0.0023;0.0199;
K{-};1.00;1.20;0.60;0.70;0.2347;0.0015;0.0182;
K{-};1.00;1.20;0.70;0.80;0.1332;0.0011;0.0173;
K{-};1.00;1.20;0.80;0.90;0.0912;0.0010;0.0112;
K{-};1.00;1.20;0.90;1.00;0.0539;0.0007;0.0097;
K{-};1.00;1.20;1.00;1.10;0.0328;0.0007;0.0022;
K{-};1.00;1.20;1.10;1.20;0.0184;0.0004;0.0021;
K{-};1.00;1.20;1.20;1.30;0.0151;0.0004;0.0029;
K{-};1.00;1.20;1.30;1.40;0.0058;0.0002;0.0020;
K{-};1.00;1.20;1.40;1.50;0.0000;0.0000;0.0000;
K{-};1.00;1.20;1.50;1.60;0.0000;0.0000;0.0000;
K{-};1.00;1.20;1.60;1.70;0.0000;0.0000;0.0000;
K{-};1.00;1.20;1.70;1.80;0.0000;0.0000;0.0000;
K{-};1.00;1.20;1.80;1.90;0.0000;0.0000;0.0000;
K{-};1.00;1.20;1.90;2.00;0.0000;0.0000;0.0000;
K{-};1.20;1.40;0.00;0.05;0.0469;0.0007;0.0024;
K{-};1.20;1.40;0.05;0.10;0.1429;0.0014;0.0052;
K{-};1.20;1.40;0.10;0.15;0.2419;0.0017;0.0082;
K{-};1.20;1.40;0.15;0.20;0.2706;0.0019;0.0091;
K{-};1.20;1.40;0.20;0.25;0.3220;0.0024;0.0064;
K{-};1.20;1.40;0.25;0.30;0.3115;0.0025;0.0073;
K{-};1.20;1.40;0.30;0.35;0.2920;0.0027;0.0125;
K{-};1.20;1.40;0.35;0.40;0.3030;0.0026;0.0138;
K{-};1.20;1.40;0.40;0.45;0.2891;0.0026;0.0089;
K{-};1.20;1.40;0.45;0.50;0.2282;0.0024;0.0055;
K{-};1.20;1.40;0.50;0.55;0.1774;0.0021;0.0098;
K{-};1.20;1.40;0.55;0.60;0.1099;0.0019;0.0044;
K{-};1.20;1.40;0.60;0.70;0.1517;0.0011;0.0106;
K{-};1.20;1.40;0.70;0.80;0.0604;0.0009;0.0044;
K{-};1.20;1.40;0.80;0.90;0.0765;0.0008;0.0086;
K{-};1.20;1.40;0.90;1.00;0.0218;0.0004;0.0016;
K{-};1.20;1.40;1.00;1.10;0.0278;0.0004;0.0019;
K{-};1.20;1.40;1.10;1.20;0.0080;0.0004;0.0007;
K{-};1.20;1.40;1.20;1.30;0.0079;0.0003;0.0010;
K{-};1.20;1.40;1.30;1.40;0.0000;0.0000;0.0000;
K{-};1.20;1.40;1.40;1.50;0.0000;0.0000;0.0000;
K{-};1.20;1.40;1.50;1.60;0.0000;0.0000;0.0000;
K{-};1.20;1.40;1.60;1.70;0.0000;0.0000;0.0000;
K{-};1.20;1.40;1.70;1.80;0.0000;0.0000;0.0000;
K{-};1.20;1.40;1.80;1.90;0.0000;0.0000;0.0000;
K{-};1.20;1.40;1.90;2.00;0.0000;0.0000;0.0000;
K{-};1.40;1.60;0.00;0.05;0.0000;0.0000;0.0000;
K{-};1.40;1.60;0.05;0.10;0.0000;0.0000;0.0000;
K{-};1.40;1.60;0.10;0.15;0.0000;0.0000;0.0000;
K{-};1.40;1.60;0.15;0.20;0.1861;0.0020;0.0076;
K{-};1.40;1.60;0.20;0.25;0.1693;0.0019;0.0031;
K{-};1.40;1.60;0.25;0.30;0.1735;0.0019;0.0057;
K{-};1.40;1.60;0.30;0.35;0.1942;0.0020;0.0018;
K{-};1.40;1.60;0.35;0.40;0.1573;0.0019;0.0073;
K{-};1.40;1.60;0.40;0.45;0.1426;0.0018;0.0041;
K{-};1.40;1.60;0.45;0.50;0.1085;0.0015;0.0063;
K{-};1.40;1.60;0.50;0.55;0.0746;0.0013;0.0022;
K{-};1.40;1.60;0.55;0.60;0.0883;0.0015;0.0018;
K{-};1.40;1.60;0.60;0.70;0.0558;0.0009;0.0045;
K{-};1.40;1.60;0.70;0.80;0.0399;0.0007;0.0015;
K{-};1.40;1.60;0.80;0.90;0.0275;0.0004;0.0027;
K{-};1.40;1.60;0.90;1.00;0.0000;0.0000;0.0000;
K{-};1.40;1.60;1.00;1.10;0.0000;0.0000;0.0000;
K{-};1.40;1.60;1.10;1.20;0.0006;0.0001;0.0025;
K{-};1.40;1.60;1.20;1.30;0.0000;0.0000;0.0000;
K{-};1.40;1.60;1.30;1.40;0.0000;0.0000;0.0000;
K{-};1.40;1.60;1.40;1.50;0.0000;0.0000;0.0000;
K{-};1.40;1.60;1.50;1.60;0.0000;0.0000;0.0000;
K{-};1.40;1.60;1.60;1.70;0.0000;0.0000;0.0000;
K{-};1.40;1.60;1.70;1.80;0.0000;0.0000;0.0000;
K{-};1.40;1.60;1.80;0.00;0.05;0.0000;0.0000;0.0000;
K{-};1.60;1.80;0.05;0.10;0.0447;0.0010;0.0058;
K{-};1.60;1.80;0.10;0.15;0.0809;0.0012;0.0067;
K{-};1.60;1.80;0.15;0.20;0.0897;0.0013;0.0027;
K{-};1.60;1.80;0.20;0.25;0.0825;0.0014;0.0041;
K{-};1.60;1.80;0.25;0.30;0.0870;0.0015;0.0051;
K{-};1.60;1.80;0.30;0.35;0.1344;0.0015;0.0034;
K{-};1.60;1.80;0.35;0.40;0.0614;0.0012;0.0062;
K{-};1.60;1.80;0.40;0.45;0.0937;0.0014;0.0045;
K{-};1.60;1.80;0.45;0.50;0.0000;0.0000;0.0000;
K{-};1.60;1.80;0.50;0.55;0.0445;0.0009;0.0063;
K{-};1.60;1.80;0.55;0.60;0.0358;0.0009;0.0002;
K{-};1.60;1.80;0.60;0.70;0.0000;0.0000;0.0000;
K{-};1.60;1.80;0.70;0.80;0.0149;0.0004;0.0014;
K{-};1.60;1.80;0.80;0.90;0.0081;0.0003;0.0004;
K{-};1.60;1.80;0.90;1.00;0.0027;0.0002;0.0002;
K{-};1.60;1.80;1.00;1.10;0.0013;0.0001;0.0002;
K{-};1.60;1.80;1.10;1.20;0.0000;0.0000;0.0000;
K{-};1.60;1.80;1.20;1.30;0.0000;0.0000;0.0000;
```

## Kaons at 30A GeV/c

s; ymin; ymx; pTmin; pTmx; dn/dypT; errstat; errsys;

```

species; ymin; ymx; pTmin; pTmx; dn/dypT; errstat; errsys;
K^{+}; -0.20; 0.00; 0.00; 0.05; 0.0000; 0.0000; 0.0000;
K^{+}; -0.20; 0.00; 0.05; 0.10; 0.0000; 0.0000; 0.0000;
K^{+}; -0.20; 0.00; 0.10; 0.15; 0.0000; 0.0000; 0.0000;
K^{+}; -0.20; 0.00; 0.15; 0.20; 0.0000; 0.0000; 0.0000;
K^{+}; -0.20; 0.00; 0.20; 0.25; 0.0000; 0.0000; 0.0000;
K^{+}; -0.20; 0.00; 0.25; 0.30; 0.0000; 0.0000; 0.0000;
K^{+}; -0.20; 0.00; 0.30; 0.35; 0.0000; 0.0000; 0.0000;
K^{+}; -0.20; 0.00; 0.35; 0.40; 0.0000; 0.0000; 0.0000;
K^{+}; -0.20; 0.00; 0.40; 0.45; 0.0000; 0.0000; 0.0000;
K^{+}; -0.20; 0.00; 0.45; 0.50; 0.0000; 0.0000; 0.0000;
K^{+}; -0.20; 0.00; 0.50; 0.55; 0.0000; 0.0000; 0.0000;
K^{+}; -0.20; 0.00; 0.55; 0.60; 0.0000; 0.0000; 0.0000;
K^{+}; -0.20; 0.00; 0.60; 0.70; 0.0000; 0.0000; 0.0000;
K^{+}; -0.20; 0.00; 0.70; 0.80; 0.0000; 0.0000; 0.0000;
K^{+}; -0.20; 0.00; 0.80; 0.90; 0.0000; 0.0000; 0.0000;
K^{+}; -0.20; 0.00; 0.90; 1.00; 0.0000; 0.0000; 0.0000;
K^{+}; -0.20; 0.00; 1.00; 1.10; 0.0000; 0.0000; 0.0000;
K^{+}; -0.20; 0.00; 1.10; 1.20; 0.0000; 0.0000; 0.0000;
K^{+}; -0.20; 0.00; 1.20; 1.30; 0.0000; 0.0000; 0.0000;
K^{+}; -0.20; 0.00; 1.30; 1.40; 0.1986; 0.0150; 0.0597;
K^{+}; -0.20; 0.00; 1.40; 1.50; 0.1238; 0.0120; 0.0480;
K^{+}; -0.20; 0.00; 1.50; 1.60; 0.1187; 0.0071; 0.0409;
K^{+}; -0.20; 0.00; 1.60; 1.70; 0.0000; 0.0000; 0.0000;
K^{+}; -0.20; 0.00; 1.70; 1.80; 0.0085; 0.0029; 0.0318;
K^{+}; -0.20; 0.00; 1.80; 1.90; 0.0000; 0.0000; 0.0000;
K^{+}; -0.20; 0.00; 1.90; 2.00; 0.0000; 0.0000; 0.0000;
K^{+}; 0.00; 0.20; 0.00; 0.05; 0.0000; 0.0000; 0.0000;
K^{+}; 0.00; 0.20; 0.05; 0.10; 0.0000; 0.0000; 0.0000;
K^{+}; 0.00; 0.20; 0.10; 0.15; 0.0000; 0.0000; 0.0000;
K^{+}; 0.00; 0.20; 0.15; 0.20; 0.0000; 0.0000; 0.0000;
K^{+}; 0.00; 0.20; 0.20; 0.25; 0.0000; 0.0000; 0.0000;
K^{+}; 0.00; 0.20; 0.25; 0.30; 0.0000; 0.0000; 0.0000;
K^{+}; 0.00; 0.20; 0.30; 0.35; 0.0000; 0.0000; 0.0000;
K^{+}; 0.00; 0.20; 0.35; 0.40; 0.0000; 0.0000; 0.0000;
K^{+}; 0.00; 0.20; 0.40; 0.45; 0.0000; 0.0000; 0.0000;
K^{+}; 0.00; 0.20; 0.45; 0.50; 0.0000; 0.0000; 0.0000;
K^{+}; 0.00; 0.20; 0.50; 0.55; 0.0000; 0.0000; 0.0000;
K^{+}; 0.00; 0.20; 0.55; 0.60; 0.0000; 0.0000; 0.0000;
K^{+}; 0.00; 0.20; 0.60; 0.70; 0.0000; 0.0000; 0.0000;
K^{+}; 0.00; 0.20; 0.70; 0.80; 0.0000; 0.0000; 0.0000;
K^{+}; 0.00; 0.20; 0.80; 0.90; 0.0000; 0.0000; 0.0000;
K^{+}; 0.00; 0.20; 0.90; 1.00; 0.0000; 0.0000; 0.0000;
K^{+}; 0.00; 0.20; 1.00; 1.10; 0.5761; 0.0080; 0.0971;
K^{+}; 0.00; 0.20; 1.10; 1.20; 0.3868; 0.0114; 0.0687;
K^{+}; 0.00; 0.20; 1.20; 1.30; 0.1943; 0.0162; 0.0462;
K^{+}; 0.00; 0.20; 1.30; 1.40; 0.2098; 0.0094; 0.0393;
K^{+}; 0.00; 0.20; 1.40; 1.50; 0.1290; 0.0049; 0.0298;
K^{+}; 0.00; 0.20; 1.50; 1.60; 0.1345; 0.0091; 0.0225;
K^{+}; 0.00; 0.20; 1.60; 1.70; 0.0483; 0.0067; 0.0200;
K^{+}; 0.00; 0.20; 1.70; 1.80; 0.0415; 0.0025; 0.0145;
K^{+}; 0.00; 0.20; 1.80; 1.90; 0.0290; 0.0020; 0.0151;
K^{+}; 0.00; 0.20; 1.90; 2.00; 0.0000; 0.0000; 0.0000;
K^{+}; 0.20; 0.40; 0.00; 0.05; 0.0000; 0.0000; 0.0000;
K^{+}; 0.20; 0.40; 0.05; 0.10; 0.0000; 0.0000; 0.0000;
K^{+}; 0.20; 0.40; 0.10; 0.15; 0.0000; 0.0000; 0.0000;
K^{+}; 0.20; 0.40; 0.15; 0.20; 0.0000; 0.0000; 0.0000;
K^{+}; 0.20; 0.40; 0.20; 0.25; 0.0000; 0.0000; 0.0000;
K^{+}; 0.20; 0.40; 0.25; 0.30; 0.0000; 0.0000; 0.0000;
K^{+}; 0.20; 0.40; 0.30; 0.35; 0.0000; 0.0000; 0.0000;
K^{+}; 0.20; 0.40; 0.35; 0.40; 0.0000; 0.0000; 0.0000;
K^{+}; 0.20; 0.40; 0.40; 0.45; 0.0000; 0.0000; 0.0000;
K^{+}; 0.20; 0.40; 0.45; 0.50; 0.0000; 0.0000; 0.0000;
K^{+}; 0.20; 0.40; 0.50; 0.55; 0.0000; 0.0000; 0.0000;
K^{+}; 0.20; 0.40; 0.55; 0.60; 0.0000; 0.0000; 0.0000;
K^{+}; 0.20; 0.40; 0.60; 0.70; 0.0000; 0.0000; 0.0000;
K^{+}; 0.20; 0.40; 0.70; 0.80; 0.0000; 0.0000; 0.0000;
K^{+}; 0.20; 0.40; 0.80; 0.90; 0.0000; 0.0000; 0.0000;
K^{+}; 0.20; 0.40; 0.90; 1.00; 0.0000; 0.0000; 0.0000;
K^{+}; 0.20; 0.40; 1.00; 1.10; 0.10; 0.3350; 0.0048; 0.0438;
K^{+}; 0.20; 0.40; 1.10; 1.20; 0.0352; 0.0036; 0.0325;
K^{+}; 0.20; 0.40; 1.20; 1.30; 0.0340; 0.0023; 0.0184;
K^{+}; 0.20; 0.40; 1.30; 1.40; 0.0507; 0.0026; 0.0176;
K^{+}; 0.20; 0.40; 1.40; 1.50; 0.0611; 0.0021; 0.0106;
K^{+}; 0.20; 0.40; 1.50; 1.60; 0.0710; 0.0037; 0.0144;
K^{+}; 0.20; 0.40; 1.60; 1.70; 0.0800; 0.0033; 0.0111;
K^{+}; 0.20; 0.40; 1.70; 1.80; 0.0900; 0.0040; 0.0122;
K^{+}; 0.20; 0.40; 1.80; 1.90; 0.1000; 0.0045; 0.0133;
K^{+}; 0.20; 0.40; 1.90; 2.00; 0.1100; 0.0050; 0.0144;
K^{+}; 0.20; 0.40; 2.00; 0.05; 0.10; 0.8143; 0.0100; 0.0479;
K^{+}; 0.20; 0.40; 2.00; 0.10; 0.15; 1.3372; 0.0106; 0.0790;
K^{+}; 0.20; 0.40; 2.00; 0.15; 0.20; 1.9072; 0.0109; 0.1095;
K^{+}; 0.20; 0.40; 2.00; 0.20; 0.25; 2.9903; 0.0119; 0.1111;
K^{+}; 0.20; 0.40; 2.00; 0.25; 0.30; 3.5744; 0.0122; 0.1208;
K^{+}; 0.20; 0.40; 2.00; 0.30; 0.35; 2.6171; 0.0125; 0.1188;
K^{+}; 0.20; 0.40; 2.00; 0.35; 0.40; 2.6676; 0.0120; 0.1097;
K^{+}; 0.20; 0.40; 2.00; 0.40; 0.45; 2.5963; 0.0137; 0.1017;
K^{+}; 1.00; 1.20; 0.45; 0.50; 2.3070; 0.0129; 0.0940;
K^{+}; 1.00; 1.20; 0.50; 0.55; 2.1215; 0.0113; 0.0958;
K^{+}; 1.00; 1.20; 0.55; 0.60; 1.9465; 0.0126; 0.1091;
K^{+}; 1.00; 1.20; 0.60; 0.70; 1.6083; 0.0069; 0.0983;
K^{+}; 1.00; 1.20; 0.70; 0.80; 1.1335; 0.0060; 0.0889;
K^{+}; 1.00; 1.20; 0.80; 0.90; 0.7902; 0.0059; 0.0723;
K^{+}; 1.00; 1.20; 0.90; 1.00; 0.4843; 0.0043; 0.0492;
K^{+}; 1.00; 1.20; 1.00; 1.10; 0.3728; 0.0039; 0.0482;
K^{+}; 1.00; 1.20; 1.10; 1.20; 0.2046; 0.0036; 0.0247;
K^{+}; 1.00; 1.20; 1.20; 1.30; 0.1511; 0.0022; 0.0225;
K^{+}; 1.00; 1.20; 1.30; 1.40; 0.1356; 0.0019; 0.0148;
K^{+}; 1.00; 1.20; 1.40; 1.50; 0.0535; 0.0018; 0.0095;
K^{+}; 1.00; 1.20; 1.50; 1.60; 0.0353; 0.0011; 0.0065;
K^{+}; 1.00; 1.20; 1.60; 1.70; 0.0000; 0.0000; 0.0000;
K^{+}; 1.00; 1.20; 1.70; 1.80; 0.0000; 0.0000; 0.0000;
K^{+}; 1.00; 1.20; 1.80; 1.90; 0.0000; 0.0000; 0.0000;
K^{+}; 1.00; 1.20; 1.90; 2.00; 0.0000; 0.0000; 0.0000;
K^{+}; 1.20; 1.40; 0.00; 0.05; 0.2976; 0.0041; 0.0170;
K^{+}; 1.20; 1.40; 0.05; 0.10; 0.6933; 0.0058; 0.0366;
K^{+}; 1.20; 1.40; 0.10; 0.15; 1.1939; 0.0084; 0.0589;
K^{+}; 1.20; 1.40; 0.15; 0.20; 1.5553; 0.0093; 0.0831;
K^{+}; 1.20; 1.40; 0.20; 0.25; 1.8305; 0.0091; 0.0993;
K^{+}; 1.20; 1.40; 0.25; 0.30; 0.2555; 0.0091; 0.0947;
K^{+}; 1.20; 1.40; 0.30; 0.35; 0.0594; 0.0093; 0.0978;
K^{+}; 1.20; 1.40; 0.35; 0.40; 0.0887; 0.0121; 0.0945;
K^{+}; 1.20; 1.40; 0.40; 0.45; 1.9806; 0.0102; 0.0892;
K^{+}; 1.20; 1.40; 0.45; 0.50; 1.9161; 0.0110; 0.0915;
K^{+}; 1.20; 1.40; 0.50; 0.55; 1.6621; 0.0098; 0.0734;
K^{+}; 1.20; 1.40; 0.55; 0.60; 1.4401; 0.0094; 0.0716;
K^{+}; 1.20; 1.40; 0.60; 0.70; 1.2511; 0.0061; 0.0613;
K^{+}; 1.20; 1.40; 0.70; 0.80; 0.7709; 0.0058; 0.0380;
K^{+}; 1.20; 1.40; 0.80; 0.90; 0.5367; 0.0055; 0.0287;
K^{+}; 1.20; 1.40; 0.90; 1.00; 0.3946; 0.0037; 0.0229;
K^{+}; 1.20; 1.40; 1.00; 1.10; 0.2421; 0.0033; 0.0199;
K^{+}; 1.20; 1.40; 1.10; 1.20; 0.1438; 0.0028; 0.0172;
K^{+}; 1.20; 1.40; 1.20; 1.30; 0.0915; 0.0022; 0.0177;
K^{+}; 1.20; 1.40; 1.30; 1.40; 0.0556; 0.0015; 0.0053;
K^{+}; 1.20; 1.40; 1.40; 1.50; 0.0000; 0.0000; 0.0000;
K^{+}; 1.20; 1.40; 1.50; 1.60; 0.0077; 0.0012; 0.0030;
K^{+}; 1.20; 1.40; 1.60; 1.70; 0.0000; 0.0000; 0.0000;
K^{+}; 1.20; 1.40; 1.70; 1.80; 0.0000; 0.0000; 0.0000;
K^{+}; 1.20; 1.40; 1.80; 1.90; 0.0000; 0.0000; 0.0000;
K^{+}; 1.20; 1.40; 1.90; 2.00; 0.0000; 0.0000; 0.0000;
K^{+}; 1.40; 1.60; 0.00; 0.05; 0.2259; 0.0030; 0.0221;
K^{+}; 1.40; 1.60; 0.05; 0.10; 0.6186; 0.0056; 0.0410;
K^{+}; 1.40; 1.60; 0.10; 0.15; 0.9030; 0.0063; 0.0501;
K^{+}; 1.40; 1.60; 0.15; 0.20; 1.2393; 0.0083; 0.0630;
K^{+}; 1.40; 1.60; 0.20; 0.25; 1.4020; 0.0089; 0.0727;
K^{+}; 1.40; 1.60; 0.25; 0.30; 1.4745; 0.0088; 0.0828;
K^{+}; 1.40; 1.60; 0.30; 0.35; 1.6442; 0.0083; 0.0868;
K^{+}; 1.40; 1.60; 0.35; 0.40; 1.5746; 0.0095; 0.0814;
K^{+}; 1.40; 1.60; 0.40; 0.45; 1.4081; 0.0094; 0.0780;
K^{+}; 1.40; 1.60; 0.45; 0.50; 1.1608; 0.0083; 0.0578;
K^{+}; 1.40; 1.60; 0.50; 0.55; 1.1542; 0.0084; 0.0514;
K^{+}; 1.40; 1.60; 0.55; 0.60; 0.8586; 0.0083; 0.0432;
K^{+}; 1.40; 1.60; 0.60; 0.70; 0.7411; 0.0057; 0.0468;
K^{+}; 1.40; 1.60; 0.70; 0.80; 0.5019; 0.0049; 0.0307;
K^{+}; 1.40; 1.60; 0.80; 0.90; 0.3674; 0.0039; 0.0236;
K^{+}; 1.40; 1.60; 0.90; 1.00; 0.2289; 0.0040; 0.0167;
K^{+}; 1.40; 1.60; 1.00; 1.10; 0.1779; 0.0027; 0.0172;
K^{+}; 1.40; 1.60; 1.10; 1.20; 0.0899; 0.0028; 0.0092;
K^{+}; 1.40; 1.60; 1.20; 1.30; 0.0246; 0.0018; 0.0027;
K^{+}; 1.40; 1.60; 1.30; 1.40; 0.0313; 0.0014; 0.0034;
K^{+}; 1.40; 1.60; 1.40; 1.50; 0.0000; 0.0000; 0.0000;
K^{+}; 1.40; 1.60; 1.50; 1.60; 0.0000; 0.0000; 0.0000;
K^{+}; 1.40; 1.60; 1.60; 1.70; 0.0000; 0.0000; 0.0000;
K^{+}; 1.40; 1.60; 1.70; 1.80; 0.0000; 0.0000; 0.0000;
K^{+}; 1.40; 1.60; 1.80; 1.90; 0.0000; 0.0000; 0.0000;
K^{+}; 1.40; 1.60; 1.90; 2.00; 0.0000; 0.0000; 0.0000;
K^{+}; 1.60; 1.80; 0.00; 0.05; 0.0000; 0.0000; 0.0000;
K^{+}; 1.60; 1.80; 0.05; 0.10; 0.4620; 0.0058; 0.0554;
K^{+}; 1.60; 1.80; 0.10; 0.15; 0.8861; 0.0075; 0.0696;
K^{+}; 1.60; 1.80; 0.15; 0.20; 0.9253; 0.0081; 0.0719;
K^{+}; 1.60; 1.80; 0.20; 0.25; 1.0106; 0.0095; 0.0661;
K^{+}; 1.60; 1.80; 0.25; 0.30; 1.1433; 0.0093; 0.0628;
K^{+}; 1.60; 1.80; 0.30; 0.35; 0.9622; 0.0103; 0.0552;
K^{+}; 1.60; 1.80; 0.35; 0.40; 1.0325; 0.0082; 0.0532;
K^{+}; 1.60; 1.80; 0.40; 0.45; 0.9347; 0.0085; 0.0608;
K^{+}; 1.60; 1.80; 0.45; 0.50; 0.7994; 0.0094; 0.0449;
K^{+}; 1.60; 1.80; 0.50; 0.55; 0.7411; 0.0083; 0.0393;
K^{+}; 1.60; 1.80; 0.55; 0.60; 0.5910; 0.0085; 0.0341;
K^{+}; 1.60; 1.80; 0.60; 0.70; 0.4730; 0.0055; 0.0284;
K^{+}; 1.60; 1.80; 0.70; 0.80; 0.3066; 0.0045; 0.0197;
K^{+}; 1.60; 1.80; 0.80; 0.90; 0.1496; 0.0034; 0.0103;
K^{+}; 1.60; 1.80; 0.90; 1.00; 0.0800; 0.0029; 0.0071;
K^{+}; 1.60; 1.80; 1.00; 1.10; 0.0466; 0.0021; 0.0040;
K^{+}; 1.60; 1.80; 1.10; 1.20; 0.0462; 0.0015; 0.0043;
K^{+}; 1.60; 1.80; 1.20; 1.30; 0.0077; 0.0015; 0.0034;
K^{+}; 1.60; 1.80; 1.30; 1.40; 0.0036; 0.0008; 0.0008;
K^{+}; 1.60; 1.80; 1.40; 1.50; 0.0000; 0.0000; 0.0000;
K^{+}; 1.60; 1.80; 1.50; 1.60; 0.0000; 0.0000; 0.0000;
K^{+}; 1.60; 1.80; 1.60; 1.70; 0.0000; 0.0000; 0.0000;
K^{+}; 1.60; 1.80; 1.70; 1.80; 0.0000; 0.0000; 0.0000;
K^{+}; 1.60; 1.80; 1.80; 1.90; 0.0000; 0.0000; 0.0000;
K^{+}; 1.60; 1.80; 1.90; 2.00; 0.0000; 0.0000; 0.0000;
K^{+}; 1.80; 2.00; 0.00; 0.05; 0.0000; 0.0000; 0.0000;
K^{+}; 1.80; 2.00; 0.05; 0.10; 0.0000; 0.0000; 0.0000;
K^{+}; 1.80; 2.00; 0.10; 0.15; 0.0000; 0.0000; 0.0000;
K^{+}; 1.80; 2.00; 0.15; 0.20; 0.0000; 0.0000; 0.0000;
K^{+}; 1.80; 2.00; 0.20; 0.25; 0.0000; 0.0000; 0.0000;
K^{+}; 1.80; 2.00; 0.25; 0.30; 0.0000; 0.0000; 0.0000;
K^{+}; 1.80; 2.00; 0.30; 0.35; 0.0000; 0.0000; 0.0000;
K^{+}; 1.80; 2.00; 0.35; 0.40; 0.0000; 0.0000; 0.0000;
K^{+}; 1.80; 2.00; 0.40; 0.45; 0.0000; 0.0000; 0.0000;
K^{+}; 1.80; 2.00; 0.45; 0.50; 0.0000; 0.0000; 0.0000;
K^{+}; 1.80; 2.00; 0.50; 0.55; 0.0000; 0.0000; 0.0000;
K^{+}; 1.80; 2.00; 0.55; 0.60; 0.0000; 0.0000; 0.0000;
K^{+}; 1.80; 2.00; 0.60; 0.70; 0.0000; 0.0000; 0.0000;
K^{+}; 1.80; 2.00; 0.70; 0.80; 0.0000; 0.0000; 0.0000;
K^{+}; 1.80; 2.00; 0.80; 0.90; 0.0000; 0.0000; 0.0000;
K^{+}; 1.80; 2.00; 0.90; 1.00; 0.0000; 0.0000; 0.0000;
K^{+}; 1.80; 2.00; 1.00; 1.10; 0.0000; 0.0000; 0.0000;
K^{+}; 1.80; 2.00; 1.10; 1.20; 0.0000; 0.0000; 0.0000;
K^{+}; 1.80; 2.00; 1.20; 1.30; 0.0000; 0.0000; 0.0000;
K^{+}; 1.80; 2.00; 1.30; 1.40; 0.0000; 0.0000; 0.0000;
K^{+}; 1.80; 2.00; 1.40; 1.50; 0.0000; 0.0000; 0.0000;
K^{+}; 1.80; 2.00; 1.50; 1.60; 0.0000; 0.0000; 0.0000;
K^{+}; 1.80; 2.00; 1.60; 1.70; 0.0000; 0.0000; 0.0000;
K^{+}; 1.80; 2.00; 1.70; 1.80; 0.0000; 0.0000; 0.0000;
K^{+}; 1.80; 2.00; 1.80; 1.90; 0.0000; 0.0000; 0.0000;
K^{+}; 1.80; 2.00; 1.90; 2.00; 0.0000; 0.0000; 0.0000;
K^{+}; 2.00; 2.20; 0.00; 0.05; 0.0000; 0.0000; 0.0000;
K^{+}; 2.00; 2.20; 0.05; 0.10; 0.0000; 0.0000; 0.0000;
K^{+}; 2.00; 2.20; 0.10; 0.15; 0.0000; 0.0000; 0.0000;
K^{+}; 2.00; 2.20; 0.15; 0.20; 0.0000; 0.0000; 0.0000;
K^{+}; 2.00; 2.20; 0.20; 0.25; 0.0000; 0.0000; 0.0000;
K^{+}; 2.00; 2.20; 0.25; 0.30; 0.0000; 0.0000; 0.0000;
K^{+}; 2.00; 2.20; 0.30; 0.35; 0.0000; 0.0000; 0.0000;
K^{+}; 2.00; 2.20; 0.35; 0.40; 0.0000; 0.0000; 0.0000;
K^{+}; 2.00; 2.20; 0.40; 0.45; 0.0000; 0.0000; 0.0000;
K^{+}; 2.00; 2.20; 0.45; 0.50; 0.0000; 0.0000; 0.0000;
K^{+}; 2.00; 2.20; 0.50; 0.55; 0.0000; 0.0000; 0.0000;
K^{+}; 2.00; 2.20; 0.55; 0.60; 0.0000; 0.0000; 0.0000;
K^{+}; 2.00; 2.20; 0.60; 0.70; 0.0000; 0.0000; 0.0000;
K^{+}; 2.00; 2.20; 0.70; 0.80; 0.0000; 0.0000; 0.0000;
K^{+}; 2.00; 2.20; 0.80; 0.90; 0.0000; 0.0000; 0.0000;
K^{+}; 2.00; 2.20; 0.90; 1.00; 0.0000; 0.0000; 0.0000;
K^{+}; 2.00; 2.20; 1.00; 1.10; 0.0000; 0.0000; 0.0000;
K^{+}; 2.00; 2.20; 1.10; 1.20; 0.0000; 0.0000; 0.0000;
K^{+}; 2.00; 2.20; 1.20; 1.30; 0.0000; 0.0000; 0.0000;
K^{+}; 2.00; 2.20; 1.30; 1.40; 0.0000; 0.0000; 0.0000;
K^{+}; 2.00; 2.20; 1.40; 1.50; 0.0000; 0.0000; 0.0000;
K^{+}; 2.00; 2.20; 1.50; 1.60; 0.0000; 0.0000; 0.0000;
K
```

K<sub>1</sub><sup>+</sup>: -0.20; 0.00; 1.30; 1.40; 0.00; 0.0000; 0.0000; 0.0000;  
K<sub>1</sub><sup>-</sup>: -0.20; 0.00; 1.40; 1.50; 0.0559; 0.0009; 0.0081;  
K<sub>2</sub><sup>+</sup>: -0.20; 0.00; 1.50; 1.60; 0.0266; 0.0005; 0.0030;  
K<sub>2</sub><sup>-</sup>: -0.20; 0.00; 1.60; 1.70; 0.0135; 0.0004; 0.0026;  
K<sub>3</sub><sup>+</sup>: -0.20; 0.00; 1.70; 1.80; 0.0088; 0.0003; 0.0007;  
K<sub>3</sub><sup>-</sup>: -0.20; 0.00; 1.80; 1.90; 0.0000; 0.0000; 0.0000;  
K<sub>4</sub><sup>+</sup>: -0.20; 0.00; 1.90; 2.00; 0.0000; 0.0000; 0.0000;  
K<sub>4</sub><sup>-</sup>: 0.00; 0.20; 0.00; 0.05; 0.0000; 0.0000; 0.0000;  
K<sub>5</sub><sup>+</sup>: 0.00; 0.20; 0.10; 0.15; 0.0000; 0.0000; 0.0000;  
K<sub>5</sub><sup>-</sup>: 0.00; 0.20; 0.15; 0.20; 0.0000; 0.0000; 0.0000;  
K<sub>6</sub><sup>+</sup>: 0.00; 0.20; 0.20; 0.25; 0.0000; 0.0000; 0.0000;  
K<sub>6</sub><sup>-</sup>: 0.00; 0.20; 0.25; 0.30; 0.0000; 0.0000; 0.0000;  
K<sub>7</sub><sup>+</sup>: 0.00; 0.20; 0.30; 0.35; 0.0000; 0.0000; 0.0000;  
K<sub>7</sub><sup>-</sup>: 0.00; 0.20; 0.35; 0.40; 0.0000; 0.0000; 0.0000;  
K<sub>8</sub><sup>+</sup>: 0.00; 0.20; 0.40; 0.45; 0.0000; 0.0000; 0.0000;  
K<sub>8</sub><sup>-</sup>: 0.00; 0.20; 0.45; 0.50; 0.0000; 0.0000; 0.0000;  
K<sub>9</sub><sup>+</sup>: 0.00; 0.20; 0.50; 0.55; 0.0000; 0.0000; 0.0000;  
K<sub>9</sub><sup>-</sup>: 0.00; 0.20; 0.55; 0.60; 0.0000; 0.0000; 0.0000;  
K<sub>10</sub><sup>+</sup>: 0.00; 0.20; 0.60; 0.70; 0.0000; 0.0000; 0.0000;  
K<sub>10</sub><sup>-</sup>: 0.00; 0.20; 0.70; 0.80; 0.0000; 0.0000; 0.0000;  
K<sub>11</sub><sup>+</sup>: 0.00; 0.20; 0.80; 0.90; 0.0000; 0.0000; 0.0000;  
K<sub>11</sub><sup>-</sup>: 0.00; 0.20; 0.90; 1.00; 0.0000; 0.0000; 0.0000;  
K<sub>12</sub><sup>+</sup>: 0.00; 0.20; 1.00; 1.10; 0.2674; 0.0015; 0.0278;  
K<sub>12</sub><sup>-</sup>: 0.00; 0.20; 1.10; 1.20; 0.1687; 0.0014; 0.0079;  
K<sub>13</sub><sup>+</sup>: 0.00; 0.20; 1.20; 1.30; 0.0221; 0.0003; 0.0119;  
K<sub>13</sub><sup>-</sup>: 0.00; 0.20; 1.30; 1.40; 0.0991; 0.0008; 0.0072;  
K<sub>14</sub><sup>+</sup>: 0.00; 0.20; 1.40; 1.50; 0.0831; 0.0007; 0.0096;  
K<sub>14</sub><sup>-</sup>: 0.00; 0.20; 1.50; 0.0375; 0.0007; 0.0029;  
K<sub>15</sub><sup>+</sup>: 0.00; 0.20; 1.60; 1.70; 0.0167; 0.0005; 0.0021;  
K<sub>15</sub><sup>-</sup>: 0.00; 0.20; 1.70; 1.80; 0.0133; 0.0003; 0.0024;  
K<sub>16</sub><sup>+</sup>: 0.00; 0.20; 1.80; 1.90; 0.0183; 0.0003; 0.0005;  
K<sub>16</sub><sup>-</sup>: 0.00; 0.20; 1.90; 2.00; 0.0000; 0.0000; 0.0000;  
K<sub>17</sub><sup>+</sup>: 0.20; 0.40; 0.00; 0.05; 0.0000; 0.0000; 0.0000;  
K<sub>17</sub><sup>-</sup>: 0.20; 0.40; 0.05; 0.10; 0.0000; 0.0000; 0.0000;  
K<sub>18</sub><sup>+</sup>: 0.20; 0.40; 0.10; 0.15; 0.0000; 0.0000; 0.0000;  
K<sub>18</sub><sup>-</sup>: 0.20; 0.40; 0.15; 0.20; 0.0000; 0.0000; 0.0000;  
K<sub>19</sub><sup>+</sup>: 0.20; 0.40; 0.20; 0.25; 0.0000; 0.0000; 0.0000;  
K<sub>19</sub><sup>-</sup>: 0.20; 0.40; 0.25; 0.30; 0.0000; 0.0000; 0.0000;  
K<sub>20</sub><sup>+</sup>: 0.20; 0.40; 0.30; 0.35; 0.0000; 0.0000; 0.0000;  
K<sub>20</sub><sup>-</sup>: 0.20; 0.40; 0.35; 0.40; 0.0000; 0.0000; 0.0000;  
K<sub>21</sub><sup>+</sup>: 0.20; 0.40; 0.40; 0.45; 0.0000; 0.0000; 0.0000;  
K<sub>21</sub><sup>-</sup>: 0.20; 0.40; 0.45; 0.50; 0.0000; 0.0000; 0.0000;  
K<sub>22</sub><sup>+</sup>: 0.20; 0.40; 0.50; 0.55; 0.0000; 0.0000; 0.0000;  
K<sub>22</sub><sup>-</sup>: 0.20; 0.40; 0.55; 0.60; 0.0000; 0.0000; 0.0000;  
K<sub>23</sub><sup>+</sup>: 0.20; 0.40; 0.60; 0.70; 0.0000; 0.0000; 0.0000;  
K<sub>23</sub><sup>-</sup>: 0.20; 0.40; 0.70; 0.80; 0.0000; 0.0000; 0.0000;  
K<sub>24</sub><sup>+</sup>: 0.20; 0.40; 0.80; 0.90; 0.3559; 0.0021; 0.0447;  
K<sub>24</sub><sup>-</sup>: 0.20; 0.40; 0.90; 1.00; 0.0776; 0.0017; 0.0358;  
K<sub>25</sub><sup>+</sup>: 0.20; 0.40; 1.00; 1.10; 0.2467; 0.0014; 0.0229;  
K<sub>25</sub><sup>-</sup>: 0.20; 0.40; 1.10; 1.20; 0.1540; 0.0011; 0.0171;  
K<sub>26</sub><sup>+</sup>: 0.20; 0.40; 1.20; 1.30; 0.0293; 0.0010; 0.0071;  
K<sub>26</sub><sup>-</sup>: 0.20; 0.40; 1.30; 1.40; 0.0735; 0.0007; 0.0040;  
K<sub>27</sub><sup>+</sup>: 0.20; 0.40; 1.40; 1.50; 0.0473; 0.0006; 0.0049;  
K<sub>27</sub><sup>-</sup>: 0.20; 0.40; 1.50; 1.60; 0.0234; 0.0004; 0.0020;  
K<sub>28</sub><sup>+</sup>: 0.20; 0.40; 1.60; 1.70; 0.0171; 0.0003; 0.0034;  
K<sub>28</sub><sup>-</sup>: 0.20; 0.40; 1.70; 1.80; 0.0185; 0.0003; 0.0111;  
K<sub>29</sub><sup>+</sup>: 0.20; 0.40; 1.80; 1.90; 0.0108; 0.0002; 0.0131;  
K<sub>29</sub><sup>-</sup>: 0.20; 0.40; 1.90; 2.00; 0.0000; 0.0000; 0.0000;  
K<sub>30</sub><sup>+</sup>: 0.40; 0.60; 0.00; 0.05; 0.0000; 0.0000; 0.0000;  
K<sub>30</sub><sup>-</sup>: 0.40; 0.60; 0.05; 0.10; 0.0000; 0.0000; 0.0000;  
K<sub>31</sub><sup>+</sup>: 0.40; 0.60; 0.10; 0.15; 0.0000; 0.0000; 0.0000;  
K<sub>31</sub><sup>-</sup>: 0.40; 0.60; 0.15; 0.20; 0.0000; 0.0000; 0.0000;  
K<sub>32</sub><sup>+</sup>: 0.40; 0.60; 0.20; 0.25; 0.0000; 0.0000; 0.0000;  
K<sub>32</sub><sup>-</sup>: 0.40; 0.60; 0.25; 0.30; 0.0000; 0.0000; 0.0000;  
K<sub>33</sub><sup>+</sup>: 0.

K<sup>+</sup>:0.60;0.80;0.30;0.35;0.0000;0.0000;0.0019;  
K<sup>+</sup>:0.60;0.80;0.35;0.40;0.0000;0.0000;0.0008;  
K<sup>+</sup>:0.60;0.80;0.40;0.45;1.3542;0.0043;0.1829;  
K<sup>+</sup>:0.60;0.80;0.40;0.45;0.50;1.0070;0.0044;0.1693;  
K<sup>+</sup>:0.60;0.80;0.50;0.55;1.1078;0.0044;0.1181;  
K<sup>+</sup>:0.60;0.80;0.55;0.60;0.9090;0.0033;0.1201;  
K<sup>+</sup>:0.60;0.80;0.60;0.70;0.7468;0.0022;0.0789;  
K<sup>+</sup>:0.60;0.80;0.70;0.80;0.5431;0.0019;0.0595;  
K<sup>+</sup>:0.60;0.80;0.80;0.90;0.0481;0.0020;0.0569;  
K<sup>+</sup>:0.60;0.80;0.90;1.00;0.2681;0.0015;0.0359;  
K<sup>+</sup>:0.60;0.80;1.00;1.0;0.1801;0.0012;0.0197;  
K<sup>+</sup>:0.60;0.80;1.10;1.20;0.1353;0.0009;0.0177;  
K<sup>+</sup>:0.60;0.80;1.20;1.30;0.0732;0.0007;0.0114;  
K<sup>+</sup>:0.60;0.80;1.30;1.40;0.0508;0.0006;0.0084;  
K<sup>+</sup>:0.60;0.80;1.40;1.50;0.0357;0.0004;0.0069;  
K<sup>+</sup>:0.60;0.80;1.50;1.60;0.0190;0.0004;0.0044;  
K<sup>+</sup>:0.60;0.80;1.60;1.70;0.0095;0.0003;0.0030;  
K<sup>+</sup>:0.60;0.80;1.70;1.80;0.0119;0.0002;0.0023;  
K<sup>+</sup>:0.60;0.80;1.80;1.90;0.0000;0.0000;0.0000;  
K<sup>+</sup>:0.60;1.00;0.00;0.05;0.0000;0.0000;0.0000;  
K<sup>+</sup>:0.60;1.00;0.05;0.10;0.0000;0.0000;0.0000;  
K<sup>+</sup>:0.60;1.00;0.10;0.15;0.0000;0.0000;0.0019;  
K<sup>+</sup>:0.60;1.00;0.15;0.20;0.0000;0.0000;0.0000;  
K<sup>+</sup>:0.60;1.00;0.20;0.25;0.0507;0.0035;0.0256;  
K<sup>+</sup>:0.60;1.00;0.25;0.30;1.0520;0.039;0.0243;  
K<sup>+</sup>:0.60;1.00;0.30;0.35;1.1571;0.037;0.0223;  
K<sup>+</sup>:0.60;1.00;0.35;0.40;1.0851;0.039;0.0204;  
K<sup>+</sup>:0.60;1.00;0.40;0.45;0.9616;0.037;0.0277;  
K<sup>+</sup>:0.60;1.00;0.50;0.55;0.8420;0.033;0.0262;  
K<sup>+</sup>:0.60;1.00;0.55;0.60;0.7513;0.030;0.0666;  
K<sup>+</sup>:0.60;1.00;0.60;0.70;0.5818;0.020;0.0575;  
K<sup>+</sup>:0.60;1.00;0.70;0.80;0.3987;0.017;0.0412;  
K<sup>+</sup>:0.60;1.00;0.80;0.90;0.2767;0.015;0.0379;  
K<sup>+</sup>:0.60;1.00;0.90;1.00;0.1926;0.011;0.0245;  
K<sup>+</sup>:0.60;1.00;1.00;1.0;0.1601;0.008;0.0233;  
K<sup>+</sup>:0.60;1.00;1.10;1.20;0.0763;0.008;0.0104;  
K<sup>+</sup>:0.60;1.00;1.20;1.30;0.0544;0.006;0.0088;  
K<sup>+</sup>:0.60;1.00;1.30;1.40;0.0311;0.005;0.0045;  
K<sup>+</sup>:0.60;1.00;1.40;1.50;0.0224;0.004;0.0040;  
K<sup>+</sup>:0.60;1.00;1.50;1.60;0.0175;0.003;0.0048;  
K<sup>+</sup>:0.60;1.00;1.60;1.70;0.0000;0.0000;0.0000;  
K<sup>+</sup>:0.60;1.00;1.70;1.80;0.0054;0.0002;0.0012;  
K<sup>+</sup>:0.60;1.00;1.80;1.90;0.0000;0.0000;0.0000;  
K<sup>+</sup>:0.60;1.00;1.90;2.00;0.0000;0.0000;0.0000;  
K<sup>+</sup>:1.00;1.20;0.00;0.05;0.1101;0.012;0.0087;  
K<sup>+</sup>:1.00;1.20;0.05;0.10;0.3385;0.018;0.0032;  
K<sup>+</sup>:1.00;1.20;0.10;0.15;0.5431;0.023;0.0031;  
K<sup>+</sup>:1.00;1.20;0.15;0.20;0.7373;0.028;0.0081;  
K<sup>+</sup>:1.00;1.20;0.20;0.25;0.7077;0.031;0.0048;  
K<sup>+</sup>:1.00;1.20;0.25;0.30;0.8281;0.033;0.0130;  
K<sup>+</sup>:1.00;1.20;0.30;0.35;0.9288;0.030;0.0208;  
K<sup>+</sup>:1.00;1.20;0.35;0.40;0.8272;0.034;0.0184;  
K<sup>+</sup>:1.00;1.20;0.40;0.45;0.8234;0.031;0.0214;  
K<sup>+</sup>:1.00;1.20;0.45;0.50;0.6770;0.027;0.0388;  
K<sup>+</sup>:1.00;1.20;0.50;0.55;0.6489;0.033;0.0261;  
K<sup>+</sup>:1.00;1.20;0.55;0.60;0.5365;0.030;0.0229;  
K<sup>+</sup>:1.00;1.20;0.60;0.70;0.4341;0.016;0.0277;  
K<sup>+</sup>:1.00;1.20;0.70;0.80;0.3256;0.013;0.0276;  
K<sup>+</sup>:1.00;1.20;0.80;0.90;0.2101;0.012;0.0231;  
K<sup>+</sup>:1.00;1.20;0.90;1.00;0.1328;0.009;0.0143;  
K<sup>+</sup>:1.00;1.20;1.00;1.0;0.0731;0.008;0.0093;  
K<sup>+</sup>:1.00;1.20;1.10;1.20;0.0577;0.006;0.0071;  
K<sup>+</sup>:1.00;1.20;1.20;1.30;0.0293;0.005;0.0055;  
K<sup>+</sup>:1.00;1.20;1.30;1.40;0.0218;0.004;0.0024;  
K<sup>+</sup>:1.00;1.20;1.40;1.50;0.0000;0.0000;0.0000;  
K<sup>+</sup>:1.00;1.20;1.50;1.60;0.0025;0.0002;0.0007;  
K<sup>+</sup>:1.00;1.20;1.60;1.70;0.0012;0.0001;0.0003;  
K<sup>+</sup>:1.00;1.20;1.70;1.80;0.0000;0.0000;0.0000;  
K<sup>+</sup>:1.00;1.20;1.80;1.90;0.0000;0.0000;0.0000;  
K<sup>+</sup>:1.00;1.20;1.90;2.00;0.0000;0.0000;0.0000;  
K<sup>+</sup>:1.20;1.40;0.00;0.05;0.0707;0.010;0.0008;  
K<sup>+</sup>:1.20;1.40;0.05;0.10;0.2320;0.016;0.0019;  
K<sup>+</sup>:1.20;1.40;0.10;0.15;0.4342;0.022;0.0082;  
K<sup>+</sup>:1.20;1.40;0.15;0.20;0.4896;0.023;0.0124;  
K<sup>+</sup>:1.20;1.40;0.20;0.25;0.6094;0.027;0.0152;  
K<sup>+</sup>:1.20;1.40;0.25;0.30;0.5885;0.024;0.0150;  
K<sup>+</sup>:1.20;1.40;0.30;0.35;0.5767;0.029;0.0122;  
K<sup>+</sup>:1.20;1.40;0.35;0.40;0.5503;0.026;0.0262;  
K<sup>+</sup>:1.20;1.40;0.40;0.45;0.5303;0.027;0.0099;  
K<sup>+</sup>:1.20;1.40;0.45;0.50;0.5445;0.023;0.0232;  
K<sup>+</sup>:1.20;1.40;0.50;0.55;0.3690;0.023;0.0086;  
K<sup>+</sup>:1.20;1.40;0.55;0.60;0.3841;0.023;0.0139;  
K<sup>+</sup>:1.20;1.40;0.60;0.70;0.2755;0.012;0

K-1;1.20;1.40;1.30;1.40.0093;0.0002;0.0012;  
K-1;1.20;1.40;1.40;1.50;0.0058;0.0002;0.002;  
K-1;1.20;1.40;1.50;1.60.0026;0.0001;0.0005;  
K-1;1.20;1.40;1.60;1.70;0.0000;0.0000;0.0000;  
K-1;1.20;1.40;1.70;1.80;0.0000;0.0000;0.0000;  
K-1;1.20;1.40;1.80;1.90;0.0000;0.0000;0.0000;  
K-1;1.20;1.40;1.90;2.00;0.0000;0.0000;0.0000;  
K-1;1.40;1.60;0.00;0.05.0.0692;0.0010;0.0053;  
K-1;1.40;1.60;0.05;0.10.0.1853;0.0013;0.0130;  
K-1;1.40;1.60;0.10;0.15;0.2609;0.0018;0.0061;  
K-1;1.40;1.60;0.15;0.20;0.3151;0.0023;0.0077;  
K-1;1.40;1.60;0.20;0.25;0.3702;0.0023;0.0119;  
K-1;1.40;1.60;0.25;0.30.0.4038;0.0021;0.0114;  
K-1;1.40;1.60;0.30;0.35;0.4363;0.0023;0.0181;  
K-1;1.40;1.60;0.35;0.40.0.3584;0.0022;0.0134;  
K-1;1.40;1.60;0.40;0.45;0.3454;0.0019;0.0077;  
K-1;1.40;1.60;0.45;0.50.0.2866;0.0018;0.0090;  
K-1;1.40;1.60;0.50;0.55;0.2662;0.0020;0.0077;  
K-1;1.40;1.60;0.55;0.60.0.1692;0.0017;0.0040;  
K-1;1.40;1.60;0.60;0.70.0.1698;0.0100;0.0060;  
K-1;1.40;1.60;0.70;0.80.0.1110;0.0008;0.0038;  
K-1;1.40;1.60;0.80;0.90.0.0759;0.0007;0.0030;  
K-1;1.40;1.60;0.90;1.00;0.0338;0.0005;0.0012;  
K-1;1.40;1.60;1.00;1.10.0.0244;0.0004;0.0018;  
K-1;1.40;1.60;1.10;1.20.0.0008;0.0003;0.0005;  
K-1;1.40;1.60;1.20;1.30.0.0094;0.0002;0.0012;  
K-1;1.40;1.60;1.30;1.40.0.0015;0.0001;0.0002;  
K-1;1.40;1.60;1.40;1.50;0.0000;0.0000;0.0000;  
K-1;1.40;1.60;1.50;1.60.0.0000;0.0000;0.0000;  
K-1;1.40;1.60;1.60;1.70;0.0000;0.0000;0.0000;  
K-1;1.40;1.60;1.70;1.80;0.0000;0.0000;0.0000;  
K-1;1.40;1.60;1.80;1.90;0.0000;0.0000;0.0000;  
K-1;1.40;1.60;1.90;2.00;0.0000;0.0000;0.0000;  
K-1;1.60;1.80;0.00;0.05.0.0283;0.0006;0.0108;  
K-1;1.60;1.80;0.05;0.10.0.1953;0.0013;0.0164;  
K-1;1.60;1.80;0.10;0.15.0.1784;0.0016;0.0096;  
K-1;1.60;1.80;0.15;0.20.0.2098;0.0018;0.0176;  
K-1;1.60;1.80;0.20;0.25;0.2154;0.0018;0.0180;  
K-1;1.60;1.80;0.25;0.30.0.2800;0.0019;0.0158;  
K-1;1.60;1.80;0.30;0.35.0.2986;0.0018;0.0122;  
K-1;1.60;1.80;0.35;0.40.0.1196;0.0015;0.0091;  
K-1;1.60;1.80;0.40;0.45;0.1663;0.0016;0.0054;  
K-1;1.60;1.80;0.45;0.50.0.1766;0.0012;0.0050;  
K-1;1.60;1.80;0.50;0.55.0.1285;0.0015;0.0037;  
K-1;1.60;1.80;0.55;0.60.0.1051;0.0013;0.0044;  
K-1;1.60;1.80;0.60;0.70.0.0789;0.0008;0.0036;  
K-1;1.60;1.80;0.70;0.80.0.0482;0.0006;0.0011;  
K-1;1.60;1.80;0.80;0.90.0.0256;0.0005;0.0020;  
K-1;1.60;1.80;0.90;1.00;0.0137;0.0003;0.0003;  
K-1;1.60;1.80;1.00;1.10.0.0000;0.0000;0.0000;  
K-1;1.60;1.80;1.10;1.20.0.0000;0.0000;0.0000;  
K-1;1.60;1.80;1.20;1.30.0.0043;0.0001;0.0008;  
K-1;1.60;1.80;1.30;1.40.0.0000;0.0000;0.0000;  
K-1;1.60;1.80;1.40;1.50;0.0000;0.0000;0.0000;  
K-1;1.60;1.80;1.50;1.60.0.0000;0.0000;0.0000;  
K-1;1.60;1.80;1.60;1.70;0.0000;0.0000;0.0000;  
K-1;1.60;1.80;1.70;1.80;0.0000;0.0000;0.0000;  
K-1;1.60;1.80;1.80;1.90;0.0000;0.0000;0.0000;  
K-1;1.60;1.80;1.90;2.00;0.0000;0.0000;0.0000;  
K-1;1.80;2.00;0.00;0.05.0.0000;0.0000;0.0000;  
K-1;1.80;2.00;0.05;0.10.0.0000;0.0000;0.0000;  
K-1;1.80;2.00;0.10;0.15.0.0933;0.0015;0.0105;  
K-1;1.80;2.00;0.15;0.20.0.1112;0.0012;0.0127;  
K-1;1.80;2.00;0.20;0.25.0.1157;0.0013;0.0129;  
K-1;1.80;2.00;0.25;0.30.0.1166;0.0013;0.0107;  
K-1;1.80;2.00;0.30;0.35.0.1485;0.0013;0.0037;  
K-1;1.80;2.00;0.35;0.40.0.1232;0.0013;0.0157;  
K-1;1.80;2.00;0.40;0.45.0.0724;0.0010;0.0051;  
K-1;1.80;2.00;0.45;0.50.0.0000;0.0000;0.0000;  
K-1;1.80;2.00;0.50;0.55;0.0072;0.0009;0.0068;  
K-1;1.80;2.00;0.55;0.60.0.0620;0.0009;0.0255;  
K-1;1.80;2.00;0.60;0.70.0.0406;0.0006;0.0012;  
K-1;1.80;2.00;0.70;0.80.0.0111;0.0004;0.0003;  
K-1;1.80;2.00;0.80;0.90.0.0000;0.0000;0.0000;  
K-1;1.80;2.00;0.90;1.00.0.0009;0.0001;0.0002;  
K-1;1.80;2.00;1.00;1.10.0.0000;0.0000;0.0000;  
K-1;1.80;2.00;1.10;1.20.0.0006;0.0001;0.0000;  
K-1;1.80;2.00;1.20;1.30.0.0000;0.0000;0.0000;  
K-1;1.80;2.00;1.30;1.40.0.0000;0.0000;0.0000;  
K-1;1.80;2.00;1.40;1.50.0.0000;0.0000;0.0000;  
K-1;1.80;2.00;1.50;1.60.0.0000;0.0000;0.0000;  
K-1;1.80;2.00;1.60;1.70;0.0000;0.0000;0.0000;  
K-1;1.80;2.00;1.70;1.80;0.0000;0.0000;0.0000;  
K-1;1.80;2.00;1.80;1.90;0.0000;0.0000;0.0000;  
K-1;1.80;2.00;1.90;2.00.0.0000;0.0000;0.0000;  
K-1;2.00;2.20;0.00;0.05.0.0000;0.0000;0.0000;  
K-1;2.00;2.20;0.05;0.10.0.0000;0.0000;0.0000;  
K-1;2.00;2.

```
K-1: -2.00; 2.00; 30.00; 0.35; 0.0576; 0.0008; 0.0081;
K-1: -2.00; 2.00; 2.00; 35.00; 0.40; 0.0412; 0.0009; 0.0023;
K-1: -2.00; 2.00; 2.00; 40.00; 0.45; 0.0282; 0.0008; 0.0017;
K-1: -2.00; 2.00; 2.00; 45.00; 0.50; 0.0211; 0.0006; 0.0033;
K-1: -2.00; 2.00; 2.00; 50.00; 0.55; 0.0237; 0.0006; 0.0021;
K-1: -2.00; 2.00; 2.00; 55.00; 0.60; 0.0000; 0.0000; 0.0000;
K-1: -2.00; 2.00; 2.00; 60.00; 0.70; 0.0027; 0.0003; 0.0005;
K-1: -2.00; 2.00; 2.00; 70.00; 0.80; 0.0054; 0.0002; 0.0008;
K-1: -2.00; 2.00; 2.00; 80.00; 0.90; 0.0000; 0.0000; 0.0000;
K-1: -2.00; 2.00; 2.00; 90.00; 1.00; 0.0000; 0.0000; 0.0000;
K-1: -2.00; 2.00; 2.01; 0.00; 1.10; 0.0000; 0.0000; 0.0000;
K-1: -2.00; 2.00; 2.01; 1.0; 1.20; 0.0000; 0.0000; 0.0000;
K-1: -2.00; 2.00; 2.01; 2.0; 1.30; 0.0000; 0.0000; 0.0000;
K-1: -2.00; 2.00; 2.01; 3.0; 1.40; 0.0000; 0.0000; 0.0000;
K-1: -2.00; 2.00; 2.01; 4.0; 1.50; 0.0000; 0.0000; 0.0000;
K-1: -2.00; 2.00; 2.01; 5.0; 1.60; 0.0000; 0.0000; 0.0000;
K-1: -2.00; 2.00; 2.01; 6.0; 1.70; 0.0000; 0.0000; 0.0000;
K-1: -2.00; 2.00; 2.01; 7.0; 1.80; 0.0000; 0.0000; 0.0000;
K-1: -2.00; 2.00; 2.01; 8.0; 1.90; 0.0000; 0.0000; 0.0000;
K-1: -2.00; 2.00; 2.01; 9.0; 2.00; 0.0000; 0.0000; 0.0000;
```

## Kaons at 40A GeV/c

s;ymín;ymx;pTmín;pTmx;dn/dypT;errstat;errsys;

```

species;ymín;ymax;pTmín;pTmax;dn/dydpT;errstat;errsys;
K^{+};-0.20;0.00;0.00;0.05;0.0000;0.0000;0.0000;
K^{+};-0.20;0.00;0.05;0.10;0.0000;0.0000;0.0000;
K^{+};-0.20;0.00;0.10;0.15;0.0000;0.0000;0.0000;
K^{+};-0.20;0.00;0.15;0.20;0.0000;0.0000;0.0000;
K^{+};-0.20;0.00;0.20;0.25;0.0000;0.0000;0.0000;
K^{+};-0.20;0.00;0.25;0.30;0.0000;0.0000;0.0000;
K^{+};-0.20;0.00;0.30;0.35;0.0000;0.0000;0.0000;
K^{+};-0.20;0.00;0.35;0.40;0.0000;0.0000;0.0000;
K^{+};-0.20;0.00;0.40;0.45;0.0000;0.0000;0.0000;
K^{+};-0.20;0.00;0.45;0.50;0.0000;0.0000;0.0000;
K^{+};-0.20;0.00;0.50;0.55;0.0000;0.0000;0.0000;
K^{+};-0.20;0.00;0.55;0.60;0.0000;0.0000;0.0000;
K^{+};-0.20;0.00;0.60;0.70;0.0000;0.0000;0.0000;
K^{+};-0.20;0.00;0.70;0.80;0.0000;0.0000;0.0000;
K^{+};-0.20;0.00;0.80;0.90;0.0000;0.0000;0.0000;
K^{+};-0.20;0.00;0.90;1.00;0.0000;0.0000;0.0000;
K^{+};-0.20;0.00;1.00;1.10;0.0000;0.0000;0.0000;
K^{+};-0.20;0.00;1.10;1.20;0.0094;0.0094;0.0757;
K^{+};-0.20;0.00;1.20;1.30;0.2260;0.0190;0.0983;
K^{+};-0.20;0.00;1.30;1.40;0.2745;0.0138;0.0548;
K^{+};-0.20;0.00;1.40;1.50;0.1941;0.0059;0.0317;
K^{+};-0.20;0.00;1.50;1.60;0.1202;0.0089;0.0243;
K^{+};-0.20;0.00;1.60;1.70;0.0898;0.0070;0.0221;
K^{+};-0.20;0.00;1.70;1.80;0.0585;0.0027;0.0132;
K^{+};-0.20;0.00;1.80;1.90;0.0476;0.0024;0.0104;
K^{+};-0.20;0.00;1.90;2.00;0.0000;0.0000;0.0000;
K^{+};0.00;0.20;0.00;0.05;0.0000;0.0000;0.0000;
K^{+};0.00;0.20;0.05;0.10;0.0000;0.0000;0.0000;
K^{+};0.00;0.20;0.10;0.15;0.0000;0.0000;0.0000;
K^{+};0.00;0.20;0.15;0.20;0.0000;0.0000;0.0000;
K^{+};0.00;0.20;0.20;0.25;0.0000;0.0000;0.0000;
K^{+};0.00;0.20;0.25;0.30;0.0000;0.0000;0.0000;
K^{+};0.00;0.20;0.30;0.35;0.0000;0.0000;0.0000;
K^{+};0.00;0.20;0.35;0.40;0.0000;0.0000;0.0000;
K^{+};0.00;0.20;0.40;0.45;0.0000;0.0000;0.0000;
K^{+};0.00;0.20;0.45;0.50;0.0000;0.0000;0.0000;
K^{+};0.00;0.20;0.50;0.55;0.0000;0.0000;0.0000;
K^{+};0.00;0.20;0.55;0.60;0.0000;0.0000;0.0000;
K^{+};0.00;0.20;0.60;0.70;0.0000;0.0000;0.0000;
K^{+};0.00;0.20;0.70;0.80;0.0000;0.0000;0.0000;
K^{+};0.00;0.20;0.80;0.90;0.0000;0.0000;0.0000;
K^{+};0.00;0.20;0.90;1.00;0.9544;0.0116;0.1171;
K^{+};0.00;0.20;1.00;1.10;0.6753;0.0093;0.0937;
K^{+};0.00;0.20;1.10;1.20;0.5071;0.0083;0.0563;
K^{+};0.00;0.20;1.20;1.30;0.3494;0.0062;0.0433;
K^{+};0.00;0.20;1.30;1.40;0.2794;0.0054;0.0281;
K^{+};0.00;0.20;1.40;1.50;0.1930;0.0047;0.0246;
K^{+};0.00;0.20;1.50;1.60;0.1221;0.0070;0.0204;
K^{+};0.00;0.20;1.60;1.70;0.1108;0.0059;0.0151;
K^{+};0.00;0.20;1.70;1.80;0.0864;0.0025;0.0106;
K^{+};0.00;0.20;1.80;1.90;0.0462;0.0025;0.0095;
K^{+};0.00;0.20;1.90;2.00;0.0000;0.0000;0.0000;
K^{+};0.20;0.40;0.00;0.05;0.0000;0.0000;0.0000;
K^{+};0.20;0.40;0.05;0.10;0.0000;0.0000;0.0000;
K^{+};0.20;0.40;0.10;0.15;0.0000;0.0000;0.0000;
K^{+};0.20;0.40;0.15;0.20;0.0000;0.0000;0.0000;
K^{+};0.20;0.40;0.20;0.25;0.0000;0.0000;0.0000;
K^{+};0.20;0.40;0.25;0.30;0.0000;0.0000;0.0000;
K^{+};0.20;0.40;0.30;0.35;0.0000;0.0000;0.0000;
K^{+};0.20;0.40;0.35;0.40;0.0000;0.0000;0.0000;
K^{+};0.20;0.40;0.40;0.45;0.0000;0.0000;0.0000;
K^{+};0.20;0.40;0.45;0.50;0.0000;0.0000;0.0000;
K^{+};0.20;0.40;0.50;0.55;0.0000;0.0000;0.0000;
K^{+};0.20;0.40;0.55;0.60;0.0000;0.0000;0.0000;
K^{+};0.20;0.40;0.60;0.70;0.0000;0.0000;0.0000;
K^{+};0.20;0.40;0.70;0.80;1.9675;0.0119;0.1701;
K^{+};0.20;0.40;0.80;0.90;1.4651;0.0085;0.1314;
K^{+};0.20;0.40;0.90;1.00;1.1324;0.0106;0.0889;
K^{+};0.20;0.40;1.00;1.10;0.8399;0.0088;0.0724;
K^{+};0.20;0.40;1.10;1.20;0.5954;0.0061;0.0455;
K^{+};0.20;0.40;1.20;1.30;0.3477;0.0044;0.0250;
K^{+};0.20;0.40;1.30;1.40;0.3197;0.0060;0.0255;
K^{+};0.20;0.40;1.40;1.50;0.2001;0.0047;0.0163;
K^{+};0.20;0.40;1.50;1.60;0.1231;0.0044;0.0125;
K^{+};0.20;0.40;1.60;1.70;0.1362;0.0035;0.0126;
K^{+};0.20;0.40;1.70;1.80;0.0594;0.0019;0.0051;
K^{+};0.20;0.40;1.80;1.90;0.0423;0.0028;0.0060;
K^{+};0.20;0.40;1.90;2.00;0.0000;0.0000;0.0000;
K^{+};0.40;0.60;0.00;0.05;0.0000;0.0000;0.0000;
K^{+};0.40;0.60;0.05;0.10;0.0000;0.0000;0.0000;
K^{+};0.40;0.60;0.10;0.15;0.0000;0.0000;0.0000;
K^{+};0.40;0.60;0.15;0.20;0.0000;0.0000;0.0000;
K^{+};0.40;0.60;0.20;0.25;0.0000;0.0000;0.0000;
K^{+};0.40;0.60;0.25;0.30;0.0000;0.0000;0.0000;
K^{+};0.40;0.60;0.30;0.35;0.0000;0.0000;0.0000;
K^{+};0.40;0.60;0.35;0.40;0.0000;0.0000;0.0000;
K^{+};0.40;0.60;0.40;0.45;0.0000;0.0000;0.0000;
K^{+};0.40;0.60;0.45;0.50;3.5876;0.0202;0.3583;
K^{+};0.40;0.60;0.50;0.55;3.5254;0.0292;0.3233;
K^{+};0.40;0.60;0.55;0.60;3.2297;0.0250;0.2827;
K^{+};0.40;0.60;0.60;0.70;2.7182;0.0126;0.2384;
K^{+};0.40;0.60;0.70;0.80;2.0225;0.0113;0.1673;
K^{+};0.40;0.60;0.80;0.90;1.5466;0.0092;0.1300;
K^{+};0.40;0.60;0.90;1.00;1.1414;0.0091;0.0851;
K^{+};0.40;0.60;1.00;1.10;0.8439;0.0071;0.0774;
K^{+};0.40;0.60;1.10;1.20;0.5597;0.0060;0.0458;
K^{+};0.40;0.60;1.20;1.30;0.4009;0.0050;0.0310;
K^{+};0.40;0.60;1.30;1.40;0.2489;0.0048;0.0262;
K^{+};0.40;0.60;1.40;1.50;0.1759;0.0049;0.0170;
K^{+};0.40;0.60;1.50;1.60;0.1195;0.0031;0.0103;
K^{+};0.40;0.60;1.60;1.70;0.0816;0.0024;0.0079;
K^{+};0.40;0.60;1.70;1.80;0.0597;0.0018;0.0030;
K^{+};0.40;0.60;1.80;1.90;0.0313;0.0020;0.0065;
K^{+};0.40;0.60;1.90;2.00;0.0000;0.0000;0.0000;
K^{+};0.60;0.80;0.00;0.05;0.0000;0.0000;0.0000;
K^{+};0.60;0.80;0.05;0.10;0.0000;0.0000;0.0000;
K^{+};0.60;0.80;0.10;0.15;0.0000;0.0000;0.0000;
K^{+};0.60;0.80;0.15;0.20;0.0000;0.0000;0.0000;
K^{+};0.60;0.80;0.20;0.25;0.0000;0.0000;0.0000;
K^{+};0.60;0.80;0.25;0.30;3.3972;0.0172;0.1476;
K^{+};0.60;0.80;0.30;0.35;3.5857;0.0214;0.1906;
K^{+};0.60;0.80;0.35;0.40;3.7050;0.0228;0.3041;
K^{+};0.60;0.80;0.40;0.45;3.6388;0.0192;0.4211;
K^{+};0.60;0.80;0.45;0.50;3.8073;0.0189;0.3599;
K^{+};0.60;0.80;0.50;0.55;3.3632;0.0177;0.3016;
K^{+};0.60;0.80;0.55;0.60;3.0937;0.0165;0.2759;
K^{+};0.60;0.80;0.60;0.70;2.5503;0.0112;0.2146;
K^{+};0.60;0.80;0.70;0.80;1.9539;0.0075;0.1799;
K^{+};0.60;0.80;0.80;0.90;1.3655;0.0088;0.1357;
K^{+};0.60;0.80;0.90;1.00;1.1033;0.0069;0.1016;
K^{+};0.60;0.80;1.00;1.10;0.7035;0.0067;0.0782;
K^{+};0.60;0.80;1.10;1.20;0.5231;0.0053;0.0552;
K^{+};0.60;0.80;1.20;1.30;0.3297;0.0052;0.0371;
K^{+};0.60;0.80;1.30;1.40;0.2032;0.0028;0.0247;
K^{+};0.60;0.80;1.40;1.50;0.1649;0.0034;0.0230;
K^{+};0.60;0.80;1.50;1.60;0.1005;0.0028;0.0114;
K^{+};0.60;0.80;1.60;1.70;0.0739;0.0021;0.0061;
K^{+};0.60;0.80;1.70;1.80;0.0332;0.0013;0.0032;
K^{+};0.60;0.80;1.80;1.90;0.0220;0.0011;0.0017;
K^{+};0.60;0.80;1.90;2.00;0.0000;0.0000;0.0000;
K^{+};0.80;1.00;0.00;0.05;0.0000;0.0000;0.0000;
K^{+};0.80;1.00;0.05;0.10;1.378;0.0109;0.0587;
K^{+};0.80;1.00;0.10;0.15;1.980;0.0128;0.0868;
K^{+};0.80;1.00;0.15;0.20;2.681;0.0136;0.1098;
K^{+};0.80;1.00;0.20;0.25;3.2146;0.0140;0.1288;
K^{+};0.80;1.00;0.25;0.30;3.5994;0.0134;0.1380;
K^{+};0.80;1.00;0.30;0.35;3.4852;0.0144;0.1323;
K^{+};0.80;1.00;0.35;0.40;3.5731;0.0131;0.1304;
K^{+};0.80;1.00;0.40;0.45;3.3652;0.0140;0.1181;
K^{+};0.80;1.00;0.45;0.50;3.2006;0.0134;0.1464;
K^{+};0.80;1.00;0.50;0.55;2.8045;0.0119;0.1881;
K^{+};0.80;1.00;0.55;0.60;2.7278;0.0117;0.1885;
K^{+};0.80;1.00;0.60;0.70;2.3083;0.0071;0.1817;
K^{+};0.80;1.00;0.70;0.80;1.7403;0.0068;0.1593;
K^{+};0.80;1.00;0.80;0.90;1.2320;0.0068;0.1301;
K^{+};0.80;1.00;0.90;1.00;0.8539;0.0057;0.0870;
K^{+};0.80;1.00;1.00;0.20;2.53;2.146;0.0140;0.1288;
K^{+};0.80;1.00;1.00;1.00;1.10;0.5969;0.0045;0.0726;
K^{+};0.80;1.00;1.00;1.10;1.10;0.3829;0.0042;0.0478;
K^{+};0.80;1.00;1.00;1.20;1.30;0.2591;0.0029;0.0333;
K^{+};0.80;1.00;1.00;1.30;1.40;0.2003;0.0022;0.0232;
K^{+};0.80;1.00;1.00;1.40;1.50;0.0958;0.0024;0.0123;
K^{+};0.80;1.00;1.00;1.50;1.60;0.0782;0.0016;0.0117;
K^{+};0.80;1.00;1.00;1.60;1.70;0.0510;0.0012;0.0033;
K^{+};0.80;1.00;1.00;1.70;1.80;0.0324;0.0015;0.0035;
K^{+};0.80;1.00;1.00;1.80;1.90;0.0250;0.0008;0.0049;
K^{+};0.80;1.00;1.00;1.90;2.00;0.0000;0.0000;0.0000;
K^{+};1.00;1.20;0.00;0.05;0.0000;0.0000;0.0000;
K^{+};1.00;1.20;0.05;0.10;0.0691;0.0059;0.0488;
K^{+};1.00;1.20;0.10;0.15;1.7062;0.0080;0.0771;
K^{+};1.00;1.20;0.15;0.20;2.1983;0.0093;0.0891;
K^{+};1.00;1.20;0.20;0.25;2.8448;0.0108;0.1153;
K^{+};1.00;1.20;0.25;0.30;2.9256;0.0099;0.1136;
K^{+};1.00;1.20;0.30;0.35;3.0219;0.0095;0.1169;
K^{+};1.00;1.20;0.35;0.40;3.0565;0.0118;0.1145;
K^{+};1.00;1.20;0.40;0.45;3.0140;0.0119;0.1044;
K^{+};1.00;1.20;0.45;0.50;3.0417;0.0112;0.1163;
K^{+};1.00;1.20;0.50;0.55;2.7854;0.0108;0.0919;
K^{+};1.00;1.20;0.55;0.60;2.3333;0.0092;0.0878;
K^{+};1.00;1.20;0.60;0.70;1.9178;0.0071;0.0685;
K^{+};1.00;1.20;0.70;0.80;1.4698;0.0067;0.0597;
K^{+};1.00;1.20;0.80;0.90;0.9515;0.0052;0.0445;
K^{+};1.00;1.20;0.90;1.00;0.6967;0.0042;0.0374;
K^{+};1.00;1.20;1.00;1.10;0.5174;0.0037;0.0369;
K^{+};1.00;1.20;1.10;1.20;0.2832;0.0032;0.0204;
K^{+};1.00;1.20;1.20;1.30;0.1900;0.0027;0.0152;
K^{+};1.00;1.20;1.30;1.40;0.1020;0.0023;0.0073;
K^{+};1.00;1.20;1.40;1.50;0.0873;0.0016;0.0066;
K^{+};1.00;1.20;1.50;1.60;0.0485;0.0016;0.0048;
K^{+};1.00;1.20;1.60;1.70;0.0275;0.0013;0.0018;
K^{+};1.00;1.20;1.70;1.80;0.0280;0.0013;0.0037;
K^{+};1.00;1.20;1.80;1.90;0.0070;0.0010;0.0008;
K^{+};1.00;1.20;1.90;2.00;0.0000;0.0000;0.0000;
K^{+};1.20;1.40;0.00;0.05;0.0000;0.0000;0.0000;
K^{+};1.20;1.40;0.05;0.10;0.9560;0.0053;0.0405;
K^{+};1.20;1.40;0.10;0.15;1.4060;0.0070;0.0616;
K^{+};1.20;1.40;0.15;0.20;1.8933;0.0076;0.0875;
K^{+};1.20;1.40;0.20;0.25;2.0756;0.0096;0.0879;
K^{+};1.20;1.40;0.25;0.30;2.4696;0.0094;0.1005;
K^{+};1.20;1.40;0.30;0.35;2.4230;0.0086;0.0995;
K^{+};1.20;1.40;0.35;0.40;2.5657;0.0094;0.1010;
K^{+};1.20;1.40;0.40;0.45;2.4475;0.0099;0.0987;
K^{+};1.20;1.40;0.45;0.50;2.1769;0.0099;0.0896;
K^{+};1.20;1.40;0.50;0.55;1.324;0.0102;0.0862;
K^{+};1.20;1.40;0.55;0.60;1.8794;0.0081;0.0846;
K^{+};1.20;1.40;0.60;0.70;1.5235;0.0069;0.0645;
K^{+};1.20;1.40;0.70;0.80;1.0566;0.0062;0.0455;
K^{+};1.20;1.40;0.80;0.90;0.8111;0.0048;0.0376;
K^{+};1.20;1.40;0.90;1.00;0.5041;0.0048;0.0291;
K^{+};1.20;1.40;1.00;1.10;0.3337;0.0037;0.0182;
K^{+};1.20;1.40;1.10;1.20;0.3008;0.0035;0.0108;
K^{+};1.20;1.40;1.20;1.30;0.1321;0.0026;0.0159;
K^{+};1.20;1.40;1.30;1.40;0.0765;0.0019;0.0051;
K^{+};1.20;1.40;1.40;1.50;0.0641;0.0016;0.0049;
K^{+};1.20;1.40;1.50;1.60;0.0337;0.0015;0.0047;
K^{+};1.20;1.40;1.60;1.70;0.0268;0.0010;0.0044;
K^{+};1.20;1.40;1.70;1.80;0.0000;0.0000;0.0000;
K^{+};1.20;1.40;1.80;1.90;0.0000;0.0000;0.0000;
K^{+};1.20;1.40;1.90;2.00;0.0000;0.0000;0.0000;
K^{+};1.40;1.60;0.00;0.05;0.0000;0.0000;0.0000;
K^{+};1.40;1.60;0.05;0.10;0.7813;0.0059;0.0338;
K^{+};1.40;1.60;0.10;0.15;1.2668;0.0074;0.0537;
K^{+};1.40;1.60;0.15;0.20;1.5064;0.0073;0.0684;
K^{+};1.40;1.60;0.20;0.25;1.7391;0.0085;0.0694;
K^{+};1.40;1.60;0.25;0.30;1.9155;0.0091;0.0742;
K^{+};1.40;1.60;0.30;0.35;2.0279;0.0098;0.0897;
K^{+};1.40;1.60;0.35;0.40;1.8941;0.0083;0.0864;
K^{+};1.40;1.60;0.40;0.45;1.8800;0.0083;0.0833;
K^{+};1.40;1.60;0.45;0.50;1.6566;0.0097;0.0837;
K^{+};1.40;1.60;0.50;0.55;1.4816;0.0092;0.0758;
K^{+};1.40;1.60;0.55;0.60;1.3087;0.0085;0.0605;
K^{+};1.40;1.60;0.60;0.70;1.0648;0.0054;0.0519;
K^{+};1.40;1.60;0.70;0.80;0.7594;0.0054;0.0363;
K^{+};1.40;1.60;0.80;0.90;0.5048;0.0040;0.0294;
K^{+};1.40;1.60;0.90;1.00;0.2967;0.0036;0.0196;
K^{+};1.40;1.60;1.00;1.10;0.2192;0.0032;0.0115;
K^{+};1.40;1.60;1.10;1.20;0.1702;0.0029;0.0122;
K^{+};1.40;1.60;1.20;1.30;0.0779;0.0024;0.0084;
K^{+};1.40;1.60;1.30;1.40;0.0388;0.0020;0.0032;
K^{+};1.40;1.60;1.40;1.50;0.0216;0.0012;0.0089;
K^{+};1.40;1.60;1.50;1.60;0.0070;0.0008;0.0024;
K^{+};1.40;1.60;1.60;1.70;0.0000;0.0000;0.0000;
K^{+};1.40;1.60;1.70;1.80;0.0000;0.0000;0.0000;
K^{+};1.40;1.60;1.80;1.90;0.0000;0.0000;0.0000;
K^{+};1.40;1.60;1.90;2.00;0.0000;0.0000;0.0000;
K^{+};1.60;1.80;0.00;0.05;0.0000;0.0000;0.0000;
K^{+};1.60;1.80;0.05;0.10;0.6648;0.0054;0.0487;
K^{+};1.60;1.80;0.10;0.15;0.1516;0.0092;0.0726;
K^{+};1.60;1.80;0.15;0.20;1.2270;0.0078;0.0729;
K^{+};1.60;1.80;0.20;0.25;1.4070;0.0099;0.0809;
K^{+};1.60;1.80;0.25;0.30;1.4677;0.0089;0.0927;
K^{+};1.60;1.80;0.30;0.35;1.4889;0.0114;0.0824;
K^{+};1.60;1.80;0.35;0.40;1.3981;0.0084;0.0750;
K^{+};1.60;1.80;0.40;0.45;1.2518;0.0083;0.0611;
K^{+};1.60;1.80;0.45;0.50;1.0380;0.0105;0.0592;
K^{+};1.60;1.80;0.50;0.55;1.0695;0.0091;0.0610;
K^{+};1.60;1.80;0.55;0.60;0.7948;0.0098;0.0454;
K^{+};1.60;1.80;0.60;0.70;0.7490;0.0063;0.0423;
K^{+};1.60;1.80;0.70;0.80;0.5432;0.0054;0.0301;
K^{+};1.60;1.80;0.80;0.90;0.3300;0.0044;0.0220;
K^{+};1.60;1.80;0.90;1.00;0.1737;0.0049;0.0150;
K^{+};1.60;1.80;1.00;1.10;0.1109;0.0031;0.0131;
K^{+};1.60;1.80;1.10;1.20;0.0499;0.0021;0.0046;
K^{+};1.60;1.80;1.20;1.30;0.0053;0.0016;0.0088;
K^{+};1.60;1.80;1.30;1.40;0.0875;0.0014;0.0034;
K^{+};1.60;1.80;1.40;1.50;0.0000;0.0000;0.0000;
K^{+};1.60;1.80;1.50;1.60;0.0000;0.0000;0.0000;
K^{+};1.60;1.80;1.60;1.70;0.0000;0.0000;0.0000;
K^{+};1.60;1.80;1.70;1.80;0.0000;0.0000;0.0000;
K^{+};1.60;1.80;1.80;1.90;0.0000;0.0000;0.0000;
K^{+};1.60;1.80;1.90;2.00;0.0000;0.0000;0.0000;
K^{+};1.80;2.00;0.00;0.05;0.0000;0.0000;0.0000;
K^{+};1.80;2.00;0.05;0.10;0.0000;0.0000;0.0000;
K^{+};1.80;2.00;0.10;
```

## C. Numerical data

```
K{-};-0.20;0.00;1.30;1.40;0.0942;0.0011;0.0114;
K{-};-0.20;0.00;1.40;1.50;0.0830;0.0008;0.0069;
K{-};-0.20;0.00;1.50;1.60;0.0772;0.0007;0.0035;
K{-};-0.20;0.00;1.60;1.70;0.0389;0.0007;0.0043;
K{-};-0.20;0.00;1.70;1.80;0.0137;0.0004;0.0010;
K{-};-0.20;0.00;1.80;1.90;0.0154;0.0003;0.0011;
K{-};-0.20;0.00;1.90;2.00;0.0000;0.0000;0.0000;
K{-};0.00;0.20;0.00;0.05;0.0000;0.0000;0.0000;
K{-};0.00;0.20;0.05;0.10;0.0000;0.0000;0.0000;
K{-};0.00;0.20;0.10;0.15;0.0000;0.0000;0.0000;
K{-};0.00;0.20;0.15;0.20;0.0000;0.0000;0.0000;
K{-};0.00;0.20;0.20;0.25;0.0000;0.0000;0.0000;
K{-};0.00;0.20;0.25;0.30;0.0000;0.0000;0.0000;
K{-};0.00;0.20;0.30;0.35;0.0000;0.0000;0.0000;
K{-};0.00;0.20;0.35;0.40;0.0000;0.0000;0.0000;
K{-};0.00;0.20;0.40;0.45;0.0000;0.0000;0.0000;
K{-};0.00;0.20;0.45;0.50;0.0000;0.0000;0.0000;
K{-};0.00;0.20;0.50;0.55;0.0000;0.0000;0.0000;
K{-};0.00;0.20;0.55;0.60;0.0000;0.0000;0.0000;
K{-};0.00;0.20;0.60;0.70;0.0000;0.0000;0.0000;
K{-};0.00;0.20;0.70;0.80;0.0000;0.0000;0.0000;
K{-};0.00;0.20;0.80;0.90;0.0000;0.0000;0.0000;
K{-};0.00;0.20;0.90;1.00;0.4837;0.0018;0.0492;
K{-};0.00;0.20;1.00;1.10;0.3931;0.0017;0.0394;
K{-};0.00;0.20;1.10;1.20;0.2116;0.0012;0.0152;
K{-};0.00;0.20;1.20;1.30;0.1728;0.0010;0.0159;
K{-};0.00;0.20;1.30;1.40;0.1071;0.0009;0.0102;
K{-};0.00;0.20;1.40;1.50;0.0685;0.0007;0.0054;
K{-};0.00;0.20;1.50;1.60;0.0460;0.0005;0.0038;
K{-};0.00;0.20;1.60;1.70;0.0333;0.0004;0.0030;
K{-};0.00;0.20;1.70;1.80;0.0133;0.0004;0.0009;
K{-};0.00;0.20;1.80;1.90;0.0170;0.0003;0.0012;
K{-};0.00;0.20;1.90;2.00;0.0000;0.0000;0.0000;
K{-};0.20;0.40;0.00;0.05;0.0000;0.0000;0.0000;
K{-};0.20;0.40;0.05;0.10;0.0000;0.0000;0.0000;
K{-};0.20;0.40;0.10;0.15;0.0000;0.0000;0.0000;
K{-};0.20;0.40;0.15;0.20;0.0000;0.0000;0.0000;
K{-};0.20;0.40;0.20;0.25;0.0000;0.0000;0.0000;
K{-};0.20;0.40;0.25;0.30;0.0000;0.0000;0.0000;
K{-};0.20;0.40;0.30;0.35;0.0000;0.0000;0.0000;
K{-};0.20;0.40;0.35;0.40;0.0000;0.0000;0.0000;
K{-};0.20;0.40;0.40;0.45;0.0000;0.0000;0.0000;
K{-};0.20;0.40;0.45;0.50;0.0000;0.0000;0.0000;
K{-};0.20;0.40;0.50;0.55;0.0000;0.0000;0.0000;
K{-};0.20;0.40;0.55;0.60;0.0000;0.0000;0.0000;
K{-};0.20;0.40;0.60;0.70;0.0000;0.0000;0.0025;
K{-};0.20;0.40;0.70;0.80;0.9559;0.0026;0.0802;
K{-};0.20;0.40;0.80;0.90;0.6710;0.0019;0.0547;
K{-};0.20;0.40;0.90;1.00;0.5392;0.0017;0.0472;
K{-};0.20;0.40;1.00;1.10;0.3588;0.0018;0.0274;
K{-};0.20;0.40;1.10;1.20;0.2288;0.0011;0.0148;
K{-};0.20;0.40;1.20;1.30;0.1360;0.0010;0.0118;
K{-};0.20;0.40;1.30;1.40;0.1241;0.0007;0.0126;
K{-};0.20;0.40;1.40;1.50;0.0870;0.0006;0.0091;
K{-};0.20;0.40;1.50;1.60;0.0472;0.0005;0.0063;
K{-};0.20;0.40;1.60;1.70;0.0273;0.0005;0.0029;
K{-};0.20;0.40;1.70;1.80;0.0254;0.0004;0.0024;
K{-};0.20;0.40;1.80;1.90;0.0000;0.0000;0.0000;
K{-};0.20;0.40;1.90;2.00;0.0000;0.0000;0.0000;
K{-};0.40;0.60;0.00;0.05;0.0000;0.0000;0.0000;
K{-};0.40;0.60;0.05;0.10;0.0000;0.0000;0.0000;
K{-};0.40;0.60;0.10;0.15;0.0000;0.0000;0.0000;
K{-};0.40;0.60;0.15;0.20;0.0000;0.0000;0.0000;
K{-};0.40;0.60;0.20;0.25;0.0000;0.0000;0.0000;
K{-};0.40;0.60;0.25;0.30;0.0000;0.0000;0.0000;
K{-};0.40;0.60;0.30;0.35;0.0000;0.0000;0.0000;
K{-};0.40;0.60;0.35;0.40;0.0000;0.0000;0.0000;
K{-};0.40;0.60;0.40;0.45;0.0000;0.0000;0.0030;
K{-};0.40;0.60;0.45;0.50;1.7001;0.0039;0.1563;
K{-};0.40;0.60;0.50;0.55;1.5794;0.0049;0.1489;
K{-};0.40;0.60;0.55;0.60;1.3528;0.0049;0.1383;
K{-};0.40;0.60;0.60;0.70;1.1667;0.0027;0.0954;
K{-};0.40;0.60;0.70;0.80;0.8648;0.0021;0.0775;
K{-};0.40;0.60;0.80;0.90;0.6029;0.0021;0.0594;
K{-};0.40;0.60;0.90;1.00;0.4229;0.0015;0.0400;
K{-};0.40;0.60;1.00;1.10;0.3092;0.0012;0.0321;
K{-};0.40;0.60;1.10;1.20;0.1884;0.0010;0.0194;
K{-};0.40;0.60;1.20;1.30;0.1242;0.0008;0.0151;
K{-};0.40;0.60;1.30;1.40;0.1049;0.0007;0.0110;
K{-};0.40;0.60;1.40;1.50;0.0577;0.0006;0.0063;
K{-};0.40;0.60;1.50;1.60;0.0392;0.0004;0.0044;
K{-};0.40;0.60;1.60;1.70;0.0390;0.0004;0.0060;
K{-};0.40;0.60;1.70;1.80;0.0211;0.0003;0.0028;
K{-};0.40;0.60;1.80;1.90;0.0000;0.0000;0.0000;
K{-};0.40;0.60;1.90;2.00;0.0000;0.0000;0.0000;
K{-};0.60;0.80;0.00;0.05;0.0000;0.0000;0.0000;
K{-};0.60;0.80;0.05;0.10;0.0000;0.0000;0.0000;
K{-};0.60;0.80;0.10;0.15;0.0000;0.0000;0.0000;
K{-};0.60;0.80;0.15;0.20;0.0000;0.0000;0.0022;
K{-};0.60;0.80;0.20;0.25;0.0000;0.0000;0.0061;
K{-};0.60;0.80;0.25;0.30;1.7504;0.0038;0.8392;
K{-};0.60;0.80;0.30;0.35;1.7823;0.0046;0.0705;
K{-};0.60;0.80;0.35;0.40;1.6856;0.0044;0.1388;
K{-};0.60;0.80;0.40;0.45;1.6234;0.0042;0.1862;
K{-};0.60;0.80;0.45;0.50;1.5002;0.0041;0.1473;
K{-};0.60;0.80;0.50;0.55;1.3838;0.0037;0.1256;
K{-};0.60;0.80;0.55;0.60;1.3301;0.0038;0.1149;
K{-};0.60;0.80;0.60;0.70;0.9501;0.0022;0.0802;
K{-};0.60;0.80;0.70;0.80;0.8016;0.0021;0.0815;
K{-};0.60;0.80;0.80;0.90;0.5257;0.0018;0.0479;
K{-};0.60;0.80;0.90;1.00;0.3965;0.0013;0.0405;
K{-};0.60;0.80;1.00;1.10;0.2466;0.0012;0.0273;
K{-};0.60;0.80;1.10;1.20;0.1615;0.0010;0.0255;
K{-};0.60;0.80;1.20;1.30;0.1012;0.0007;0.0131;
K{-};0.60;0.80;1.30;1.40;0.0931;0.0006;0.0139;
K{-};0.60;0.80;1.40;1.50;0.0622;0.0005;0.0071;
K{-};0.60;0.80;1.50;1.60;0.0251;0.0004;0.0035;
K{-};0.60;0.80;1.60;1.70;0.0160;0.0003;0.0026;
K{-};0.60;0.80;1.70;1.80;0.0091;0.0003;0.0013;
K{-};0.60;0.80;1.80;1.90;0.0093;0.0002;0.0020;
K{-};0.60;0.80;1.90;2.00;0.0000;0.0000;0.0000;
K{-};0.80;1.00;0.00;0.05;0.0000;0.0015;0.0027;
K{-};0.80;1.00;0.05;0.10;0.5719;0.0022;0.0056;
K{-};0.80;1.00;0.10;0.15;0.8753;0.0027;0.0076;
K{-};0.80;1.00;0.15;0.20;1.1512;0.0033;0.0336;
K{-};0.80;1.00;0.20;0.25;1.4063;0.0039;0.0103;
K{-};0.80;1.00;0.25;0.30;1.4265;0.0033;0.0278;
K{-};0.80;1.00;0.30;0.35;1.5083;0.0035;0.0378;
K{-};0.80;1.00;0.35;0.40;1.4285;0.0037;0.0179;
K{-};0.80;1.00;0.40;0.45;1.3714;0.0033;0.0346;
K{-};0.80;1.00;0.45;0.50;1.2645;0.0036;0.0527;
K{-};0.80;1.00;0.50;0.55;1.1014;0.0034;0.0723;
K{-};0.80;1.00;0.55;0.60;0.9795;0.0037;0.0680;
K{-};0.80;1.00;0.60;0.70;0.8003;0.0020;0.0661;
K{-};0.80;1.00;0.70;0.80;0.5881;0.0018;0.0444;
K{-};0.80;1.00;0.80;0.90;0.4242;0.0012;0.0446;
K{-};0.80;1.00;0.90;1.00;0.2877;0.0014;0.0264;
K{-};0.80;1.00;1.00;1.10;0.2081;0.0009;0.0222;
K{-};0.80;1.00;1.10;1.20;0.1144;0.0008;0.0087;
K{-};0.80;1.00;1.20;1.30;0.0685;0.0006;0.0087;
K{-};0.80;1.00;1.30;1.40;0.0000;0.0000;0.0000;
K{-};0.80;1.00;1.40;1.50;0.0338;0.0004;0.0056;
K{-};0.80;1.00;1.50;1.60;0.0156;0.0003;0.0032;
K{-};0.80;1.00;1.60;1.70;0.0148;0.0002;0.0021;
K{-};0.80;1.00;1.70;1.80;0.0095;0.0002;0.0022;
K{-};0.80;1.00;1.80;1.90;0.0000;0.0000;0.0000;
K{-};0.80;1.00;1.90;2.00;0.0000;0.0000;0.0000;
K{-};1.00;1.20;0.00;0.05;0.1436;0.0011;0.0016;
K{-};1.00;1.20;0.05;0.10;0.4703;0.0021;0.0073;
K{-};1.00;1.20;0.10;0.15;0.6742;0.0024;0.0069;
K{-};1.00;1.20;0.15;0.20;0.9850;0.0029;0.0133;
K{-};1.00;1.20;0.20;0.25;1.0545;0.0031;0.0325;
K{-};1.00;1.20;0.25;0.30;1.1459;0.0032;0.0172;
K{-};1.00;1.20;0.30;0.35;1.1937;0.0035;0.0258;
K{-};1.00;1.20;0.35;0.40;1.1695;0.0035;0.0348;
K{-};1.00;1.20;0.40;0.45;1.0760;0.0033;0.0203;
K{-};1.00;1.20;0.45;0.50;1.0760;0.0034;0.0192;
K{-};1.00;1.20;0.50;0.55;0.9100;0.0028;0.0191;
K{-};1.00;1.20;0.55;0.60;0.7398;0.0029;0.0132;
K{-};1.00;1.20;0.60;0.70;0.6490;0.0016;0.0226;
K{-};1.00;1.20;0.70;0.80;0.4264;0.0013;0.0190;
K{-};1.00;1.20;0.80;0.90;0.3187;0.0012;0.0152;
K{-};1.00;1.20;0.90;0.90;0.2277;0.0009;0.0164;
K{-};1.00;1.20;1.00;1.10;0.1298;0.0008;0.0090;
K{-};1.00;1.20;1.10;1.20;0.0811;0.0006;0.0043;
K{-};1.00;1.20;1.20;1.30;0.0645;0.0005;0.0048;
K{-};1.00;1.20;1.30;1.40;0.0278;0.0004;0.0025;
K{-};1.00;1.20;1.40;1.50;0.0323;0.0003;0.0034;
K{-};1.00;1.20;1.50;1.60;0.0090;0.0003;0.0006;
K{-};1.00;1.20;1.60;1.70;0.0042;0.0002;0.0009;
K{-};1.00;1.20;1.70;1.80;0.0058;0.0001;0.0013;
K{-};1.00;1.20;1.80;1.90;0.0000;0.0000;0.0000;
K{-};1.00;1.20;1.90;2.00;0.0000;0.0000;0.0000;
K{-};1.20;1.40;0.00;0.05;0.0925;0.0010;0.0028;
K{-};1.20;1.40;0.05;0.10;0.3590;0.0019;0.0057;
K{-};1.20;1.40;0.10;0.15;0.5546;0.0023;0.0067;
K{-};1.20;1.40;0.15;0.20;0.6575;0.0024;0.0050;
K{-};1.20;1.40;0.20;0.25;0.7564;0.0026;0.0210;
K{-};1.20;1.40;0.25;0.30;0.8401;0.0028;0.0218;
K{-};1.20;1.40;0.30;0.35;0.8058;0.0026;0.0078;
K{-};1.20;1.40;0.35;0.40;0.7812;0.0026;0.0062;
K{-};1.20;1.40;0.40;0.45;0.8173;0.0030;0.0147;
K{-};1.20;1.40;0.45;0.50;0.6869;0.0027;0.0102;
K{-};1.20;1.40;0.50;0.55;0.6462;0.0026;0.0084;
K{-};1.20;1.40;0.55;0.60;0.5788;0.0019;0.0088;
K{-};1.20;1.40;0.60;0.70;0.4106;0.0016;0.0077;
K{-};1.20;1.40;0.70;0.80;0.2938;0.0012;0.0075;
K{-};1.20;1.40;0.80;0.90;0.2137;0.0012;0.0065;
K{-};1.20;1.40;0.90;1.00;0.1146;0.0009;0.0031;
K{-};1.20;1.40;1.00;1.10;0.0716;0.0006;0.0022;
K{-};1.20;1.40;1.10;1.20;0.0532;0.0004;0.0031;
K{-};1.20;1.40;1.20;1.30;0.0169;0.0004;0.0007;
K{-};1.20;1.40;1.30;1.40;0.0329;0.0003;0.0026;
K{-};1.20;1.40;1.40;1.50;0.0055;0.0002;0.0004;
K{-};1.20;1.40;1.50;1.60;0.0000;0.0000;0.0000;
K{-};1.20;1.40;1.60;1.70;0.0006;0.0002;0.0006;
K{-};1.20;1.40;1.70;1.80;0.0000;0.0000;0.0000;
K{-};1.20;1.40;1.80;1.90;0.0006;0.0001;0.0001;
K{-};1.20;1.40;1.90;2.00;0.0000;0.0000;0.0000;
K{-};1.40;1.60;0.00;0.05;0.0844;0.0011;0.0026;
K{-};1.40;1.60;0.05;0.10;0.2196;0.0017;0.0061;
K{-};1.40;1.60;0.10;0.15;0.3777;0.0018;0.0059;
K{-};1.40;1.60;0.15;0.20;0.4917;0.0022;0.0099;
K{-};1.40;1.60;0.20;0.25;0.5644;0.0021;0.0137;
K{-};1.40;1.60;0.25;0.30;0.6239;0.0025;0.0137;
K{-};1.40;1.60;0.30;0.35;0.5997;0.0024;0.0060;
K{-};1.40;1.60;0.35;0.40;0.5088;0.0021;0.0114;
K{-};1.40;1.60;0.40;0.45;0.5003;0.0019;0.0153;
K{-};1.40;1.60;0.45;0.50;0.4049;0.0020;0.0144;
K{-};1.40;1.60;0.50;0.55;0.3711;0.0020;0.0122;
K{-};1.40;1.60;0.55;0.60;0.3132;0.0019;0.0086;
K{-};1.40;1.60;0.60;0.70;0.2479;0.0012;0.0098;
K{-};1.40;1.60;0.70;0.80;0.1741;0.0010;0.0050;
K{-};1.40;1.60;0.80;0.90;0.1064;0.0008;0.0026;
K{-};1.40;1.60;0.90;1.00;0.0596;0.0005;0.0016;
K{-};1.40;1.60;1.00;1.10;0.0428;0.0004;0.0009;
K{-};1.40;1.60;1.10;1.20;0.0311;0.0003;0.0007;
K{-};1.40;1.60;1.20;1.30;0.0175;0.0002;0.0021;
K{-};1.40;1.60;1.30;1.40;0.0094;0.0002;0.0004;
K{-};1.40;1.60;1.40;1.50;0.0021;0.0001;0.0005;
K{-};1.40;1.60;1.50;1.60;0.0000;0.0000;0.0000;
K{-};1.40;1.60;1.60;1.70;0.0000;0.0000;0.0000;
K{-};1.40;1.60;1.70;1.80;0.0000;0.0000;0.0000;
K{-};1.40;1.60;1.80;1.90;0.0000;0.0000;0.0000;
K{-};1.40;1.60;1.90;2.00;0.0000;0.0000;0.0000;
K{-};1.60;1.80;0.00;0.05;0.0674;0.0008;0.0070;
K{-};1.60;1.80;0.05;0.10;0.1730;0.0012;0.0196;
K{-};1.60;1.80;0.10;0.15;0.2708;0.0014;0.0195;
K{-};1.60;1.80;0.15;0.20;0.3312;0.0017;0.0212;
K{-};1.60;1.80;0.20;0.25;0.3517;0.0019;0.0234;
K{-};1.60;1.80;0.25;0.30;0.3597;0.0018;0.0237;
K{-};1.60;1.80;0.30;0.35;0.3634;0.0019;0.0158;
K{-};1.60;1.80;0.35;0.40;0.3594;0.0020;0.0158;
K{-};1.60;1.80;0.40;0.45;0.3364;0.0019;0.0186;
K{-};1.60;1.80;0.45;0.50;0.2908;0.0016;0.0176;
K{-};1.60;1.80;0.50;0.55;0.2285;0.0014;0.0070;
K{-};1.60;1.80;0.55;0.60;0.2226;0.0014;0.0099;
K{-};1.60;1.80;0.60;0.70;0.1293;0.0009;0.0046;
K{-};1.60;1.80;0.70;0.80;0.0890;0.0007;0.0036;
K{-};1.60;1.80;0.80;0.90;0.0627;0.0006;0.0036;
K{-};1.60;1.80;0.90;1.00;0.0000;0.0000;0.0000;
K{-};1.60;1.80;1.00;1.10;0.0159;0.0004;0.0008;
K{-};1.60;1.80;1.10;1.20;0.0000;0.0000;0.0000;
K{-};1.60;1.80;1.20;1.30;0.0056;0.0001;0.0003;
K{-};1.60;1.80;1.30;1.40;0.0000;0.0000;0.0000;
K{-};1.60;1.80;1.40;1.50;0.0004;0.0001;0.0003;
K{-};1.60;1.80;1.50;1.60;0.0000;0.0000;0.0000;
K{-};1.60;1.80;1.60;1.70;0.0000;0.0000;0.0000;
K{-};1.60;1.80;1.70;1.80;0.0000;0.0000;0.0000;
K{-};1.60;1.80;1.80;1.90;0.0000;0.0000;0.0000;
K{-};1.60;1.80;1.90;2.00;0.0000;0.0000;0.0000;
K{-};1.80;2.00;0.00;0.05;0.0000;0.0000;0.0000;
K{-};1.80;2.00;0.05;0.10;0.1140;0.0009;0.0445;
K{-};1.80;2.00;0.10;0.15;0.1480;0.0012;0.0304;
K{-};1.80;2.00;0.15;0.20;0.1500;0.0016;0.0243;
K{-};1.80;2.00;0.20;0.25;0.2241;0.0015;0.0286;
K{-};1.80;2.00;0.25;0.30;0.2042;0.0015;0.0164;
K{-};1.80;2.00;0.30;0.35;0.1948;0.0014;0.0137;
K{-};1.80;2.00;0.35;0.40;0.1466;0.0014;0.0092;
K{-};1.80;2.00;0.40;0.45;0.1614;0.0013;0.0085;
K{-};1.80;2.00;0.45;0.50;0.1459;0.0012;0.0097;
K{-};1.80;2.00;0.50;0.55;0.1291;0.0011;0.0069;
K{-};1.80;2.00;0.55;0.60;0.1015;0.0011;0.0057;
K{-};1.80;2.00;0.60;0.70;0.0493;0.0006;0.0024;
K{-};1.80;2.00;0.70;0.80;0.0318;0.0005;0.0017;
K{-};1.80;2.00;0.80;0.90;0.0123;0.0004;0.0006;
K{-};1.80;2.00;0.90;1.00;0.0157;0.0002;0.0018;
K{-};1.80;2.00;1.00;1.10;0.0071;0.0002;0.0007;
K{-};1.80;2.00;1.10;1.20;0.0011;0.0001;0.0002;
K{-};1.80;2.00;1.20;1.30;0.0000;0.0000;0.0000;
K{-};1.80;2.00;1.30;1.40;0.0000;0.0000;0.0000;
K{-};1.80;2.00;1.40;1.50;0.0000;0.0000;0.0000;
K{-};1.80;2.00;1.50;1.60;0.0000;0.0000;0.0000;
K{-};1.80;2.00;1.60;1.70;0.0000;0.0000;0.0000;
K{-};1.80;2.00;1.70;1.80;0.0000;0.0000;0.0000;
K{-};1.80;2.00;1.80;1.90;0.0000;0.0000;0.0000;
K{-};1.80;2.00;1.90;2.00;0.0000;0.0000;0.0000;
K{-};2.00;2.20;0.00;0.05;0.0000;0.0000;0.0000;
K{-};2.00;2.20;0.05;0.10;0.0000;0.0000;0.0000;
K{-};2.00;2.20;0.10;0.15;0.0000;0.0000;0.0000;
K{-};2.00;2.20;0.15;0.20;0.0638;0.0009;0.0091;
K{-};2.00;2.20;0.20;0.25;0.1357;0.0013;0.0204;
K{-};2.00;2.20;0.25;0.30;0.1223;0.0012;0.0097;
```

## Kaons at 75A GeV/c

s; ymin; ymx; pTmin; pTmx; dn/dypT; errstat; errsys;

```

species; ymin; ymx; pTmin; pTmx; dn/dypT; errstat; errsys;
K^{+}; -0.20; 0.00; 0.00; 0.05; 0.0000; 0.0000; 0.0000;
K^{+}; -0.20; 0.00; 0.05; 0.10; 0.0000; 0.0000; 0.0000;
K^{+}; -0.20; 0.00; 0.10; 0.15; 0.0000; 0.0000; 0.0000;
K^{+}; -0.20; 0.00; 0.15; 0.20; 0.0000; 0.0000; 0.0000;
K^{+}; -0.20; 0.00; 0.20; 0.25; 0.0000; 0.0000; 0.0000;
K^{+}; -0.20; 0.00; 0.25; 0.30; 0.0000; 0.0000; 0.0000;
K^{+}; -0.20; 0.00; 0.30; 0.35; 0.0000; 0.0000; 0.0000;
K^{+}; -0.20; 0.00; 0.35; 0.40; 0.0000; 0.0000; 0.0000;
K^{+}; -0.20; 0.00; 0.40; 0.45; 0.0000; 0.0000; 0.0000;
K^{+}; -0.20; 0.00; 0.45; 0.50; 0.0000; 0.0000; 0.0000;
K^{+}; -0.20; 0.00; 0.50; 0.55; 0.0000; 0.0000; 0.0000;
K^{+}; -0.20; 0.00; 0.55; 0.60; 0.0000; 0.0000; 0.0000;
K^{+}; -0.20; 0.00; 0.60; 0.70; 0.0000; 0.0000; 0.0000;
K^{+}; -0.20; 0.00; 0.70; 0.80; 0.0000; 0.0000; 0.0001;
K^{+}; -0.20; 0.00; 0.80; 0.90; 1.7481; 0.0095; 0.1538;
K^{+}; -0.20; 0.00; 0.90; 1.00; 1.2930; 0.0091; 0.1176;
K^{+}; -0.20; 0.00; 1.00; 1.10; 1.0365; 0.0077; 0.0821;
K^{+}; -0.20; 0.00; 1.10; 1.20; 0.7178; 0.0064; 0.0566;
K^{+}; -0.20; 0.00; 1.20; 1.30; 0.5451; 0.0042; 0.0430;
K^{+}; -0.20; 0.00; 1.30; 1.40; 0.4015; 0.0050; 0.0284;
K^{+}; -0.20; 0.00; 1.40; 1.50; 0.2599; 0.0043; 0.0202;
K^{+}; -0.20; 0.00; 1.50; 1.60; 0.1970; 0.0055; 0.0201;
K^{+}; -0.20; 0.00; 1.60; 1.70; 0.1245; 0.0045; 0.0159;
K^{+}; -0.20; 0.00; 1.70; 1.80; 0.1080; 0.0017; 0.0122;
K^{+}; -0.20; 0.00; 1.80; 1.90; 0.0802; 0.0033; 0.0077;
K^{+}; -0.20; 0.00; 1.90; 2.00; 0.0000; 0.0000; 0.0000;
K^{+}; 0.00; 0.20; 0.00; 0.05; 0.0000; 0.0000; 0.0000;
K^{+}; 0.00; 0.20; 0.05; 0.10; 0.0000; 0.0000; 0.0000;
K^{+}; 0.00; 0.20; 0.10; 0.15; 0.0000; 0.0000; 0.0000;
K^{+}; 0.00; 0.20; 0.15; 0.20; 0.0000; 0.0000; 0.0000;
K^{+}; 0.00; 0.20; 0.20; 0.25; 0.0000; 0.0000; 0.0000;
K^{+}; 0.00; 0.20; 0.25; 0.30; 0.0000; 0.0000; 0.0000;
K^{+}; 0.00; 0.20; 0.30; 0.35; 0.0000; 0.0000; 0.0000;
K^{+}; 0.00; 0.20; 0.35; 0.40; 0.0000; 0.0000; 0.0000;
K^{+}; 0.00; 0.20; 0.40; 0.45; 0.0000; 0.0000; 0.0000;
K^{+}; 0.00; 0.20; 0.45; 0.50; 0.0000; 0.0000; 0.0000;
K^{+}; 0.00; 0.20; 0.50; 0.55; 0.0000; 0.0000; 0.0010;
K^{+}; 0.00; 0.20; 0.55; 0.60; 3.9750; 0.0208; 0.3480;
K^{+}; 0.00; 0.20; 0.60; 0.70; 3.1924; 0.0127; 0.2864;
K^{+}; 0.00; 0.20; 0.70; 0.80; 2.4968; 0.0090; 0.1942;
K^{+}; 0.00; 0.20; 0.80; 0.90; 1.9406; 0.0078; 0.1411;
K^{+}; 0.00; 0.20; 0.90; 1.00; 1.3877; 0.0095; 0.1027;
K^{+}; 0.00; 0.20; 1.00; 1.10; 1.0594; 0.0060; 0.0693;
K^{+}; 0.00; 0.20; 1.10; 1.20; 0.7700; 0.0058; 0.0451;
K^{+}; 0.00; 0.20; 1.20; 1.30; 0.5258; 0.0041; 0.0375;
K^{+}; 0.00; 0.20; 1.30; 1.40; 0.4240; 0.0045; 0.0313;
K^{+}; 0.00; 0.20; 1.40; 1.50; 0.2921; 0.0048; 0.0206;
K^{+}; 0.00; 0.20; 1.50; 1.60; 0.2093; 0.0035; 0.0214;
K^{+}; 0.00; 0.20; 1.60; 1.70; 0.1379; 0.0026; 0.0124;
K^{+}; 0.00; 0.20; 1.70; 1.80; 0.0959; 0.0017; 0.0108;
K^{+}; 0.00; 0.20; 1.80; 1.90; 0.0635; 0.0021; 0.0052;
K^{+}; 0.00; 0.20; 1.90; 2.00; 0.0000; 0.0000; 0.0000;
K^{+}; 0.20; 0.40; 0.00; 0.05; 0.0000; 0.0000; 0.0000;
K^{+}; 0.20; 0.40; 0.05; 0.10; 0.0000; 0.0000; 0.0000;
K^{+}; 0.20; 0.40; 0.10; 0.15; 0.0000; 0.0000; 0.0000;
K^{+}; 0.20; 0.40; 0.15; 0.20; 0.0000; 0.0000; 0.0000;
K^{+}; 0.20; 0.40; 0.20; 0.25; 0.0000; 0.0000; 0.0000;
K^{+}; 0.20; 0.40; 0.25; 0.30; 0.0000; 0.0000; 0.0000;
K^{+}; 0.20; 0.40; 0.30; 0.35; 0.0000; 0.0000; 0.0000;
K^{+}; 0.20; 0.40; 0.35; 0.40; 4.7853; 0.0177; 0.6882;
K^{+}; 0.20; 0.40; 0.40; 0.45; 4.7346; 0.0220; 0.5831;
K^{+}; 0.20; 0.40; 0.45; 0.50; 4.6474; 0.0209; 0.5255;
K^{+}; 0.20; 0.40; 0.50; 0.55; 4.3192; 0.0204; 0.4626;
K^{+}; 0.20; 0.40; 0.55; 0.60; 3.8765; 0.0153; 0.4060;
K^{+}; 0.20; 0.40; 0.60; 0.70; 3.3532; 0.0107; 0.3277;
K^{+}; 0.20; 0.40; 0.70; 0.80; 2.7268; 0.0098; 0.2419;
K^{+}; 0.20; 0.40; 0.80; 0.90; 2.0206; 0.0069; 0.1751;
K^{+}; 0.20; 0.40; 0.90; 1.00; 1.4893; 0.0070; 0.1166;
K^{+}; 0.20; 0.40; 1.00; 1.10; 1.0661; 0.0058; 0.0963;
K^{+}; 0.20; 0.40; 1.10; 1.20; 0.7903; 0.0044; 0.0740;
K^{+}; 0.20; 0.40; 1.20; 1.30; 0.5600; 0.0056; 0.0617;
K^{+}; 0.20; 0.40; 1.30; 1.40; 0.3818; 0.0040; 0.0420;
K^{+}; 0.20; 0.40; 1.40; 1.50; 0.2719; 0.0033; 0.0310;
K^{+}; 0.20; 0.40; 1.50; 1.60; 0.2118; 0.0029; 0.0226;
K^{+}; 0.20; 0.40; 1.60; 1.70; 0.1323; 0.0024; 0.0161;
K^{+}; 0.20; 0.40; 1.70; 1.80; 0.0938; 0.0016; 0.0123;
K^{+}; 0.20; 0.40; 1.80; 1.90; 0.0579; 0.0013; 0.0077;
K^{+}; 0.20; 0.40; 1.90; 2.00; 0.0000; 0.0000; 0.0000;
K^{+}; 0.40; 0.60; 0.00; 0.05; 0.0000; 0.0000; 0.0003;
K^{+}; 0.40; 0.60; 0.05; 0.10; 0.0000; 0.0000; 0.0003;
K^{+}; 0.40; 0.60; 0.10; 0.15; 2.6989; 0.0116; 0.0943;
K^{+}; 0.40; 0.60; 0.15; 0.20; 3.6090; 0.0151; 0.1232;
K^{+}; 0.40; 0.60; 0.20; 0.25; 4.1446; 0.0166; 0.1331;
K^{+}; 0.40; 0.60; 0.25; 0.30; 4.4372; 0.0176; 0.1571;
K^{+}; 0.40; 0.60; 0.30; 0.35; 4.8087; 0.0171; 0.2045;
K^{+}; 0.40; 0.60; 0.35; 0.40; 4.8381; 0.0141; 0.2727;
K^{+}; 0.40; 0.60; 0.40; 0.45; 4.6407; 0.0140; 0.3751;
K^{+}; 0.40; 0.60; 0.45; 0.50; 4.5499; 0.0155; 0.4452;
K^{+}; 0.40; 0.60; 0.50; 0.55; 4.3843; 0.0131; 0.4613;
K^{+}; 0.40; 0.60; 0.55; 0.60; 3.8614; 0.0122; 0.4129;
K^{+}; 0.40; 0.60; 0.60; 0.70; 3.2949; 0.0075; 0.3352;
K^{+}; 0.40; 0.60; 0.70; 0.80; 2.6040; 0.0070; 0.2595;
K^{+}; 0.40; 0.60; 0.80; 0.90; 1.9494; 0.0063; 0.1892;
K^{+}; 0.40; 0.60; 0.90; 1.00; 1.4463; 0.0053; 0.1625;
K^{+}; 0.40; 0.60; 1.00; 1.10; 1.0454; 0.0055; 0.1240;
K^{+}; 0.40; 0.60; 1.10; 1.20; 0.7417; 0.0043; 0.0851;
K^{+}; 0.40; 0.60; 1.20; 1.30; 0.5097; 0.0030; 0.0608;
K^{+}; 0.40; 0.60; 1.30; 1.40; 0.4074; 0.0026; 0.0511;
K^{+}; 0.40; 0.60; 1.40; 1.50; 0.2507; 0.0027; 0.0308;
K^{+}; 0.40; 0.60; 1.50; 1.60; 0.1893; 0.0017; 0.0232;
K^{+}; 0.40; 0.60; 1.60; 1.70; 0.1193; 0.0017; 0.0130;
K^{+}; 0.40; 0.60; 1.70; 1.80; 0.0900; 0.0014; 0.0137;
K^{+}; 0.40; 0.60; 1.80; 1.90; 0.0560; 0.0009; 0.0089;
K^{+}; 0.40; 0.60; 1.90; 2.00; 0.0000; 0.0000; 0.0000;
K^{+}; 0.60; 0.80; 0.00; 0.05; 0.5691; 0.0033; 0.0177;
K^{+}; 0.60; 0.80; 0.05; 0.10; 1.7202; 0.0082; 0.0494;
K^{+}; 0.60; 0.80; 0.10; 0.15; 2.7253; 0.0083; 0.0781;
K^{+}; 0.60; 0.80; 0.15; 0.20; 3.5602; 0.0105; 0.1009;
K^{+}; 0.60; 0.80; 0.20; 0.25; 4.1928; 0.0124; 0.1155;
K^{+}; 0.60; 0.80; 0.25; 0.30; 4.3427; 0.0114; 0.1232;
K^{+}; 0.60; 0.80; 0.30; 0.35; 4.7875; 0.0110; 0.1261;
K^{+}; 0.60; 0.80; 0.35; 0.40; 4.7082; 0.0097; 0.1267;
K^{+}; 0.60; 0.80; 0.40; 0.45; 4.6147; 0.0112; 0.1238;
K^{+}; 0.60; 0.80; 0.45; 0.50; 4.3390; 0.0104; 0.1217;
K^{+}; 0.60; 0.80; 0.50; 0.55; 4.0203; 0.0107; 0.1152;
K^{+}; 0.60; 0.80; 0.55; 0.60; 3.7159; 0.0100; 0.1457;
K^{+}; 0.60; 0.80; 0.60; 0.70; 3.0623; 0.0059; 0.1814;
K^{+}; 0.60; 0.80; 0.70; 0.80; 2.3649; 0.0051; 0.1934;
K^{+}; 0.60; 0.80; 0.80; 0.90; 1.8048; 0.0053; 0.1589;
K^{+}; 0.60; 0.80; 0.90; 1.00; 1.3211; 0.0040; 0.1287;
K^{+}; 0.60; 0.80; 1.00; 1.10; 9.9409; 0.0046; 0.1024;
K^{+}; 0.60; 0.80; 1.10; 1.20; 7.1279; 0.0037; 0.0816;
K^{+}; 0.60; 0.80; 1.20; 1.30; 5.0344; 0.0026; 0.0550;
K^{+}; 0.60; 0.80; 1.30; 1.40; 3.2330; 0.0030; 0.0343;
K^{+}; 0.60; 0.80; 1.40; 1.50; 2.2310; 0.0020; 0.0194;
K^{+}; 0.60; 0.80; 1.50; 1.60; 0.1746; 0.0018; 0.0162;
K^{+}; 0.60; 0.80; 1.60; 1.70; 0.1149; 0.0014; 0.0141;
K^{+}; 0.60; 0.80; 1.70; 1.80; 0.0717; 0.0021; 0.0121;
K^{+}; 0.60; 0.80; 1.80; 1.90; 0.0583; 0.0011; 0.0066;
K^{+}; 0.60; 0.80; 1.90; 2.00; 0.0000; 0.0000; 0.0000;
K^{+}; 0.80; 1.00; 0.00; 0.05; 0.5210; 0.0036; 0.0161;
K^{+}; 0.80; 1.00; 0.05; 0.10; 1.5812; 0.0057; 0.0406;
K^{+}; 0.80; 1.00; 0.10; 0.15; 2.5384; 0.0071; 0.0652;
K^{+}; 0.80; 1.00; 0.15; 0.20; 3.9776; 0.0091; 0.0980;
K^{+}; 0.80; 1.00; 0.20; 0.25; 3.3039; 0.0097; 0.1075;
K^{+}; 0.80; 1.00; 0.25; 0.30; 4.3039; 0.0097; 0.1075;
K^{+}; 0.80; 1.00; 0.30; 0.35; 4.4571; 0.0098; 0.1126;
K^{+}; 0.80; 1.00; 0.35; 0.40; 4.4497; 0.0101; 0.1225;
K^{+}; 0.80; 1.00; 0.40; 0.45; 4.4354; 0.0099; 0.1179;
K^{+}; 0.80; 1.00; 0.45; 0.50; 3.9815; 0.0099; 0.1077;
K^{+}; 0.80; 1.00; 0.50; 0.55; 3.7289; 0.0095; 0.1134;
K^{+}; 0.80; 1.00; 0.55; 0.60; 3.4573; 0.0089; 0.0901;
K^{+}; 0.80; 1.00; 0.60; 0.70; 2.9679; 0.0055; 0.0846;
K^{+}; 0.80; 1.00; 0.70; 0.80; 2.2377; 0.0060; 0.0687;
K^{+}; 0.80; 1.00; 0.80; 0.90; 1.6734; 0.0048; 0.0503;
K^{+}; 0.80; 1.00; 0.90; 1.00; 1.1951; 0.0038; 0.0370;
K^{+}; 0.80; 1.00; 1.00; 1.10; 8.8405; 0.0039; 0.0296;
K^{+}; 0.80; 1.00; 1.10; 1.20; 5.8333; 0.0031; 0.0287;
K^{+}; 0.80; 1.00; 1.20; 1.30; 4.3096; 0.0020; 0.0136;
K^{+}; 0.80; 1.00; 1.40; 1.50; 2.2110; 0.0021; 0.0074;
K^{+}; 0.80; 1.00; 1.60; 1.70; 0.1452; 0.0021; 0.0074;
K^{+}; 0.80; 1.00; 1.80; 1.90; 0.0834; 0.0014; 0.0071;
K^{+}; 0.80; 1.00; 1.70; 1.80; 0.0583; 0.0020; 0.0035;
K^{+}; 0.80; 1.00; 1.80; 1.90; 0.0471; 0.0015; 0.0021;
K^{+}; 0.80; 1.00; 1.90; 2.00; 0.0000; 0.0000; 0.0000;
K^{+}; 1.00; 1.20; 0.00; 0.05; 4.7900; 0.0033; 0.0140;
K^{+}; 1.00; 1.20; 0.05; 0.10; 1.4127; 0.0060; 0.0369;
K^{+}; 1.00; 1.20; 0.10; 0.15; 2.3631; 0.0069; 0.0603;
K^{+}; 1.00; 1.20; 0.15; 0.20; 2.9982; 0.0077; 0.0751;
K^{+}; 1.00; 1.20; 0.20; 0.25; 3.5815; 0.0078; 0.0874;
K^{+}; 1.00; 1.20; 0.25; 0.30; 4.0187; 0.0099; 0.1036;
K^{+}; 1.00; 1.20; 0.30; 0.35; 4.0948; 0.0086; 0.1207;
K^{+}; 1.00; 1.20; 0.35; 0.40; 4.1967; 0.0095; 0.1151;
K^{+}; 1.00; 1.20; 0.40; 0.45; 3.8607; 0.0096; 0.1121;
K^{+}; 1.00; 1.20; 0.45; 0.50; 3.7473; 0.0100; 0.1119;
K^{+}; 1.00; 1.20; 0.50; 0.55; 3.5302; 0.0098; 0.1079;
K^{+}; 1.00; 1.20; 0.55; 0.60; 3.0916; 0.0073; 0.0931;
K^{+}; 1.00; 1.20; 0.60; 0.70; 2.7134; 0.0053; 0.0818;
K^{+}; 1.00; 1.20; 0.70; 0.80; 1.9652; 0.0051; 0.0703;
K^{+}; 1.00; 1.20; 0.80; 0.90; 1.4970; 0.0045; 0.0549;
K^{+}; 1.00; 1.20; 0.90; 1.00; 1.0956; 0.0043; 0.0413;
K^{+}; 1.00; 1.20; 1.00; 1.10; 0.7534; 0.0038; 0.0311;
K^{+}; 1.00; 1.20; 1.10; 1.20; 0.5749; 0.0039; 0.0316;
K^{+}; 1.00; 1.20; 1.20; 1.30; 0.4002; 0.0033; 0.0227;
K^{+}; 1.00; 1.20; 1.30; 1.40; 0.2612; 0.0032; 0.0137;
K^{+}; 1.00; 1.20; 1.40; 1.50; 0.1745; 0.0027; 0.0088;
K^{+}; 1.00; 1.20; 1.50; 1.60; 0.1158; 0.0024; 0.0106;
K^{+}; 1.00; 1.20; 1.60; 1.70; 0.0600; 0.0014; 0.0083;
K^{+}; 1.00; 1.20; 1.70; 1.80; 0.0668; 0.0013; 0.0065;
K^{+}; 1.00; 1.20; 1.80; 1.90; 0.0477; 0.0011; 0.0058;
K^{+}; 1.00; 1.20; 1.90; 2.00; 0.0000; 0.0000; 0.0000;
K^{+}; 1.20; 1.40; 0.00; 0.05; 0.4198; 0.0035; 0.0112;
K^{+}; 1.20; 1.40; 0.05; 0.10; 1.3592; 0.0073; 0.0364;
K^{+}; 1.20; 1.40; 0.10; 0.15; 0.1196; 0.0063; 0.0564;
K^{+}; 1.20; 1.40; 0.15; 0.20; 2.6336; 0.0072; 0.0749;
K^{+}; 1.20; 1.40; 0.20; 0.25; 3.1496; 0.0074; 0.0891;
K^{+}; 1.20; 1.40; 0.25; 0.30; 3.6130; 0.0082; 0.1048;
K^{+}; 1.20; 1.40; 0.30; 0.35; 3.5425; 0.0109; 0.1169;
K^{+}; 1.20; 1.40; 0.35; 0.40; 3.4217; 0.0086; 0.1059;
K^{+}; 1.20; 1.40; 0.40; 0.45; 3.4019; 0.0089; 0.1156;
K^{+}; 1.20; 1.40; 0.45; 0.50; 3.1657; 0.0099; 0.1138;
K^{+}; 1.20; 1.40; 0.50; 0.55; 2.9625; 0.0098; 0.1105;
K^{+}; 1.20; 1.40; 0.55; 0.60; 2.6823; 0.0098; 0.0980;
K^{+}; 1.20; 1.40; 0.60; 0.70; 2.2039; 0.0061; 0.0781;
K^{+}; 1.20; 1.40; 0.70; 0.80; 1.7145; 0.0053; 0.0722;
K^{+}; 1.20; 1.40; 0.80; 0.90; 1.2272; 0.0050; 0.0608;
K^{+}; 1.20; 1.40; 0.90; 1.00; 0.8897; 0.0053; 0.0481;
K^{+}; 1.20; 1.40; 1.00; 1.10; 0.6435; 0.0048; 0.0357;
K^{+}; 1.20; 1.40; 1.10; 1.20; 0.4006; 0.0038; 0.0241;
K^{+}; 1.20; 1.40; 1.20; 1.30; 0.2533; 0.0037; 0.0211;
K^{+}; 1.20; 1.40; 1.30; 1.40; 0.1630; 0.0025; 0.0155;
K^{+}; 1.20; 1.40; 1.40; 1.50; 0.1019; 0.0019; 0.0119;
K^{+}; 1.20; 1.40; 1.50; 1.60; 0.0589; 0.0015; 0.0118;
K^{+}; 1.20; 1.40; 1.60; 1.70; 0.0336; 0.0010; 0.0077;
K^{+}; 1.20; 1.40; 1.80; 1.90; 0.0235; 0.0007; 0.0077;
K^{+}; 1.20; 1.40; 1.90; 2.00; 0.0000; 0.0000; 0.0000;
K^{+}; 1.40; 1.60; 0.00; 0.05; 0.4015; 0.0040; 0.0125;
K^{+}; 1.40; 1.60; 0.05; 0.10; 1.1050; 0.0048; 0.0341;
K^{+}; 1.40; 1.60; 0.10; 0.15; 1.7405; 0.0094; 0.0597;
K^{+}; 1.40; 1.60; 0.15; 0.20; 2.1096; 0.0078; 0.0763;
K^{+}; 1.40; 1.60; 0.20; 0.25; 2.5754; 0.0085; 0.0899;
K^{+}; 1.40; 1.60; 0.25; 0.30; 2.8302; 0.0085; 0.1030;
K^{+}; 1.40; 1.60; 0.30; 0.35; 2.9865; 0.0094; 0.1115;
K^{+}; 1.40; 1.60; 0.35; 0.40; 2.7175; 0.0105; 0.1054;
K^{+}; 1.40; 1.60; 0.40; 0.45; 2.7138; 0.0096; 0.1172;
K^{+}; 1.40; 1.60; 0.45; 0.50; 2.5767; 0.0107; 0.1039;
K^{+}; 1.40; 1.60; 0.50; 0.55; 2.3224; 0.0090; 0.1074;
K^{+}; 1.40; 1.60; 0.55; 0.60; 2.1185; 0.0107; 0.0821;
K^{+}; 1.40; 1.60; 0.60; 0.70; 1.7230; 0.0078; 0.0773;
K^{+}; 1.40; 1.60; 0.70; 0.80; 1.3047; 0.0082; 0.0742;
K^{+}; 1.40; 1.60; 0.80; 0.90; 0.9514; 0.0071; 0.0609;
K^{+}; 1.40; 1.60; 0.90; 1.00; 0.6648; 0.0060; 0.0512;
K^{+}; 1.40; 1.60; 1.00; 1.10; 0.4718; 0.0041; 0.0346;
K^{+}; 1.40; 1.60; 1.10; 1.20; 0.2445; 0.0041; 0.0361;
K^{+}; 1.40; 1.60; 1.20; 1.30; 0.1612; 0.0027; 0.0213;
K^{+}; 1.40; 1.60; 1.30; 1.40; 0.0960; 0.0019; 0.0197;
K^{+}; 1.40; 1.60; 1.40; 1.50; 0.0595; 0.0016; 0.0140;
K^{+}; 1.40; 1.60; 1.50; 1.60; 0.0356; 0.0013; 0.0067;
K^{+}; 1.40; 1.60; 1.60; 1.70; 0.0227; 0.0013; 0.0070;
K^{+}; 1.40; 1.60; 1.70; 1.80; 0.0098; 0.0008; 0.0040;
K^{
```

## C. Numerical data

K{-};-0.20;0.00;1.30;1.40;0.1706;0.0012;0.0125;  
K{-};-0.20;0.00;1.40;1.50;0.1077;0.0011;0.0124;  
K{-};-0.20;0.00;1.50;1.60;0.0793;0.0009;0.0084;  
K{-};-0.20;0.00;1.60;1.70;0.0567;0.0007;0.0070;  
K{-};-0.20;0.00;1.70;1.80;0.0391;0.0005;0.0046;  
K{-};-0.20;0.00;1.80;1.90;0.0279;0.0005;0.0023;  
K{-};-0.20;0.00;1.90;2.00;0.0000;0.0000;0.0000;  
K{-};0.00;0.20;0.00;0.05;0.0000;0.0000;0.0000;  
K{-};0.00;0.20;0.05;0.10;0.0000;0.0000;0.0000;  
K{-};0.00;0.20;0.10;0.15;0.0000;0.0000;0.0000;  
K{-};0.00;0.20;0.15;0.20;0.0000;0.0000;0.0000;  
K{-};0.00;0.20;0.20;0.25;0.0000;0.0000;0.0000;  
K{-};0.00;0.20;0.25;0.30;0.0000;0.0000;0.0000;  
K{-};0.00;0.20;0.30;0.35;0.0000;0.0000;0.0000;  
K{-};0.00;0.20;0.35;0.40;0.0000;0.0000;0.0000;  
K{-};0.00;0.20;0.40;0.45;0.0000;0.0000;0.0000;  
K{-};0.00;0.20;0.45;0.50;0.0000;0.0000;0.0025;  
K{-};0.00;0.20;0.50;0.55;0.0000;0.0000;0.0026;  
K{-};0.00;0.20;0.55;0.60;2.3454;0.0061;0.3228;  
K{-};0.00;0.20;0.60;0.70;1.9002;0.0044;0.2188;  
K{-};0.00;0.20;0.70;0.80;1.4571;0.0034;0.1661;  
K{-};0.00;0.20;0.80;0.90;1.0252;0.0027;0.1011;  
K{-};0.00;0.20;0.90;1.00;0.7442;0.0028;0.0770;  
K{-};0.00;0.20;1.00;1.10;0.5598;0.0018;0.0513;  
K{-};0.00;0.20;1.10;1.20;0.3791;0.0018;0.0339;  
K{-};0.00;0.20;1.20;1.30;0.2639;0.0013;0.0285;  
K{-};0.00;0.20;1.30;1.40;0.1840;0.0010;0.0165;  
K{-};0.00;0.20;1.40;1.50;0.1318;0.0010;0.0160;  
K{-};0.00;0.20;1.50;1.60;0.0893;0.0009;0.0101;  
K{-};0.00;0.20;1.60;1.70;0.0514;0.0007;0.0075;  
K{-};0.00;0.20;1.70;1.80;0.0438;0.0006;0.0050;  
K{-};0.00;0.20;1.80;1.90;0.0230;0.0004;0.0022;  
K{-};0.00;0.20;1.90;2.00;0.0000;0.0000;0.0000;  
K{-};0.20;0.40;0.00;0.05;0.0000;0.0000;0.0000;  
K{-};0.20;0.40;0.05;0.10;0.0000;0.0000;0.0000;  
K{-};0.20;0.40;0.10;0.15;0.0000;0.0000;0.0000;  
K{-};0.20;0.40;0.15;0.20;0.0000;0.0000;0.0000;  
K{-};0.20;0.40;0.20;0.25;0.0000;0.0000;0.0089;  
K{-};0.20;0.40;0.25;0.30;0.0000;0.0000;0.0040;  
K{-};0.20;0.40;0.30;0.35;0.0000;0.0000;0.0040;  
K{-};0.20;0.40;0.35;0.40;2.8673;0.0065;0.4380;  
K{-};0.20;0.40;0.40;0.45;2.7461;0.0072;0.4169;  
K{-};0.20;0.40;0.45;0.50;2.5812;0.0072;0.4200;  
K{-};0.20;0.40;0.50;0.55;2.3984;0.0064;0.3770;  
K{-};0.20;0.40;0.55;0.60;2.1732;0.0064;0.3088;  
K{-};0.20;0.40;0.60;0.70;1.8290;0.0037;0.1940;  
K{-};0.20;0.40;0.70;0.80;1.3760;0.0031;0.1340;  
K{-};0.20;0.40;0.80;0.90;1.0594;0.0028;0.1418;  
K{-};0.20;0.40;0.90;1.00;0.7706;0.0023;0.1092;  
K{-};0.20;0.40;1.00;1.10;0.5291;0.0020;0.0738;  
K{-};0.20;0.40;1.10;1.20;0.3585;0.0016;0.0547;  
K{-};0.20;0.40;1.20;1.30;0.2419;0.0012;0.0420;  
K{-};0.20;0.40;1.30;1.40;0.1845;0.0010;0.0262;  
K{-};0.20;0.40;1.40;1.50;0.1036;0.0008;0.0174;  
K{-};0.20;0.40;1.50;1.60;0.0795;0.0007;0.0136;  
K{-};0.20;0.40;1.60;1.70;0.0496;0.0006;0.0107;  
K{-};0.20;0.40;1.70;1.80;0.0366;0.0005;0.0053;  
K{-};0.20;0.40;1.80;1.90;0.0289;0.0004;0.0027;  
K{-};0.20;0.40;1.90;2.00;0.0000;0.0000;0.0000;  
K{-};0.40;0.60;0.00;0.05;0.0000;0.0000;0.0017;  
K{-};0.40;0.60;0.05;0.10;1.0321;0.0028;0.0208;  
K{-};0.40;0.60;0.10;0.15;1.7116;0.0035;0.0299;  
K{-};0.40;0.60;0.15;0.20;2.1794;0.0048;0.0245;  
K{-};0.40;0.60;0.20;0.25;2.5282;0.0061;0.0180;  
K{-};0.40;0.60;0.25;0.30;2.8115;0.0068;0.0932;  
K{-};0.40;0.60;0.30;0.35;2.7720;0.0062;0.0931;  
K{-};0.40;0.60;0.35;0.40;2.8459;0.0058;0.1058;  
K{-};0.40;0.60;0.40;0.45;2.6230;0.0059;0.1678;  
K{-};0.40;0.60;0.45;0.50;2.3908;0.0058;0.2383;  
K{-};0.40;0.60;0.50;0.55;2.2374;0.0058;0.2756;  
K{-};0.40;0.60;0.55;0.60;2.0176;0.0053;0.2526;  
K{-};0.40;0.60;0.60;0.70;1.7268;0.0037;0.2088;  
K{-};0.40;0.60;0.70;0.80;1.3042;0.0031;0.1674;  
K{-};0.40;0.60;0.80;0.90;0.9994;0.0024;0.1232;  
K{-};0.40;0.60;0.90;1.00;0.6727;0.0022;0.0956;  
K{-};0.40;0.60;1.00;1.10;0.4931;0.0018;0.0724;  
K{-};0.40;0.60;1.10;1.20;0.3411;0.0015;0.0478;  
K{-};0.40;0.60;1.20;1.30;0.2575;0.0013;0.0362;  
K{-};0.40;0.60;1.30;1.40;0.1540;0.0010;0.0262;  
K{-};0.40;0.60;1.40;1.50;0.1088;0.0008;0.0202;  
K{-};0.40;0.60;1.50;1.60;0.0607;0.0007;0.0100;  
K{-};0.40;0.60;1.60;1.70;0.0456;0.0005;0.0077;  
K{-};0.40;0.60;1.70;1.80;0.0375;0.0005;0.0049;  
K{-};0.40;0.60;1.80;1.90;0.0254;0.0003;0.0033;  
K{-};0.40;0.60;1.90;2.00;0.0000;0.0000;0.0000;  
K{-};0.60;0.80;0.00;0.05;0.2957;0.0017;0.0053;  
K{-};0.60;0.80;0.05;0.10;0.9465;0.0032;0.0170;  
K{-};0.60;0.80;0.10;0.15;1.6007;0.0041;0.0122;  
K{-};0.60;0.80;0.15;0.20;1.9839;0.0047;0.0118;  
K{-};0.60;0.80;0.20;0.25;2.1928;0.0046;0.0171;  
K{-};0.60;0.80;0.25;0.30;2.4890;0.0046;0.0136;  
K{-};0.60;0.80;0.30;0.35;2.5290;0.0053;0.0380;  
K{-};0.60;0.80;0.35;0.40;2.5362;0.0056;0.0531;  
K{-};0.60;0.80;0.40;0.45;2.4295;0.0049;0.0433;  
K{-};0.60;0.80;0.45;0.50;2.2587;0.0048;0.0415;  
K{-};0.60;0.80;0.50;0.55;2.1481;0.0048;0.0325;  
K{-};0.60;0.80;0.55;0.60;1.8939;0.0046;0.0551;  
K{-};0.60;0.80;0.60;0.70;1.5985;0.0032;0.0781;  
K{-};0.60;0.80;0.70;0.80;1.1335;0.0026;0.0835;  
K{-};0.60;0.80;0.80;0.90;0.8753;0.0023;0.0738;  
K{-};0.60;0.80;0.90;1.00;0.6322;0.0022;0.0594;  
K{-};0.60;0.80;1.00;1.10;0.4255;0.0015;0.0440;  
K{-};0.60;0.80;1.10;1.20;0.2893;0.0014;0.0275;  
K{-};0.60;0.80;1.20;1.30;0.1989;0.0011;0.0205;  
K{-};0.60;0.80;1.30;1.40;0.1513;0.0010;0.0148;  
K{-};0.60;0.80;1.40;1.50;0.0888;0.0007;0.0114;  
K{-};0.60;0.80;1.50;1.60;0.0692;0.0007;0.0070;  
K{-};0.60;0.80;1.60;1.70;0.0436;0.0006;0.0035;  
K{-};0.60;0.80;1.70;1.80;0.0251;0.0004;0.0036;  
K{-};0.60;0.80;1.80;1.90;0.0258;0.0003;0.0023;  
K{-};0.60;0.80;1.90;2.00;0.0000;0.0000;0.0000;  
K{-};0.80;1.00;0.00;0.05;0.2803;0.0018;0.0031;  
K{-};0.80;1.00;0.05;0.10;0.8080;0.0027;0.0091;  
K{-};0.80;1.00;0.10;0.15;1.3394;0.0034;0.0184;  
K{-};0.80;1.00;0.15;0.20;1.7540;0.0045;0.0209;  
K{-};0.80;1.00;0.20;0.25;2.0632;0.0053;0.0175;  
K{-};0.80;1.00;0.25;0.30;2.2146;0.0049;0.0196;  
K{-};0.80;1.00;0.30;0.35;2.2435;0.0052;0.0237;  
K{-};0.80;1.00;0.35;0.40;2.1960;0.0053;0.0166;  
K{-};0.80;1.00;0.40;0.45;2.1497;0.0047;0.0419;  
K{-};0.80;1.00;0.45;0.50;2.0445;0.0045;0.0343;  
K{-};0.80;1.00;0.50;0.55;1.7185;0.0048;0.0368;  
K{-};0.80;1.00;0.55;0.60;1.5806;0.0041;0.0281;  
K{-};0.80;1.00;0.60;0.70;1.3056;0.0024;0.0239;  
K{-};0.80;1.00;0.70;0.80;1.0254;0.0023;0.0165;  
K{-};0.80;1.00;0.80;0.90;0.7609;0.0022;0.0122;  
K{-};0.80;1.00;0.90;1.00;0.5328;0.0018;0.0124;  
K{-};0.80;1.00;1.00;1.10;0.3305;0.0015;0.0084;  
K{-};0.80;1.00;1.10;1.20;0.2288;0.0014;0.0080;  
K{-};0.80;1.00;1.20;1.30;0.1606;0.0014;0.0058;  
K{-};0.80;1.00;1.30;1.40;0.1229;0.0007;0.0043;  
K{-};0.80;1.00;1.40;1.50;0.0704;0.0007;0.0033;  
K{-};0.80;1.00;1.50;1.60;0.0475;0.0005;0.0025;  
K{-};0.80;1.00;1.60;1.70;0.0325;0.0006;0.0026;  
K{-};0.80;1.00;1.70;1.80;0.0210;0.0004;0.0016;  
K{-};0.80;1.00;1.80;1.90;0.0113;0.0003;0.0010;  
K{-};0.80;1.00;1.90;2.00;0.0000;0.0000;0.0000;  
K{-};1.00;1.20;0.00;0.05;0.2584;0.0018;0.0096;  
K{-};1.00;1.20;0.05;0.10;0.7133;0.0030;0.0090;  
K{-};1.00;1.20;0.10;0.15;1.2058;0.0041;0.0180;  
K{-};1.00;1.20;0.15;0.20;1.5255;0.0045;0.0338;  
K{-};1.00;1.20;0.20;0.25;1.6980;0.0044;0.0262;  
K{-};1.00;1.20;0.25;0.30;1.8798;0.0047;0.0183;  
K{-};1.00;1.20;0.30;0.35;1.9041;0.0053;0.0219;  
K{-};1.00;1.20;0.35;0.40;1.8732;0.0047;0.0227;  
K{-};1.00;1.20;0.40;0.45;1.8382;0.0048;0.0255;  
K{-};1.00;1.20;0.45;0.50;1.6561;0.0045;0.0245;  
K{-};1.00;1.20;0.50;0.55;1.5298;0.0046;0.0196;  
K{-};1.00;1.20;0.55;0.60;1.3858;0.0040;0.0216;  
K{-};1.00;1.20;0.60;0.70;1.1290;0.0028;0.0211;  
K{-};1.00;1.20;0.70;0.80;0.8292;0.0022;0.0182;  
K{-};1.00;1.20;0.80;0.90;0.6020;0.0019;0.0139;  
K{-};1.00;1.20;0.90;1.00;0.4121;0.0015;0.0099;  
K{-};1.00;1.20;1.00;1.10;0.2647;0.0014;0.0065;  
K{-};1.00;1.20;1.10;1.20;0.1851;0.0011;0.0041;  
K{-};1.00;1.20;1.20;1.30;0.1296;0.0010;0.0037;  
K{-};1.00;1.20;1.30;1.40;0.0843;0.0008;0.0039;  
K{-};1.00;1.20;1.40;1.50;0.0543;0.0007;0.0017;  
K{-};1.00;1.20;1.50;1.60;0.0345;0.0005;0.0015;  
K{-};1.00;1.20;1.60;1.70;0.0191;0.0004;0.0009;  
K{-};1.00;1.20;1.70;1.80;0.0094;0.0003;0.0013;  
K{-};1.00;1.20;1.80;1.90;0.0078;0.0003;0.0005;  
K{-};1.00;1.20;1.90;2.00;0.0000;0.0000;0.0000;  
K{-};1.20;1.40;0.00;0.05;0.2045;0.0017;0.0035;  
K{-};1.20;1.40;0.05;0.10;0.6386;0.0028;0.0110;  
K{-};1.20;1.40;0.10;0.15;1.0108;0.0040;0.0170;  
K{-};1.20;1.40;0.15;0.20;1.2857;0.0038;0.0220;  
K{-};1.20;1.40;0.20;0.25;1.4846;0.0044;0.0308;  
K{-};1.20;1.40;0.25;0.30;1.5788;0.0049;0.0287;  
K{-};1.20;1.40;0.30;0.35;1.5995;0.0046;0.0299;  
K{-};1.20;1.40;0.35;0.40;1.5186;0.0043;0.0300;  
K{-};1.20;1.40;0.40;0.45;1.4785;0.0045;0.0304;  
K{-};1.20;1.40;0.45;0.50;1.3565;0.0044;0.0272;  
K{-};1.20;1.40;0.50;0.55;1.1768;0.0042;0.0242;  
K{-};1.20;1.40;0.55;0.60;1.0190;0.0040;0.0282;  
K{-};1.20;1.40;0.60;0.70;0.8447;0.0023;0.0171;  
K{-};1.20;1.40;0.70;0.80;0.6193;0.0018;0.0144;  
K{-};1.20;1.40;0.80;0.90;0.4076;0.0018;0.0091;  
K{-};1.20;1.40;0.90;1.00;0.2942;0.0014;0.0091;  
K{-};1.20;1.40;1.00;1.10;0.2153;0.0014;0.0079;  
K{-};1.20;1.40;1.10;1.20;0.1151;0.0009;0.0038;  
K{-};1.20;1.40;1.20;1.30;0.0793;0.0008;0.0031;  
K{-};1.20;1.40;1.30;1.40;0.0471;0.0006;0.0026;  
K{-};1.20;1.40;1.40;1.50;0.0360;0.0005;0.0026;  
K{-};1.20;1.40;1.50;1.60;0.0257;0.0004;0.0010;  
K{-};1.20;1.40;1.60;1.70;0.0131;0.0002;0.0006;  
K{-};1.20;1.40;1.70;1.80;0.0049;0.0002;0.0006;  
K{-};1.20;1.40;1.80;1.90;0.0043;0.0002;0.0006;  
K{-};1.20;1.40;1.90;2.00;0.0000;0.0000;0.0000;  
K{-};1.40;1.60;0.00;0.05;0.1425;0.0015;0.0065;  
K{-};1.40;1.60;0.05;0.10;0.5065;0.0025;0.0143;  
K{-};1.40;1.60;0.10;0.15;0.7085;0.0031;0.0159;  
K{-};1.40;1.60;0.15;0.20;0.9334;0.0034;0.0195;  
K{-};1.40;1.60;0.20;0.25;0.9904;0.0035;0.0202;  
K{-};1.40;1.60;0.25;0.30;1.1108;0.0042;0.0246;  
K{-};1.40;1.60;0.30;0.35;1.1094;0.0035;0.0242;  
K{-};1.40;1.60;0.35;0.40;1.0836;0.0040;0.0269;  
K{-};1.40;1.60;0.40;0.45;1.0575;0.0029;0.0271;  
K{-};1.40;1.60;0.45;0.50;0.9114;0.0036;0.0252;  
K{-};1.40;1.60;0.50;0.55;0.8139;0.0038;0.0247;  
K{-};1.40;1.60;0.55;0.60;0.7537;0.0034;0.0224;  
K{-};1.40;1.60;0.60;0.70;0.6361;0.0020;0.0149;  
K{-};1.40;1.60;0.70;0.80;0.4017;0.0017;0.0117;  
K{-};1.40;1.60;0.80;0.90;0.2722;0.0015;0.0125;  
K{-};1.40;1.60;0.90;1.00;0.2087;0.0012;0.0102;  
K{-};1.40;1.60;1.00;1.10;0.1321;0.0010;0.0060;  
K{-};1.40;1.60;1.10;1.20;0.0794;0.0008;0.0048;  
K{-};1.40;1.60;1.20;1.30;0.0537;0.0006;0.0034;  
K{-};1.40;1.60;1.30;1.40;0.0255;0.0005;0.0023;  
K{-};1.40;1.60;1.40;1.50;0.0186;0.0004;0.0006;  
K{-};1.40;1.60;1.50;1.60;0.0110;0.0003;0.0007;  
K{-};1.40;1.60;1.60;1.70;0.0056;0.0002;0.0006;  
K{-};1.40;1.60;1.70;1.80;0.0028;0.0002;0.0018;  
K{-};1.40;1.60;1.80;1.90;0.0006;0.0001;0.0016;  
K{-};1.40;1.60;1.90;2.00;0.0000;0.0000;0.0000;  
K{-};1.60;1.80;0.00;0.05;0.1117;0.0015;0.0033;  
K{-};1.60;1.80;0.05;0.10;0.3455;0.0028;0.0106;  
K{-};1.60;1.80;0.10;0.15;0.5477;0.0033;0.0166;  
K{-};1.60;1.80;0.15;0.20;0.7345;0.0038;0.0218;  
K{-};1.60;1.80;0.20;0.25;0.8653;0.0039;0.0252;  
K{-};1.60;1.80;0.25;0.30;0.8817;0.0041;0.0237;  
K{-};1.60;1.80;0.30;0.35;0.8190;0.0030;0.0223;  
K{-};1.60;1.80;0.35;0.40;0.8079;0.0036;0.0228;  
K{-};1.60;1.80;0.40;0.45;0.7843;0.0043;0.0252;  
K{-};1.60;1.80;0.45;0.50;0.6494;0.0042;0.0217;  
K{-};1.60;1.80;0.50;0.55;0.6033;0.0038;0.0227;  
K{-};1.60;1.80;0.55;0.60;0.5179;0.0035;0.0219;  
K{-};1.60;1.80;0.60;0.70;0.4011;0.0018;0.0144;  
K{-};1.60;1.80;0.70;0.80;0.2528;0.0017;0.0104;  
K{-};1.60;1.80;0.80;0.90;0.1674;0.0012;0.0093;  
K{-};1.60;1.80;0.90;1.00;0.1097;0.0009;0.0060;  
K{-};1.60;1.80;1.00;1.10;0.0722;0.0008;0.0038;  
K{-};1.60;1.80;1.10;1.20;0.0638;0.0006;0.0037;  
K{-};1.60;1.80;1.20;1.30;0.0252;0.0005;0.0017;  
K{-};1.60;1.80;1.30;1.40;0.0086;0.0003;0.0010;  
K{-};1.60;1.80;1.40;1.50;0.0094;0.0003;0.0006;  
K{-};1.60;1.80;1.50;1.60;0.0019;0.0002;0.0003;  
K{-};1.60;1.80;1.60;1.70;0.0015;0.0002;0.0003;  
K{-};1.60;1.80;1.70;1.80;0.0000;0.0000;0.0000;  
K{-};1.60;1.80;1.80;1.90;0.0000;0.0000;0.0000;  
K{-};1.60;1.80;1.90;2.00;0.0000;0.0000;0.0000;  
K{-};1.80;2.00;0.00;0.05;0.1035;0.0022;0.0035;  
K{-};1.80;2.00;0.05;0.10;0.2680;0.0032;0.0098;  
K{-};1.80;2.00;0.10;0.15;0.3953;0.0044;0.0203;  
K{-};1.80;2.00;0.15;0.20;0.4455;0.0040;0.0213;  
K{-};1.80;2.00;0.20;0.25;0.5589;0.0036;0.0195;  
K{-};1.80;2.00;0.25;0.30;0.5735;0.0039;0.0236;  
K{-};1.80;2.00;0.30;0.35;0.4925;0.0041;0.0212;  
K{-};1.80;2.00;0.35;0.40;0.5280;0.0042;0.0355;  
K{-};1.80;2.00;0.40;0.45;0.4676;0.0034;0.0405;  
K{-};1.80;2.00;0.45;0.50;0.3922;0.0036;0.0317;  
K{-};1.80;2.00;0.50;0.55;0.3670;0.0024;0.0352;  
K{-};1.80;2.00;0.55;0.60;0.2866;0.0024;0.0266;  
K{-};1.80;2.00;0.60;0.70;0.2320;0.0016;0.0208;  
K{-};1.80;2.00;0.70;0.80;0.1479;0.0011;0.0106;  
K{-};1.80;2.00;0.80;0.90;0.0832;0.0009;0.0069;  
K{-};1.80;2.00;0.90;1.00;0.0672;0.0007;0.0042;  
K{-};1.80;2.00;1.00;1.10;0.0268;0.0005;0.0021;  
K{-};1.80;2.00;1.10;1.20;0.0159;0.0004;0.0018;  
K{-};1.80;2.00;1.20;1.30;0.0078;0.0003;0.0008;  
K{-};1.80;2.00;1.30;1.40;0.0016;0.0002;0.0005;  
K{-};1.80;2.00;1.40;1.50;0.0024;0.0001;0.0002;  
K{-};1.80;2.00;1.50;1.60;0.0000;0.0000;0.0000;  
K{-};1.80;2.00;1.60;1.70;0.0000;0.0000;0.0000;  
K{-};1.80;2.00;1.70;1.80;0.0000;0.0000;0.0000;  
K{-};1.80;2.00;1.80;1.90;0.0000;0.0000;0.0000;  
K{-};1.80;2.00;1.90;2.00;0.0000;0.0000;0.0000;  
K{-};2.00;2.20;0.00;0.05;0.058



## Kaons at 150A GeV/c

s;ymín;ymx;pTmín;pTmx;dn/dydpT;errsat;errsys;

```

species;ymín;ymax;pTmín;pTmax;dn/dydpT;errsat;errsys;
K^{+};-0.20;0.00;0.00;0.05;0.0000;0.0000;0.0000;
K^{+};-0.20;0.00;0.05;0.10;0.0000;0.0000;0.0000;
K^{+};-0.20;0.00;0.10;0.15;0.0000;0.0000;0.0000;
K^{+};-0.20;0.00;0.15;0.20;0.0000;0.0000;0.0000;
K^{+};-0.20;0.00;0.20;0.25;0.0000;0.0000;0.0000;
K^{+};-0.20;0.00;0.25;0.30;0.0000;0.0000;0.0000;
K^{+};-0.20;0.00;0.30;0.35;0.0000;0.0000;0.0034;
K^{+};-0.20;0.00;0.35;0.40;0.0000;0.0000;0.0017;
K^{+};-0.20;0.00;0.40;0.45;5.7978;0.0175;1.0373;
K^{+};-0.20;0.00;0.45;0.50;5.2570;0.0254;0.8502;
K^{+};-0.20;0.00;0.50;0.55;4.7590;0.0262;0.6269;
K^{+};-0.20;0.00;0.55;0.60;4.5861;0.0201;0.6054;
K^{+};-0.20;0.00;0.60;0.70;4.0115;0.0126;0.5032;
K^{+};-0.20;0.00;0.70;0.80;3.0886;0.0114;0.3221;
K^{+};-0.20;0.00;0.80;0.90;2.3518;0.0087;0.2540;
K^{+};-0.20;0.00;0.90;1.00;1.8452;0.0081;0.1702;
K^{+};-0.20;0.00;1.00;1.10;1.2852;0.0070;0.1243;
K^{+};-0.20;0.00;1.10;1.20;0.9917;0.0052;0.1013;
K^{+};-0.20;0.00;1.20;1.30;0.7897;0.0060;0.0846;
K^{+};-0.20;0.00;1.30;1.40;0.5615;0.0057;0.0624;
K^{+};-0.20;0.00;1.40;1.50;0.3044;0.0044;0.0456;
K^{+};-0.20;0.00;1.50;1.60;0.2525;0.0031;0.0379;
K^{+};-0.20;0.00;1.60;1.70;0.1763;0.0030;0.0247;
K^{+};-0.20;0.00;1.70;1.80;0.1604;0.0023;0.0186;
K^{+};-0.20;0.00;1.80;1.90;0.1094;0.0023;0.0120;
K^{+};-0.20;0.00;1.90;2.00;0.0000;0.0000;0.0000;
K^{+};0.00;0.20;0.00;0.05;0.0000;0.0000;0.0000;
K^{+};0.00;0.20;0.05;0.10;0.0000;0.0000;0.0019;
K^{+};0.00;0.20;0.10;0.15;0.0000;0.0000;0.0012;
K^{+};0.00;0.20;0.15;0.20;0.0000;0.0000;0.0035;
K^{+};0.00;0.20;0.20;0.25;0.0121;0.0164;0.0795;
K^{+};0.00;0.20;0.25;0.30;4.3888;0.0190;0.9582;
K^{+};0.00;0.20;0.30;0.35;3.9370;0.0186;1.1063;
K^{+};0.00;0.20;0.35;0.40;5.8566;0.0182;1.0249;
K^{+};0.00;0.20;0.40;0.45;5.7716;0.0156;0.8962;
K^{+};0.00;0.20;0.45;0.50;5.6557;0.0154;0.8636;
K^{+};0.00;0.20;0.50;0.55;5.1572;0.0159;0.7577;
K^{+};0.00;0.20;0.55;0.60;4.8704;0.0150;0.8068;
K^{+};0.00;0.20;0.60;0.70;4.2316;0.0087;0.5926;
K^{+};0.00;0.20;0.70;0.80;3.4069;0.0089;0.4309;
K^{+};0.00;0.20;0.80;0.90;2.4806;0.0078;0.3309;
K^{+};0.00;0.20;0.90;1.00;1.8744;0.0067;0.2632;
K^{+};0.00;0.20;1.00;1.10;1.3568;0.0070;0.2038;
K^{+};0.00;0.20;1.10;1.20;0.9958;0.0052;0.1445;
K^{+};0.00;0.20;1.20;1.30;0.7403;0.0042;0.1123;
K^{+};0.00;0.20;1.30;1.40;0.5609;0.0034;0.0808;
K^{+};0.00;0.20;1.40;1.50;0.3992;0.0035;0.0602;
K^{+};0.00;0.20;1.50;1.60;0.2673;0.0027;0.0427;
K^{+};0.00;0.20;1.60;1.70;0.2029;0.0020;0.0249;
K^{+};0.00;0.20;1.70;1.80;0.1602;0.0021;0.0239;
K^{+};0.00;0.20;1.80;1.90;0.1112;0.0016;0.0202;
K^{+};0.00;0.20;1.90;2.00;0.0000;0.0000;0.0000;
K^{+};0.20;0.40;0.00;0.05;0.6747;0.0044;0.0182;
K^{+};0.20;0.40;0.05;0.10;1.9656;0.0099;0.0579;
K^{+};0.20;0.40;0.10;0.15;3.0458;0.0112;0.0911;
K^{+};0.20;0.40;0.15;0.20;4.0580;0.0125;0.1071;
K^{+};0.20;0.40;0.20;0.25;4.9613;0.0160;0.1298;
K^{+};0.20;0.40;0.25;0.30;5.1587;0.0143;0.1711;
K^{+};0.20;0.40;0.30;0.35;5.6390;0.0159;0.3073;
K^{+};0.20;0.40;0.35;0.40;5.7576;0.0137;0.3923;
K^{+};0.20;0.40;0.40;0.45;5.6461;0.0145;0.4194;
K^{+};0.20;0.40;0.45;0.50;5.4765;0.0146;0.4230;
K^{+};0.20;0.40;0.50;0.55;4.9075;0.0142;0.4276;
K^{+};0.20;0.40;0.55;0.60;4.7159;0.0128;0.4494;
K^{+};0.20;0.40;0.60;0.70;3.9820;0.0079;0.4451;
K^{+};0.20;0.40;0.70;0.80;3.1509;0.0076;0.4210;
K^{+};0.20;0.40;0.80;0.90;2.3982;0.0076;0.3558;
K^{+};0.20;0.40;0.90;1.00;1.8621;0.0054;0.2511;
K^{+};0.20;0.40;1.00;1.10;1.4118;0.0059;0.1796;
K^{+};0.20;0.40;1.10;1.20;0.9622;0.0049;0.1239;
K^{+};0.20;0.40;1.20;1.30;0.7237;0.0038;0.0931;
K^{+};0.20;0.40;1.30;1.40;0.5077;0.0038;0.0724;
K^{+};0.20;0.40;1.40;1.50;0.3392;0.0032;0.0521;
K^{+};0.20;0.40;1.50;1.60;0.3081;0.0023;0.0342;
K^{+};0.20;0.40;1.60;1.70;0.2010;0.0023;0.0242;
K^{+};0.20;0.40;1.70;1.80;0.1159;0.0027;0.0202;
K^{+};0.20;0.40;1.80;1.90;0.0917;0.0016;0.0186;
K^{+};0.20;0.40;1.90;2.00;0.0000;0.0000;0.0000;
K^{+};0.40;0.60;0.00;0.05;0.7650;0.0054;0.0276;
K^{+};0.40;0.60;0.05;0.10;1.9630;0.0077;0.0382;
K^{+};0.40;0.60;0.10;0.15;3.0723;0.0092;0.0631;
K^{+};0.40;0.60;0.15;0.20;4.0876;0.0119;0.0941;
K^{+};0.40;0.60;0.20;0.25;4.8852;0.0113;0.1402;
K^{+};0.40;0.60;0.25;0.30;5.4401;0.0127;0.1294;
K^{+};0.40;0.60;0.30;0.35;5.5702;0.0122;0.1323;
K^{+};0.40;0.60;0.35;0.40;5.6866;0.0129;0.1207;
K^{+};0.40;0.60;0.40;0.45;5.5178;0.0126;0.1416;
K^{+};0.40;0.60;0.45;0.50;5.2084;0.0137;0.1290;
K^{+};0.40;0.60;0.50;0.55;4.9727;0.0130;0.1306;
K^{+};0.40;0.60;0.55;0.60;4.5676;0.0113;0.1323;
K^{+};0.40;0.60;0.60;0.70;4.0189;0.0075;0.1188;
K^{+};0.40;0.60;0.70;0.80;3.1588;0.0065;0.1063;
K^{+};0.40;0.60;0.80;0.90;2.4097;0.0065;0.1048;
K^{+};0.40;0.60;0.90;1.00;1.8164;0.0059;0.1001;
K^{+};0.40;0.60;1.00;1.10;1.3609;0.0051;0.0721;
K^{+};0.40;0.60;1.10;1.20;0.9477;0.0046;0.0610;
K^{+};0.40;0.60;1.20;1.30;0.7227;0.0038;0.0500;
K^{+};0.40;0.60;1.30;1.40;0.5417;0.0030;0.0304;
K^{+};0.40;0.60;1.40;1.50;0.3432;0.0027;0.0312;
K^{+};0.40;0.60;1.50;1.60;0.2660;0.0028;0.0186;
K^{+};0.40;0.60;1.60;1.70;0.1829;0.0022;0.0159;
K^{+};0.40;0.60;1.70;1.80;0.1198;0.0029;0.0103;
K^{+};0.40;0.60;1.80;1.90;0.0692;0.0021;0.0077;
K^{+};0.40;0.60;1.90;2.00;0.0000;0.0000;0.0000;
K^{+};0.60;0.80;0.00;0.05;0.6262;0.0051;0.0132;
K^{+};0.60;0.80;0.05;0.10;1.8883;0.0082;0.0364;
K^{+};0.60;0.80;0.10;0.15;3.1529;0.0106;0.0830;
K^{+};0.60;0.80;0.15;0.20;4.0010;0.0112;0.0760;
K^{+};0.60;0.80;0.20;0.25;4.8948;0.0125;0.1070;
K^{+};0.60;0.80;0.25;0.30;5.1922;0.0119;0.0981;
K^{+};0.60;0.80;0.30;0.35;5.5699;0.0127;0.1367;
K^{+};0.60;0.80;0.35;0.40;5.5246;0.0136;0.1129;
K^{+};0.60;0.80;0.40;0.45;4.6036;0.0157;0.1230;
K^{+};0.60;0.80;0.45;0.50;5.0647;0.0140;0.1129;
K^{+};0.60;0.80;0.50;0.55;4.7422;0.0127;0.0970;
K^{+};0.60;0.80;0.55;0.60;4.2744;0.0129;0.0970;
K^{+};0.60;0.80;0.60;0.70;3.7259;0.0078;0.1043;
K^{+};0.60;0.80;0.70;0.80;3.0063;0.0072;0.0910;
K^{+};0.60;0.80;0.80;0.90;2.3387;0.0062;0.0741;
K^{+};0.60;0.80;0.90;1.00;1.7136;0.0058;0.0585;
K^{+};0.60;0.80;1.00;1.10;1.2249;0.0051;0.0416;
K^{+};0.60;0.80;1.10;1.20;0.9368;0.0053;0.0363;
K^{+};0.60;0.80;1.20;1.30;0.6657;0.0041;0.0226;
K^{+};0.60;0.80;1.30;1.40;0.4834;0.0037;0.0180;
K^{+};0.60;0.80;1.40;1.50;0.3794;0.0036;0.0184;
K^{+};0.60;0.80;1.50;1.60;0.2381;0.0033;0.0136;
K^{+};0.60;0.80;1.60;1.70;0.1677;0.0021;0.0066;
K^{+};0.60;0.80;1.70;1.80;0.1158;0.0023;0.0066;
K^{+};0.60;0.80;1.80;1.90;0.0827;0.0018;0.0105;
K^{+};0.60;0.80;1.90;2.00;0.0000;0.0000;0.0000;
K^{+};0.80;1.00;0.00;0.05;0.7058;0.0053;0.0197;
K^{+};0.80;1.00;0.05;0.10;1.8522;0.0090;0.0480;
K^{+};0.80;1.00;0.10;0.15;3.1679;0.0116;0.0729;
K^{+};0.80;1.00;0.15;0.20;4.0699;0.0122;0.0746;
K^{+};0.80;1.00;0.20;0.25;4.9092;0.0146;0.0960;
K^{+};0.80;1.00;0.25;0.30;4.9889;0.0131;0.0914;
K^{+};0.80;1.00;0.30;0.35;4.266;0.0140;0.1039;
K^{+};0.80;1.00;0.35;0.40;5.3381;0.0122;0.1093;
K^{+};0.80;1.00;0.40;0.45;5.3672;0.0128;0.1441;
K^{+};0.80;1.00;0.45;0.50;4.9493;0.0126;0.1147;
K^{+};0.80;1.00;0.50;0.55;4.5663;0.0105;0.1073;
K^{+};0.80;1.00;0.55;0.60;4.2201;0.0121;0.1398;
K^{+};0.80;1.00;0.60;0.70;3.7156;0.0082;0.1034;
K^{+};0.80;1.00;0.70;0.80;2.7582;0.0074;0.0774;
K^{+};0.80;1.00;0.80;0.90;2.2254;0.0068;0.0658;
K^{+};0.80;1.00;0.90;1.00;1.6360;0.0064;0.0579;
K^{+};0.80;1.00;1.00;1.10;1.1562;0.0062;0.0462;
K^{+};0.80;1.00;1.10;1.20;0.8562;0.0055;0.0398;
K^{+};0.80;1.00;1.20;0.30;6.186;0.0051;0.0313;
K^{+};0.80;1.00;1.30;1.40;4.4659;0.0041;0.0264;
K^{+};0.80;1.00;1.40;1.50;3.530;0.0031;0.0156;
K^{+};0.80;1.00;1.50;1.60;2.263;0.0032;0.0204;
K^{+};0.80;1.00;1.60;1.70;1.714;0.0022;0.0145;
K^{+};0.80;1.00;1.70;1.80;0.8848;0.0019;0.0092;
K^{+};0.80;1.00;1.80;1.90;0.6673;0.0015;0.0091;
K^{+};0.80;1.00;1.90;2.00;0.0000;0.0000;0.0000;
K^{+};1.00;1.20;0.00;0.05;0.7266;0.0055;0.0176;
K^{+};1.00;1.20;0.05;0.10;1.7762;0.0076;0.0420;
K^{+};1.00;1.20;0.10;0.15;2.9607;0.0110;0.0569;
K^{+};1.00;1.20;0.15;0.20;3.8270;0.0120;0.0807;
K^{+};1.00;1.20;0.20;0.25;4.6847;0.0111;0.1082;
K^{+};1.00;1.20;0.25;0.30;4.7848;0.0134;0.1255;
K^{+};1.00;1.20;0.30;0.35;5.0848;0.0125;0.1081;
K^{+};1.00;1.20;0.35;0.40;5.1120;0.0125;0.1154;
K^{+};1.00;1.20;0.40;0.45;5.1464;0.0137;0.1514;
K^{+};1.00;1.20;0.45;0.50;4.8232;0.0143;0.1528;
K^{+};1.00;1.20;0.50;0.55;4.5645;0.0134;0.1245;
K^{+};1.00;1.20;0.55;0.60;4.2397;0.0137;0.1262;
K^{+};1.00;1.20;0.60;0.70;3.6518;0.0093;0.1215;
K^{+};1.00;1.20;0.70;0.80;2.7843;0.0084;0.1058;
K^{+};1.00;1.20;0.80;0.90;2.0390;0.0089;0.0956;
K^{+};1.00;1.20;0.90;1.00;1.5793;0.0079;0.0840;
K^{+};1.00;1.20;1.00;1.10;1.0935;0.0066;0.0630;
K^{+};1.00;1.20;1.10;1.20;0.7330;0.0062;0.0761;
K^{+};1.00;1.20;1.20;1.30;0.5474;0.0050;0.0471;
K^{+};1.00;1.20;1.30;1.40;0.4003;0.0039;0.0342;
K^{+};1.00;1.20;1.40;1.50;0.2563;0.0030;0.0221;
K^{+};1.00;1.20;1.50;1.60;0.1700;0.0026;0.0197;
K^{+};1.00;1.20;1.60;1.70;0.1091;0.0027;0.0128;
K^{+};1.00;1.20;1.70;1.80;0.0770;0.0020;0.0153;
K^{+};1.00;1.20;1.80;1.90;0.0570;0.0020;0.0082;
K^{+};1.00;1.20;1.90;2.00;0.0000;0.0000;0.0000;
K^{+};1.20;1.40;0.00;0.05;0.6079;0.0051;0.0168;
K^{+};1.20;1.40;0.05;0.10;1.6963;0.0077;0.0565;
K^{+};1.20;1.40;0.10;0.15;2.7549;0.0094;0.0621;
K^{+};1.20;1.40;0.15;0.20;3.6280;0.0109;0.0908;
K^{+};1.20;1.40;0.20;0.25;4.2499;0.0125;0.1049;
K^{+};1.20;1.40;0.25;0.30;4.4880;0.0126;0.1377;
K^{+};1.20;1.40;0.30;0.35;4.8008;0.0151;0.1476;
K^{+};1.20;1.40;0.35;0.40;4.5674;0.0153;0.1388;
K^{+};1.20;1.40;0.40;0.45;4.6449;0.0144;0.1533;
K^{+};1.20;1.40;0.45;0.50;4.3793;0.0149;0.1628;
K^{+};1.20;1.40;0.50;0.55;4.1293;0.0154;0.1570;
K^{+};1.20;1.40;0.55;0.60;3.7332;0.0142;0.1743;
K^{+};1.20;1.40;0.60;0.70;3.2287;0.0125;0.1515;
K^{+};1.20;1.40;0.70;0.80;4.312;0.0113;0.1409;
K^{+};1.20;1.40;0.80;0.90;1.6706;0.0091;0.1375;
K^{+};1.20;1.40;0.90;1.00;1.2169;0.0069;0.1111;
K^{+};1.20;1.40;1.00;1.10;0.9125;0.0065;0.0837;
K^{+};1.20;1.40;1.10;1.20;0.5757;0.0052;0.0802;
K^{+};1.20;1.40;1.20;1.30;0.3868;0.0048;0.0538;
K^{+};1.20;1.40;1.30;1.40;0.2677;0.0041;0.0362;
K^{+};1.20;1.40;1.40;1.50;0.2136;0.0032;0.0287;
K^{+};1.20;1.40;1.50;1.60;0.1218;0.0029;0.0220;
K^{+};1.20;1.40;1.60;1.70;0.0918;0.0030;0.0137;
K^{+};1.20;1.40;1.70;1.80;0.0619;0.0023;0.0102;
K^{+};1.20;1.40;1.80;1.90;0.0481;0.0020;0.0088;
K^{+};1.20;1.40;1.90;2.00;0.0000;0.0000;0.0000;
K^{+};1.40;1.60;0.00;0.05;0.5323;0.0052;0.0182;
K^{+};1.40;1.60;0.05;0.10;1.5487;0.0092;0.0571;
K^{+};1.40;1.60;0.10;0.15;2.5300;0.0126;0.0897;
K^{+};1.40;1.60;0.15;0.20;3.0406;0.0125;0.1262;
K^{+};1.40;1.60;0.20;0.25;3.8276;0.0152;0.1458;
K^{+};1.40;1.60;0.25;0.30;4.2087;0.0148;0.1611;
K^{+};1.40;1.60;0.30;0.35;4.2449;0.0157;0.1903;
K^{+};1.40;1.60;0.35;0.40;4.3196;0.0142;0.2009;
K^{+};1.40;1.60;0.40;0.45;4.1209;0.0220;0.2016;
K^{+};1.40;1.60;0.45;0.50;3.8660;0.0206;0.2226;
K^{+};1.40;1.60;0.50;0.55;3.5612;0.0207;0.2055;
K^{+};1.40;1.60;0.55;0.60;3.2534;0.0164;0.2321;
K^{+};1.40;1.60;0.60;0.70;2.6791;0.0099;0.1869;
K^{+};1.40;1.60;0.70;0.80;2.1062;0.0081;0.1820;
K^{+};1.40;1.60;0.80;0.90;1.2158;0.0075;0.1491;
K^{+};1.40;1.60;0.90;1.00;0.9108;0.0065;0.1263;
K^{+};1.40;1.60;1.00;1.10;0.6538;0.0058;0.0937;
K^{+};1.40;1.60;1.10;1.20;0.4320;0.0050;0.0734;
K^{+};1.40;1.60;1.20;1.30;0.2233;0.0059;0.0594;
K^{+};1.40;1.60;1.30;1.40;0.1933;0.0048;0.0372;
K^{+};1.40;1.60;1.40;1.50;0.1613;0.0037;0.0299;
K^{+};1.40;1.60;1.50;1.60;0.0832;0.0035;0.0204;
K^{+};1.40;1.60;1.60;1.70;0.0867;0.0036;0.0174;
K^{+};1.40;1.60;1.70;1.80;0.0661;0.0029;0.0188;
K^{+};1.40;1.60;1.80;1.90;0.0000;0.0000;0.0000;
K^{+};1.40;1.60;1.90;2.00;0.0000;0.0000;0.0000;
K^{+};1.60;1.80;0.00;0.05;0.4183;0.0058;0.0205;
K^{+};1.60;1.80;0.05;0.10;1.3203;0.0107;0.0671;
K^{+};1.60;1.80;0.10;0.15;2.1932;0.0128;0.1006;
K^{+};1.60;1.80;0.15;0.20;2.8625;0.0132;0.1360;
K^{+};1.60;1.80;0.20;0.25;3.3300;0.0149;0.1687;
K^{+};1.60;1.80;0.25;0.30;3.6615;0.0190;0.2000;
K^{+};1.60;1.80;0.30;0.35;3.6797;0.0186;0.2306;
K^{+};1.60;1.80;0.35;0.40;3.5209;0.0197;0.2209;
K^{+};1.60;1.80;0.40;0.45;3.2353;0.0168;0.2468;
K^{+};1.60;1.80;0.45;0.50;3.0394;0.0155;0.2754;
K^{+};1.60;1.80;0.50;0.55;2.9852;0.0136;0.2499;
K^{+};1.60;1.80;0.55;0.60;2.5932;0.0123;0.2554;
K^{+};1.60;1.80;0.60;0.70;2.1084;0.0088;0.2205;
K^{+};1.60;1.80;0.70;0.80;1.4638;0.0094;0.2047;
K^{+};1.60;1.80;0.80;0.90;0.9584;0.0075;0.1686;
K^{+};1.60;1.80;0.90;1.00;0.6897;0.0070;0.1255;
K^{+};1.60;1.80;1.00;1.10;0.3740;0.0060;0.0950;
K^{+};1.60;1.80;1.10;1.20;0.2792;0.0056;0.0763;
K^{+};1.60;1.80;1.20;1.30;0.1199;0.0063;0.0647;
K^{+};1.60;1.80;1.30;1.40;0.0684;0.0046;0.0391;
K^{+};1.60;1.80;1.40;1.50;0.0868;0.0041;0.0293;
K^{+};1.60;1.80;1.50;1.60;0.0000;0.0000;0.0000;
K^{+};1.60;1.80;1.60;1.70;0.0000;0.0000;0.0000;
K^{+};1.60;1.80;1.70;1.80;0.0000;0.0000;0.0000;
K^{+};1.60;1.80;1.80;1.90;0.0000;0.0000;0.0000;
K^{+};1.60;1.80;1.90;2.00;0.0000;0.0000;0.0000;
K^{+};1.80;2.00;0.00;0.05;0.3516;0.0065;0.0284;
K^{+};1.80;2.00;0.05;0.10;1.1940;0.0142;0.0850;
K^{+};1.80;2.00;0.10;0.15;1.7431;0.0129;0.1181;
K^{+};1.80;2.00;0.15;0.20;2.2570;0.0130;0.1743;
K^{+};1.80;2.00;0.20;0.25;2.6
```

## C. Numerical data

```
K{-};-0.20;0.00;1.30;1.40;0.2595;0.0022;0.0552;
K{-};-0.20;0.00;1.40;1.50;0.1746;0.0016;0.0267;
K{-};-0.20;0.00;1.50;1.60;0.1311;0.0021;0.0198;
K{-};-0.20;0.00;1.60;1.70;0.0836;0.0014;0.0149;
K{-};-0.20;0.00;1.70;1.80;0.0611;0.0010;0.0106;
K{-};-0.20;0.00;1.80;1.90;0.0462;0.0008;0.0077;
K{-};-0.20;0.00;1.90;2.00;0.0000;0.0000;0.0000;
K{-};0.00;0.20;0.00;0.05;0.0000;0.0000;0.0011;
K{-};0.00;0.20;0.05;0.10;0.0000;0.0000;0.0029;
K{-};0.00;0.20;0.10;0.15;0.0000;0.0000;0.0080;
K{-};0.00;0.20;0.15;0.20;0.0000;0.0000;0.0063;
K{-};0.00;0.20;0.20;0.25;3.6538;0.0083;0.8091;
K{-};0.00;0.20;0.25;0.30;3.8442;0.0102;0.8175;
K{-};0.00;0.20;0.30;0.35;3.9084;0.0113;1.1678;
K{-};0.00;0.20;0.35;0.40;3.7891;0.0101;1.0960;
K{-};0.00;0.20;0.40;0.45;3.7134;0.0097;1.0099;
K{-};0.00;0.20;0.45;0.50;3.6366;0.0100;1.1398;
K{-};0.00;0.20;0.50;0.55;3.3165;0.0108;1.0361;
K{-};0.00;0.20;0.55;0.60;3.1054;0.0085;0.9301;
K{-};0.00;0.20;0.60;0.65;2.5772;0.0057;0.7143;
K{-};0.00;0.20;0.70;0.80;1.9348;0.0051;0.4516;
K{-};0.00;0.20;0.80;0.90;1.5432;0.0048;0.3639;
K{-};0.00;0.20;0.90;1.00;1.0528;0.0040;0.2398;
K{-};0.00;0.20;1.00;1.10;0.7516;0.0039;0.1710;
K{-};0.00;0.20;1.10;1.20;0.5055;0.0028;0.1103;
K{-};0.00;0.20;1.20;1.30;0.3721;0.0022;0.0721;
K{-};0.00;0.20;1.30;1.40;0.2836;0.0022;0.0585;
K{-};0.00;0.20;1.40;1.50;0.1803;0.0016;0.0370;
K{-};0.00;0.20;1.50;1.60;0.1115;0.0012;0.0234;
K{-};0.00;0.20;1.60;1.70;0.0955;0.0013;0.0167;
K{-};0.00;0.20;1.70;1.80;0.0668;0.0011;0.0121;
K{-};0.00;0.20;1.80;1.90;0.0458;0.0008;0.0109;
K{-};0.00;0.20;1.90;2.00;0.0000;0.0000;0.0000;
K{-};0.20;0.40;0.00;0.05;0.4653;0.0033;0.0088;
K{-};0.20;0.40;0.05;0.10;1.4356;0.0066;0.0324;
K{-};0.20;0.40;0.10;0.15;2.1747;0.0077;0.0419;
K{-};0.20;0.40;0.15;0.20;2.8179;0.0082;0.0419;
K{-};0.20;0.40;0.20;0.25;3.3644;0.0118;0.0592;
K{-};0.20;0.40;0.25;0.30;3.7871;0.0108;0.0719;
K{-};0.20;0.40;0.30;0.35;3.9255;0.0113;0.1260;
K{-};0.20;0.40;0.35;0.40;4.0278;0.0102;0.2083;
K{-};0.20;0.40;0.40;0.45;3.7813;0.0099;0.3619;
K{-};0.20;0.40;0.45;0.50;3.5000;0.0109;0.3798;
K{-};0.20;0.40;0.50;0.55;3.1211;0.0098;0.3198;
K{-};0.20;0.40;0.55;0.60;3.0575;0.0095;0.3718;
K{-};0.20;0.40;0.60;0.65;2.4955;0.0060;0.3978;
K{-};0.20;0.40;0.70;0.80;1.9115;0.0048;0.3146;
K{-};0.20;0.40;0.80;0.90;1.4525;0.0044;0.2743;
K{-};0.20;0.40;0.90;1.00;1.0587;0.0038;0.1776;
K{-};0.20;0.40;1.00;1.10;0.7392;0.0032;0.1158;
K{-};0.20;0.40;1.10;1.20;0.5300;0.0026;0.0876;
K{-};0.20;0.40;1.20;1.30;0.3819;0.0025;0.0584;
K{-};0.20;0.40;1.30;1.40;0.2706;0.0019;0.0409;
K{-};0.20;0.40;1.40;1.50;0.1869;0.0017;0.0256;
K{-};0.20;0.40;1.50;1.60;0.1342;0.0014;0.0221;
K{-};0.20;0.40;1.60;1.70;0.0977;0.0012;0.0154;
K{-};0.20;0.40;1.70;1.80;0.0552;0.0011;0.0086;
K{-};0.20;0.40;1.80;1.90;0.0434;0.0008;0.0094;
K{-};0.20;0.40;1.90;2.00;0.0000;0.0000;0.0000;
K{-};0.40;0.60;0.00;0.05;0.4693;0.0034;0.0043;
K{-};0.40;0.60;0.05;0.10;1.4010;0.0062;0.0121;
K{-};0.40;0.60;0.10;0.15;2.1707;0.0073;0.0434;
K{-};0.40;0.60;0.15;0.20;2.8356;0.0084;0.0394;
K{-};0.40;0.60;0.20;0.25;3.3131;0.0092;0.0512;
K{-};0.40;0.60;0.25;0.30;3.5983;0.0104;0.0568;
K{-};0.40;0.60;0.30;0.35;3.8232;0.0095;0.0706;
K{-};0.40;0.60;0.35;0.40;3.9082;0.0107;0.0395;
K{-};0.40;0.60;0.40;0.45;3.8604;0.0107;0.1139;
K{-};0.40;0.60;0.45;0.50;3.4663;0.0098;0.1326;
K{-};0.40;0.60;0.50;0.55;3.1622;0.0103;0.1187;
K{-};0.40;0.60;0.55;0.60;2.8823;0.0100;0.1027;
K{-};0.40;0.60;0.60;0.70;2.4673;0.0059;0.0632;
K{-};0.40;0.60;0.70;0.80;1.8364;0.0048;0.0602;
K{-};0.40;0.60;0.80;0.90;1.4320;0.0046;0.0423;
K{-};0.40;0.60;0.90;1.00;0.9721;0.0038;0.0408;
K{-};0.40;0.60;1.00;1.10;0.7565;0.0031;0.0379;
K{-};0.40;0.60;1.10;1.20;0.5173;0.0029;0.0232;
K{-};0.40;0.60;1.20;1.30;0.3523;0.0023;0.0214;
K{-};0.40;0.60;1.30;1.40;0.2493;0.0018;0.0131;
K{-};0.40;0.60;1.40;1.50;0.1480;0.0014;0.0099;
K{-};0.40;0.60;1.50;1.60;0.1125;0.0014;0.0093;
K{-};0.40;0.60;1.60;1.70;0.0768;0.0012;0.0059;
K{-};0.40;0.60;1.70;1.80;0.0609;0.0011;0.0031;
K{-};0.40;0.60;1.80;1.90;0.0377;0.0010;0.0020;
K{-};0.40;0.60;1.90;2.00;0.0000;0.0000;0.0000;
K{-};0.60;0.80;0.00;0.05;0.4587;0.0038;0.0066;
K{-};0.60;0.80;0.05;0.10;1.3510;0.0059;0.0361;
K{-};0.60;0.80;0.10;0.15;2.0416;0.0079;0.0228;
K{-};0.60;0.80;0.15;0.20;2.5753;0.0076;0.0458;
K{-};0.60;0.80;0.20;0.25;3.1501;0.0090;0.0318;
K{-};0.60;0.80;0.25;0.30;3.3621;0.0091;0.0323;
K{-};0.60;0.80;0.30;0.35;3.4195;0.0094;0.0344;
K{-};0.60;0.80;0.35;0.40;3.5028;0.0094;0.0430;
K{-};0.60;0.80;0.40;0.45;3.3800;0.0088;0.0363;
K{-};0.60;0.80;0.45;0.50;3.1826;0.0093;0.0372;
K{-};0.60;0.80;0.50;0.55;2.9669;0.0088;0.0436;
K{-};0.60;0.80;0.55;0.60;2.7510;0.0087;0.0415;
K{-};0.60;0.80;0.60;0.70;2.1994;0.0061;0.0487;
K{-};0.60;0.80;0.70;0.80;1.6961;0.0051;0.0432;
K{-};0.60;0.80;0.80;0.90;1.2614;0.0043;0.0286;
K{-};0.60;0.80;0.90;1.00;0.8494;0.0033;0.0210;
K{-};0.60;0.80;1.00;1.10;0.6861;0.0028;0.0161;
K{-};0.60;0.80;1.10;1.20;0.4555;0.0027;0.0094;
K{-};0.60;0.80;1.20;1.30;0.3136;0.0024;0.0084;
K{-};0.60;0.80;1.30;1.40;0.2194;0.0021;0.0062;
K{-};0.60;0.80;1.40;1.50;0.1472;0.0017;0.0062;
K{-};0.60;0.80;1.50;1.60;0.0878;0.0012;0.0020;
K{-};0.60;0.80;1.60;1.70;0.0744;0.0013;0.0021;
K{-};0.60;0.80;1.70;1.80;0.0428;0.0009;0.0027;
K{-};0.60;0.80;1.80;1.90;0.0297;0.0008;0.0011;
K{-};0.60;0.80;1.90;2.00;0.0000;0.0000;0.0000;
K{-};0.80;1.00;0.00;0.05;0.3907;0.0035;0.0052;
K{-};0.80;1.00;0.05;0.10;1.2577;0.0070;0.0149;
K{-};0.80;1.00;0.10;0.15;1.9037;0.0075;0.0237;
K{-};0.80;1.00;0.15;0.20;2.4570;0.0083;0.0349;
K{-};0.80;1.00;0.20;0.25;3.0588;0.0093;0.0404;
K{-};0.80;1.00;0.25;0.30;3.2446;0.0094;0.0669;
K{-};0.80;1.00;0.30;0.35;3.1917;0.0094;0.0467;
K{-};0.80;1.00;0.35;0.40;3.1904;0.0092;0.0545;
K{-};0.80;1.00;0.40;0.45;3.0951;0.0102;0.0391;
K{-};0.80;1.00;0.45;0.50;2.7045;0.0082;0.0416;
K{-};0.80;1.00;0.50;0.55;2.6192;0.0084;0.0606;
K{-};0.80;1.00;0.55;0.60;2.3069;0.0074;0.0344;
K{-};0.80;1.00;0.60;0.70;1.9728;0.0060;0.0379;
K{-};0.80;1.00;0.70;0.80;1.5263;0.0050;0.0345;
K{-};0.80;1.00;0.80;0.90;1.1331;0.0040;0.0275;
K{-};0.80;1.00;0.90;1.00;0.7938;0.0038;0.0207;
K{-};0.80;1.00;1.00;1.10;0.5549;0.0038;0.0150;
K{-};0.80;1.00;1.10;1.20;0.3988;0.0026;0.0105;
K{-};0.80;1.00;1.20;1.30;0.2493;0.0023;0.0087;
K{-};0.80;1.00;1.30;1.40;0.1815;0.0017;0.0066;
K{-};0.80;1.00;1.40;1.50;0.1247;0.0017;0.0072;
K{-};0.80;1.00;1.50;1.60;0.1119;0.0015;0.0036;
K{-};0.80;1.00;1.60;1.70;0.0588;0.0012;0.0021;
K{-};0.80;1.00;1.70;1.80;0.0330;0.0010;0.0031;
K{-};0.80;1.00;1.80;1.90;0.0210;0.0007;0.0015;
K{-};0.80;1.00;1.90;2.00;0.0000;0.0000;0.0000;
K{-};1.00;1.20;0.00;0.05;0.3580;0.0034;0.0073;
K{-};1.00;1.20;0.05;0.10;1.1123;0.0054;0.0284;
K{-};1.00;1.20;0.10;0.15;1.6787;0.0070;0.0269;
K{-};1.00;1.20;0.15;0.20;2.2502;0.0082;0.0363;
K{-};1.00;1.20;0.20;0.25;2.6610;0.0084;0.0418;
K{-};1.00;1.20;0.25;0.30;2.7487;0.0103;0.0488;
K{-};1.00;1.20;0.30;0.35;2.8791;0.0088;0.0489;
K{-};1.00;1.20;0.35;0.40;2.9643;0.0104;0.0603;
K{-};1.00;1.20;0.40;0.45;2.6277;0.0089;0.0570;
K{-};1.00;1.20;0.45;0.50;2.6264;0.0094;0.0488;
K{-};1.00;1.20;0.50;0.55;2.3339;0.0080;0.0503;
K{-};1.00;1.20;0.55;0.60;2.1540;0.0089;0.0468;
K{-};1.00;1.20;0.60;0.70;1.7784;0.0057;0.0393;
K{-};1.00;1.20;0.70;0.80;1.3198;0.0055;0.0310;
K{-};1.00;1.20;0.80;0.90;0.9650;0.0046;0.0253;
K{-};1.00;1.20;0.90;1.00;0.6499;0.0036;0.0199;
K{-};1.00;1.20;1.00;1.10;0.4370;0.0031;0.0134;
K{-};1.00;1.20;1.10;1.20;0.3486;0.0029;0.0137;
K{-};1.00;1.20;1.20;1.30;0.2093;0.0024;0.0130;
K{-};1.00;1.20;1.30;1.40;0.1398;0.0018;0.0061;
K{-};1.00;1.20;1.40;1.50;0.1089;0.0017;0.0076;
K{-};1.00;1.20;1.50;1.60;0.0526;0.0013;0.0032;
K{-};1.00;1.20;1.60;1.70;0.0487;0.0012;0.0023;
K{-};1.00;1.20;1.70;1.80;0.0285;0.0011;0.0043;
K{-};1.00;1.20;1.80;1.90;0.0093;0.0006;0.0013;
K{-};1.00;1.20;1.90;2.00;0.0000;0.0000;0.0000;
K{-};1.20;1.40;0.00;0.05;0.3168;0.0035;0.0158;
K{-};1.20;1.40;0.05;0.10;0.9054;0.0065;0.0242;
K{-};1.20;1.40;0.10;0.15;1.4921;0.0069;0.0398;
K{-};1.20;1.40;0.15;0.20;1.8456;0.0082;0.0475;
K{-};1.20;1.40;0.20;0.25;2.1580;0.0101;0.0611;
K{-};1.20;1.40;0.25;0.30;2.3140;0.0094;0.0663;
K{-};1.20;1.40;0.30;0.35;2.4680;0.0103;0.0654;
K{-};1.20;1.40;0.35;0.40;2.4812;0.0097;0.0693;
K{-};1.20;1.40;0.40;0.45;2.3421;0.0096;0.0579;
K{-};1.20;1.40;0.45;0.50;2.2627;0.0091;0.0736;
K{-};1.20;1.40;0.50;0.55;2.0274;0.0084;0.0791;
K{-};1.20;1.40;0.55;0.60;1.8103;0.0083;0.0515;
K{-};1.20;1.40;0.60;0.70;1.4740;0.0062;0.0396;
K{-};1.20;1.40;0.70;0.80;1.0451;0.0051;0.0323;
K{-};1.20;1.40;0.80;0.90;0.7421;0.0041;0.0287;
K{-};1.20;1.40;0.90;1.00;0.4985;0.0043;0.0229;
K{-};1.20;1.40;1.00;1.10;0.3444;0.0028;0.0189;
K{-};1.20;1.40;1.10;1.20;0.2189;0.0024;0.0100;
K{-};1.20;1.40;1.20;1.30;0.1360;0.0022;0.0088;
K{-};1.20;1.40;1.30;1.40;0.0983;0.0018;0.0059;
K{-};1.20;1.40;1.40;1.50;0.0785;0.0015;0.0032;
K{-};1.20;1.40;1.50;1.60;0.0279;0.0011;0.0027;
K{-};1.20;1.40;1.60;1.70;0.0292;0.0009;0.0038;
K{-};1.20;1.40;1.70;1.80;0.0198;0.0012;0.0020;
K{-};1.20;1.40;1.80;1.90;0.0104;0.0006;0.0009;
K{-};1.20;1.40;1.90;2.00;0.0000;0.0000;0.0000;
K{-};1.40;1.60;0.00;0.05;0.3335;0.0054;0.0153;
K{-};1.40;1.60;0.05;0.10;1.7389;0.0077;0.0342;
K{-};1.40;1.60;0.10;0.15;1.2285;0.0101;0.0446;
K{-};1.40;1.60;0.15;0.20;1.6675;0.0115;0.0574;
K{-};1.40;1.60;0.20;0.25;1.9209;0.0097;0.0732;
K{-};1.40;1.60;0.25;0.30;2.0181;0.0114;0.0746;
K{-};1.40;1.60;0.30;0.35;2.0587;0.0107;0.0730;
K{-};1.40;1.60;0.35;0.40;2.0953;0.0118;0.0800;
K{-};1.40;1.60;0.40;0.45;1.9639;0.0109;0.0757;
K{-};1.40;1.60;0.45;0.50;1.7424;0.0113;0.0738;
K{-};1.40;1.60;0.50;0.55;1.6410;0.0112;0.0571;
K{-};1.40;1.60;0.55;0.60;1.3956;0.0087;0.0582;
K{-};1.40;1.60;0.60;0.70;1.2055;0.0060;0.0427;
K{-};1.40;1.60;0.70;0.80;0.8305;0.0055;0.0360;
K{-};1.40;1.60;0.80;0.90;0.5390;0.0042;0.0279;
K{-};1.40;1.60;0.90;1.00;0.3252;0.0037;0.0194;
K{-};1.40;1.60;1.00;1.10;0.2450;0.0027;0.0123;
K{-};1.40;1.60;1.10;1.20;0.1835;0.0024;0.0085;
K{-};1.40;1.60;1.20;1.30;0.1114;0.0025;0.0126;
K{-};1.40;1.60;1.30;1.40;0.0687;0.0017;0.0060;
K{-};1.40;1.60;1.40;1.50;0.0346;0.0012;0.0024;
K{-};1.40;1.60;1.50;1.60;0.0203;0.0012;0.0061;
K{-};1.40;1.60;1.60;1.70;0.0057;0.0007;0.0018;
K{-};1.40;1.60;1.70;1.80;0.0094;0.0006;0.0023;
K{-};1.40;1.60;1.80;1.90;0.0080;0.0003;0.0010;
K{-};1.40;1.60;1.90;2.00;0.0000;0.0000;0.0000;
K{-};1.60;1.80;0.00;0.05;0.2420;0.0046;0.0150;
K{-};1.60;1.80;0.05;0.10;0.5355;0.0070;0.0267;
K{-};1.60;1.80;0.10;0.15;1.0362;0.0108;0.0510;
K{-};1.60;1.80;0.15;0.20;1.2970;0.0133;0.0510;
K{-};1.60;1.80;0.20;0.25;1.4780;0.0163;0.0631;
K{-};1.60;1.80;0.25;0.30;1.4780;0.0163;0.0631;
K{-};1.60;1.80;0.30;0.35;1.5556;0.0092;0.0700;
K{-};1.60;1.80;0.35;0.40;1.3864;0.0093;0.0638;
K{-};1.60;1.80;0.40;0.45;1.3864;0.0084;0.0584;
K{-};1.60;1.80;0.45;0.50;1.2084;0.0083;0.0584;
K{-};1.60;1.80;0.50;0.55;1.2500;0.0073;0.0468;
K{-};1.60;1.80;0.55;0.60;1.0358;0.0076;0.0416;
K{-};1.60;1.80;0.60;0.70;0.8440;0.0053;0.0416;
K{-};1.60;1.80;0.70;0.80;0.5760;0.0049;0.0287;
K{-};1.60;1.80;0.80;0.90;0.3912;0.0039;0.0217;
K{-};1.60;1.80;0.90;1.00;0.2121;0.0032;0.0165;
K{-};1.60;1.80;1.00;1.10;0.1395;0.0027;0.0161;
K{-};1.60;1.80;1.10;1.20;0.1172;0.0020;0.0144;
K{-};1.60;1.80;1.20;1.30;0.0724;0.0022;0.0117;
K{-};1.60;1.80;1.30;1.40;0.0449;0.0017;0.0075;
K{-};1.60;1.80;1.40;1.50;0.0268;0.0013;0.0044;
K{-};1.60;1.80;1.50;1.60;0.0000;0.0000;0.0000;
K{-};1.60;1.80;1.60;1.70;0.0000;0.0000;0.0000;
K{-};1.60;1.80;1.70;1.80;0.0000;0.0000;0.0000;
K{-};1.60;1.80;1.80;1.90;0.0000;0.0000;0.0000;
K{-};1.60;1.80;1.90;2.00;0.0000;0.0000;0.0000;
K{-};1.80;2.00;0.00;0.05;0.1663;0.0043;0.0173;
K{-};1.80;2.00;0.05;0.10;0.4088;0.0065;0.0265;
K{-};1.80;2.00;0.10;0.15;0.7632;0.0109;0.0515;
K{-};1.80;2.00;0.15;0.20;0.9795;0.0095;0.0560;
K{-};1.80;2.00;0.20;0.25;1.1550;0.0103;0.0651;
K{-};1.80;2.00;0.25;0.30;1.2712;0.0094;0.0672;
K{-};1.80;2.00;0.30;0.35;1.2063;0.0082;0.0665;
K{-};1.80;2.00;0.35;0.40;1.1866;0.0085;0.0691;
K{-};1.80;2.00;0.40;0.45;1.0421;0.0077;0.0515;
K{-};1.80;2.00;0.45;0.50;0.9086;0.0076;0.0442;
K{-};1.80;2.00;0.50;0.55;0.9093;0.0084;0.0433;
K{-};1.80;2.00;0.55;0.60;0.6694;0.0071;0.0379;
K{-};1.80;2.00;0.60;0.70;0.5186;0.0043;0.0339;
K{-};1.80;2.00;0.70;0.80;0.3650;0.0037;0.0454;
K{-};1.80;2.00;0.80;0.90;0.2958;0.0036;0.0297;
K{-};1.80;2.00;0.90;1.00;0.1421;0.0028;0.0200;
K{-};1.80;2.00;1.00;1.10;0.0887;0.0028;0.0164;
K{-};1.80;2.00;1.10;1.20;0.0639;0.0020;0.0076;
K{-};1.80;2.00;1.20;1.30;0.0000;0.0000;0.0000;
K{-};1.80;2.00;1.30;1.40;0.0000;0.0000;0.0000;
K{-};1.80;2.00;1.40;1.50;0.0000;0.0000;0.0000;
K{-};1.80;2.00;1.50;1.60;0.0000;0.0000;0.0000;
K{-};1.80;2.00;1.60;1.70;0.0000;0.0000;0.0000;
K{-};1.80;2.00;1.70;1.80;0.0000;0.0000;0.0000;
K{-};1.80;2.00;1.80;1.90;0.0000;0.0000;0.0000;
K{-};1.80;2.00;1.90;2.00;0.0000;0.0000;0.0000;
K{-};2.00;2.20;0.00;0.05;0.1564;0.0032;0.0152;
K{-};2.00;2.20;0.05;0.10;0.3051;0.0053;0.0208;
K{-};2.00;2.20;0.10;0.15;0.4879;0.0073;0.0272;
K{-};2.00;2.20;0.15;0.20;0.6558;0.0065;0.0520;
K{-};2.00;2.20;0.20;0.25;0.7040;0.0077;0.0384;
K{-};2.00;2.20;0.25;0.30;0.7024;0.0061;0.0539;
```

## C.2 Proton $y$ - $p_T$ spectra

## C.3 Kaon rapidity spectra

### 13A GeV/c

```
species;ymin;ymax;dn/dyd;errstat;errsys;
K^+;1.00;1.20;0.8047;0.8047;0.8047;
K^+;1.20;1.40;0.5124;0.5124;0.5124;
K^+;1.40;1.60;0.3001;0.3001;0.3001;
K^+;1.60;1.80;0.1642;0.1642;0.1642;
K^-;1.00;1.20;0.1250;0.1250;0.1250;
K^-;1.20;1.40;0.0762;0.0762;0.0762;
K^-;1.40;1.60;0.0298;0.0298;0.0298;
K^-;1.60;1.80;0.0107;0.0107;0.0107;
```

```
K^+;2.00;2.20;1.3396;1.3396;1.3396;
K^-;0.40;0.60;2.6587;2.6587;2.6587;
K^-;0.60;0.80;2.4225;2.4225;2.4225;
K^-;0.80;1.00;2.1941;2.1941;2.1941;
K^-;1.00;1.20;1.9363;1.9363;1.9363;
K^-;1.20;1.40;1.5988;1.5988;1.5988;
K^-;1.40;1.60;1.3025;1.3025;1.3025;
K^-;1.60;1.80;0.9390;0.9390;0.9390;
K^-;1.80;2.00;0.6825;0.6825;0.6825;
K^-;2.00;2.20;0.4278;0.4278;0.4278;
```

### 19A GeV/c

```
species;ymin;ymax;dn/dyd;errstat;errsys;
K^+;1.00;1.20;1.0992;1.0992;1.0992;
K^+;1.20;1.40;0.8691;0.8691;0.8691;
K^+;1.40;1.60;0.5668;0.5668;0.5668;
K^-;1.00;1.20;0.2684;0.2684;0.2684;
K^-;1.20;1.40;0.1723;0.1723;0.1723;
K^-;1.40;1.60;0.0881;0.0881;0.0881;
```

### 30A GeV/c

```
species;ymin;ymax;dn/dyd;errstat;errsys;
K^+;0.80;1.00;2.0580;2.0580;2.0580;
K^+;1.00;1.20;1.6836;1.6836;1.6836;
K^+;1.20;1.40;1.2952;1.2952;1.2952;
K^+;1.40;1.60;0.9024;0.9024;0.9024;
K^+;1.60;1.80;0.5863;0.5863;0.5863;
K^-;0.80;1.00;0.6831;0.6831;0.6831;
K^-;1.00;1.20;0.5160;0.5160;0.5160;
K^-;1.20;1.40;0.3502;0.3502;0.3502;
K^-;1.40;1.60;0.2142;0.2142;0.2142;
K^-;1.60;1.80;0.1177;0.1177;0.1177;
```

### 40A GeV/c

```
species;ymin;ymax;dn/dyd;errstat;errsys;
K^+;0.80;1.00;2.4106;2.4106;2.4106;
K^+;1.00;1.20;2.0633;2.0633;2.0633;
K^+;1.20;1.40;1.6379;1.6379;1.6379;
K^+;1.40;1.60;1.2096;1.2096;1.2096;
K^+;1.60;1.80;0.8569;0.8569;0.8569;
K^-;0.80;1.00;0.9246;0.9246;0.9246;
K^-;1.00;1.20;0.7330;0.7330;0.7330;
K^-;1.20;1.40;0.5019;0.5019;0.5019;
K^-;1.40;1.60;0.3226;0.3226;0.3226;
K^-;1.60;1.80;0.1982;0.1982;0.1982;
```

### 75A GeV/c

```
species;ymin;ymax;dn/dyd;errstat;errsys;
K^+;0.60;0.80;3.3503;3.3503;3.3503;
K^+;0.80;1.00;3.1389;3.1389;3.1389;
K^+;1.00;1.20;2.8545;2.8545;2.8545;
K^+;1.20;1.40;2.3975;2.3975;2.3975;
K^+;1.40;1.60;1.8957;1.8957;1.8957;
K^+;1.60;1.80;1.4787;1.4787;1.4787;
K^+;1.80;2.00;1.0916;1.0916;1.0916;
K^+;2.00;2.20;0.8160;0.8160;0.8160;
K^-;0.60;0.80;1.7261;1.7261;1.7261;
K^-;0.80;1.00;1.4905;1.4905;1.4905;
K^-;1.00;1.20;1.2545;1.2545;1.2545;
K^-;1.20;1.40;0.9904;0.9904;0.9904;
K^-;1.40;1.60;0.6928;0.6928;0.6928;
K^-;1.60;1.80;0.4926;0.4926;0.4926;
K^-;1.80;2.00;0.3028;0.3028;0.3028;
K^-;2.00;2.20;0.1790;0.1790;0.1790;
```

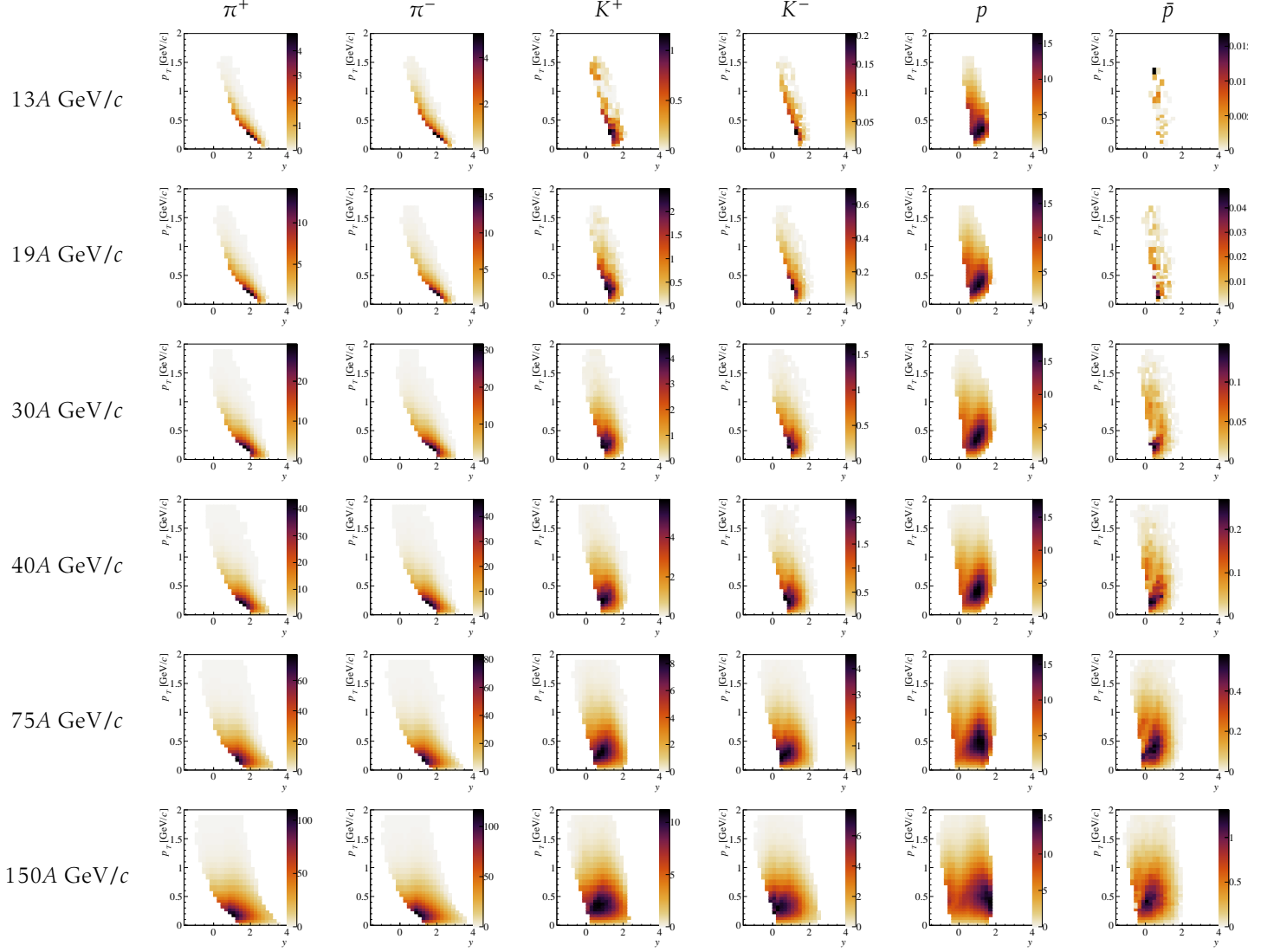
### 150A GeV/c

```
species;ymin;ymax;dn/dyd;errstat;errsys;
K^+;0.40;0.60;4.2164;4.2164;4.2164;
K^+;0.60;0.80;4.0517;4.0517;4.0517;
K^+;0.80;1.00;3.9320;3.9320;3.9320;
K^+;1.00;1.20;3.7651;3.7651;3.7651;
K^+;1.20;1.40;3.3241;3.3241;3.3241;
K^+;1.40;1.60;2.8565;2.8565;2.8565;
K^+;1.60;1.80;2.2722;2.2722;2.2722;
K^+;1.80;2.00;1.7200;1.7200;1.7200;
```

**C.4 Proton rapidity spectra**

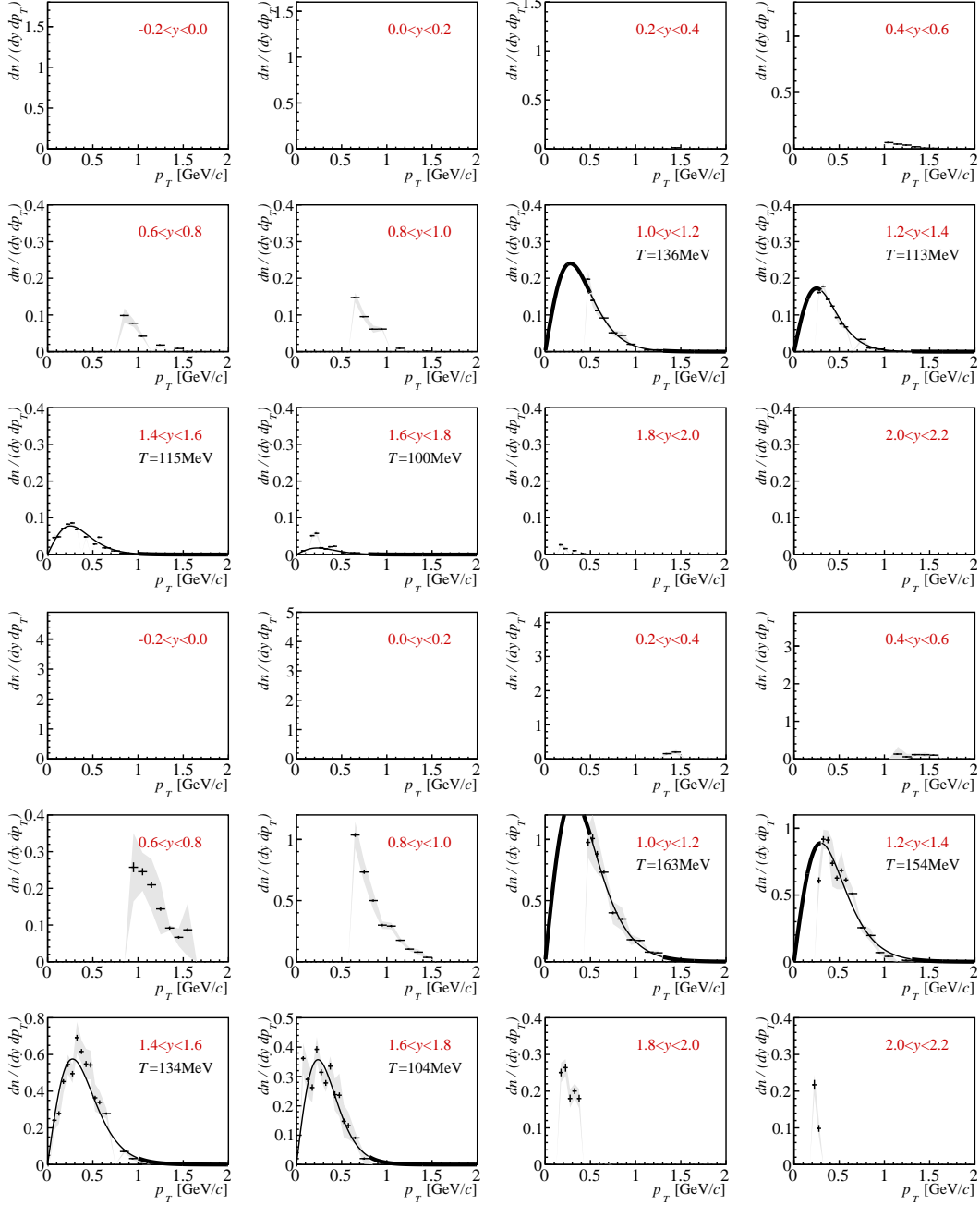
**D Supplementary plots of fitted  $p_T$  distributions**

## D.1 Two-dimensional spectra



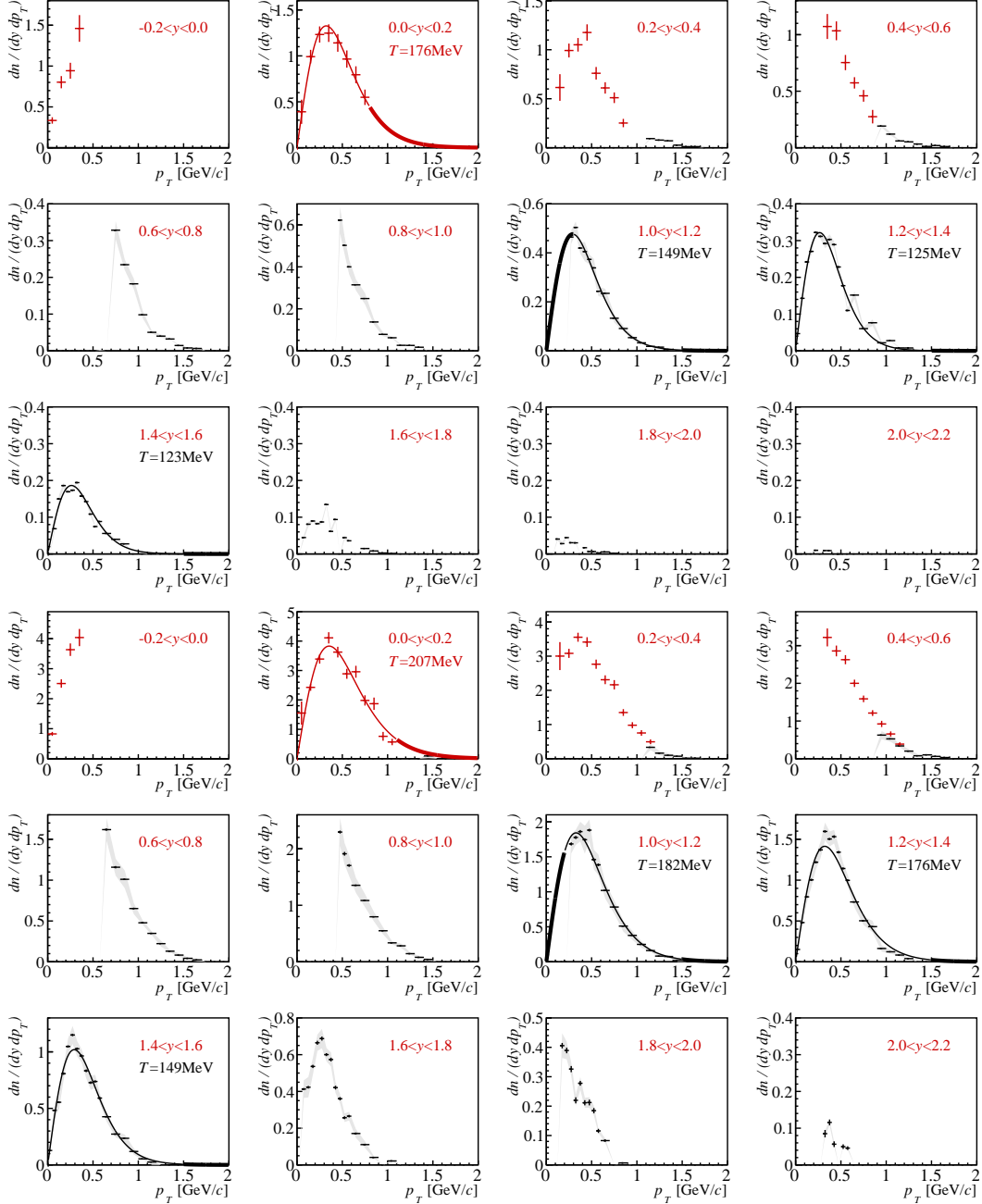
## D.2 Charged kaon $p_T$ distributions

Kaons (top  $K^-$ , bottom  $K^+$ ) at 13A GeV/c



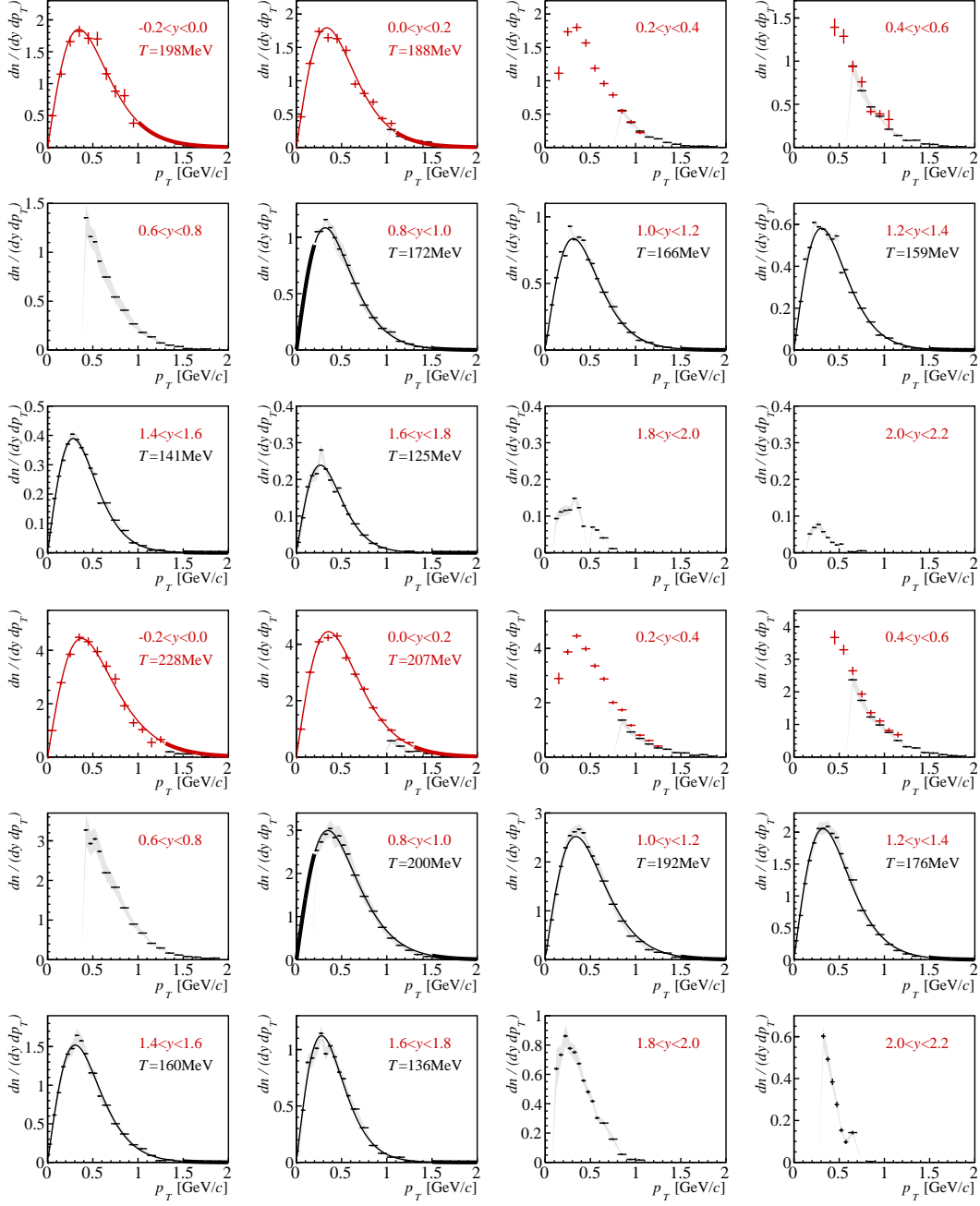
### D. Supplementary plots of fitted $p_T$ distributions

Kaons (top  $K^-$ , bottom  $K^+$ ) at 19A GeV/c



### D. Supplementary plots of fitted $p_T$ distributions

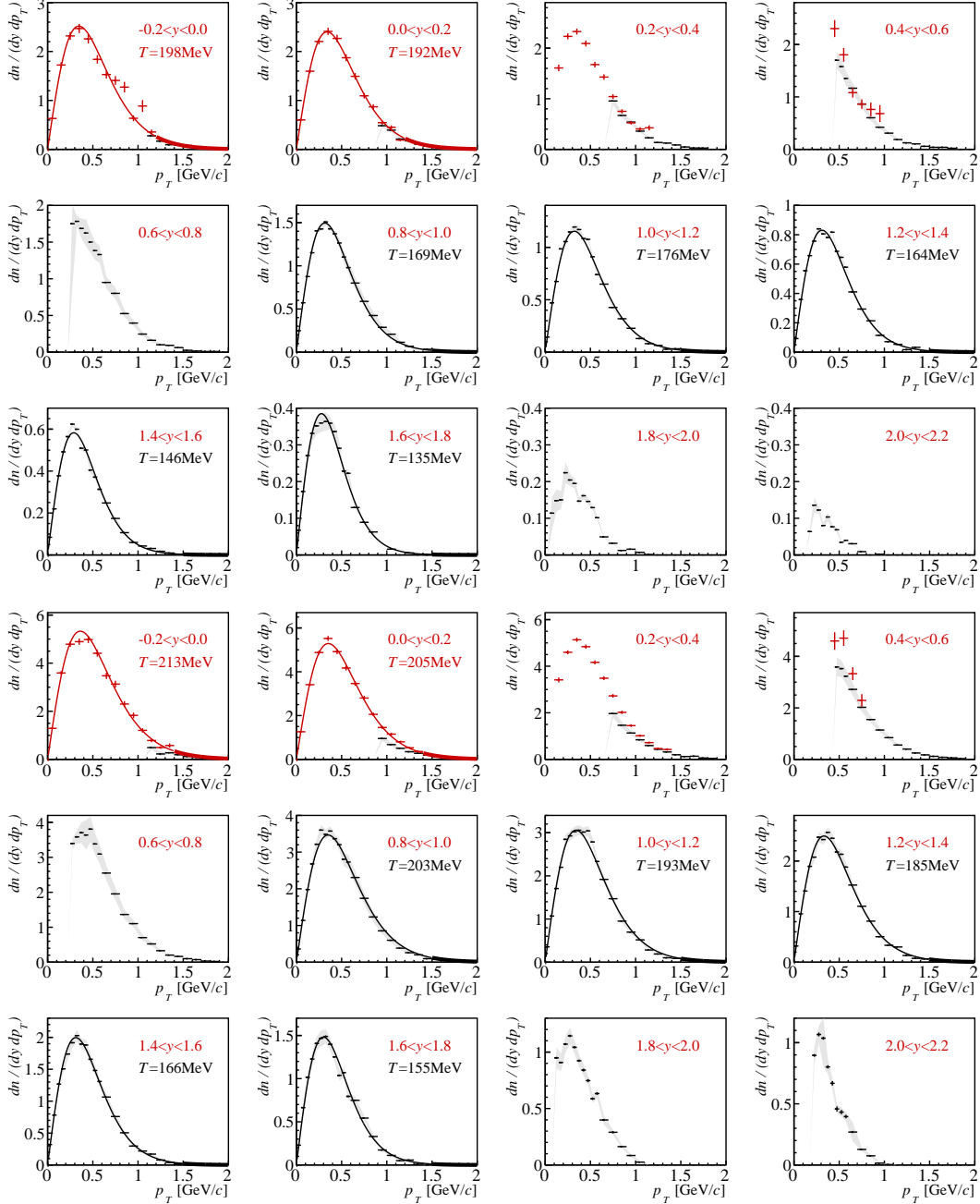
Kaons (top  $K^-$ , bottom  $K^+$ ) at 30A GeV/c





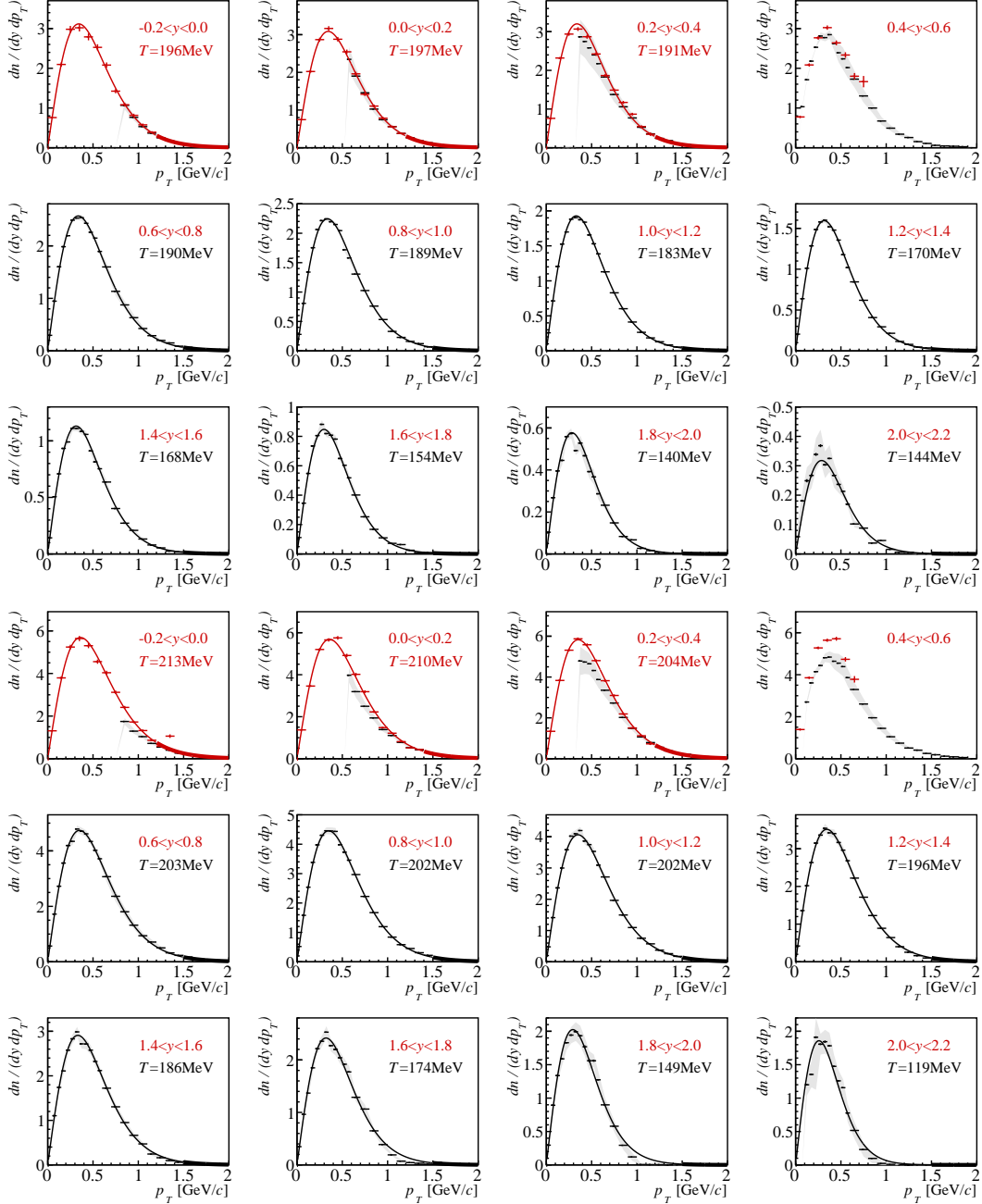
## D. Supplementary plots of fitted $p_T$ distributions

Kaons (top  $K^-$ , bottom  $K^+$ ) at 40A GeV/c



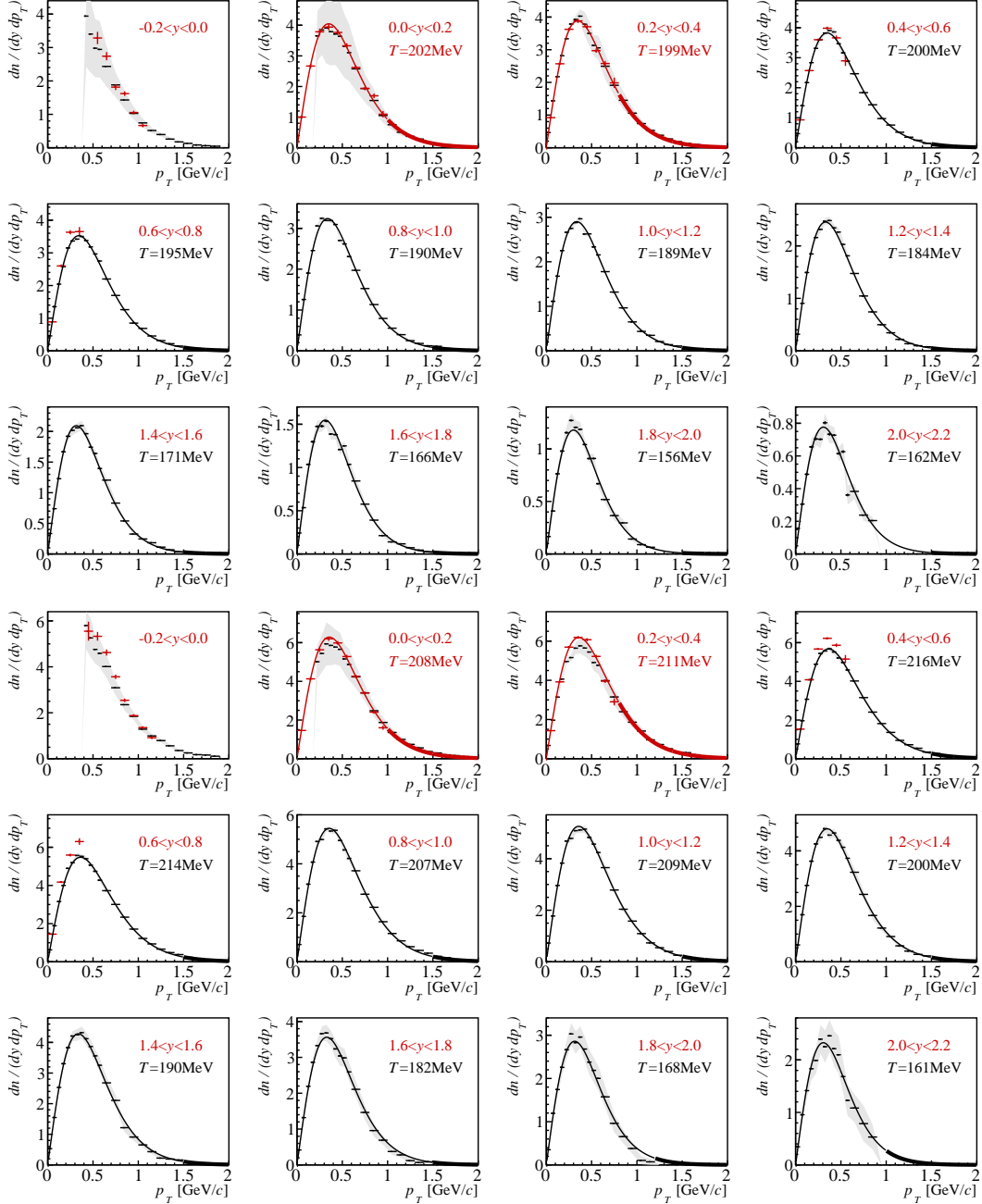
## D. Supplementary plots of fitted $p_T$ distributions

Kaons (top  $K^-$ , bottom  $K^+$ ) at 75A GeV/c



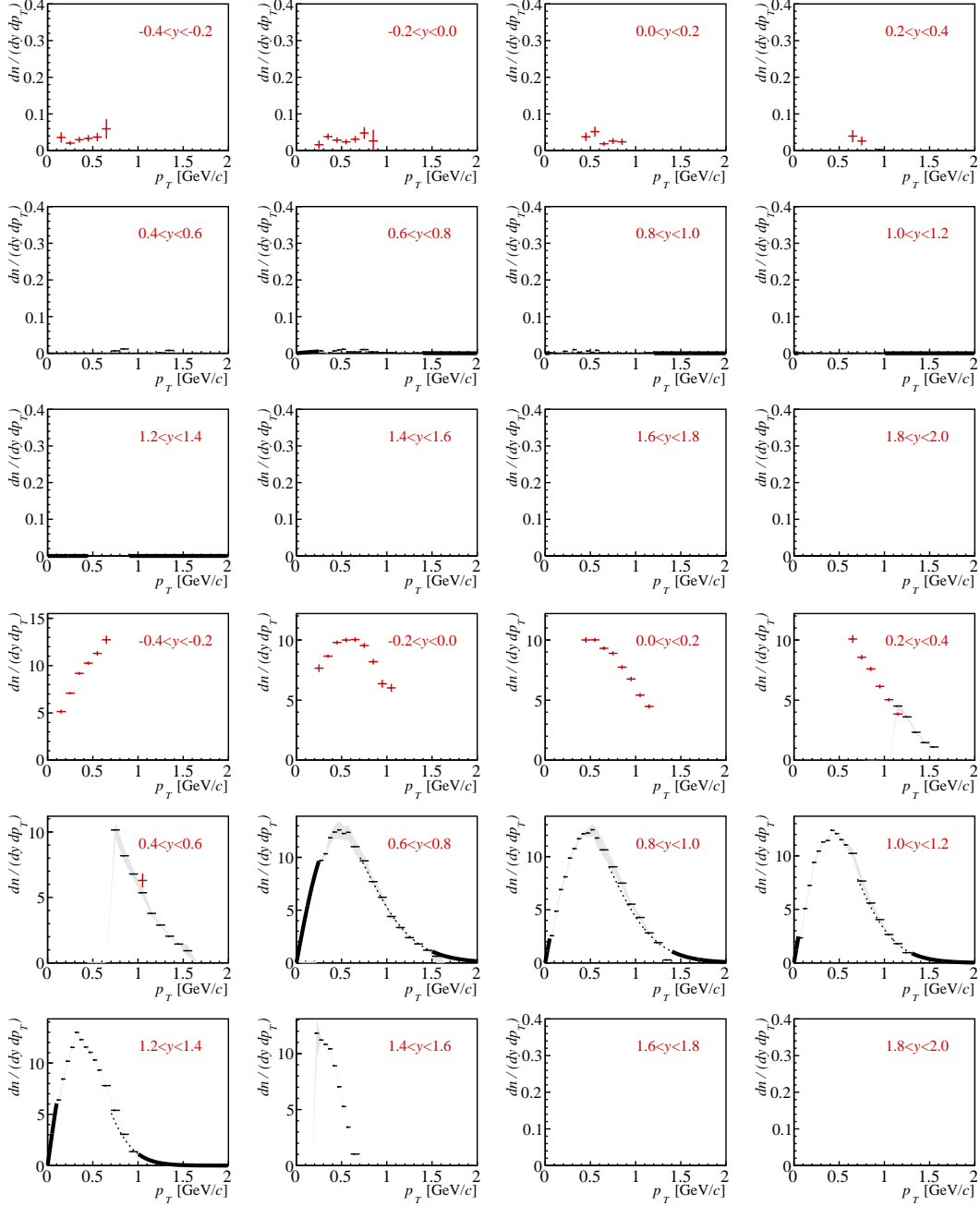
## D. Supplementary plots of fitted $p_T$ distributions

Kaons (top  $K^-$ , bottom  $K^+$ ) at 150A GeV/c



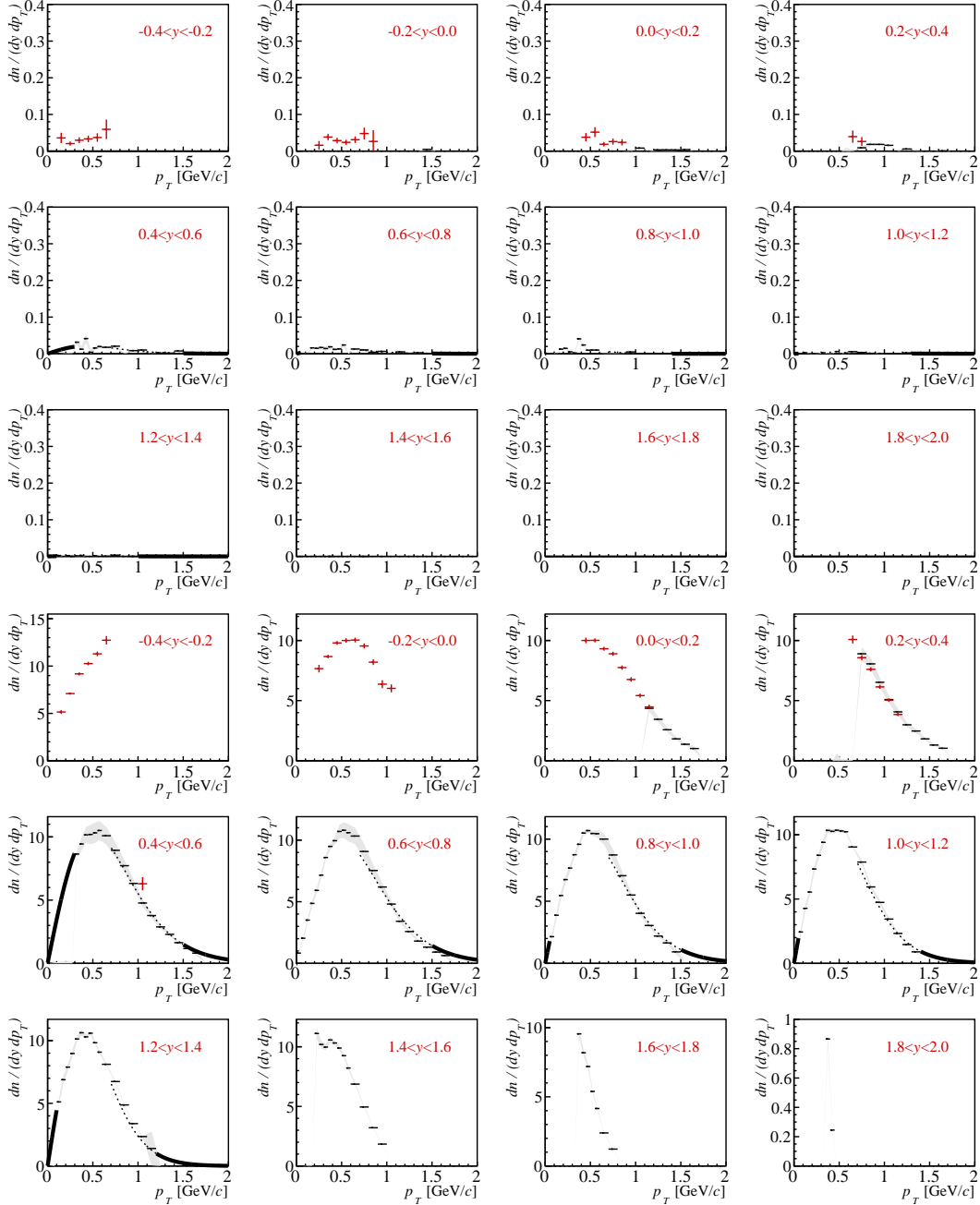
### D.3 Proton and antiproton $p_T$ distributions

Top:  $\bar{p}$ , bottom:  $p$  at 13A GeV/c



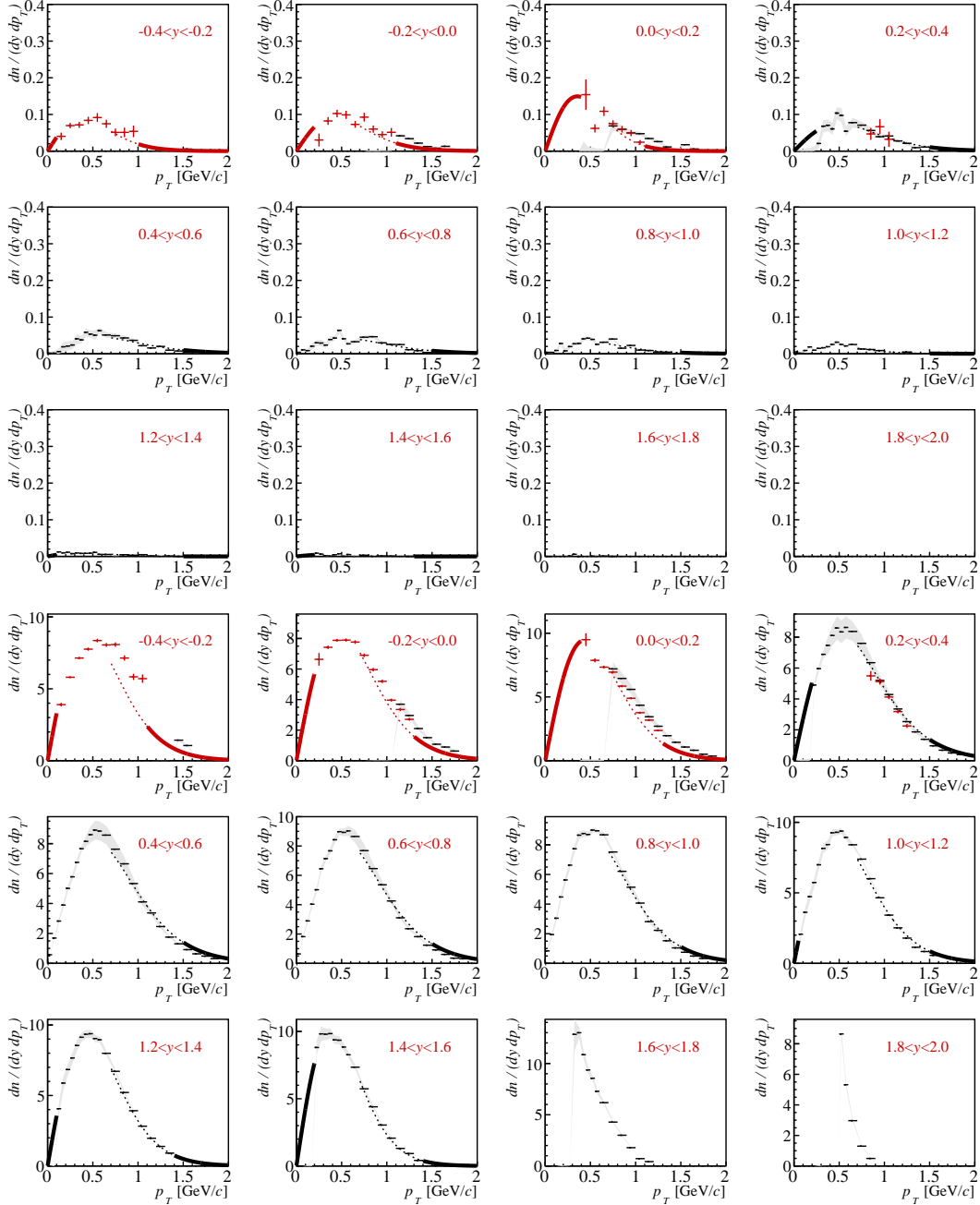
### D. Supplementary plots of fitted $p_T$ distributions

Top:  $\bar{p}$ , bottom:  $p$  at 19A GeV/c



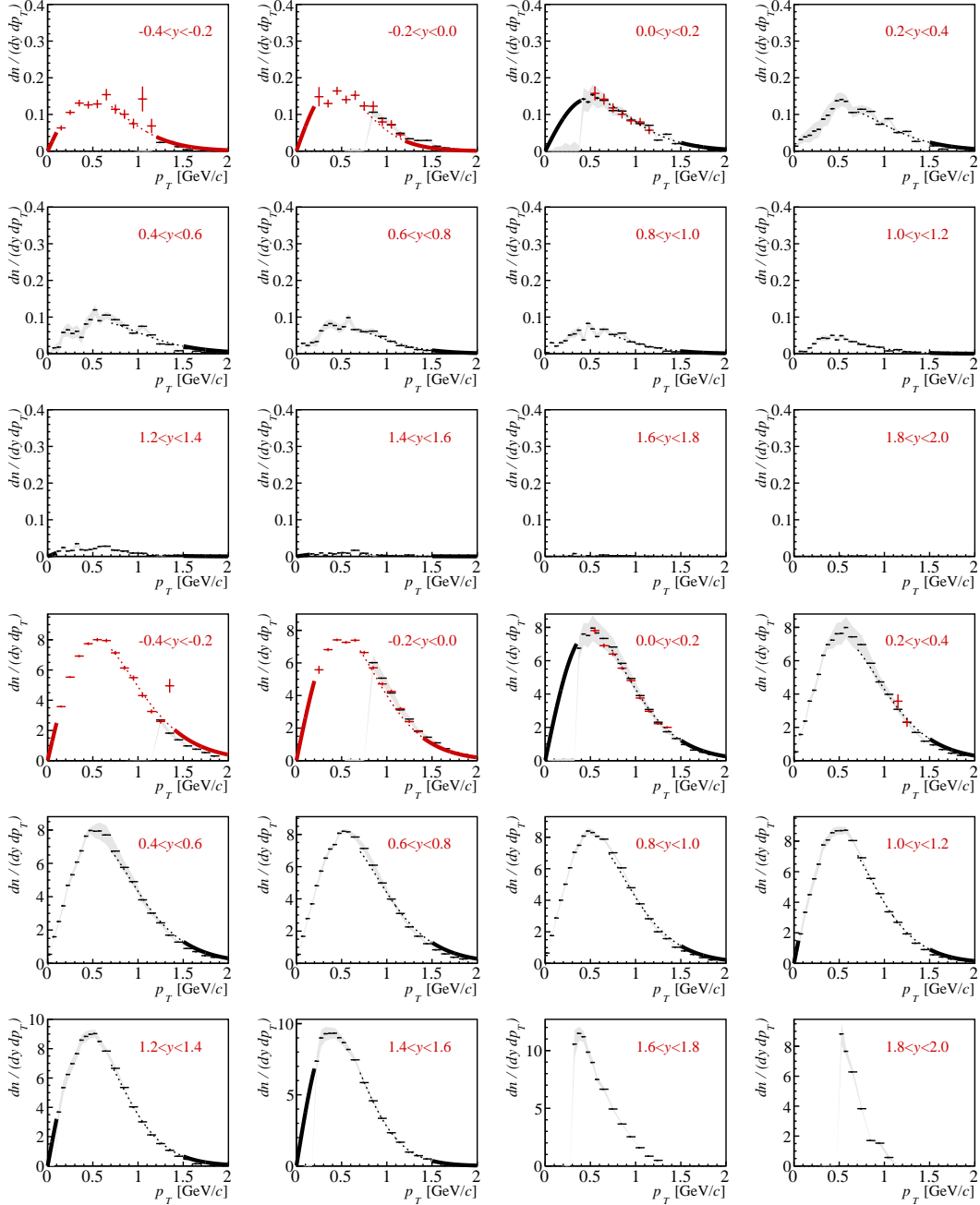
### D. Supplementary plots of fitted $p_T$ distributions

Top:  $\bar{p}$ , bottom:  $p$  at 30A GeV/c



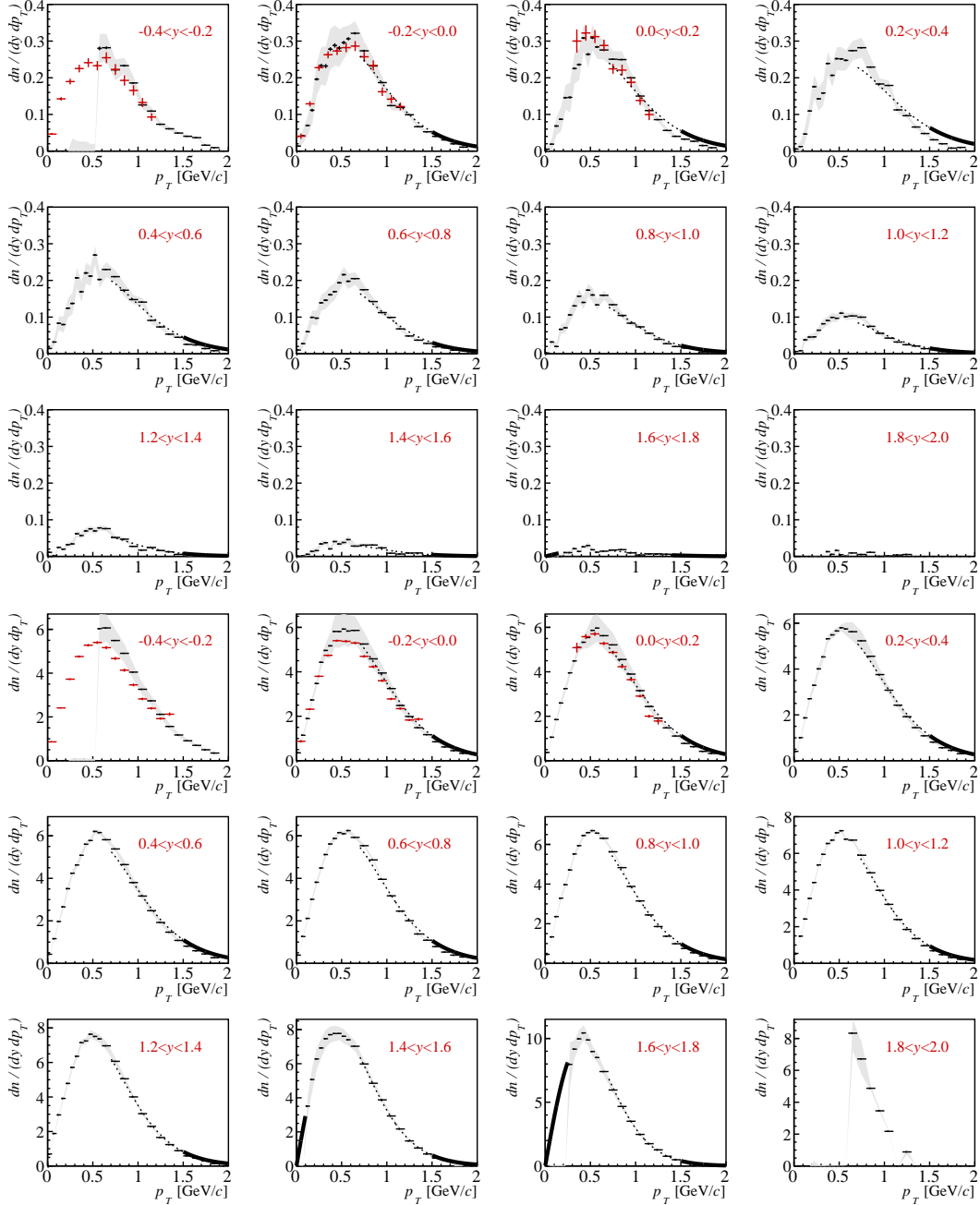
### D. Supplementary plots of fitted $p_T$ distributions

Top:  $\bar{p}$ , bottom:  $p$  at 40A GeV/c



### D. Supplementary plots of fitted $p_T$ distributions

Top:  $\bar{p}$ , bottom:  $p$  at 75A GeV/c





## D. Supplementary plots of fitted $p_T$ distributions

Top:  $\bar{p}$ , bottom:  $p$  at 150A GeV/c

